UCRL-CR-105184

GRI-90/0189

FEM3A SIMULATIONS OF SELECTED LNG VAPOR BARRIER VERIFICATION FIELD TESTS

S. T. Chan

This report was prepared for the
GAS RESEARCH INSTITUTE

October 1990

Lawrence Livermore National Laboratory

DISCLAIMER

50272-101

REPORT DOCUMENTATION PAGE	1. REPORT NO. GRI-90/0189	2.	3. Recipient's Accession No.

4. Title and Subtitle
FEM3A Simulations of Selected LNG Vapor Barrier Verification Field TEsts

5. Report Date
October 1990

6.

7. Author(s)
S.T. Chan

8. Performing Organization Rept. No
UCRL-CR-105184

UCRL-CR--105184

DE91 004201

9. Performing Organization Name and Address
Lawrence Livermore National Laboratory
P.O. Box 808, L-262
Livermore, California 94550

10. Project/Task/Work Unit No.
5088-252-1704

11. Contract(C) or Grant(G) No.
(C) 5088-252-1704
(G)

12. Sponsoring Organization Name and Address
Gas Research Institue
8600 West Bryn Mawr Avenue
Chicago, IL 60631

13. Type of Report & Period Covered
Final
Oct. 1988 - June 1990

14.

15. Supplementary Notes

16. Abstract (Limit: 200 words)

The FEM3A model, with minor modifications, has been applied to simulate the vapor dispersion of four large-scale LNG vapor barrier field experiments (of the Falcon series) and a comparison was made with relevant field data. The model was able to reproduce results consistent with the field measurements, mostly within a factor of two. For Falcon-1, with the addition of a certain amount of heat to model the superheating effects, results consistent with field observations were obtained. In particular, a vapor cloud over-filling the fenced enclosure was reproduced, as opposed to a vapor cloud essentially contained within the fence at all times observed in a pre-spill wind tunnel simulation. The simple approach currently taken to model turbulence and heat transfer in the source area has performed reasonably well; however, more sophisticated modeling of the source conditions may be necessary in order to simulate the cloud dispersion accurately at all locations. Results from simulations of the Falcon-2 and Falcon-4 experiments indicated that a vapor fence can significantly reduce the downwind hazardous distances. However, a vapor fence could also prolong the cloud persistence time in the source area, thus increasing the potential for ignition and combustion within the vapor fence and the area nearby.

17. Document Analysis a. Descriptors

Liquefied natural gas (LNG), heavy gas dispersion, atmospheric dispersion, hydrodynamic computer model, density-stratified flow, finite element method.

b. Identifiers/Open-Ended Terms

c. COSATI Field/Group

18. Availability Statement	19. Security Class (This Report)	21. No. of Pages
Available from GRI or LLNL	Unclassified	165
	20. Security Class (This Page)	22. Price

(See ANSI-Z39.18) See Instructions on Reverse OPTIONAL FORM 272 (4-77)
(Formerly NTIS-35)
Department of Commerce

RESEARCH SUMMARY

Title	FEM3A Simulations of Selected LNG Vapor Barrier Verification Field Tests
Contractor	Lawrence Livermore National Laboratory GRI Contract Number: 5088-252-1704
Principal Investigator	S. T. Chan
Report Period	October 1988–June 1990 Final Report
Objectives	To determine the ability and limitations of FEM3A as a numerical tool for simulating LNG vapor dispersion involving vapor fences and to improve the understanding of such complex vapor dispersion processes. Also, to complement the results of field and wind tunnel experiments such as providing plausible explanations for unexpected results and filling in data gaps due to instrument failure or limited array size.
Technical Perspective	There is a need for physical (wind tunnel) and mathematical models to predict realistic LNG vapor dispersion scenarios involving complex gas sources and flow effects due to terrain and obstructions. Although physical modeling is usually very useful for such studies, it has certain practical difficulties under conditions of low wind speed, low level of turbulence, and significant heat transfer. Under such conditions, advanced numerical modeling can be an effective and complementary tool to physical modeling because the physical parameters can be controlled more easily.
Results	The FEM3A model, with minor modifications, has been applied to simulate the vapor dispersion of four large-scale LNG vapor barrier field experiments and a comparison was made with relevant field data. The model was able to reproduce the essential results of the experiments within a factor of two under most circumstances. With the addition of certain amount of heat flux to the vapor source of Falcon-1 (to model the superheating effects), results consistent with field observations were obtained. In particular, a vapor cloud overfilling the fenced enclosure was reproduced, as opposed to a vapor cloud essentially contained within the fence at all times observed in a pre-spill wind tunnel simulation. The simple approach currently taken to model turbulence and heat transfer in the source area has performed reasonably well; however, more sophisticated modeling of the source conditions may be necessary for more accurate results at all locations. Results from simulations of the Falcon-2 and Falcon-4 experiments indicated that vapor fences can significantly reduce the downwind distances of flammable vapor clouds. However, a vapor fence could also prolong the cloud persistence time in the source area, thus increasing the potential for ignition and combustion within the vapor fence and the area nearby.

Technical Approach A numerical approach was taken to accomplish the objectives of this study. Specifically, relevant measurements of the field tests were examined and the FEM3A model was modified to accommodate special features of the Falcon tests. Two series of 2-D simulations, among others, were then conducted to aid the parameterization of the complex processes of turbulence and heat transfer in the source area. Finally, the modified FEM3A model was applied to simulate the selected field tests and a detailed model-data comparison was conducted.

Project Implications Results of the project have demonstrated that advanced three-dimensional numerical models such as FEM3A can be a useful tool for evaluating the effectiveness of LNG vapor fences. With further developments in the areas of turbulence, heat transfer, and humidity effects, such numerical models can be expected to greatly complement physical models, especially under the conditions of low wind speed, low level of turbulence, and significant heat transfer. While most of the reported simulations require significant computing resources on a super computer - Cray 2, it is anticipated that continuing gains in computing speed, storage, and graphics will make advanced numerical modeling more accessible for engineering applications. In contrast, field experiments can only be used for verification of modeling due to a number of considerations, including currently high and increasing cost, lack of repeatability, lack of control of ambient variables, and inherent uncertainty within field instrumentation and data.

Ted Willims
GRI Project Manager

TABLE OF CONTENTS

LIST OF TABLES

LIST OF FIGURES

Page

Page

Page

Page

Page

Page

1. INTRODUCTION

In order to evaluate and eventually predict the possible mitigating effects of vapor fences on the dispersion of the vapor cloud resulting from an accidental liquefied natural gas (LNG) spill in storage areas, the U.S. Department of Transportation (DOT) and the Gas Research Institute (GRI) initiated a research program to evaluate methods for predicting LNG dispersion distances for realistic facility configurations. As part of the program, Lawrence Livermore National Laboratory (LLNL) conducted a series of large-scale field experiments called the LNG Vapor Barrier Verification Field Trials (also referred to as the Falcon Series) at the U.S. Department of Energy's Liquefied Gaseous Fuels Spill Test Facility (LGFSTF), Nevada, in the summer of 1987. The objectives of the experiments were: (1) to provide a data base on LNG vapor dispersion from spill involving complex field obstacles to assist in validation of wind tunnel and mathematical models, and (2) to assess the effectiveness of vapor fences for mitigating LNG vapor dispersion hazards in the event of an accidental spill.

Five spill experiments were conducted, covering releases of LNG at rates of 9 to 30 m^3/min and spill volumes ranging from 21 to 66 m^3. The spills were conducted on water in order to generate vapor at rates equivalent to the liquid spill rates. To this end, a 40 m by 60 m recirculating pond was constructed (and filled with water to about 0.76 m in depth) at the end of the spill pipes from the LGFSTF. A 0.3-m diameter spill line was connected to a system of four 0.15-m diameter spill distribution lines (referred to as the spill "spider") to distribute rapidly spilling LNG across the pond surface. The pond was enclosed by a fiberglass vapor fence of 88 m long, 44 m wide, and 8.7 m high. In addition, a 17.1 m wide by 13.3 m high billboard-like barrier was erected upwind of the pond to simulate the presence of a storage tank. A sketch of the vapor fence is shown in Fig. 1.1. Details of the experiments and field data can be found in the GRI Report No. 89/0138.

Due to the complexity in both physics and geometry of the spill scenarios, wind tunnel modeling has generally been regarded as the best-suited, economical way for predicting

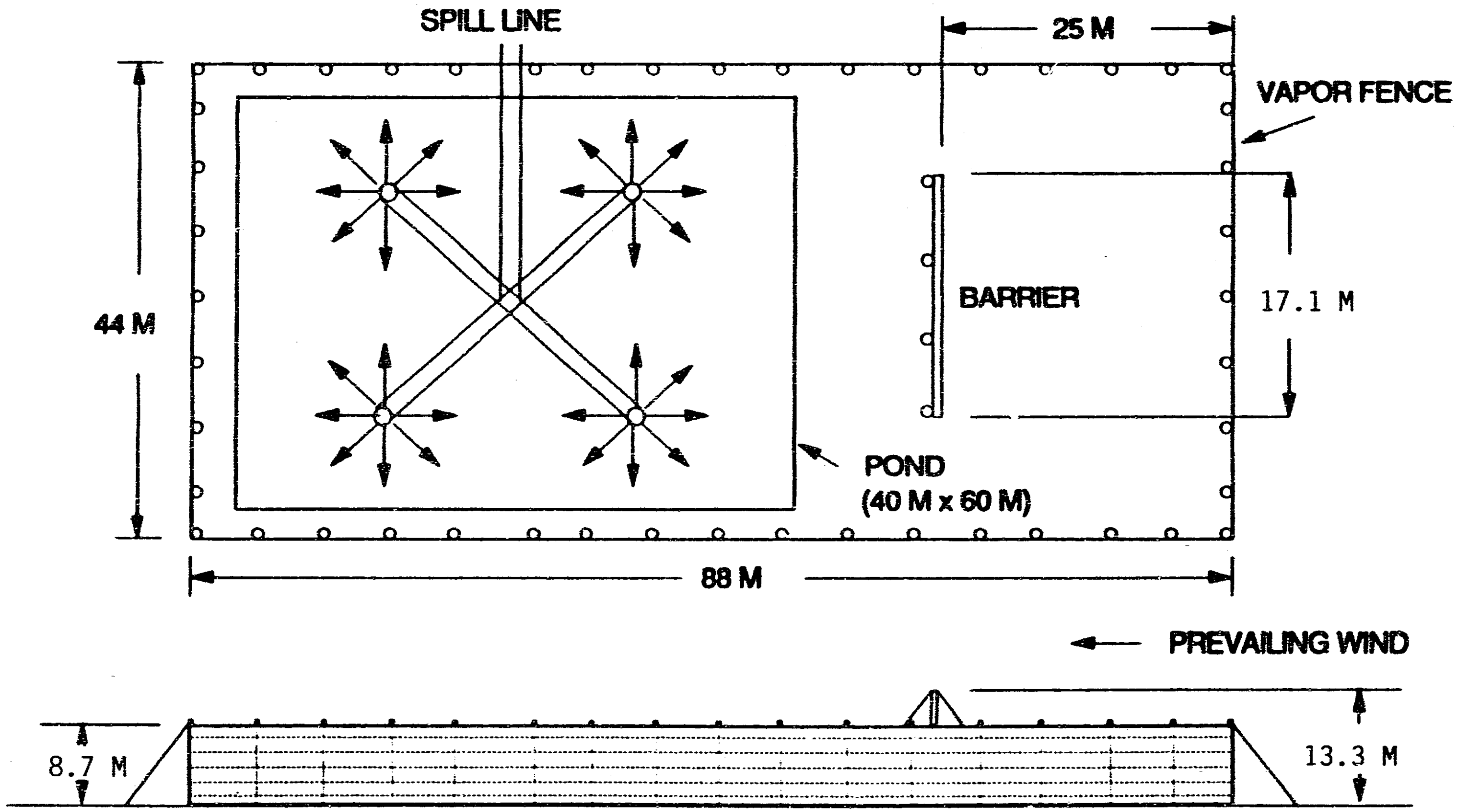

Fig. 1.1. The vapor fence configuration for the Falcon series spill experiments.

the dispersion distances of hazardous concentrations of LNG vapor. However, under conditions of low wind speed, low level of turbulence, and significant heat transfer involving cryogenic gases, wind tunnel modeling of a dense-gas plume has certain practical difficulties and is generally more contentious than a comparable positively buoyant release (Britter, 1989). In fact, a pre-test wind tunnel simulation of the Falcon-1 test produced a vapor cloud which was essentially contained within the vapor fence for all times, which strongly contrasted with the Falcon-1 field release where the vapor cloud greatly overfilled the fenced enclosure. In many cases, especially under the above circumstances, accurate three-dimensional mathematical models can be an effective and complementary tool to wind tunnel modeling. With numerical models, the physical parameters can be controlled more easily and detailed temporal and spatial results can often provide insights into the physical processes involved in the cloud dispersion. Actually, the usefulness of currently available numerical models such as FEM3 for simulating a wide range of heavy-gas dispersion scenarios has already been demonstrated (see, e.g., Chan and Ermak, 1984 and Chan et al., 1987). More recently, an improved version of FEM3, called FEM3A (Chan, 1988), was applied for the first time to evaluate the effectiveness of vapor fences for controlling LNG dispersion (Wiersma and Williams, 1990).

In this study, the FEM3A model was applied to simulate four of the Falcon experiments. The objectives of this study were, through numerical modeling and a detailed model-data comparison: (1) to improve our understanding of LNG vapor dispersion involving vapor barriers, (2) to assess FEM3A in modeling such complex vapor dispersion scenarios, and (3) to complement the results of field and wind tunnel tests, such as providing plausible explanations for unexpected results and filling in data gaps due to instrument failure or limited array size. Toward these goals, the relevant field measurements were analyzed and several series of 2-D and 3-D simulations were carried out. The 2-D simulations were performed mainly to improve our understanding of the physics involved in the spill scenarios and to aid the modeling of turbulence and heat transfer in the source area. The

3-D calculations were conducted to complement the field and wind tunnel experiments and to assess the performance of the numerical model via a detailed model-data comparison of the simulated tests.

In the next section, the major characteristics of the simulated tests, including some early simulations to aid the parameterization of turbulence and heat transfer in the source area, are described. In Section 3, a detailed model-data comparison for the simulated tests, Falcon 1 through 4, is presented and discussed. Additionally, a brief assessment of the effectiveness of the vapor barrier is conducted for Falcon-4. Finally, some conclusions and recommendations are presented in the last section.

2. SIMULATIONS OF FIELD TESTS

2.1 Selected Field Tests

Five LNG vapor dispersion tests were conducted in the Falcon series of experiments (GRI report No. 89/0138). During the last test, i.e., Falcon-5, large rapid phase transition (RPT) explosions occurred at approximately 60 s after the spill and a fireball started inside the vapor fence at 81 s. Since Falcon-5 has only limited data up to about 100 s (for sensors outside of the fence), it was excluded from the present study. Although the remaining four tests, except perhaps Falcon-4, are deficient in one way or the other, these tests have produced sufficient good quality data and were thus all included in this study. Listed in Table 2.1 are the spill and meteorological parameters of these tests.

Table 2.1 Spill and meteorological parameters

Parameter \ Test	Falcon-1	Falcon-2	Falcon-3	Falcon-4
Spill volume (m^3)	66.4	20.6	50.7	44.9
Spill rate (m^3/min)	28.7	15.9	18.9	8.7
Water temperature (°C) (pre/post spill)	28.4/22.4	23.6/20.6	no data	23.2/22.0
Temperature at 2m (°C)	32.8	31.6	34.9	31.1
Avg. windspeed at 2m (m/s)	1.7	4.7	4.1	5.2
Air pressure (mb)	908.9	905.0	900.8	906.3
Stability class	G	D	D	D/E
Momentum diffusivity at 2m (m^2/s)	0.0165	0.313	0.255	0.265
Richardson number at 2m	0.1337	−0.0193	−0.0047	0.0252
Friction velocity (m/s)	0.0605	0.3565	0.3053	0.3694
Monin-Obukhov length (m)	4.963	−103.4	−422.2	69.38
Roughness length (m)	0.008	0.008	0.008	0.008

The major characteristics and any deficiencies of the select d tests are summarized below:

Falcon 1—This test is important in that it had the highest spill volume and the highest spill rate (excluding Falcon 5) and was conducted under very stable atmospheric conditions. The vapor cloud in this test overflowed the vapor fence on all four sides in contrast to the pre-test wind tunnel simulation which produced a vapor cloud essentially contained within the fence enclosure for all times. Although the sensor array was apparently too narrow to capture the entire cloud, very useful data are still available for model validation purposes. This test is markedly different from the rest of the tests, as it represents an LNG cloud dispersion resulting from high spill rate and calm wind conditions.

Falcon 2—This test had an intermediate spill rate and a relatively short spill duration (78 s), and was conducted under neutral ambient conditions. Unfortunately, due to internal software problems, no data from the LLL-IR gas sensors was available. However, temperature measurements and concentration data from the MSA gas sensors (mostly deployed at downwind locations and at 5 m high and above) are available.

Falcon 3—This test is more or less a repeat of Falcon-2. but with a spill duration roughly twice as long (161 s). It produced a large quantity of good quality data; however, it was plagued to some extent by significant RPTs, which started at approximately 60 s after the spill began. The RPT effects must indeed be taken into consideration in the model-data comparison.

Falcon 4—This test had the smallest spill rate, the longest spill duration (310 s), and was conducted under neutral to slightly stable conditions. Due to its relatively long spill duration, this test could be considered, for most practical purposes, as having a continuous source with all the field variables reaching their respective steady state. Compared to the results of other tests, the data of this test appear to contain more high-frequency components (or more turbulent intermittency), because of its low spill rate and high wind speed.

As part of an investigation into the surprising results of Falcon-1, some of the field data are examined and compared herein. Depicted in Fig. 2.1 are the time series of concentration at two almost identical locations (near the fence side and almost aligned with the billboard) within the fence enclosure. Data at a few other locations also exist for these tests except for Falcon-1, which has only one operational gas sensor within the vapor fence. These time series are mostly consistent with the spill and atmospheric conditions. For instance, Falcon-3 has significantly higher concentration and longer persistence time than Falcon-2, because it has higher spill rate and much longer spill duration. Also, the low spill rate of Falcon-4 has yielded concentration considerably lower than the above two tests. Surprisingly, the maximum concentration of Falcon-1 is markedly lower than those measured in Falcon-2 and Falcon-3, despite the fact that its spill rate is almost twice that of Falcon-2 and 50% higher than Falcon-3.

In Fig. 2.2, the measured temperature at the center of spill are compared (unfortunately, due to RPTs, no data was available beyond 60 s for Falcon-3). Although the data for Falcon-3 are incomplete, it does seem true that a significantly lower temperature than all the other tests was realized. In contrast, the measured temperature of Falcon-1 is unusually high, despite this test having the highest spill rate. Specifically, its minimum temperature is 20°C above that of Falcon-2, almost 40°C higher than Falcon-3, and is comparable to that of Falcon-4.

There are three possible explanations for the "anomaly" of Falcon-1: (1) the concentration and temperature data are invalid, (2) turbulent mixing increased greatly during the spill, and (3) the evaporated LNG has been heated above its normal boiling point temperature (the so-called superheating) by the water underneath, thus yielding a much warmer and more diluted vapor source.

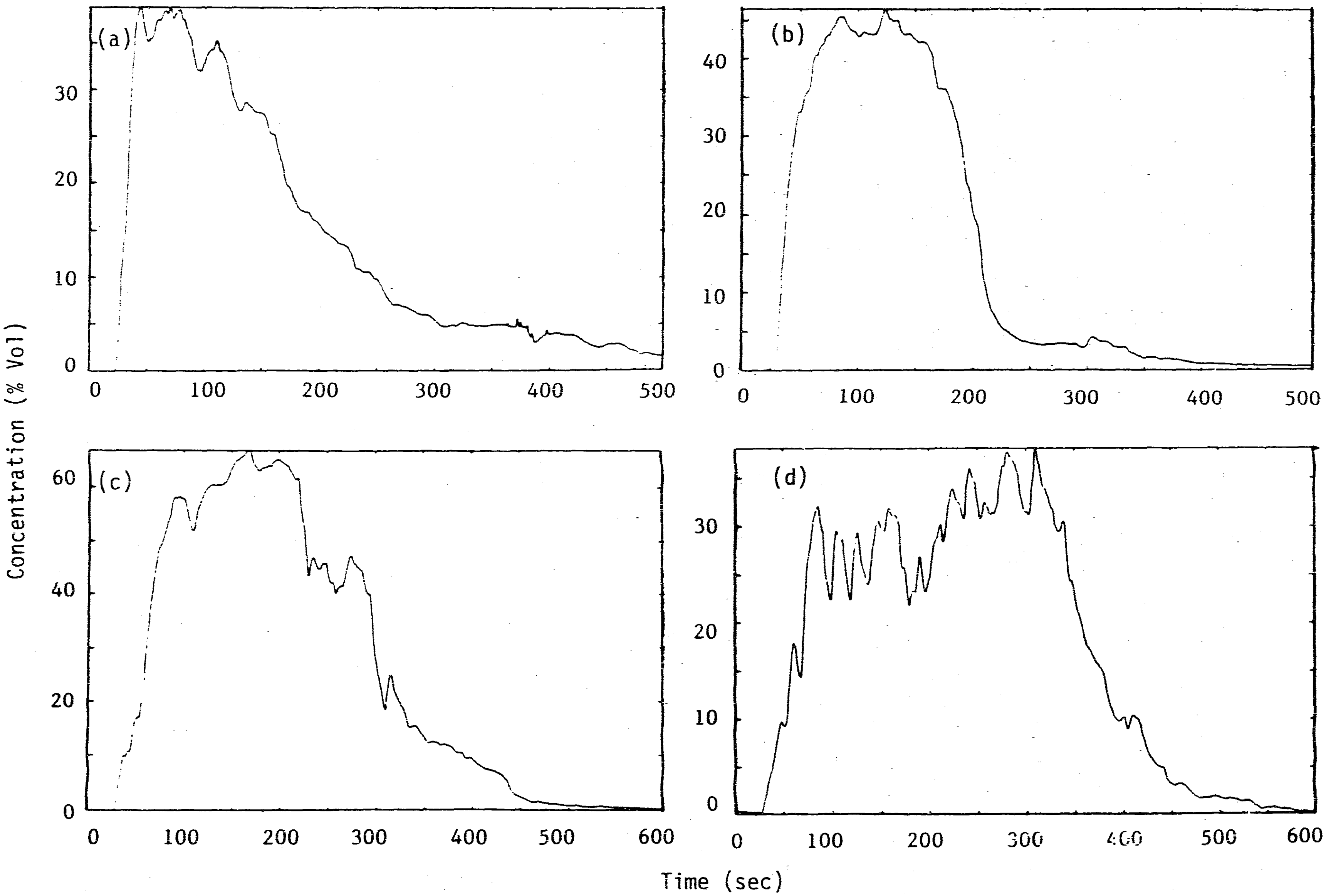

Fig. 2.1 Measured concentration inside the vapor fence at:
(x, y, z) = (-62m, 20m, 1m) for (a) Falcon-1 and (b) Falcon-2,
(x, y, z) = (-62m, 20m, 2m) for (c) Falcon-3 and (d) Falcon-4.

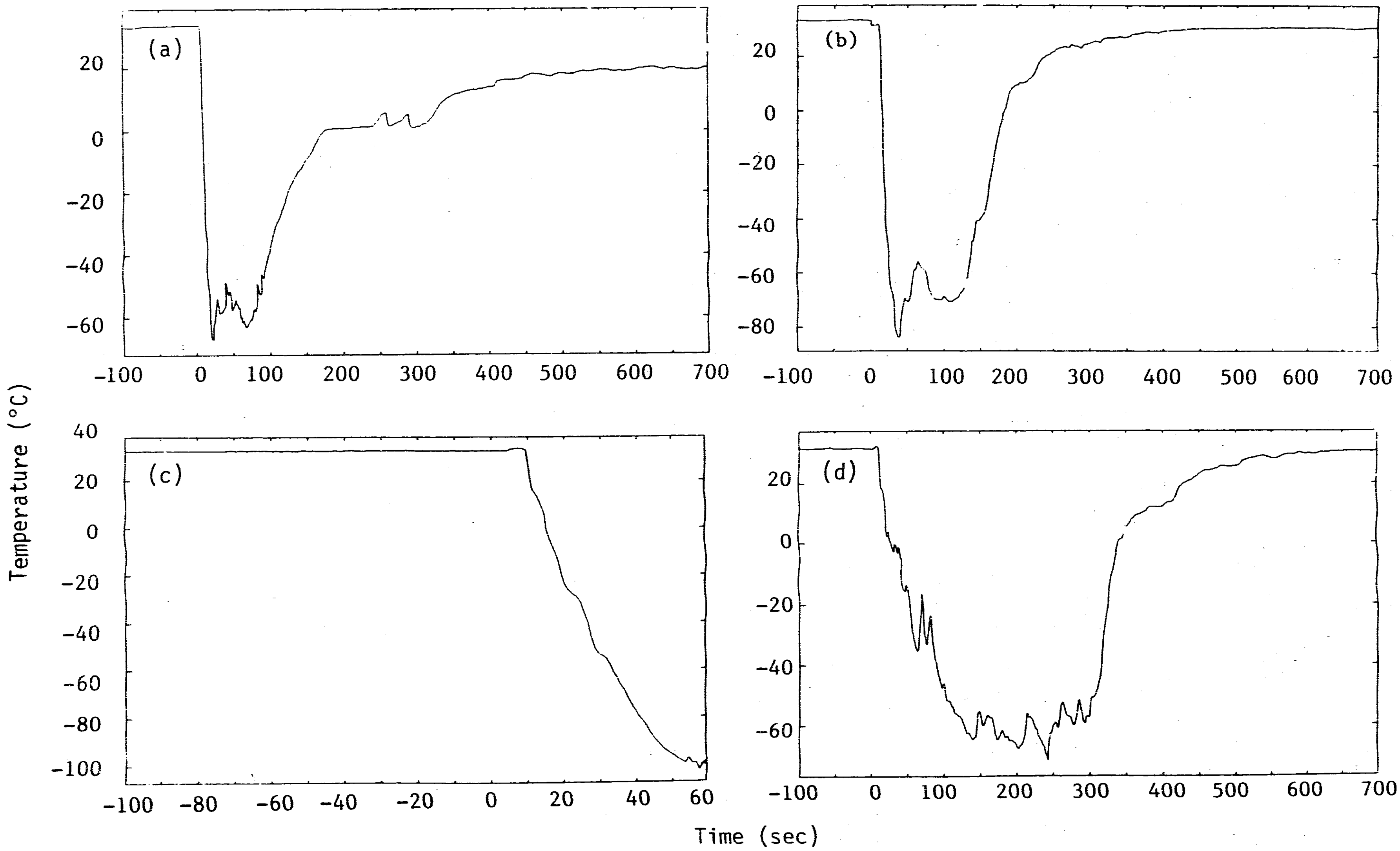

Fig. 2.2 Measured temperature inside the vapor fence at (x, y, z) - (-32m, 0, 1m) for: (a) Falcon-1, (b) Falcon-2, (c) Falcon-3, and (d) Falcon-4.

Regarding the field measurements, a close examination of the measured data from Falcon-1 has revealed nothing particularly unusual. For the dozen or so thermocouples deployed inside the vapor fence, all the measured temperatures appear to be consistently above -70°C. Unfortunately, there was only one operational gas sensor within the fence and no corresponding temperature was available to allow us to cross-check the heat balance at that location.

With regard to turbulence enhancement, since Falcon-1 has higher LNG exiting velocity (65 m/s versus 32.5 m/s for Falcons 2 and 3), more turbulent mixing can be expected in the spill area. In this regard, a series of 2-D simulations with various levels of turbulence was conducted, whose numerical results (to be discussed in Subsection 2.4) indicated that very intensive turbulent mixing would be required in order to make the predicted concentration field agree well with the measured data, but then the corresponding temperature field tended to remain much colder than observed. Although a further increase in diffusion could presumably bring the predicted temperature to agree better with field data, however, the predicted concentrations would drift away from the measured values. Therefore the reasoning of enhanced turbulence alone (without extra heating of the vapor source) is not a very satisfactory answer.

It is highly probable that the results of Falcon-1 were caused by enhanced turbulence and superheating. The latter is strongly supported by Fig. 2.3, which indicates an unusually large drop in water temperature near the center of spill (~8°C in this case versus 1 to 2°C for Falcon-4). Further evidence is provided by the measured cloud temperature and concentration in Fig. 2.4. For concentration above 10% or so, the measured temperature is approximately 10 to 20°C higher than the value obtained by mixing adiabatically the given NG concentration with the ambient air. The possibility of superheated vapor was discussed in a pre-spill document by the Department of Transportation (DOT, 1985), in which a vapor temperature increase between 10 to 35°C was considered credible. Ruff, et al. (1988) have reported similar superheating phenomenon (with as much as 40°C rise in

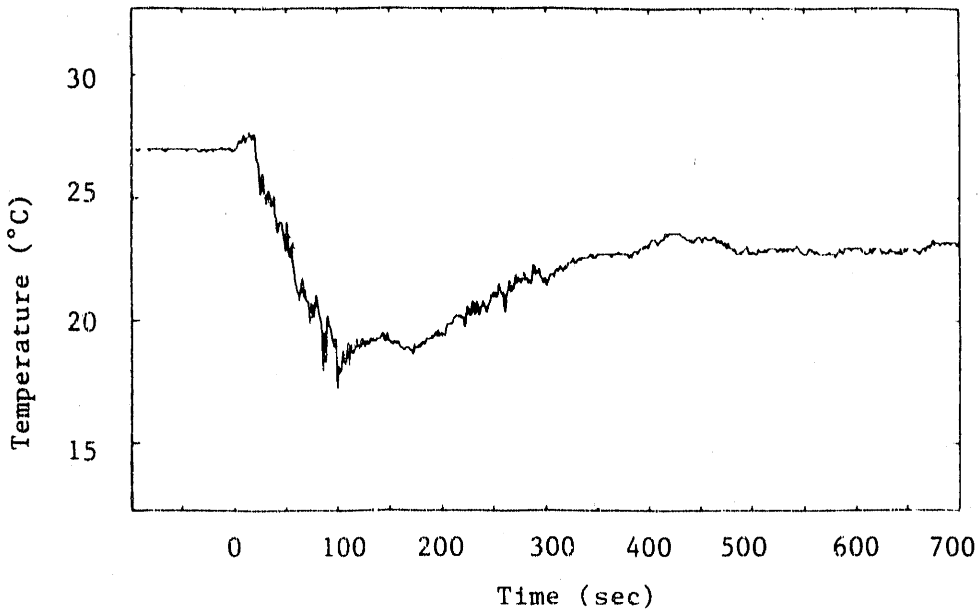

Fig. 2.3 Measured temperature beneath the water surface at (x,y,z) = (-32 m, 0, -0.05 m) in the water pond.

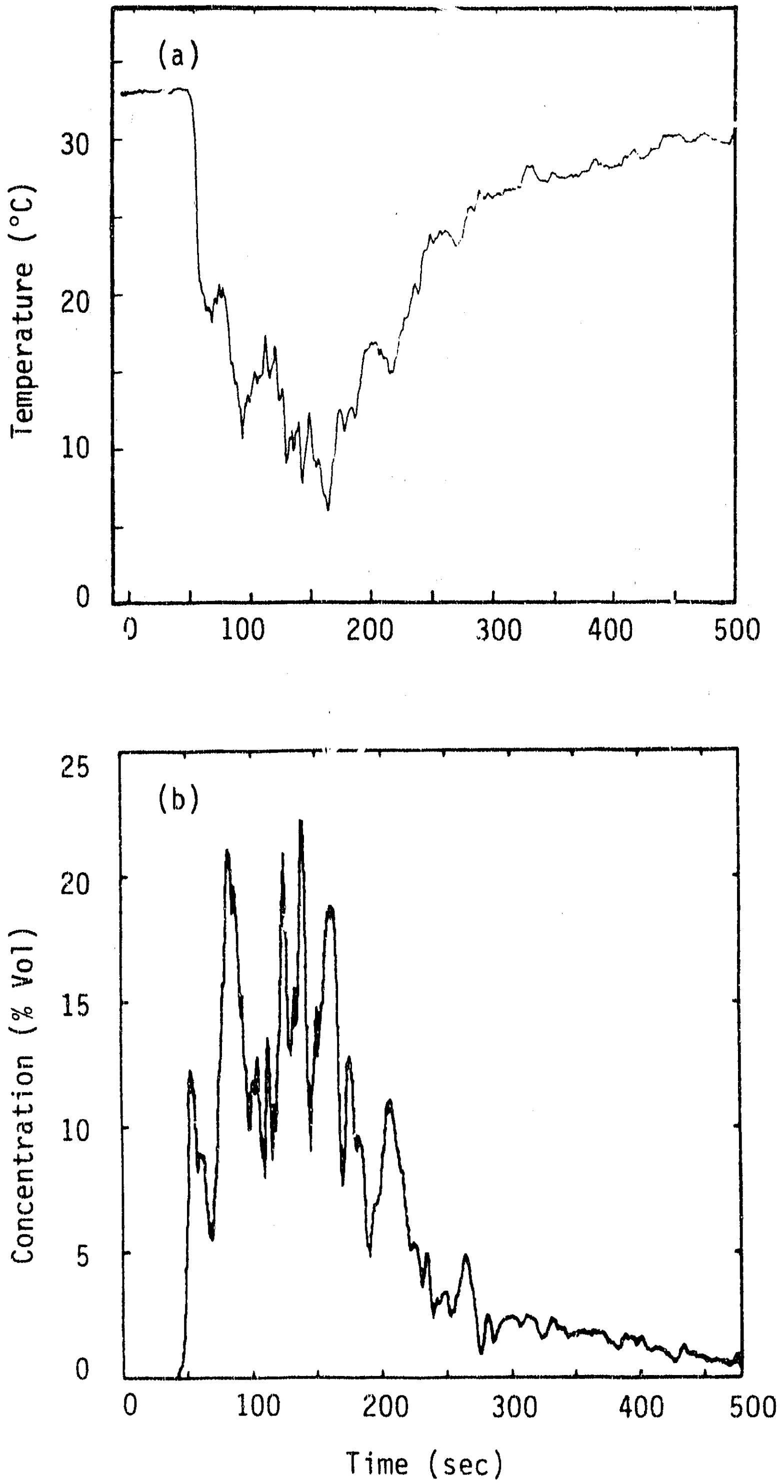

Fig. 2.4 Measured temperature and concentration from gas sensor G04, which is 50 m behind the rear fence and near the cloud centerline. Its exact location is (x, y, z) = (50 m, -22 m, 1 m).

vapor source temperature attributing to heat transfer from the bulk water underneath) in their laboratory experiments of confined spills of LN_2. It is conjectured that the high spill rate and low level of ambient turbulence of the Falcon-1 spill test are some of the factors that allow the LNG source to be warmed up considerably above its boiling point (See Subsection 2.4 for results from numerical experiments).

2.2 FEM3A and Modifications

The major features of FEM3A are described in the Appendix. In order to be able to simulate the Falcon tests, however, certain modifications were necessary. These included generalization of the base state to include a linear temperature profile, modification of turbulence modeling in the vicinity of the fence enclosure, and the addition of superheating effects in the source submodel. These changes are detailed below.

Generalization of the base state

For some of the tests being simulated, the background temperature was not a constant but could be better-approximated by a linear function of height. Corresponding to such a background temperature, there exist a hydrostatic pressure field and a motionless state. For reasons of numerical accuracy and the convenience of applying outflow boundary conditions, it is desirable to eliminate the above base state from the momentum equations. To do so, the background temperature, its associated hydrostatic pressure, and the corresponding density in the code have been generalized to be,

$$T = T_o - \gamma z, \tag{1}$$

$$P_h = P_o(1 - \frac{\gamma z}{T_o})^{M_a\, g/R\gamma}, \tag{2}$$

and

$$\rho_h = \frac{P_h M_a}{RT}, \tag{3}$$

in which T_o is the reference temperature, γ is the constant lapse rate of temperature, z is the height, P_o is the reference pressure, M_a is the molecular weight of air, g is the constant of gravitational acceleration, and R is the universal gas constant.

Modification of turbulence modeling

Because the existing turbulence submodel in FEM3A was based on similarity theory of the atmospheric boundary layer over flat terrain and without obstructions, it is not appropriate for complex situations such as the source region or near the vapor fence/billboard. For instance, the presence of the fenced enclosure and billboard will generally result in turbulence enhancements; the spill mechanism (i.e., jetting of LNG onto the pond) will also create additional turbulence in the source area. Further complications are the presence of convective mixing inside the gas cloud caused by the warm water underneath. All these processes are not in the existing submodel and are difficult to model accurately. For these reasons, an approach combining the existing variable K-model and constant diffusivities was used in the final 3-D simulations reported in Section 3. Specifically, the existing K-model with heavy-gas effects was applied everywhere except within and near the vapor fence (defined by x = -101 m to 30 m, y = 0 to 26 m, and z = 0 to 20 m in Fig. 2.5) wherein a constant value of diffusivities was employed to approximate the net amount of turbulence (production plus suppression) contributed by all sources, including ambient turbulence and those due to the presence of vapor fence/billboard, spill mechanism, convective mixing, and turbulence suppression due to the presence of a negatively buoyant gas cloud. Justifications for taking the present simple approach include: (1) there was no validated turbulence submodel that could be readily adapted for the present spill scenarios, (2) developing a more sophisticated submodel would require substantial effort beyond the scope of the present study, and (3) lack of sufficient experimental measurements on turbulence and heat transfer in the source area further hinders the development of a more sophisticated parameterization.

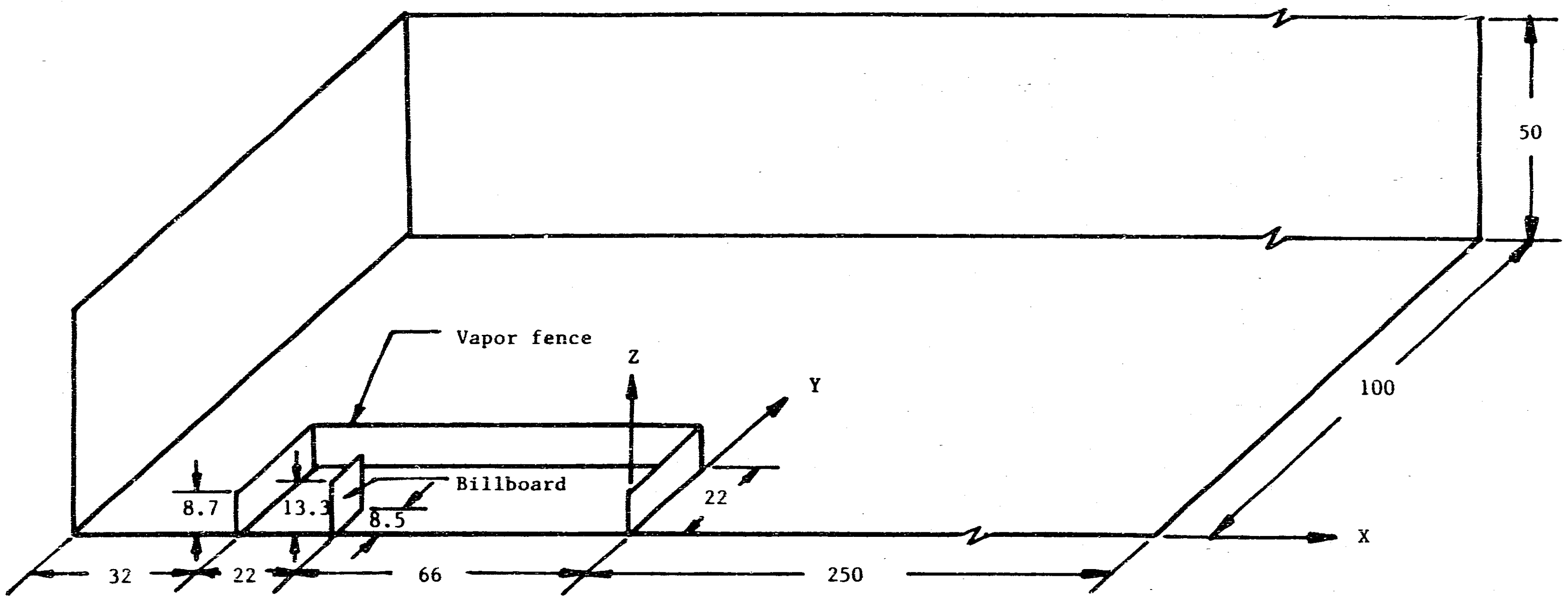

Fig. 2.5 Sketch of computational domain and dimensions (in meters) of one-half of the vapor fence and billboard. The X-Z plane is assumed to be the plane of symmetry.

Currently the following ad hoc formula is used to estimate a constant value of diffusivities to be used (in all directions) within and near the fence enclosure:

$$K = CK_2 + V_i L. \tag{4}$$

in which the first term represents the ambient turbulence and the enhancement by the presence of vapor fence/billboard, the second term is for contributions related to the spill and source conditions. The respective symbols are: C = empirical constant (currently taken to be 1.5), K_2 = vertical diffusivity at 2 m high in the ambient atmosphere, V_i = source injection velocity, and L = length scale (currently taken to be 8.7 m, which is the height of the vapor fence).

The above simple-minded scheme of parameterization was adapted, based on a few 2-D simulations of the Falcon spill tests and a brief comparison of the simulated results with the measured data in the spill area. Apparently, estimates based on such a formula are very crude for the actual, complex turbulence mixing process but hopefully they are reasonable enough to represent the bulk (or average) of turbulent mixing occurring inside and near the vapor fence. As will be seen in Table 2.2 in Subsection 2.5, the second term (for contributions from the spill and source conditions) is a dominating factor for Falcon-1, is equally important as the first term for Falcon-2 and Falcon-3, and accounts for approximately one-third of the total diffusivity in the case of Falcon-4.

Source submodel and superheating effects

As pointed out by Waite, et al. (1983), the spread of a liquid on another liquid of greater density is difficult to describe mathematically. When the spreading liquid is a cryogen such as LNG, the simultaneous heat transfer and vaporization render the process even more intractable. They also pointed out that experimental information on the concomitant heat transfer was rather incomplete. For instance, estimates of the heat flux from water to the liquefied gas pools have ranged over a factor of 4, from 25 to 100 kW/m^2. Although a fairly general model has been proposed for modeling the pool spread and heat transfer and was briefly tested against certain experimental results, substantial efforts are required to implement and evaluate it for the present applications.

For the above reasons, a simple approach has been taken in the present study. The current source submodel assumes that the spilled LNG evaporates as fast as it is spilled, uniformly in time and over the entire pond surface area. Additionally, depending on experimental evidence. extra heat flux may be supplied to superheat the vapor source such as the case of Falcon-1. Currently, the superheating effects are modelled by adding a predetermined amount of heat flux (to the temperature equation) over the source area during the period of simulated spill. Specifically, such heat flux is added to the right-hand side of equation (A.10) of the Appendix in the form of $q/(\rho \text{ Cp})$, in which q is the specified amount of heat flux in units of Watts/m^2.

2.3 Computational Mesh

The computational domain for simulations with the presence of fence enclosure is shown in Fig. 2.5. In order to conserve computing costs, the x-z plane was assumed to be the plane of symmetry. thus only one-half of the field was simulated in all cases. The domain is 370 m long (starting at 120 m upwind of the rear fence and ending at the 250-m row of gas sensors), 100 m wide (for one-half of the field in the crosswind direction), and 50 m high. The choice of such a computational domain and the associated mesh design were largely dictated by the desire to capture the most important flow/cloud structures and, at the same time, to keep the computing costs at a reasonable level (say, no more than 5 to 10 hours of computer time per simulation on a Cray-2 computer).

The domain was subdivided into 27,200 grid points (85 x 20 x 16 in the longitudinal, lateral and vertical directions, respectively), distributed nonuniformly for higher cost-effectiveness. The 2-D computational domain was composed of the 1,360 mesh points (85 x 16) on the vertical plane of symmetry in the 3-D mesh. The minimum grid spacings were 0.4 m vertically and 1 m in the two horizontal directions. The maximum grid spacings were 10 m and 15 m, respectively. Even with such relatively fine grid spacings, the small-scale structures of the flow field such as the thin boundary layer near the fence (which was actually modelled as 1-m thick solid walls so as to avoid the stringent time step size and high computing cost otherwise required in the numerical simulations) and the ground are not expected to be well resolved. However, large-scale structures of the flow and the cloud are hopefully captured with reasonable accuracy.

In order to investigate the relative performance of the present vapor barrier, Falcon-4 was also simulated without the fence enclosure. The computational domain was extended to 400 m downwind and a graded mesh consisting of 16,884 mesh points (67 x 18 x 14) was used.

2.4 Early Simulations

During the early phase of this study, certain 2-D and 3-D simulations were performed. The calculations were conducted primarily for the following purposes: (1) to determine the usefulness and cost-effectiveness of 2-D simulations in approximating the actual field experiments, and (2) to improve our understanding of the physics pertaining to the LNG vapor barrier field experiments and to aid the modeling of turbulence and heat transfer in the source area through the much less expensive 2-D simulations.

Among the early trials were a number of 2-D and a 3-D simulations of the Falcon-4 experiment. First, a calculation using the existing turbulence submodel (with heavy-gas effects) was performed and found to yield too much turbulence damping within the vapor fence, apparently due to the omission of turbulence enhancement provided by the fence/billboard and the spill mechanism. To account for such effects, a 2-D and a 3-D simulations were then conducted using the turbulence level preexisting in the ambient atmosphere only. The assumptions were that the heavy-gas cloud and the fence enclosure (including the spill mechanism) have compensating effects on turbulent mixing, and their net perturbation to the ambient turbulence was negligible. For this particular test, the above assumptions actually turned out to be quite reasonable, based on a comparison of certain 3-D results with the field data.

In Fig. 2.6, the predicted concentration contours at time = 180 s obtained from the 2-D simulation are compared with those on the vertical plane of symmetry in the 3-D simulation. The most obvious difference is perhaps the blocking of the 2-D cloud by the billboard and the relatively high windspeed nearby (not shown). In the 3-D simulation no such blocking was observed, because the billboard has a finite width, thus permitting the vapor cloud to spread laterally and fill the space in-between the front fence and the billboard. Additionally, the 3-D cloud is somewhat lower and shorter than its 2-D counterpart, obviously due to its spreading and diffusion in the lateral direction. Thus, for a given downwind location, a 2-D simulation generally yields higher concentration and faster cloud arrival time than those from an equivalent 3-D simulation. In spite of the above differences, the two clouds are very similar qualitatively and therefore useful information can be obtained from an inexpensive 2-D simulation, which usually takes only a few minutes instead of hours for a 3-D simulation.

Based on the above premise, two series of 2-D simulations were conducted for Falcon-1 in an attempt to come up with some reasonable estimates of relevant physical parameters to be used in the source area. Specifically, the first series of simulations was carried out to estimate the diffusivities required to represent the complex mixing process in the vicinity of the vapor fence; the second series was performed to determine the approximate extent of superheating.

In the first series of numerical experiments, the following four cases were run with: (a) the ambient turbulence level (with $u_* = 0.06$ m/s and L = 5 m), (b) constant diffusivities of $K_v = K_h = 0.3$ m^2/s, (c) twice the turbulence level of (b), and (d) four times the turbulence level of case (b).

Sample results are presented in Figs. 2.7 through 2.10 for the predicted temperature and concentration at the center of spill and a location 50 m behind the rear fence. Compared

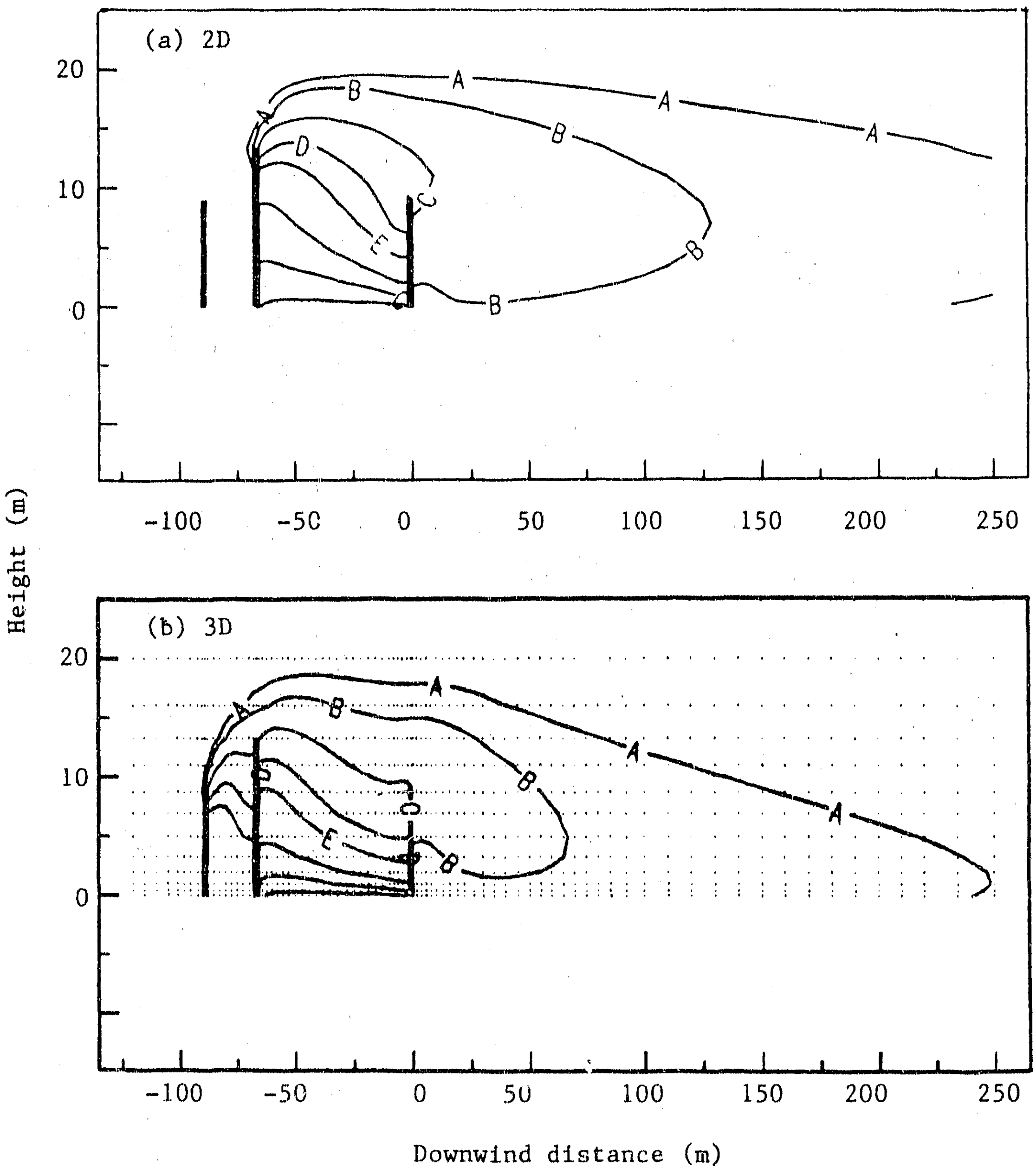

Fig. 2.6. Comparison of predicted concentration contours on the vertical plane of symmetry at t = 180 sec as obtained with two-dimensional and three-dimensional simulations. The contour levels are (in % vol): A=1, B=2, C=5, D=10, E=15, F=25, G=35, and H=50.

with the field data in Figs. 2.2(a), results from all the runs (Fig. 2.7) imply a cloud which is too cold and lingers too long within the vapor fence. As a consequence, the predicted results behind the fence (Figs. 2.9 and 2.10) also imply a cloud which is too cold and its arrival time is significantly slower than observed (Fig. 2.4). As demonstrated in Fig. 2.6, the above trends are also to be expected in 3-D simulations.

Among the four cases simulated, the results of case (a) differ the most from the actual field data implying that the actual level of turbulence inside the fence was far more intensive than the ambient turbulence level. Results from the other three simulations were more reasonable. In particular, case (d) has probably delivered the "best" overall results. The predicted temperature at the center of spill, nevertheless, was still much lower than the measured value (-132°C versus -65°C). Based on these results, an increase in turbulence level by another factor of two to three would be required in order to bring the temperature to a closer agreement with data. However, the corresponding concentration would become lower than observed and the results at x = 50 m would also drift away from the measured data. Therefore enhanced turbulence *alone* (in the context of constant diffusivities) does not appear to be a satisfactory answer to resolve all the above discrepancies.

As a plausible mechanism to explain the large discrepancy still remaining between the predicted and measured temperature, the possibility of superheating in the source area was numerically investigated. One piece of evidence supporting the above hypothesis is provided by the temperature measured beneath the water surface at the center of spill (see Fig. 2.3), which indicates a temperature drop of roughly 8°C in 100 s. A simple heat balance calculation reveals that, in order to vaporize all the LNG spilled, the water temperature in the spill pond has to drop uniformly by 3.3°C. Although the entire body of water in the pond might not have cooled uniformly by 8°C, the temperature was probably fairly uniform because there were circulation lines in the pond to keep the water well mixed. Thus it is not inconceivable to expect the water in the pond to cool down 4 to 5°C on average, which is more than sufficient to provide the heat required to vaporize all the

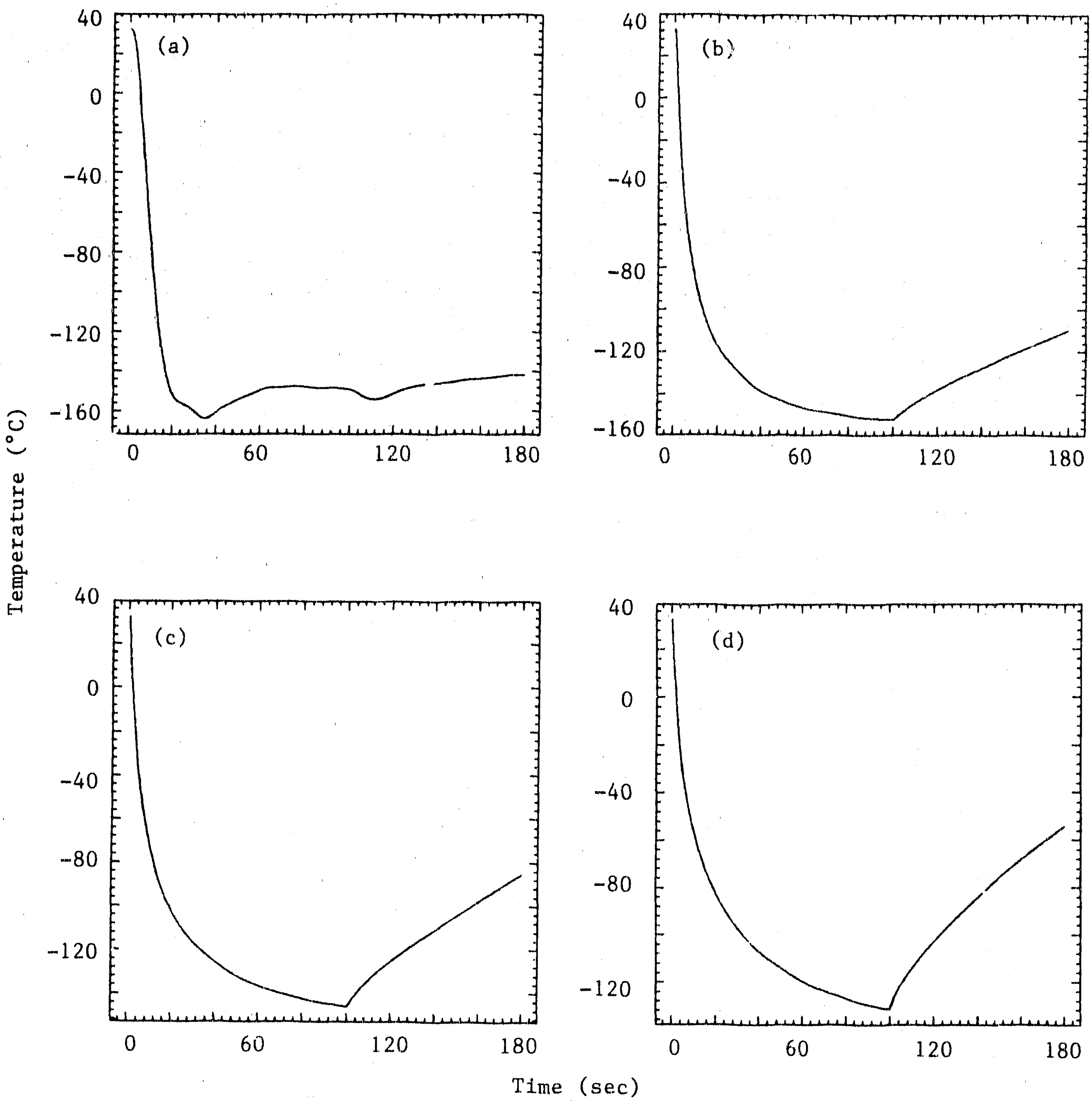

Fig. 2.7. 2D simulation results of temperature near the center of spill at (x,z) = (-32 m, 1 m), as obtained with various levels of turbulent mixing:
(a) ambient turbulence, (b) K = 0.3 m^2/sec,
(c) K = 0.6 m^2/sec, (d) K = 1.2 m^2/sec.

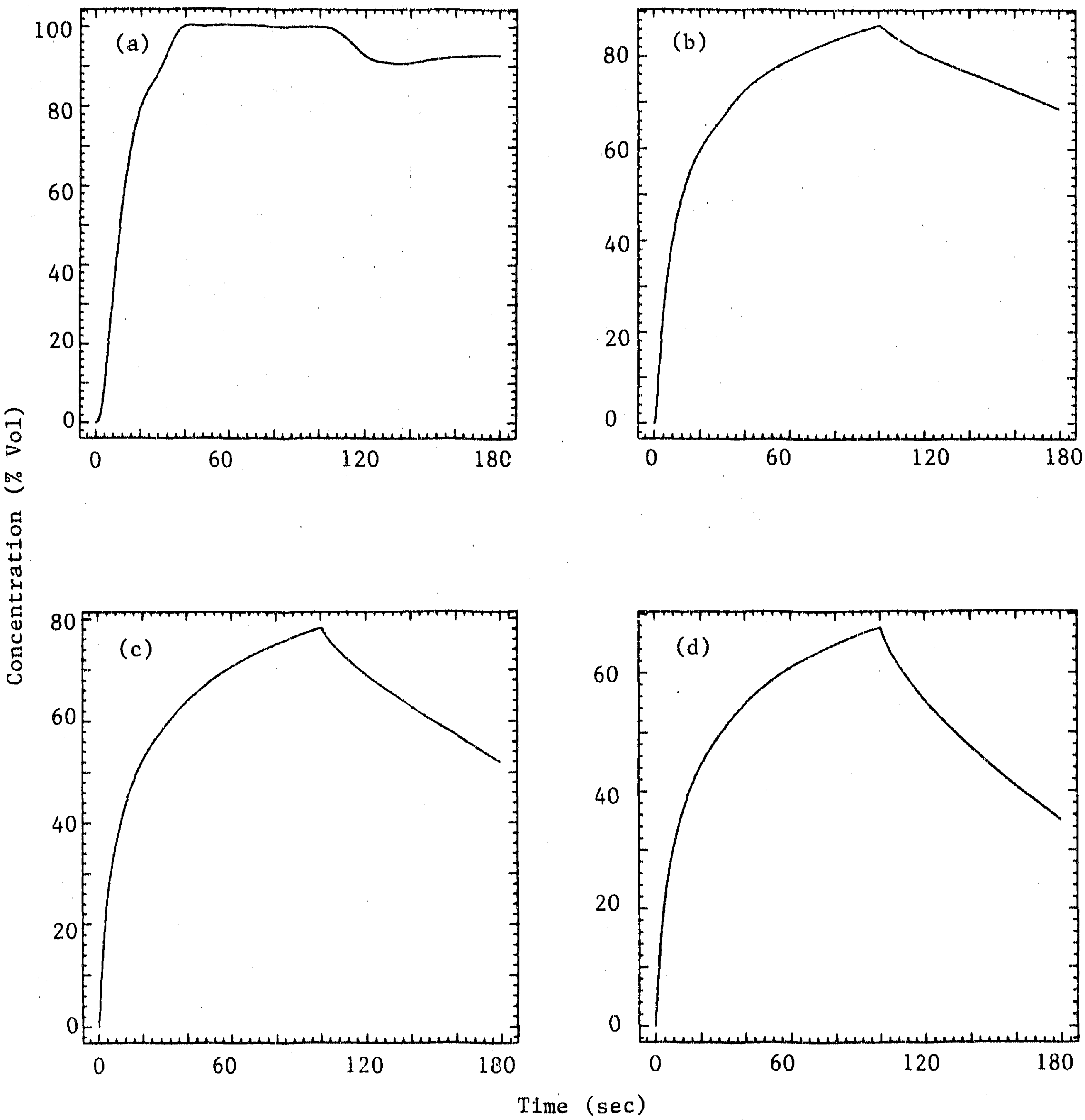

Fig. 2.8. Same as Fig. 2.7 except the comparison is for concentration.

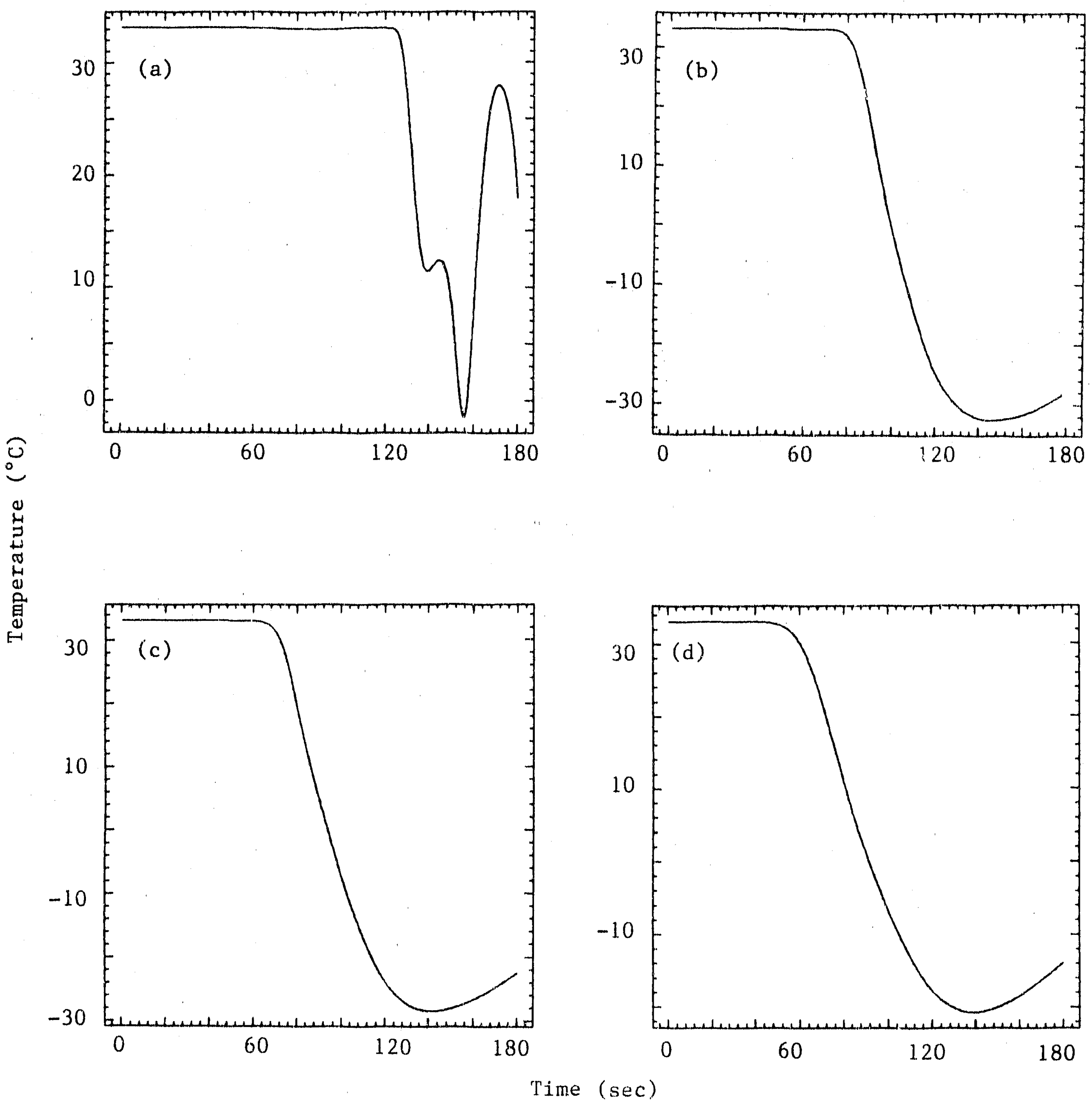

2.9. 2D simulation results of temperature behind the rear fence at (x,y) = (50 m, 1 m) as obtained with various level of turbulent mixing:
(a) ambient turbulence, (b) K = 0.3 m^2/sec,
(c) K = 0.6 m^2/sec, (d) K = 1.2 m^2/sec.

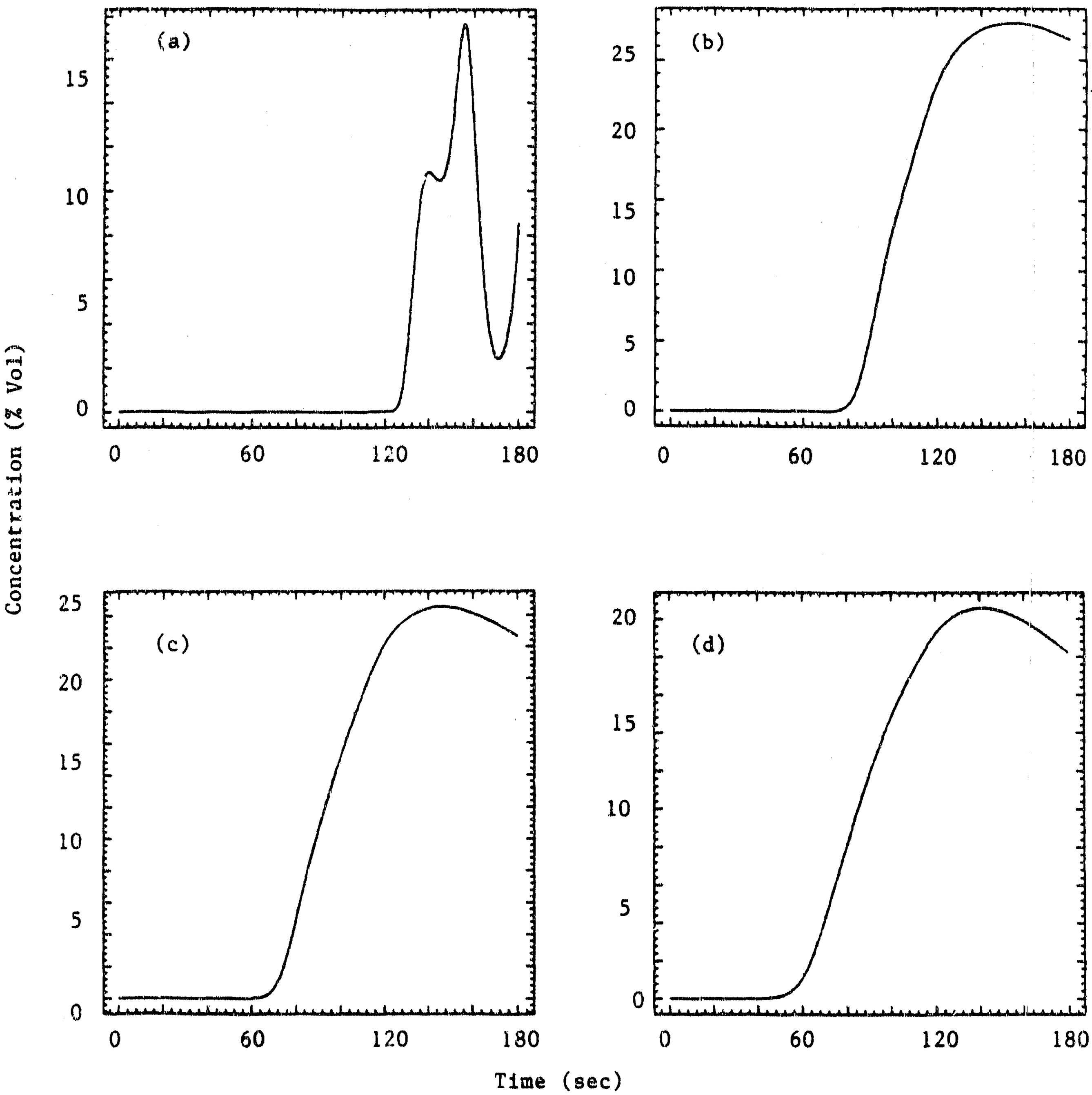

Fig. 2.10. Same as Fig. 2.9 except the comparison is for concentration.

LNG spilled and the extra energy necessary to superheat the vaporized LNG. As will be shown later, a drop of 1°C in water temperature could make the vapor cloud 60°C warmer at a location 1 m above the water surface. A similar heat balance calculation for Falcon-4 indicates the water temperature has to drop on average 2.25°C in order to provide the heat necessary to vaporize all the LNG spilled. For this case, none of the temperature measurements within the pond seem to suggest the occurrence of superheating.

In order to estimate the actual level of superheating, another series of numerical experiments was conducted. For the four cases studied, the degree of superheating was varied but the level of turbulence was kept basically the same ($K_h = K_v = 0.6$ m^2/s was applied everywhere in all cases except in the last case). The cases studied are: (a) no superheating, (b) with a heat flux of 9,100 W/m (which corresponds to a 0.5°C drop in water temperature in 100 s) over the source area, (c) twice the above heat flux, and (d) same as case (b) except that constant K value of 0.6 m^2/s was used only in an extended source region (x = -101 m to 30 m and z = 0 to 25 m) and the existing K-model with heavy-gas effects was applied elsewhere.

In Figs. 2.11 through 2.14, the predicted results for temperature and concentration at two representative locations are again compared. From these figures, it is seen that the temperature in the vapor cloud is very sensitive to the level of superheating. For instance, the value of minimum temperature at the center of spill increases by nearly 30°C when the water temperature drops by 0.5°C (and 60°C change for 1°C drop in water temperature). For the station outside of the fence, the increase in temperature is approximately half as much. Although superheating and turbulence enhancement have similar (yet quantitatively different) effects on the predicted temperature and concentration outside of the fence, their effects are somewhat different inside the fence. While a change in turbulence level appears to affect both temperature and concentration almost equally, superheating is seen to affect the temperature more than concentration. Therefore, in

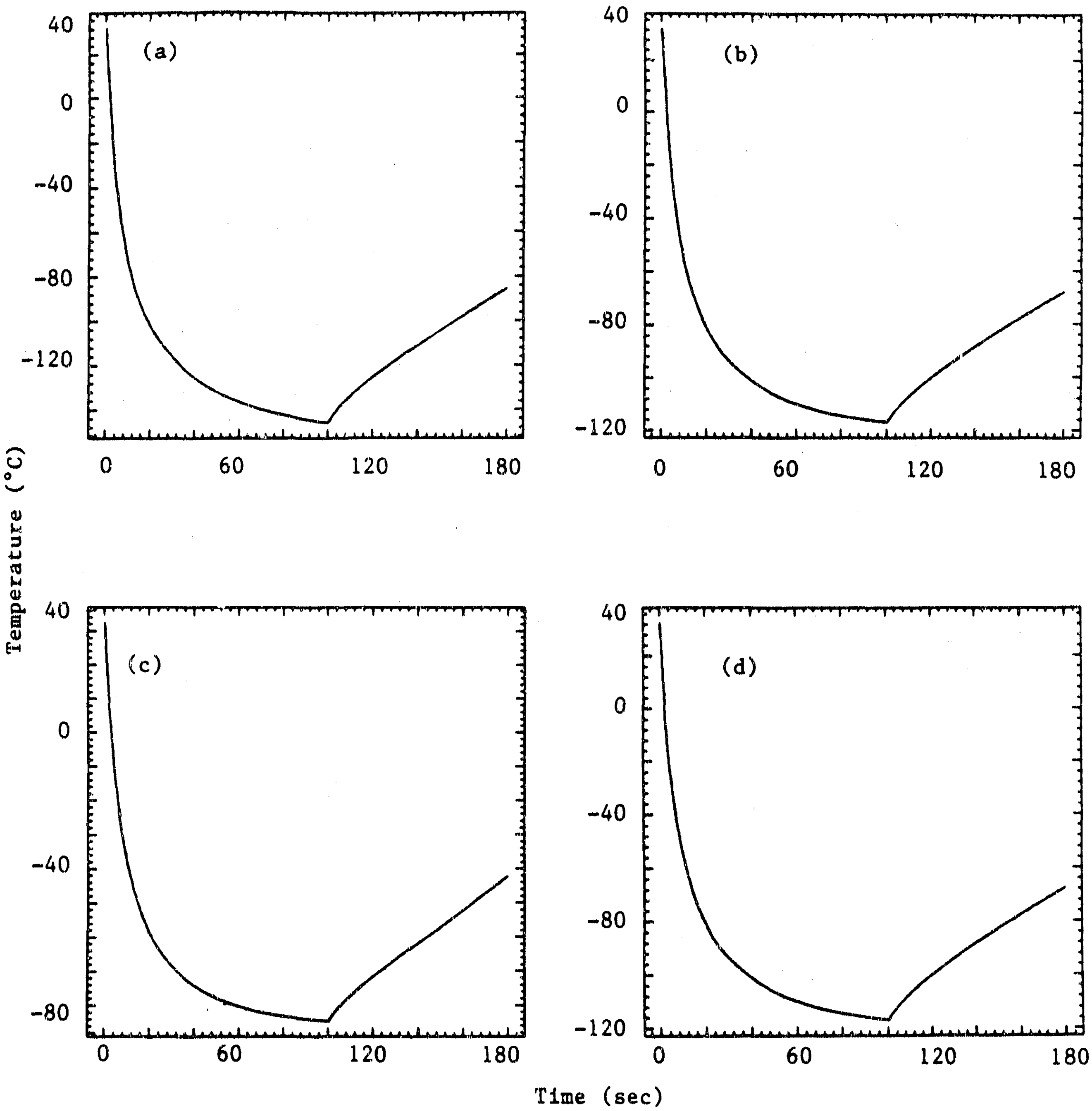

2.11. 2D simulation results of temperature near the center of spill at (x,z) = (-32 m, 1 m), as obtained with various degree of superheating over the source area:

(a) q = 0, (b) q = 9,100 W/m, (c) q = 18,200 W/m,
(d) q = 9,100 W/m plus turbulence suppression outside of the fence.

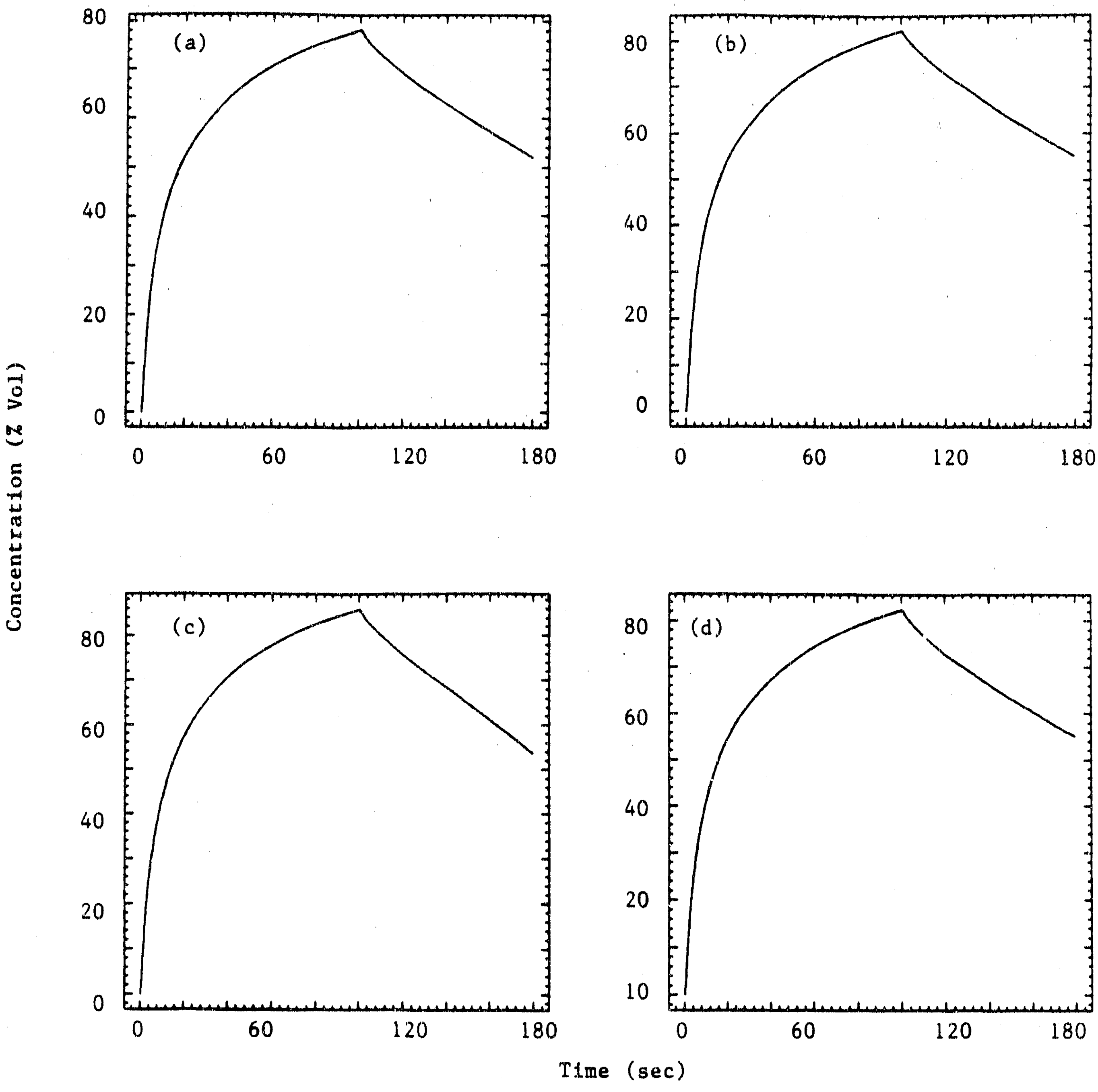

Fig. 2.12. Same as Fig. 2.11 except the comparison is for concentration.

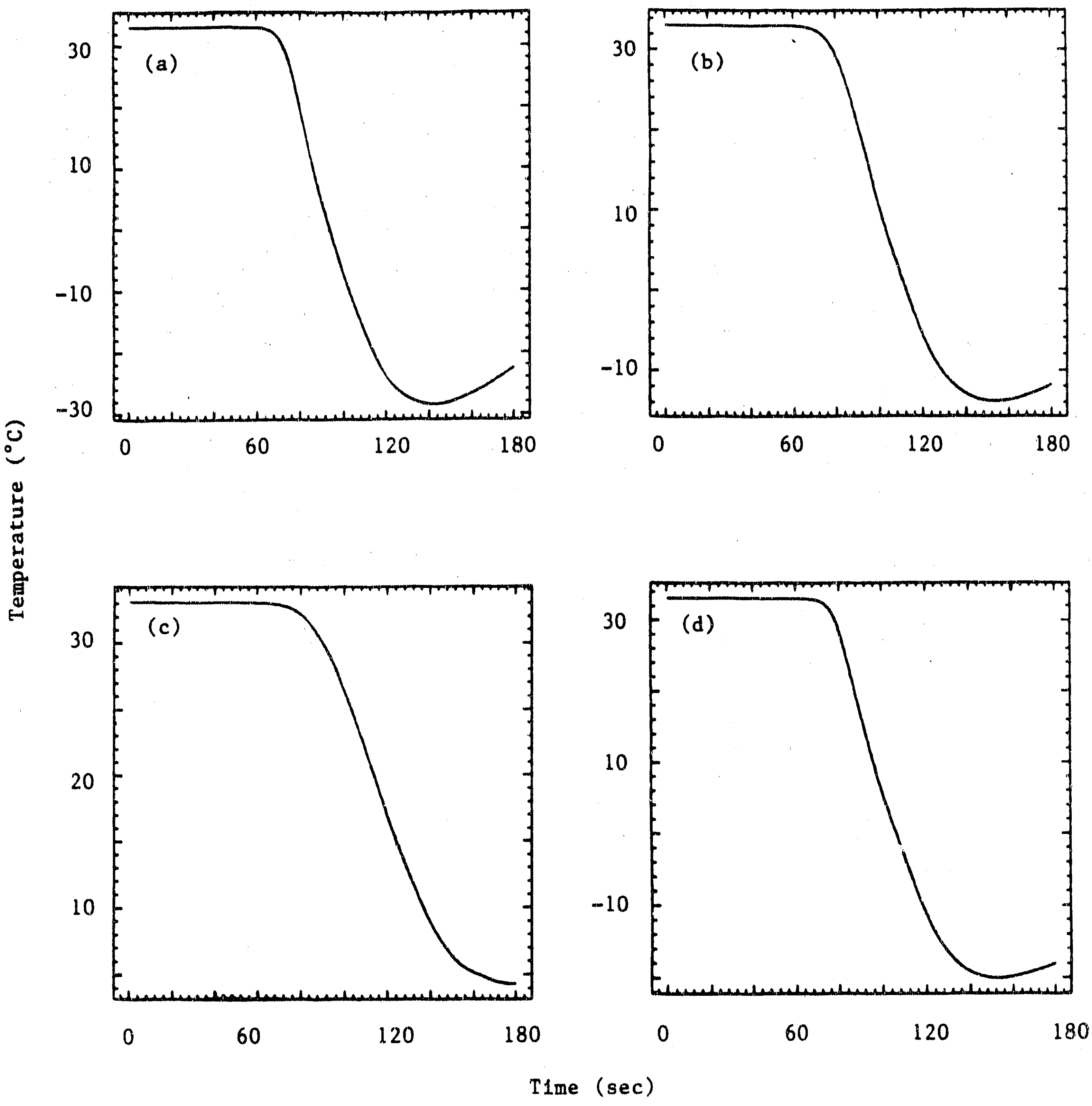

2.13. 2D simulation results of temperature behind the rear fence at (x,y) = (50 m, 1 m), as obtained with various degree of superheating over the source area:

(a) q = 0, (b) q = 9,100 W/m, (c) q = 18,200 W/m,
(d) q = 9,100 W/m plus turbulence suppression outside of the fence.

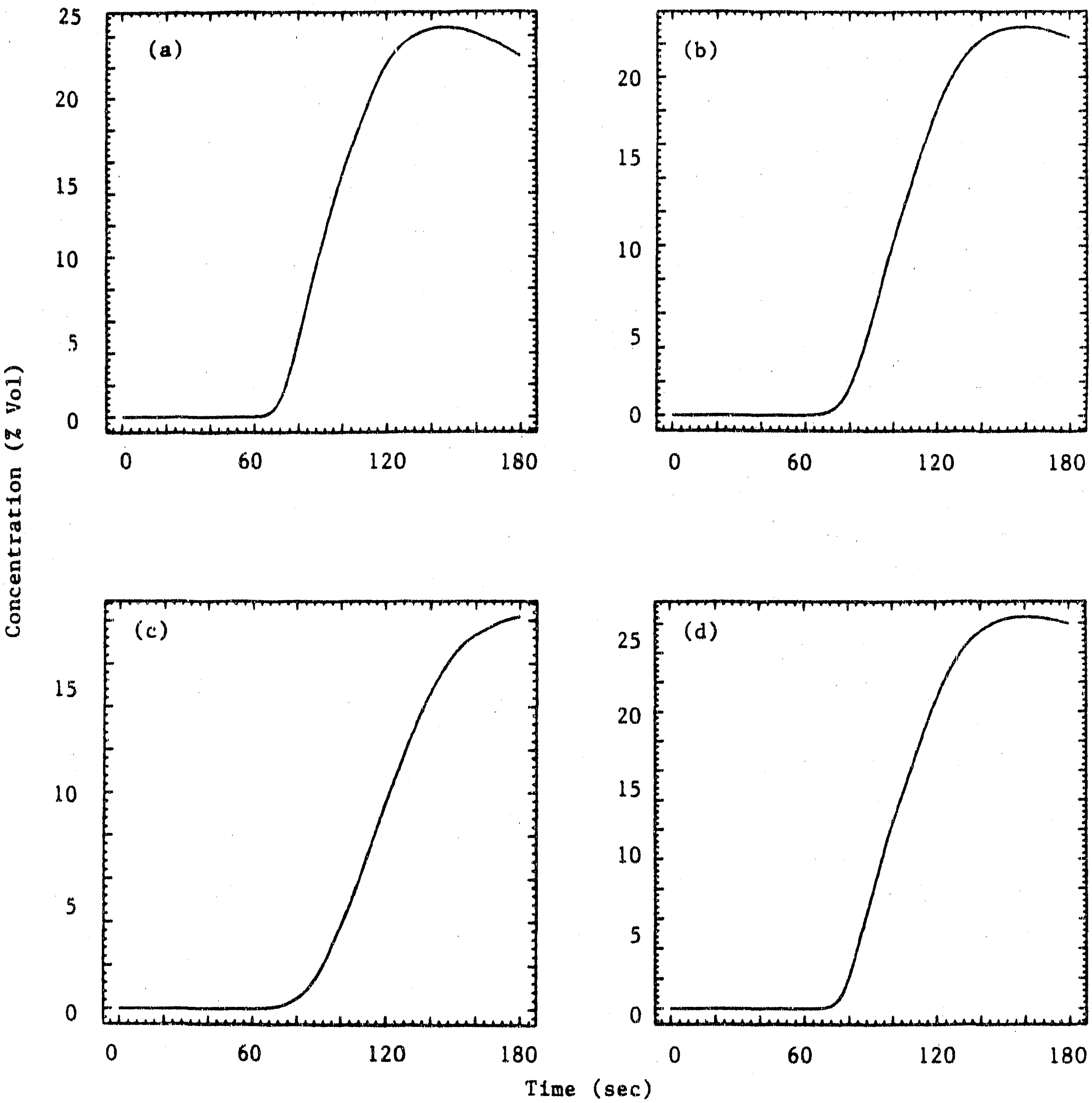

Fig. 2.14. Same as Fig. 2.13 except the comparison is for concentration.

order to be able to produce consistent results for both temperature and concentration at all locations, reasonable parameterization of both processes seem to be required.

Among the four cases studies, results from (b) and (d) appear to be the most reasonable. Actually the predicted results from cases (b) and (d) are virtually the same at the center of spill (see Figs. 2.11 and 2.12), because the same level of turbulence was used there. However, the predicted results for these cases in Figs. 2.13 and 2.14 (for a location 50 m behind the fence) are noticeably different, due to the difference in turbulence modeling. Everything considered, the results obtained in case (d) appear to be more realistic, because the existing K-model is considered more appropriate than the simple, constant K approach at such a location.

2.5 Simulated Field Tests

In this Subsection, 3-D simulations of the selected field tests are described. The spill and meteorological parameters used in these simulations are summarized in Table 2.2; the simulation times and associated computing costs are listed in Table 2.3. Herein, we will focus on the general results and characteristics of each test and leave model-data comparison to be conducted in Section 3.

Falcon-1

As indicated in Table 2.1, this test has the highest spill volume and spill rate, and was conducted under very stable atmospheric conditions. The relevant atmospheric and spill parameters are described in Table 2.2. The mesh described in Section 2.3 and open lateral boundary conditions were used in the simulation to allow both the flow and the vapor cloud to leave the domain in a natural way. Based on the 2-D results discussed earlier, a heat flux of 9,600 W/m^2 was added to account for the superheating effects. The existing K-model with heavy-gas effects was applied everywhere except within and near the fence enclosure (defined in Subsection 2.2) wherein a constant K value of 1 m^2/s was used.

Table 2.2. Spill and meteorological parameters used in numerical simulations

Parameter \ Test	Falcon-1	Falcon-2	Falcon-3	Falcon-4
Area of source (m^2)	2400	2400	2400	2400
Injection velocity (m/s)	0.108	0.043	0.050	0.023
Duration of source (s)	100	78	161	310
Air pressure (N/m^2)	92,094	91,699	91,274	91,831
Reference temperature (°K)	305.5	304.8	308.0	304.2
Friction velocity (m/s)	0.0605	0.3565	0.3053	0.3694
Monin-Obukhov length (m)	5.0	-103.4	-422.2	69.38
Wind profile (m/s)	(1)	(2)	(3)	(4)
Air temperature profile (°C)	32.5 + 0.1 z	31.8	35.0	31.2 + 0.05z
Superheating (W/m^2)	9,600	0.0	0.0	0.0
Effectrive energy transfer velocity (m/s)	0.005	0.01	0.01	0.01
Water temperature (°C)	28.4	23.6	28.0	23.2
Diffusivity within fence and its vicinity (m^2/s)*	1.0	0.8	0.8	0.6

(1) $u(z) = 0.8 + 0.4167\, z - 0.01667\, z^2$ for $z < 9$ m
$= 3.2$ for $z \geq 9$ m

(2) $u(z) = 0.7466\,[\ln(1 + z/0.008) + 0.7694]$

(3) $u(z) = 0.6985\,[\ln(1 + z/0.008) + 0.3445]$

(4) $u(z) = 3.689 + 0.658\, z - 0.0248\, z^2$ for $z < 16$ m
$= 7.877$ for $z \geq 16$ m

*Based on Equation (4) and rounded to the nearest tenth.

Table 2.3 Timing information on gas dispersion simulations using a Cray-2 comptuer

Timing Information \ Test	Falcon-1	Falcon-2	Falcon-3	Falcon-4
Simulation time (s)	480	480	600	600
Time step size (s)	0.03	0.03	0.015	0.04
Total CPU cost (s)	12,378	8,531	33,860	10,966
Cost per sec of simulation (s)	25.79	17.71	56.43	18.28
Cost per time step (s)	0.7736	0.5332	0.8465	0.7311

Remarks:

Total number of nodal points = 27,200,
Total number of elements = 23,940,
Number of unknowns per node = 6,
Number of unknown per element = 1.

As discussed earlier, in order to conserve computer resources the vapor cloud was assumed to be symmetric about the center plane of the fence enclosure, thus only one-half of the vapor cloud was simulated. Such an assumption is obviously not very appropriate for Falcon-1 as evidenced by the significant deviation (about 20 degrees) of the wind trajectory from such a plane. However, 30 to 40 hours of Cray-2 time would have been required to simulate the entire cloud with similar grid resolution. Due to budgetary constraints, it was decided to postpone such an endeavor for future studies. Nevertheless, the present simulation is still very useful in improving the understanding of the dispersion processes of this particular vapor cloud.

The evolution of the vapor cloud during the first three minutes is depicted in Figs. 2.15 through 2.18 on four representative planes. On the vertical plane of symmetry (Fig. 2.15) the vapor cloud (defined, say, by the 0.5% concentration contour) has risen slightly over 20 m and reached 100 m downwind after 60 s. The cloud near the ground did not travel as far because it was impeded by wake effects and surface drag. For subsequent times, the cloud continued to disperse downwind and stayed close to the ground because of negative buoyancy and turbulence suppression within the vapor cloud. The gravity spreading, especially in the lateral directions, can be clearly seen in Fig. 2.16. By 120 s, the vapor cloud already reached the lateral boundary. The slumping and spreading of the vapor cloud can also be seen in Fig. 2.17 for the crosswind plane passing through the center of spill. In Fig. 2.18, the evolution of the vapor cloud on another crosswind plane (50 m behind the rear fence) is shown, which demonstrates vividly how the cloud falls toward the ground, spreads out, and hugs the ground. These results appear to correlate well with what was observed in the field experiment, i.e., a cloud overfilling the fence enclosure soon after the start of the spill.

To illustrate how much the flow field was changed by the vapor cloud, velocity projections on three representative planes are compared in Figs. 2.19 through 2.21 for times before the spill and 120 s after the spill. Profound changes in the velocity field can be seen in all three directions, especially on the 1-m horizontal plane (Fig. 2.20). The significant zone of circulation outside of the fence in Fig. 2.21 was induced by the heavy-gas cloud or, more precisely, caused by the density gradient in the lateral direction. Due to stable density stratification, the flow field within the fence is nearly quiescent. Because of its high spill rate and spill volume, Falcon-1 has produced the most profound perturbation to the relatively calm ambient atmosphere.

Falcon-2

With an intermediate spill rate and a relatively short spill duration, this test was conducted under neutral atmospheric conditions. The same computational domain and boundary conditions similar to those used in Falcon-1 were also employed in this simulation. For turbulence modeling, the existing K-model with heavy-gas effect was applied

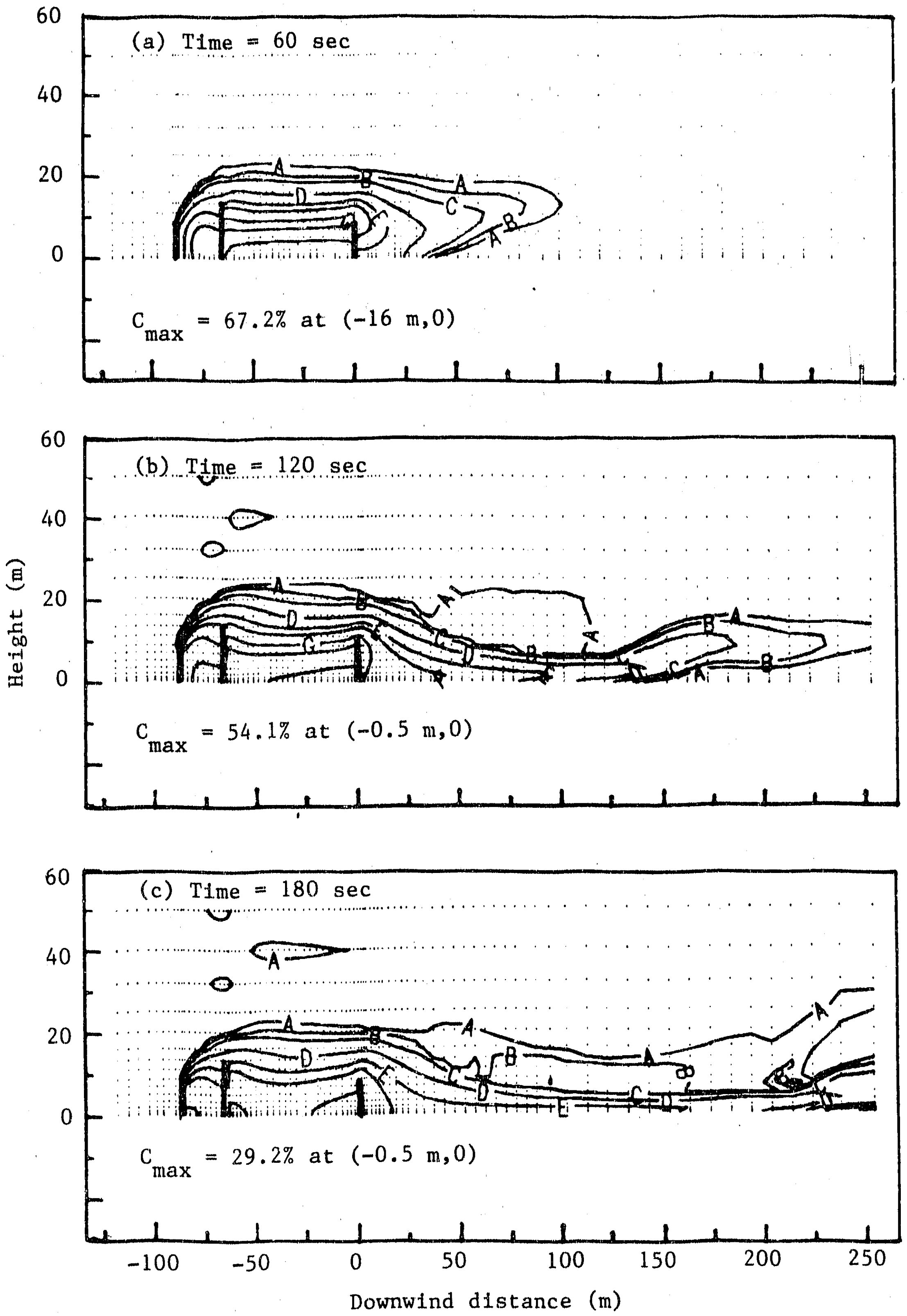

Fig. 2.15. Falcon-1 predicted concentration contours on the vertical plane of symmetry during the first three minutes of simulation. The contour levels are (in % Vol): A=0.5, B=1, C=2, D=5, E=10, F=15, G=25, H=35, and I=50.

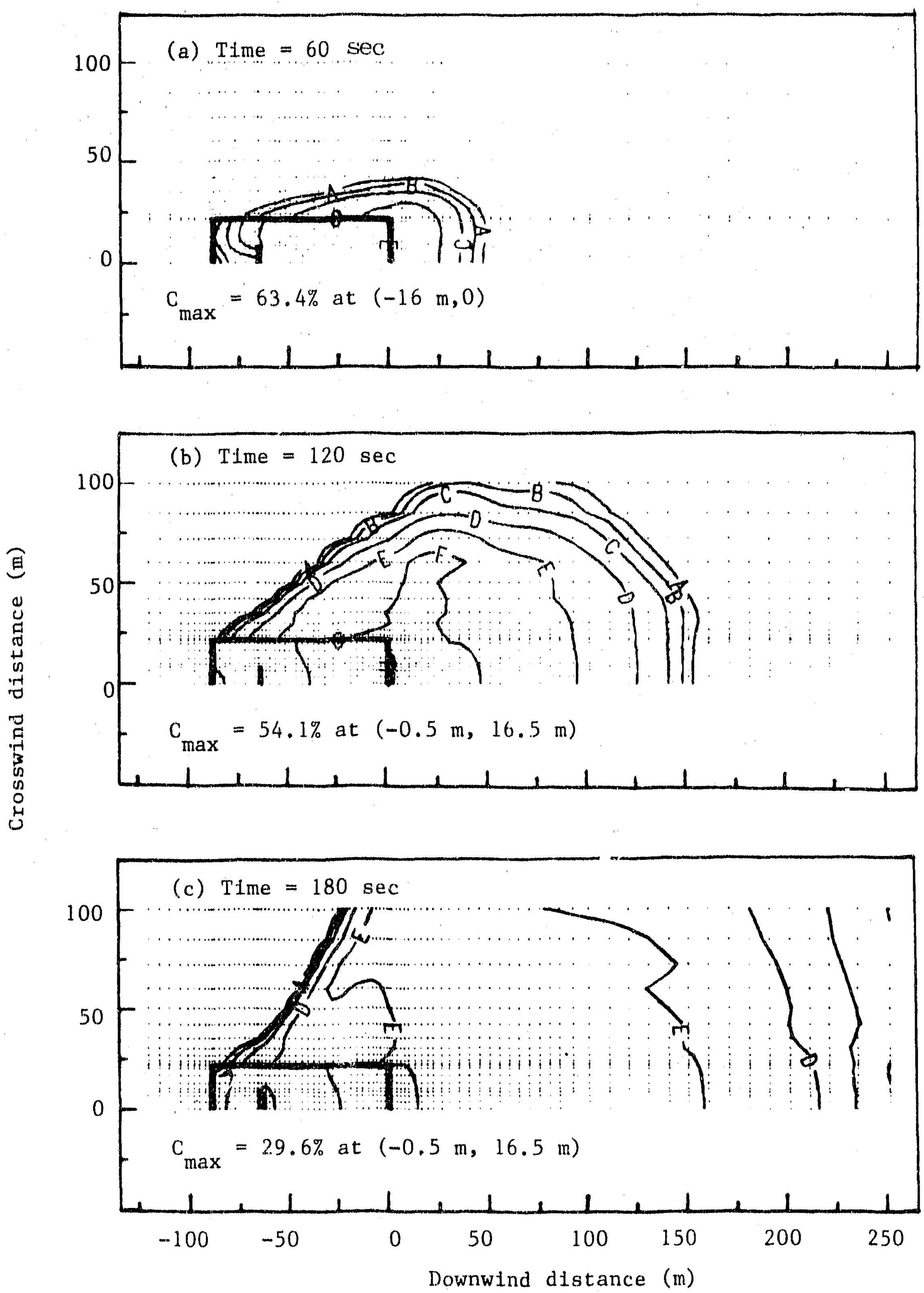

Fig. 2.16. Falcon-1 predicted concentration contours on the horizontal plane 1 m above the ground surface during the first three minutes of simulation. The contour levels are (in % Vol): A=0.5, B=1, C=2, D=5, E=10, F=15, G=25, H=35, and I=50.

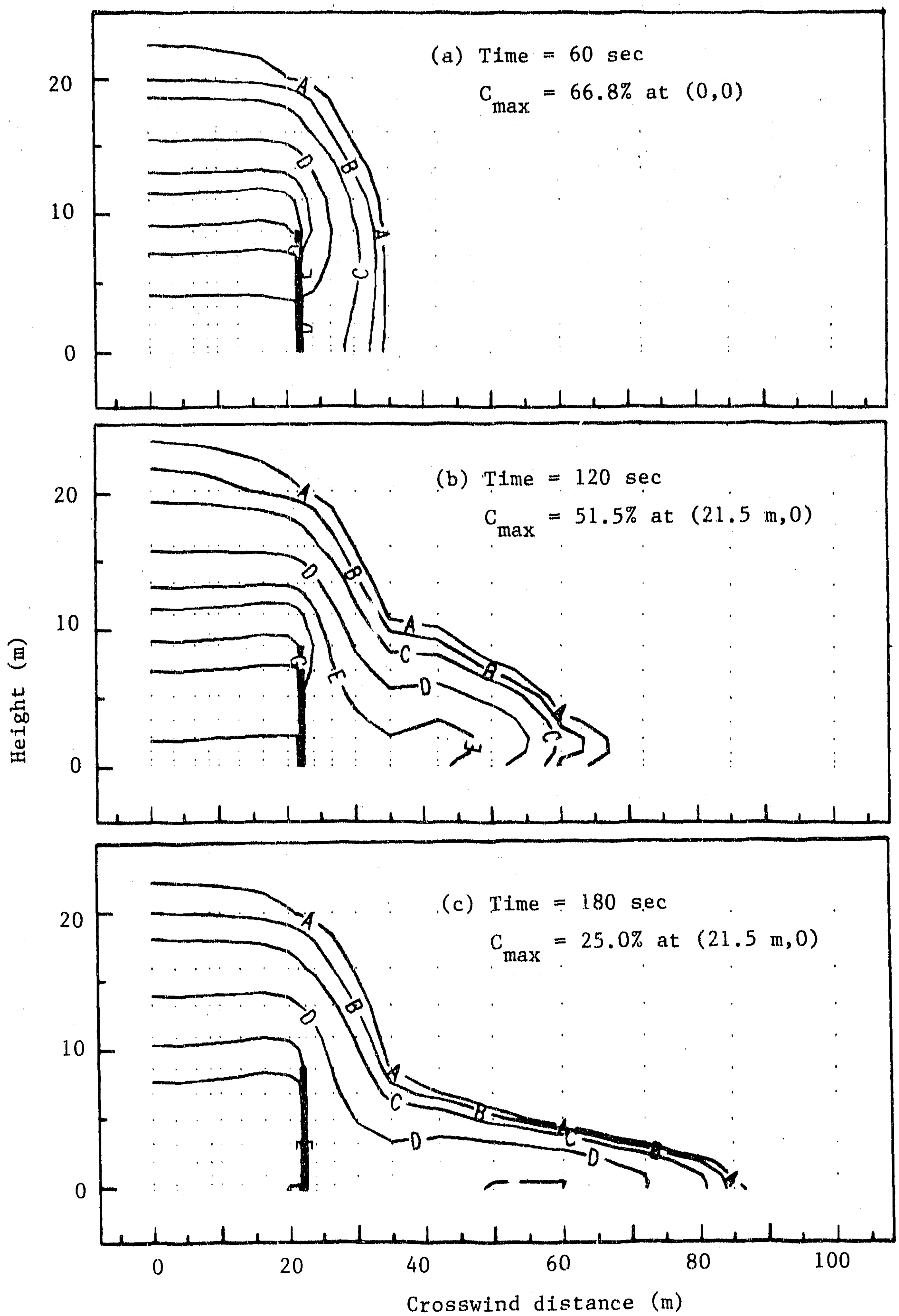

Fig. 2.17. Falcon-1 predicted concentration contours on the crosswind plane passing through the center of spill during the first three minutes of simulation. The contour levels are (in % Vol): A=0.5, B=1, C=2, D=5, E=10, F=15, G=25, H=35, and I=50.

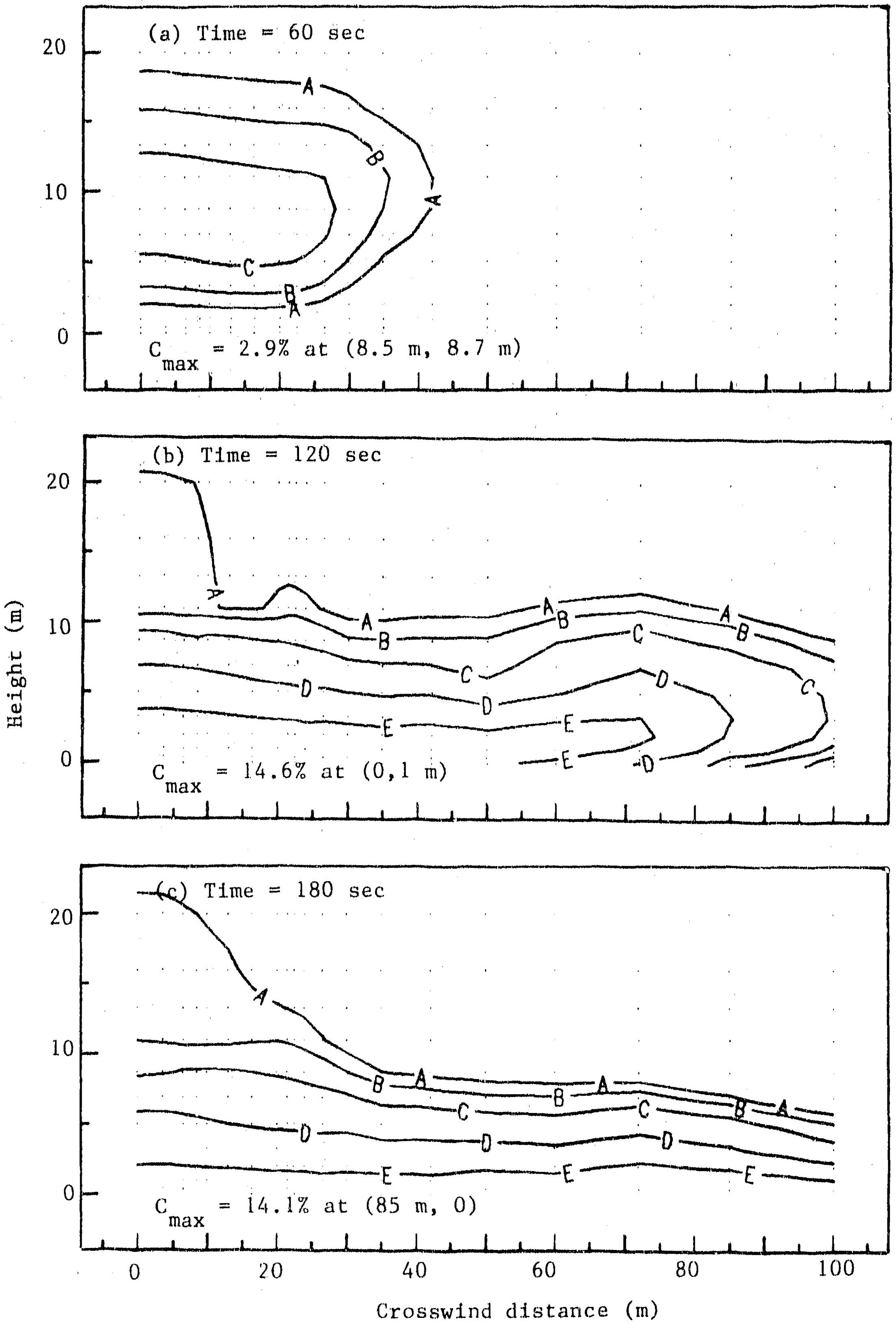

Fig. 2.18. Falcon-1 predicted concentration contours on the crosswind plane 50 m behind the rear fence during the first three minutes of simulation. The contour levels are (in % Vol): A=0.5, B=1, C=2, D=5, and E=10.

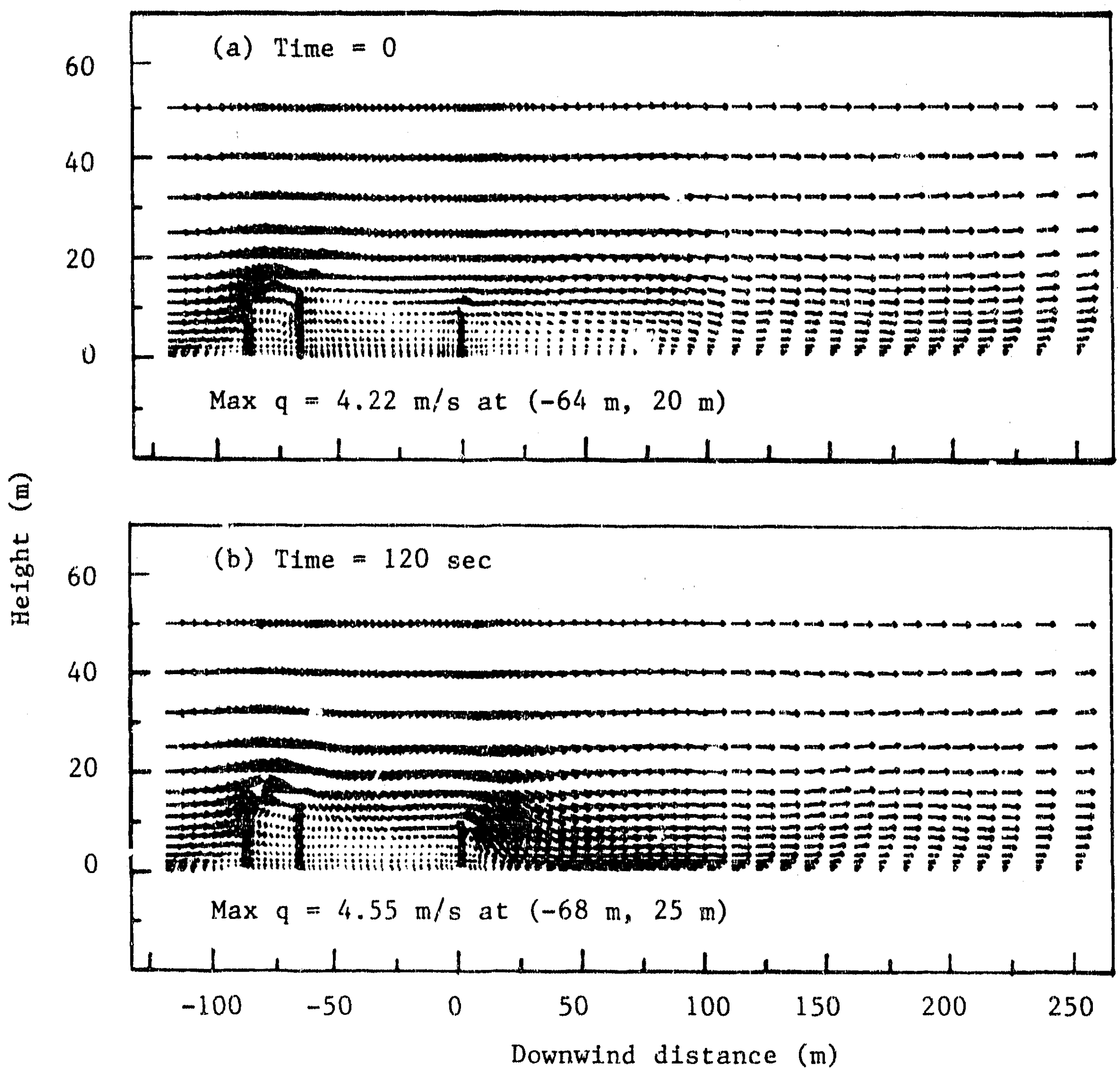

Fig. 2.19. Falcon-1 predicted velocity vectors on the vertical plane of symmetry for times before and two mintues after the spill.

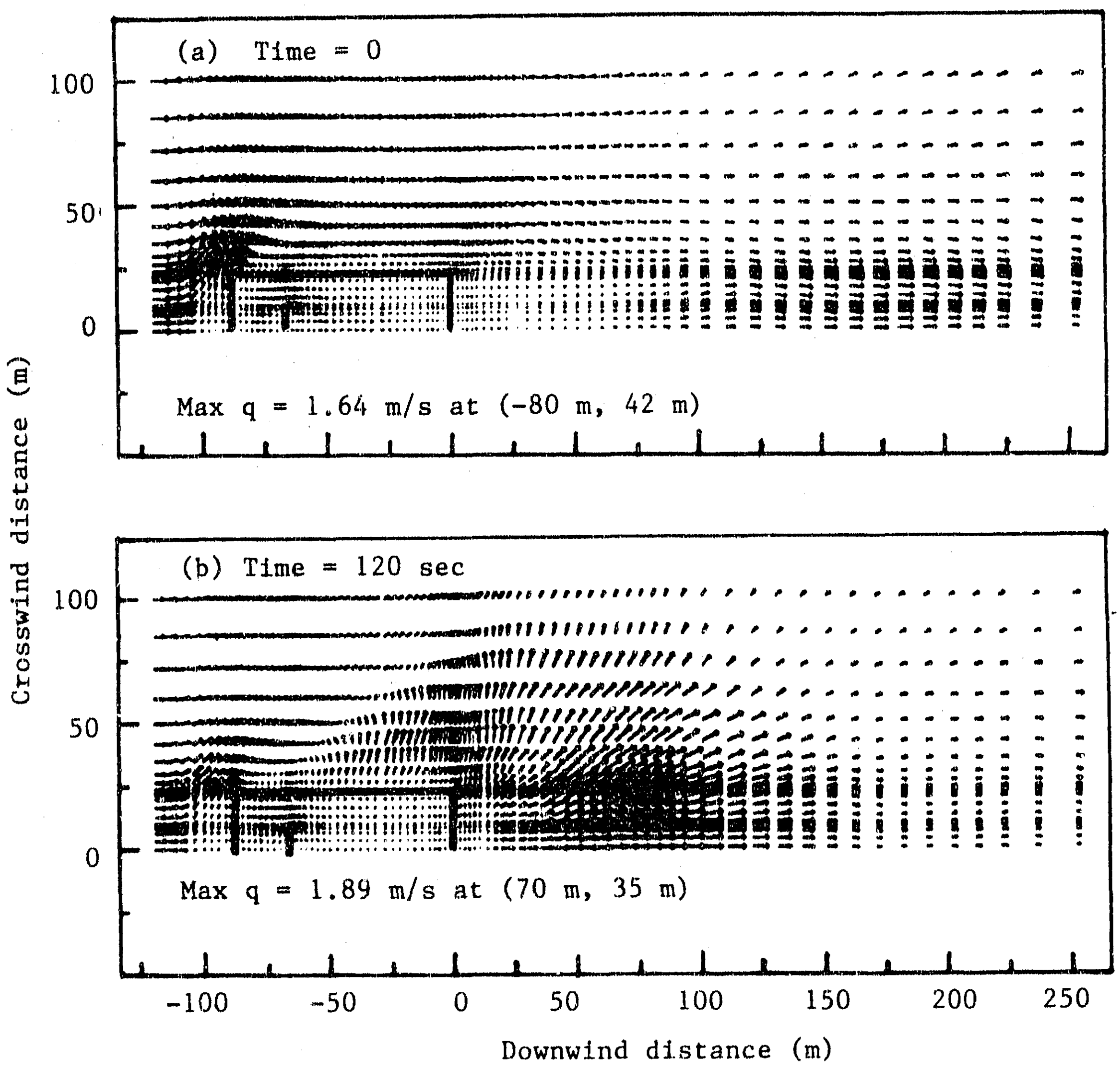

Fig. 2.20. Falcon-1 predicted velocity vectors on the horizontal plane 1 m above t. ground surface for times before and two minutes after the spill.

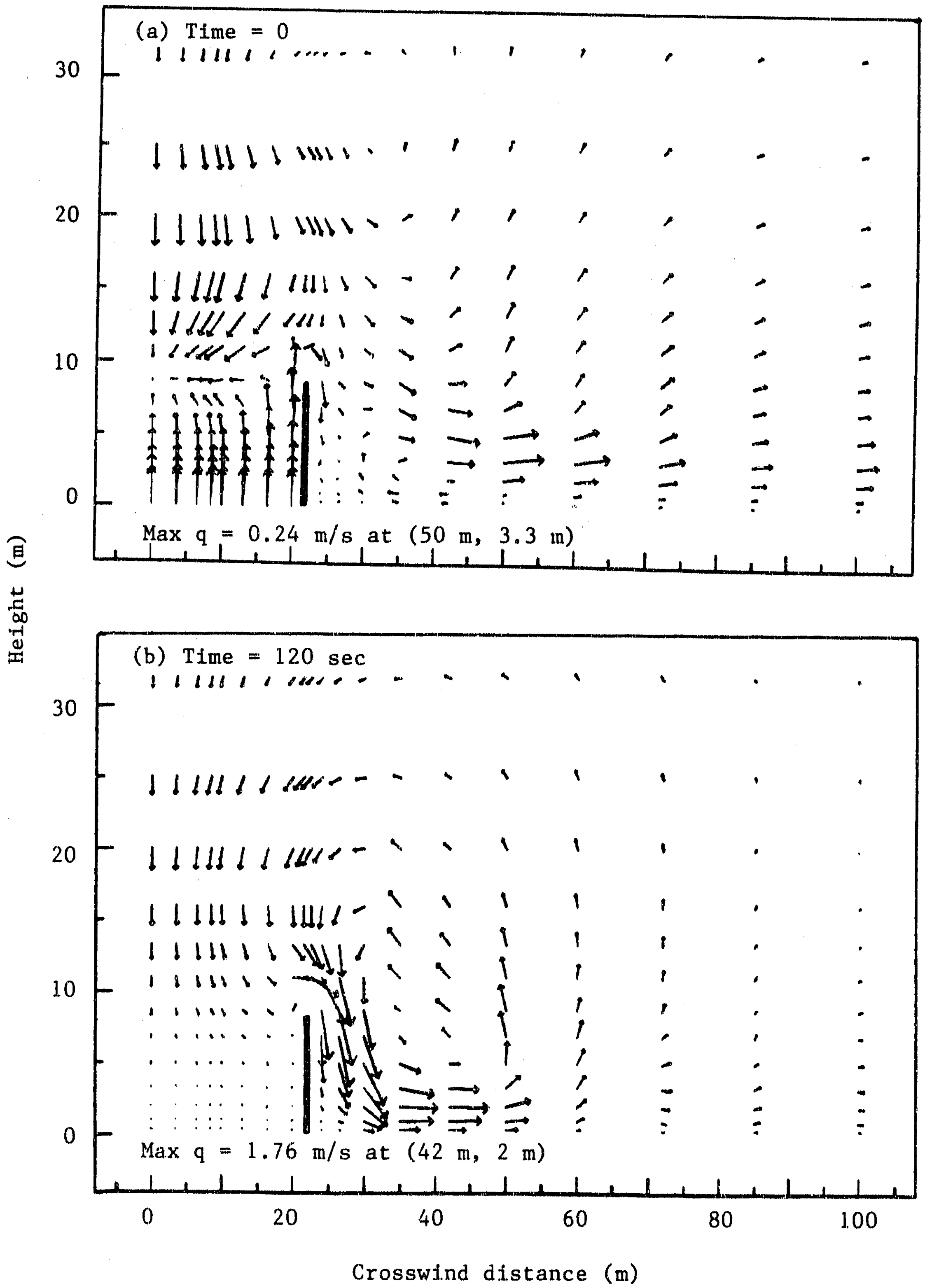

Fig. 2.21. Falcon-1 predicted velocity vectors on the crosswind plane passing through the center of spill for times before and two minutes after the spill.

everywhere except within and near the fence enclosure, wherein a constant K value of 0.8 m^2/s was used.

For this case, the empirical constant associated with turbulent mixing in the horizontal direction was set equal to 1.0, rather than 6.5 as used for other cases. This change was made because field data obtained in the atmospheric boundary layer seem to suggest that the ratio of diffusivities between the horizontal and vertical directions approaches unity as the atmospheric stability changes from stable to neutral conditions. Also, this change is beneficial for cost-effectiveness because a time step size of three times smaller would have been required based on the very stringent diffusion stability limit.

The evolution of the vapor cloud during the first three minutes of simulation is depicted in Figs. 2.22 and 2.23 on two representative planes. On the vertical plane of symmetry (Fig. 2.22), the vapor cloud has risen to 20 m and reached 75 m downwind after 60 s. Again, the part of cloud near the ground did not travel as fast because it was impeded by the wake effects and surface drag. Due to negative buoyancy and turbulence suppression, the vapor cloud is decreasing slowly in height (Fig. 2.22) and increasing in width (Fig. 2.23) as it disperses downwind. Velocity projections on the two planes at time = 180 s are shown in Fig. 2.24 which, together with Figs. 2.22(c) and 2.23(c), illustrate the coupling between the vapor cloud and the velocity field. Compared with Falcon-1, the vapor cloud of Falcon-2 is, as expected, much narrower and its perturbation to the ambient velocity field is much weaker.

In order to assess the mitigating effects of the fenced enclosure, this test was also simulated without the vapor fence and billboard. For brevity, such results are not included herein, but can be found in Wiersma and Williams (1990).

Falcon-3

Falcon-3 is basically a repeat of the Falcon-2 test except it has slightly higher spill rate and roughly twice as long (161 s versus 78 s) in spill duration. Although this test has been

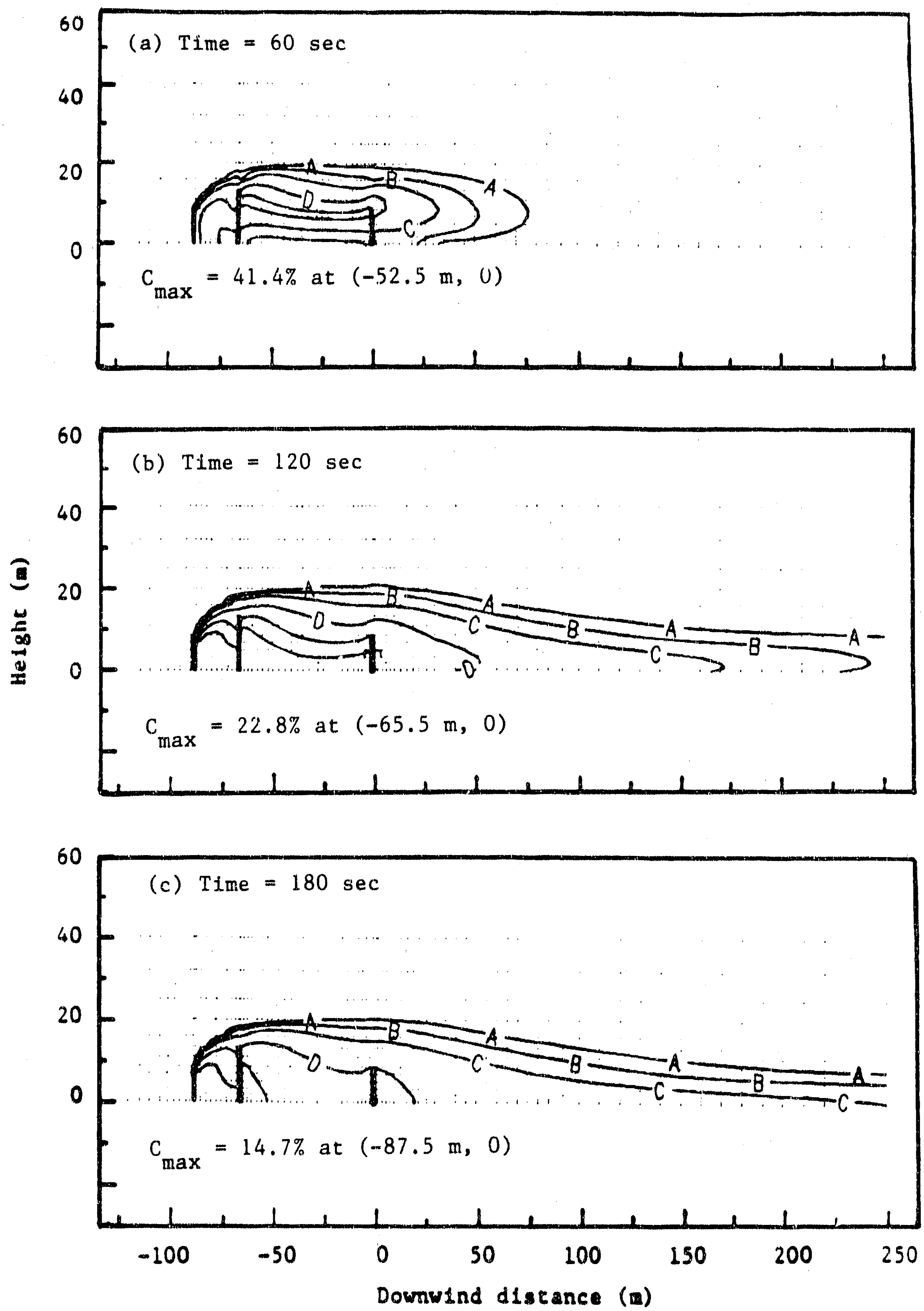

Fig. 2.22. Falcon 2 predicted concentration contours on the vertical plane of symmetry during the first three minutes of simulations. The contour levels are (in % Vol): A=0.5, B=1, C=2, D=5, E=10, F=15, G=25, and H=35.

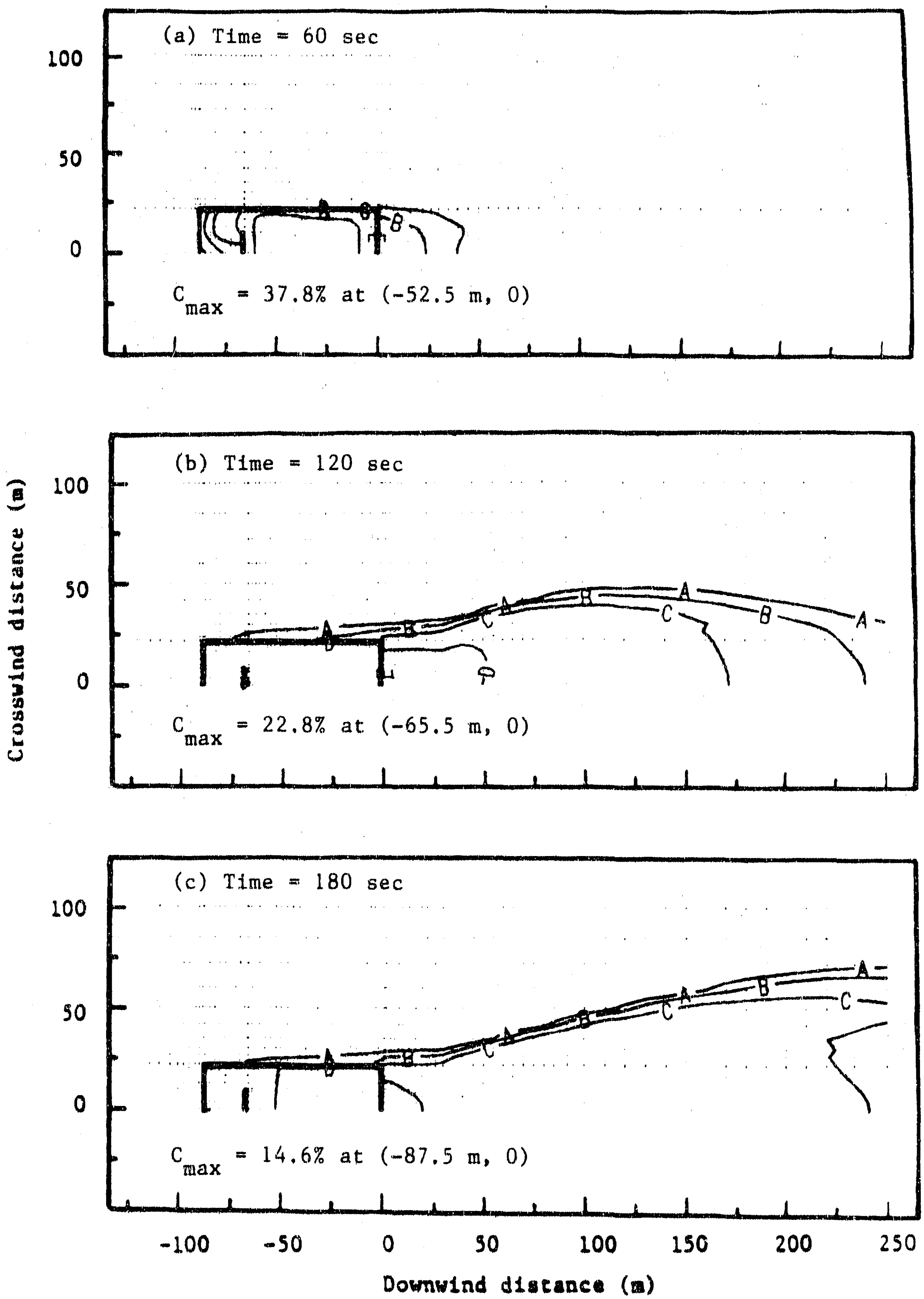

Fig. 2.23. Falcon-2 predicted concentration contours on the horizontal plane 1 m above the ground surface during the first three minutes of simulation. The contour levels are (in % Vol): A=0.5, B=1, C=2, D=5, E=10, F=15, G=25, and H=35.

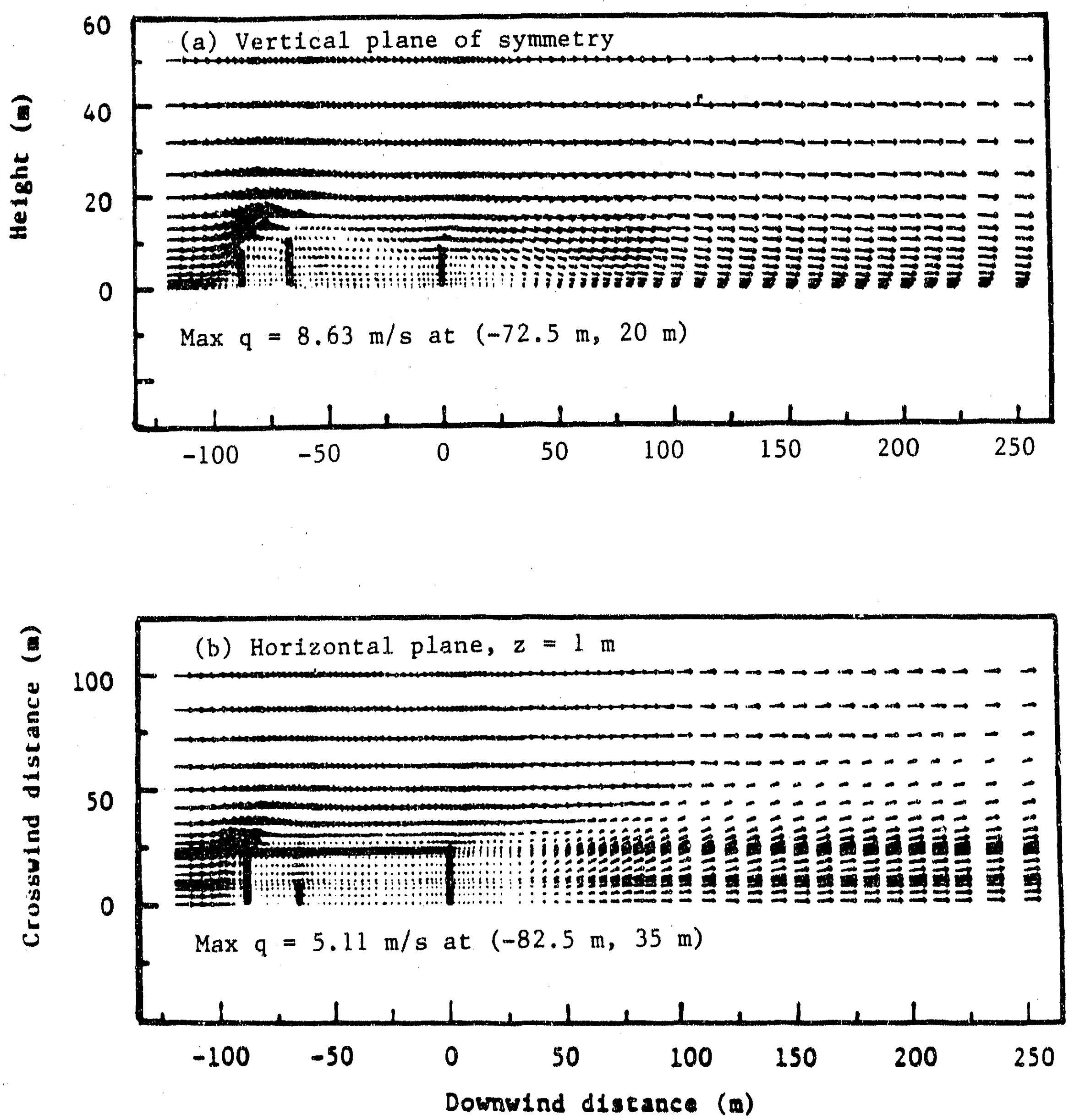

Fig. 2.24. Falcon-2 predicted velocity vectors on two representative planes at time = 180 sec.

plagued to some extent by the occurrence of many RPTs, sufficient good quality data still exist for comparison purposes. The approach used to model turbulence and the source in Falcon-2 was also used here for Falcon-3.

The evolution of the vapor cloud during the first four minutes is depicted in Figs. 2.25 and 2.26 on two representative planes. On the vertical plane of symmetry (Fig. 2.25), the vapor cloud has risen to nearly 20 m and reached 90 m downwind after 60 s. The gravity spreading in the lateral direction can be seen clearly in Fig. 2.26. In contrast to Falcon-2, this vapor cloud spread much wider and even went beyond the lateral boundary. The velocity projections on the two planes at time = 240 s are shown in Fig. 2.27. Due to similar atmospheric conditions and LNG spill rate, the vapor cloud of Falcon-3 is very much like that of Falcon-2 during the first 120 s. For late times, however, the cloud of Falcon-3 is significantly wider, apparently attributable to its slightly higher spill rate and the much longer spill duration.

Falcon-4

In this test, 45 m^3 of LNG was released over a period of 310 s, under neutral ambient conditions with an average wind speed of 5.2 m/s. The relatively low spill rate, long spill duration, and nearly steady atmospheric conditions made this test behave like a continuous spill. In order to evaluate the relative performance of the fence enclosure, two simulations were performed for this test: one with the fence/billboard and one without. The computational domain shown in Fig. 2.5 was used for the former case and a domain extended to 400 m downwind was used for the latter.

First, results obtained from the simulation with the fence enclosure are presented in Fig. 2.28. The evolution of the vapor cloud during the first three minutes is depicted on the plane of symmetry. After 60 s of release, the vapor cloud is nearly 20 m high in the fence region and just starts to fall toward the ground. Similar to other tests, surface drag and wake effects have impeded noticeably the transport of the vapor cloud near the ground

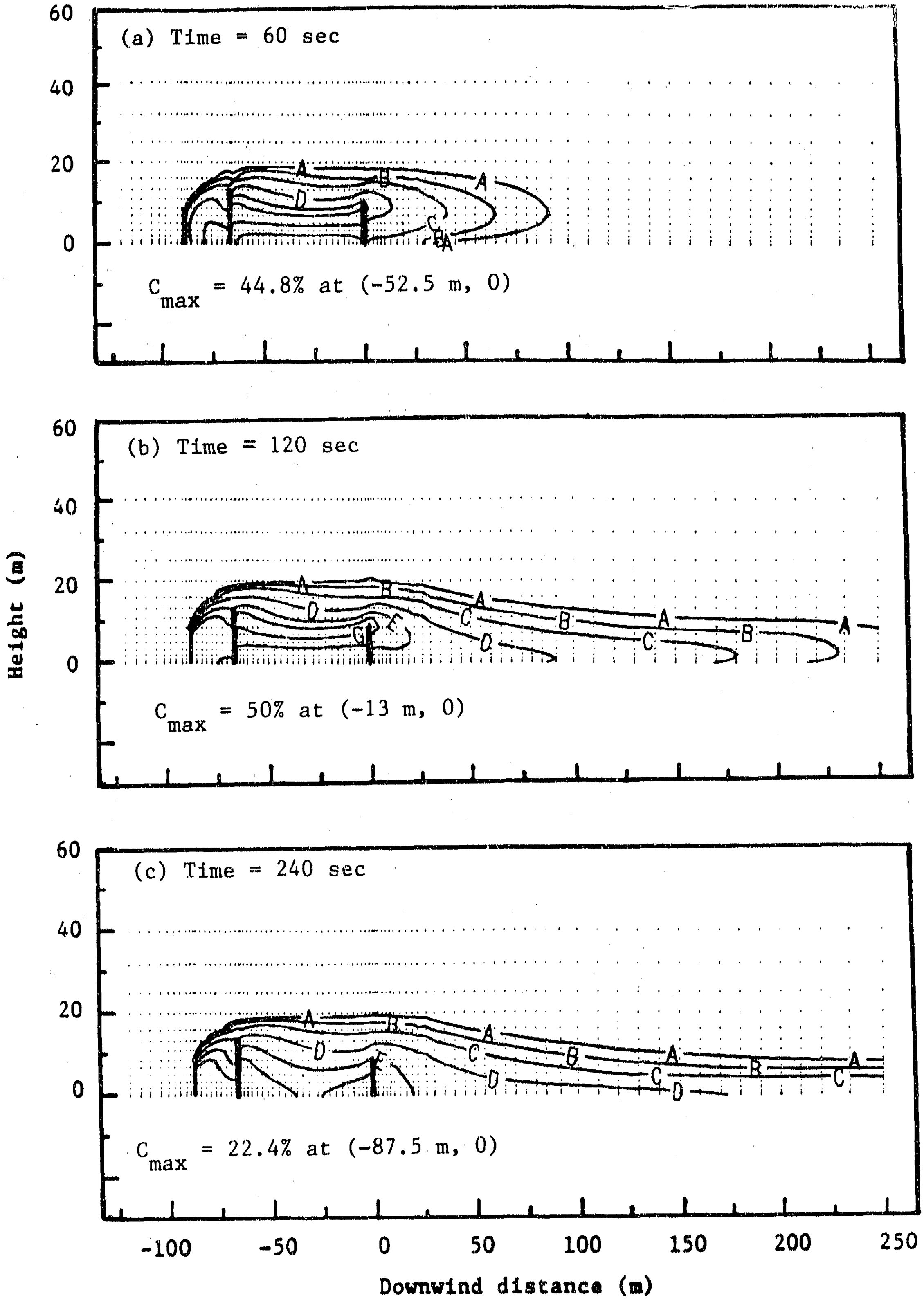

Fig. 2.25. Falcon-3 predicted concentration contours on the vertical plane of symmetry during the first four minutes of simulations. The contour levels are (in % Vol): A=0.5, B=1, C=2, D=5, E=10, F=15, G=25, and H=35.

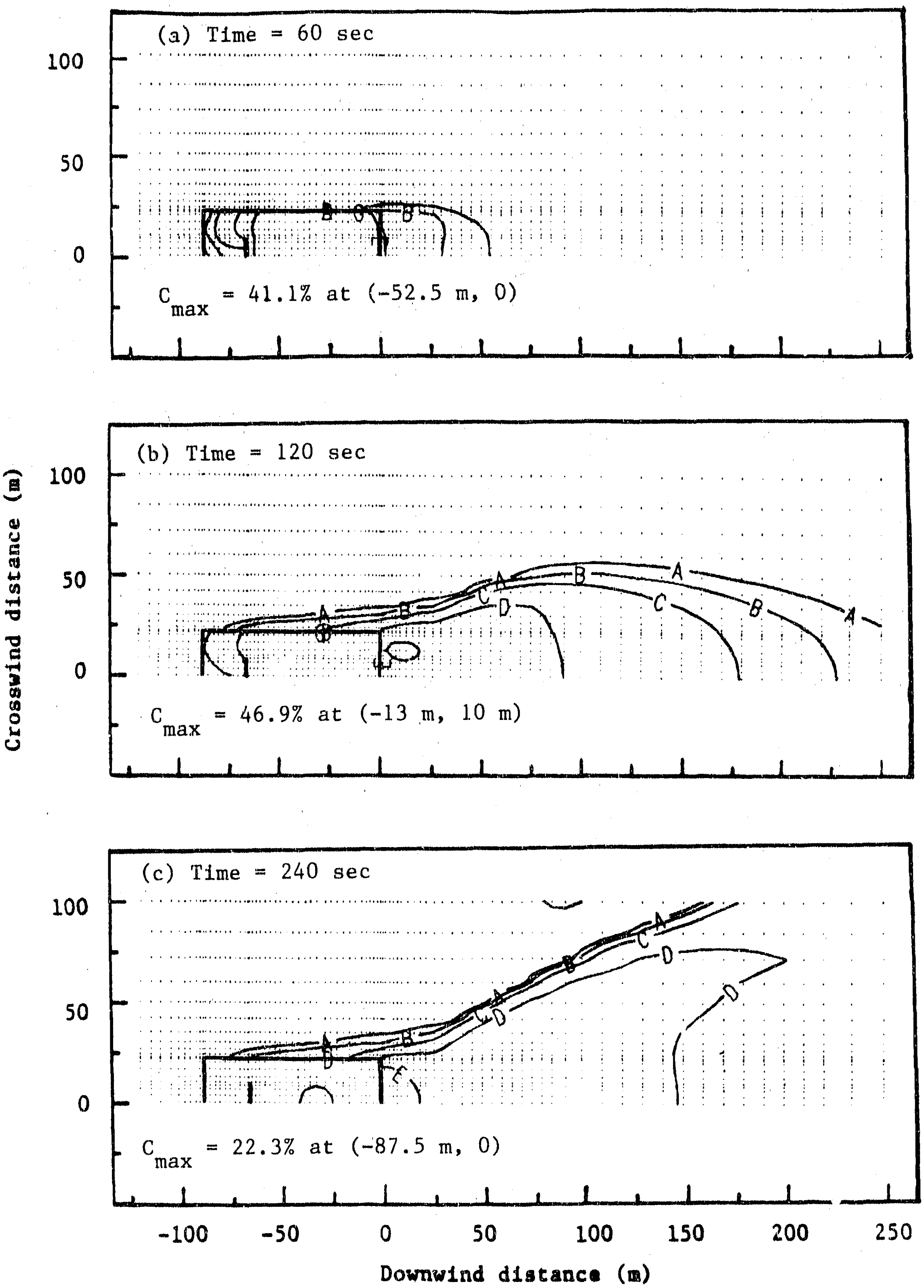

Fig. 2.26. Falcon-3 predicted concentration contours on the horizontal plane 1 m above the ground surface during the first four minutes of simulation. The contour levels are (in % Vol): A=0.5, B=1, C=2, D=5, E=10, F=15, G=25, and H=35.

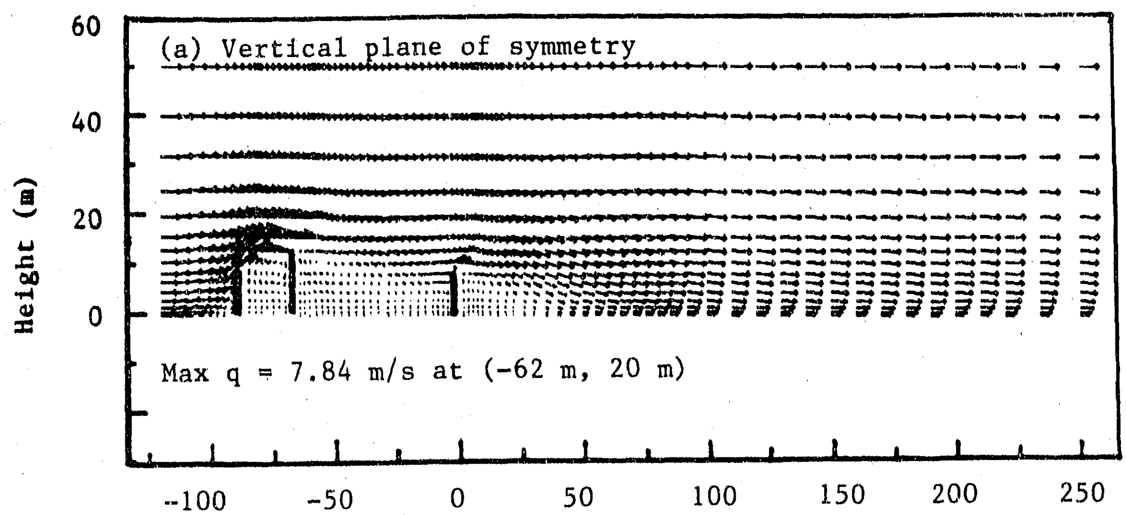

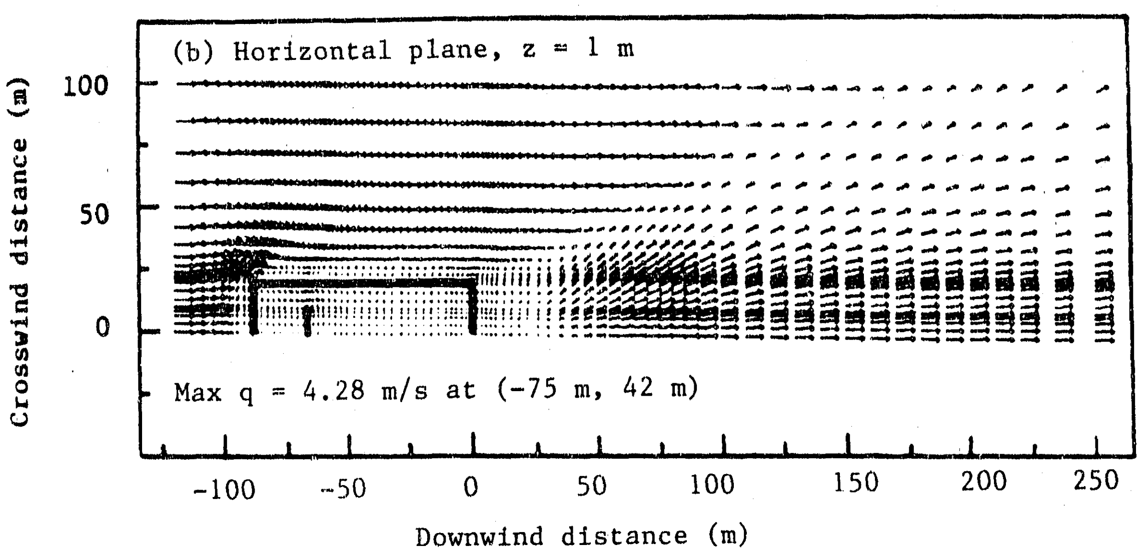

Fig. 2.27. Falcon-3 predicted velocity vectors on two representative planes at time = 240 sec.

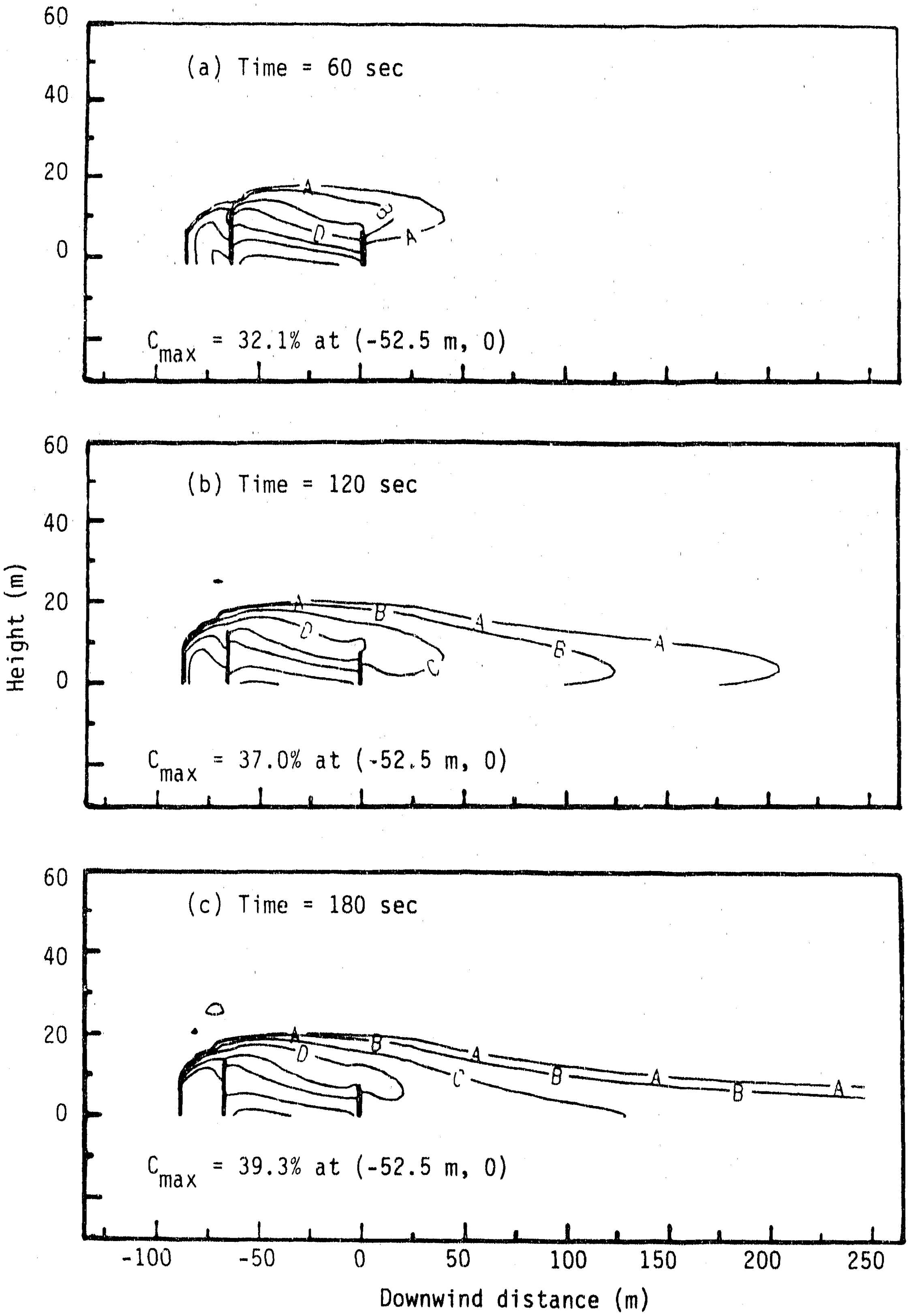

Fig. 2.28. Falcon-4 predicted concentration contours on the vertical plane of symmetry during the first three minutes of simulation. The contour levels are (in % vol): A = 0.5, B = 1, C = 2.5, D = 5, E = 10, F = 15, G = 25, and H = 35.

during the early phase of cloud dispersion. However, as the spill continues and gravity spreading plays a more important role, such effects gradually diminish. Despite the continuous generation of gas vapor during the spill, the vapor cloud remains at approximately 20 m in height and tends to hug the ground owing to its negative buoyancy.

In the next three figures, the steady state results at $t = 300$ s are depicted. In Fig. 2.29, the predicted concentration contours on the vertical plane of symmetry and on the horizontal plane 1 m above the ground surface are displayed. This figure indicates a cloud with its height varying from 20 m to slightly below 10 m and its half-width expanding to almost 65 m at 250 m downwind. Velocity projections on the two planes are shown in Fig. 2.30, which indicates a relatively quiescent flow regime inside the fence and a fairly complicated flow field near the fence, such as the various sizes of eddies and the regions of diverging/converging flow. The concentration contours on three selected downwind planes are displayed in Fig 2.31, which shows a cloud becoming lower and wider in the downwind direction as a combined result of the vapor fence and heavy-gas effects.

The characteristics of the vapor cloud for late times are illustrated in Fig. 2.32. Due to negative buoyancy and turbulence suppression, the vapor cloud is seen to linger within the fence enclosure for a long period of time, even though the spill has been terminated at $t = 310$ s. By 480 s, the vapor cloud still persists and the maximum concentration within the vapor fence is still above 13%. Even at the end of the simulation ($t = 600$ s), the maximum concentration is still over 4% at a place between the front fence and the billboard. Such cloud behaviors appear to be consistent with what was recorded on the video tape of the field experiment.

Representative results from the simulation without vapor fence are shown in Figs. 2.33 through 2.35. The first of these figures illustrates the evolution of the vapor cloud on the vertical plane of symmetry during the first three minutes. In this case, the cloud is dispersed quickly in the downwind direction and remains relatively low, rising to only 9 m at 250 m downwind. The wedge-shaped cloud at the leading edge is a result of the density

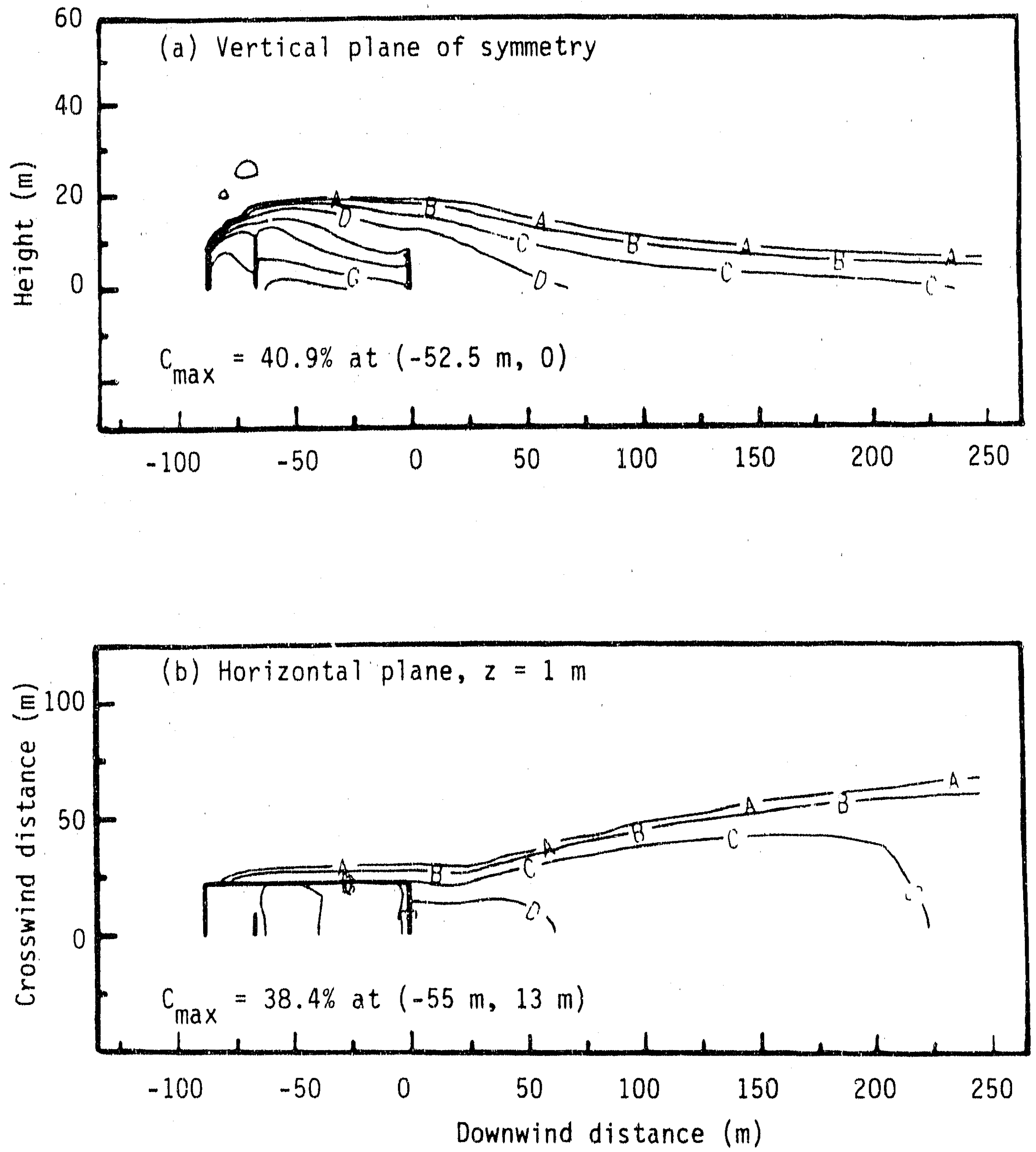

Fig. 2.29. Falcon-4 predicted concentration contours for: (a) vertical plane of symmetry, and (b) horizontal plane at z = 1 m and t = 300 sec. The contour levels are (in % vol): A = 0.5, B = 1, C = 2.5, D = 5, E = 10, F = 15, G = 25, and H = 35.

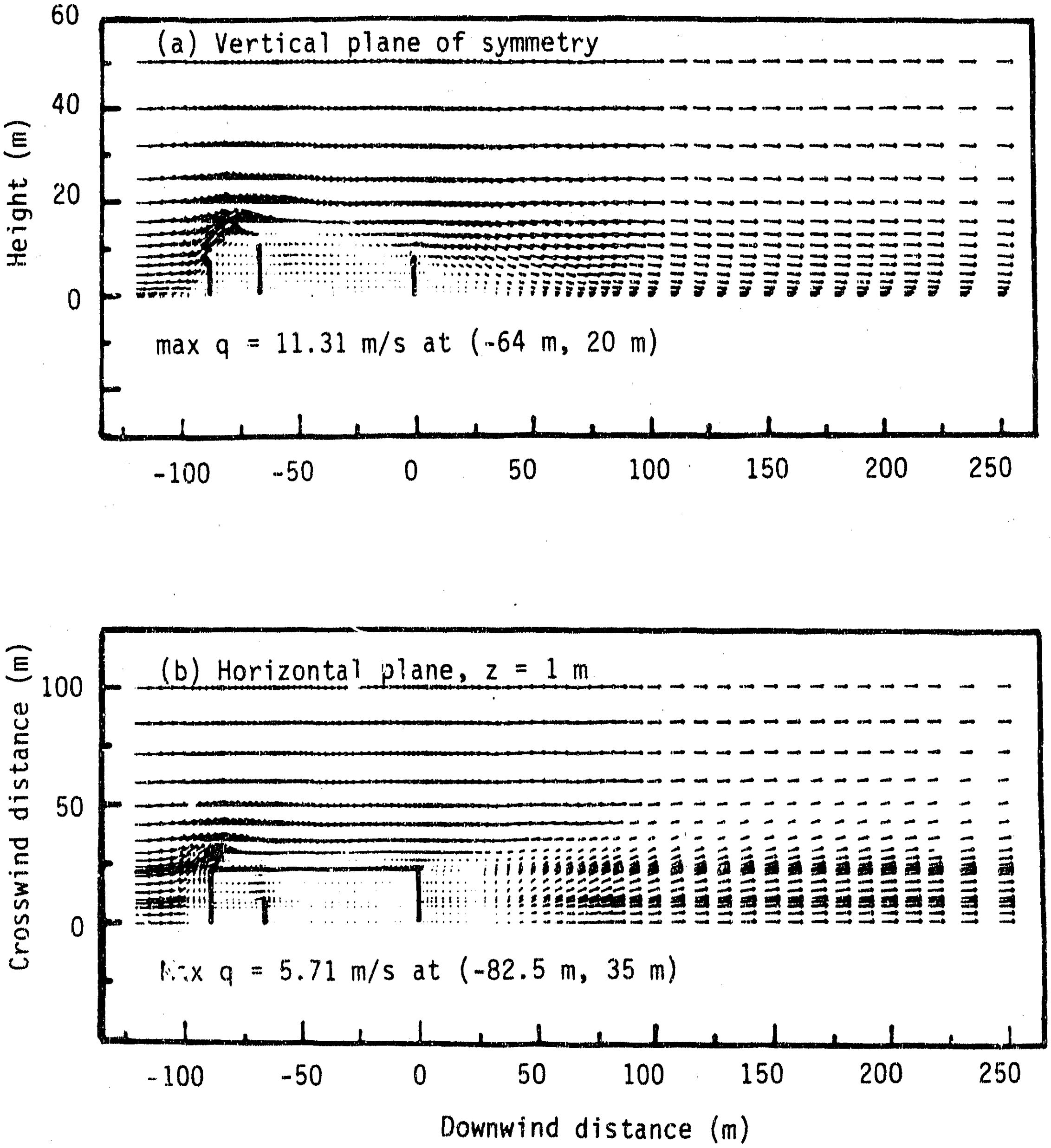

Fig. 2.30. Falcon-4 velocity vectors on two representative planes at t = 300 sec: (a) vertical plane of symmetry, and (b) horizontal plane at z = 1 m.

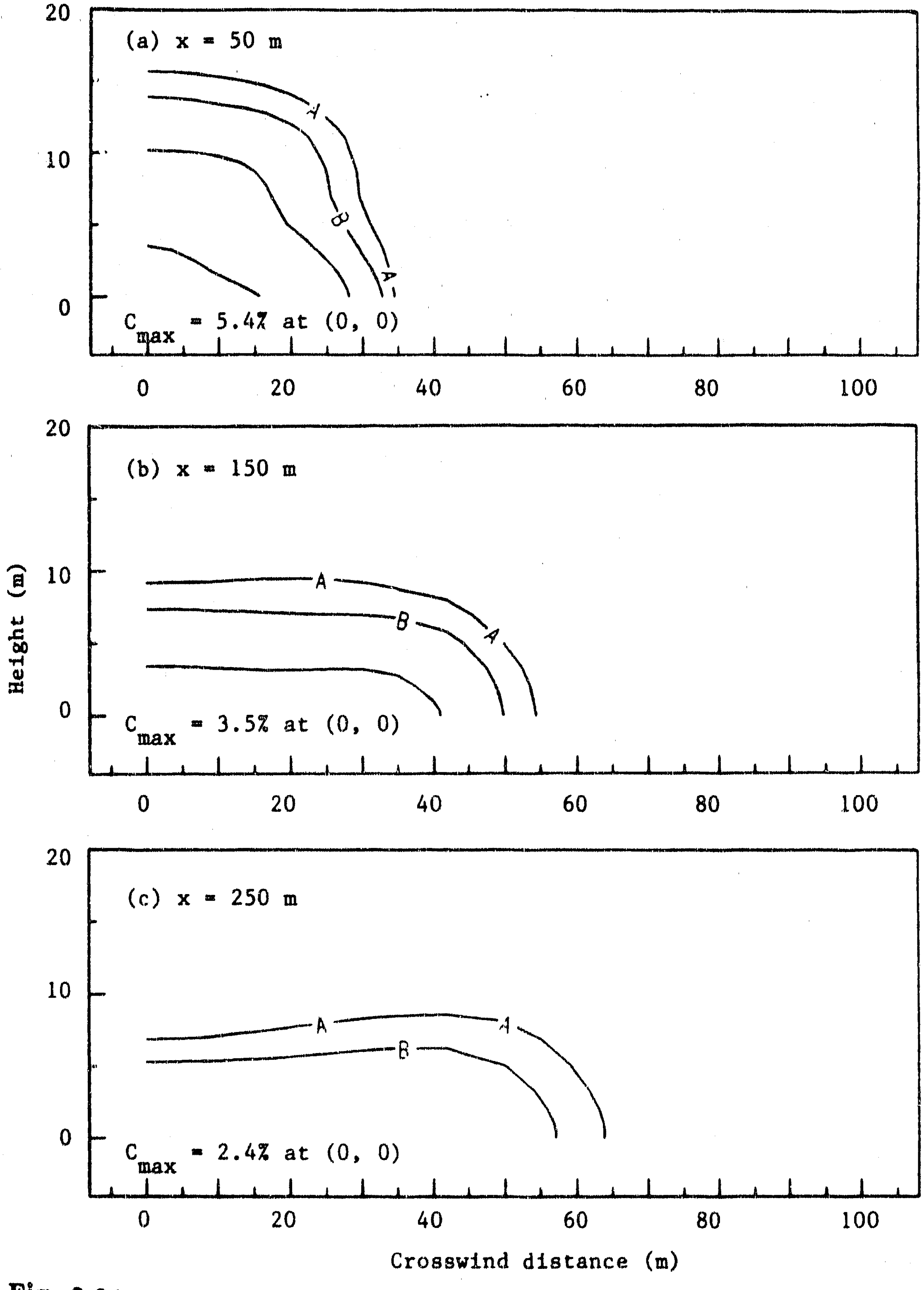

Fig. 2.31. Falcon-4 predicted concentration contours for three different downwind locations behind the rear fence at t = 300 sec. The contour levels are (in % vol): A = 0.5, B = 1, C = 2.5, and D = 5.

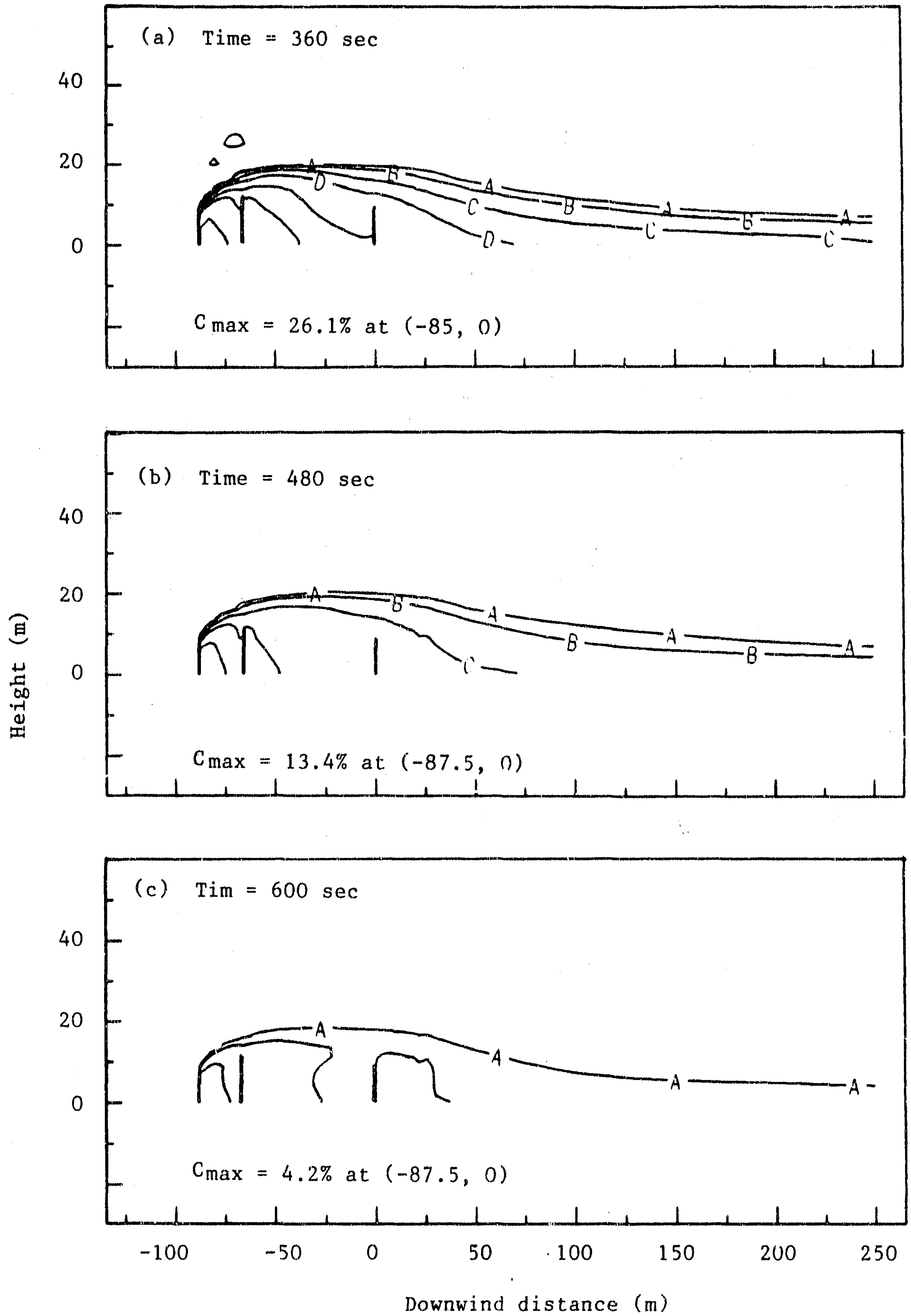

Fig. 2.32. Falcon-4 predicted concentration contours on the vertical plane of symmetry during late times of the vapor dispersion simulation. The contour levels are (in % Vol): A=0.5, B=1, C=2.5, D=5, E=10, F=15, and G=25.

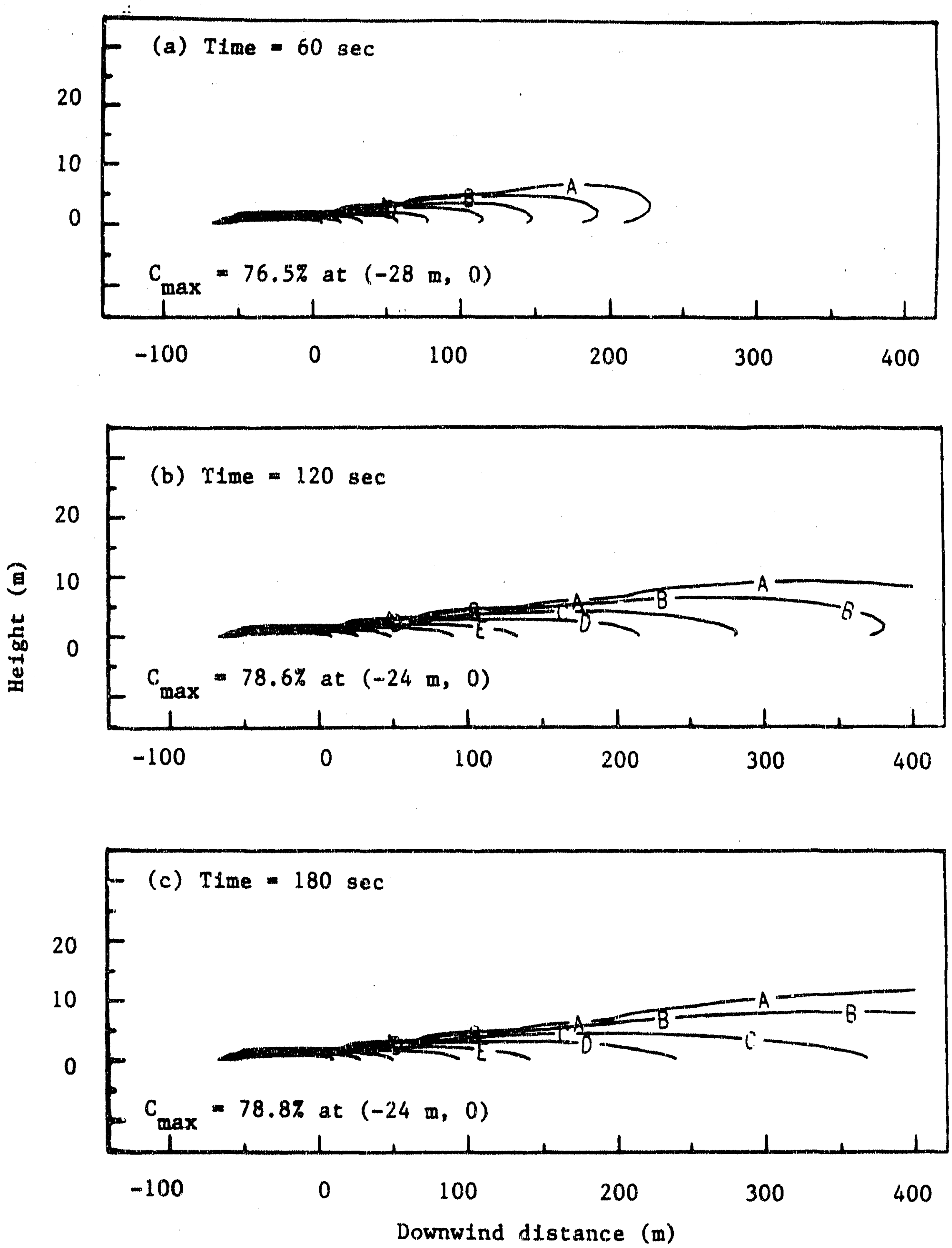

Fig. 2.33. Falcon-4 predicted concentration contours on the vertical plane of symmetry during the first three minutes in a simulation without the vapor fence. The contour levels are (in % vol): A = 0.5, B = 1, C = 2.5, D = 5, E = 10, F = 15, G = 25, H = 35, and I = 50.

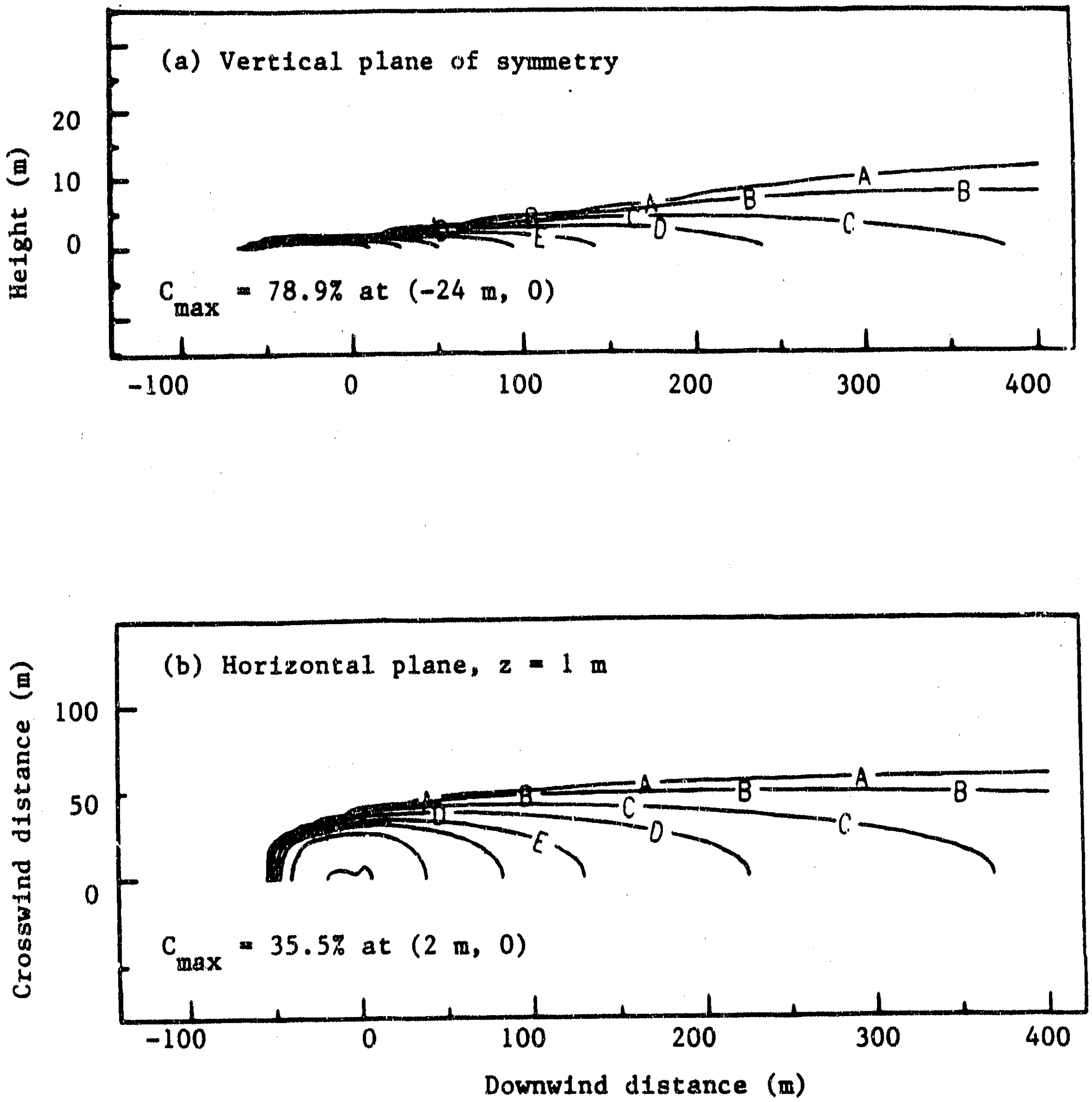

Fig. 2.34. Falcon-4 predicted concentration contours for: (a) vertical plane of symmetry, and (b) horizontal plane at z = 1 m and t = 300 sec in a simulation without the vapor fence. The contour levles are (in % vol): A = 0.5, B = 1, C = 2.5, D = 5, E = 10, F = 15, G = 25, H = 35, and I = 50.

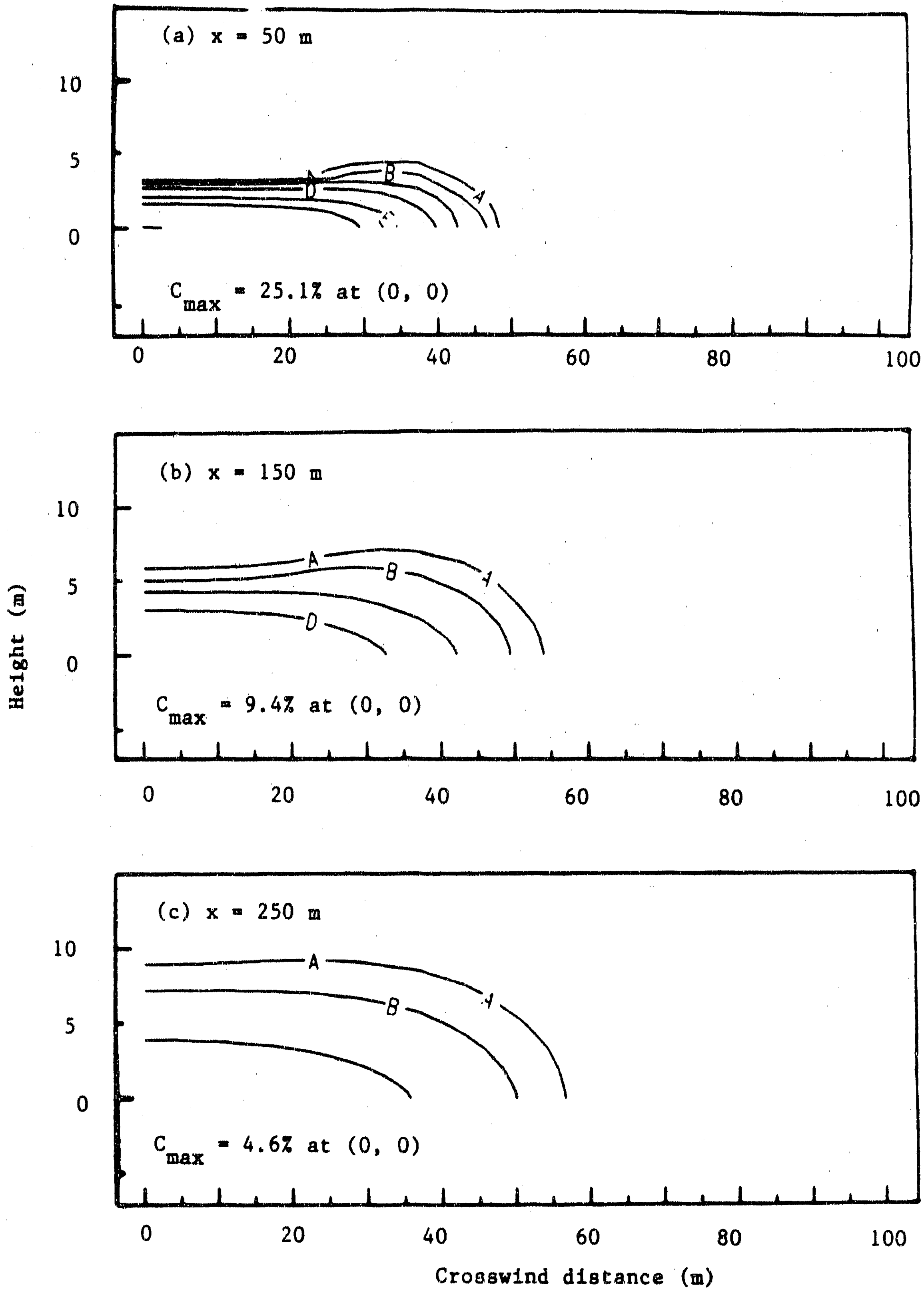

Fig. 2.35. Falcon-4 predicted concentration contours for three downwind locations behind the rear fence at t = 300 sec in a simulation without the vapor fence. The contour levels are (in % vol): A = 0.5, B = 1, C = 2.5 D = 5, E = 10, F = 15, and G = 25.

front opposed by the shear stresses near the ground. Compared with the cloud produced by the vapor fence, the present cloud is dispersed downwind much faster and its values of concentration near the ground are much higher. Also, the shapes of the clouds are markedly different, as can be seen in Figs. 2.29 and 2.34 (and Figs. 2.31 and 2.35 as well). With the fence enclosure, the cloud is high and narrow near the fence and, because of negative buoyancy, it spreads out gradually and decreases slowly in height toward downwind. On the other hand, without the vapor fence (thus unconfined laterally), the cloud tends to spread out immediately in the source region and results in a wider and lower cloud thereby. Far away from the fence, as the effects of the fence/billboard taper off, the two clouds are more comparable in shape and size.

The time series of concentration for four selected locations near or behind the source are compared in Figs. 2.36 and 2.37 between the two simulations. At the center of spill (Fig. 2.36a), the spill conditions appear to be dominating over the fence effects, thus the two curves are very close to each other over much of the spill duration. However, after the spill has been terminated (t = 310 s), the curves are drastically different regarding cloud persistence. As a result, the concentration is above 2.5% for approximately 530 s in the case with vapor fence, as opposed to 330 s without the vapor fence. Similar effects are seen in Fig. 2.36(b) for the location near the downwind edge of the area source. These results suggest that, in spite of its advantages, e.g., reducing the level of concentration and curtailing the downwind distance of hazardous area, an LNG vapor fence could prolong the cloud persistence time within the fence, thus greatly increasing the potential for ignition and combustion in such an area. At locations behind the source (Fig. 2.37), the simulation with vapor fence has produced much delayed cloud ·rrival time and significantly lower concentration.

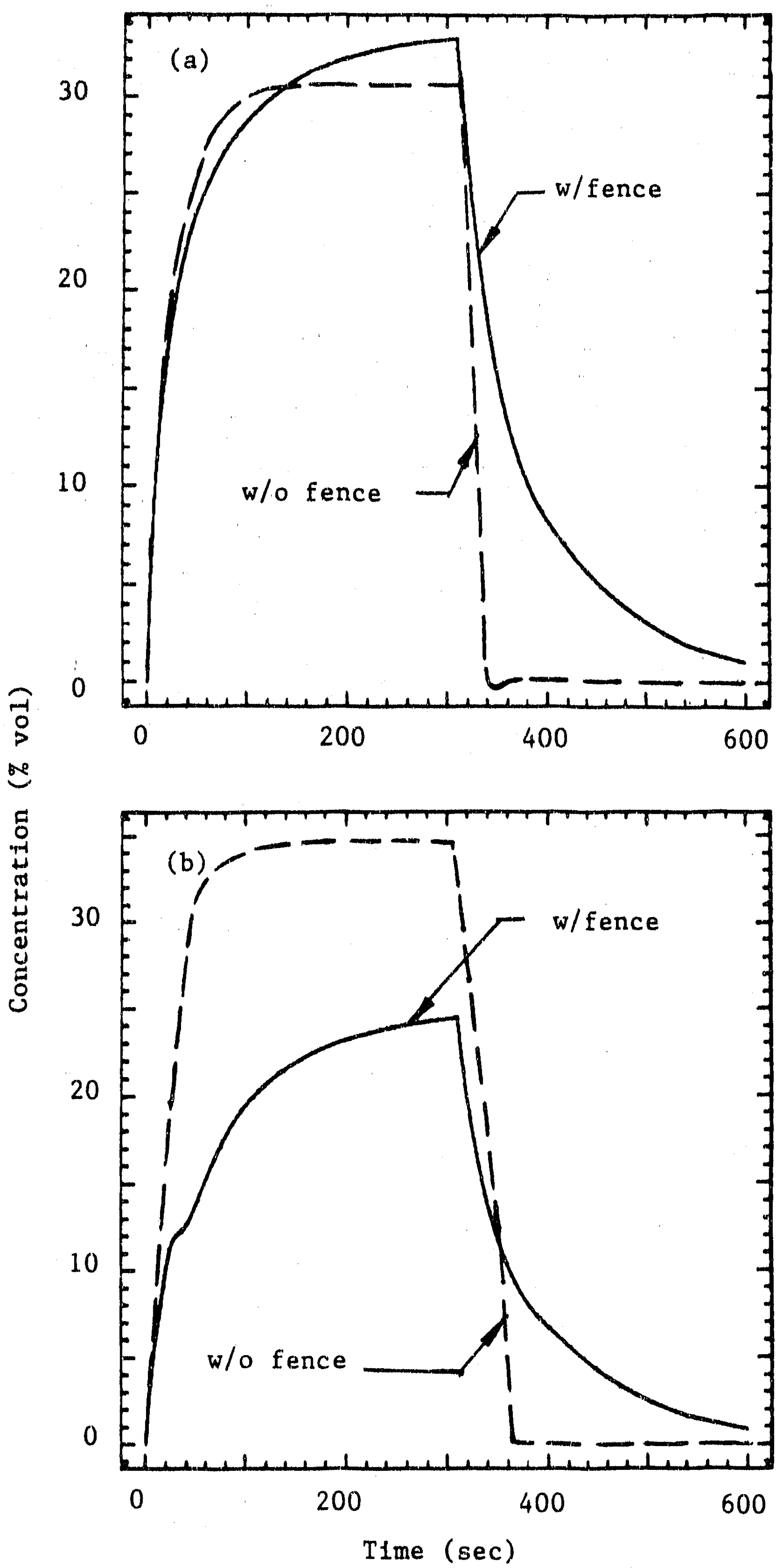

Fig. 2.36. Comparison of predicted time series of concentration for Falcon-4 in the source area: (a) at the center of spill and 1 m high, (b) at 30 m dowrwind from the center of spill and 1 m high.

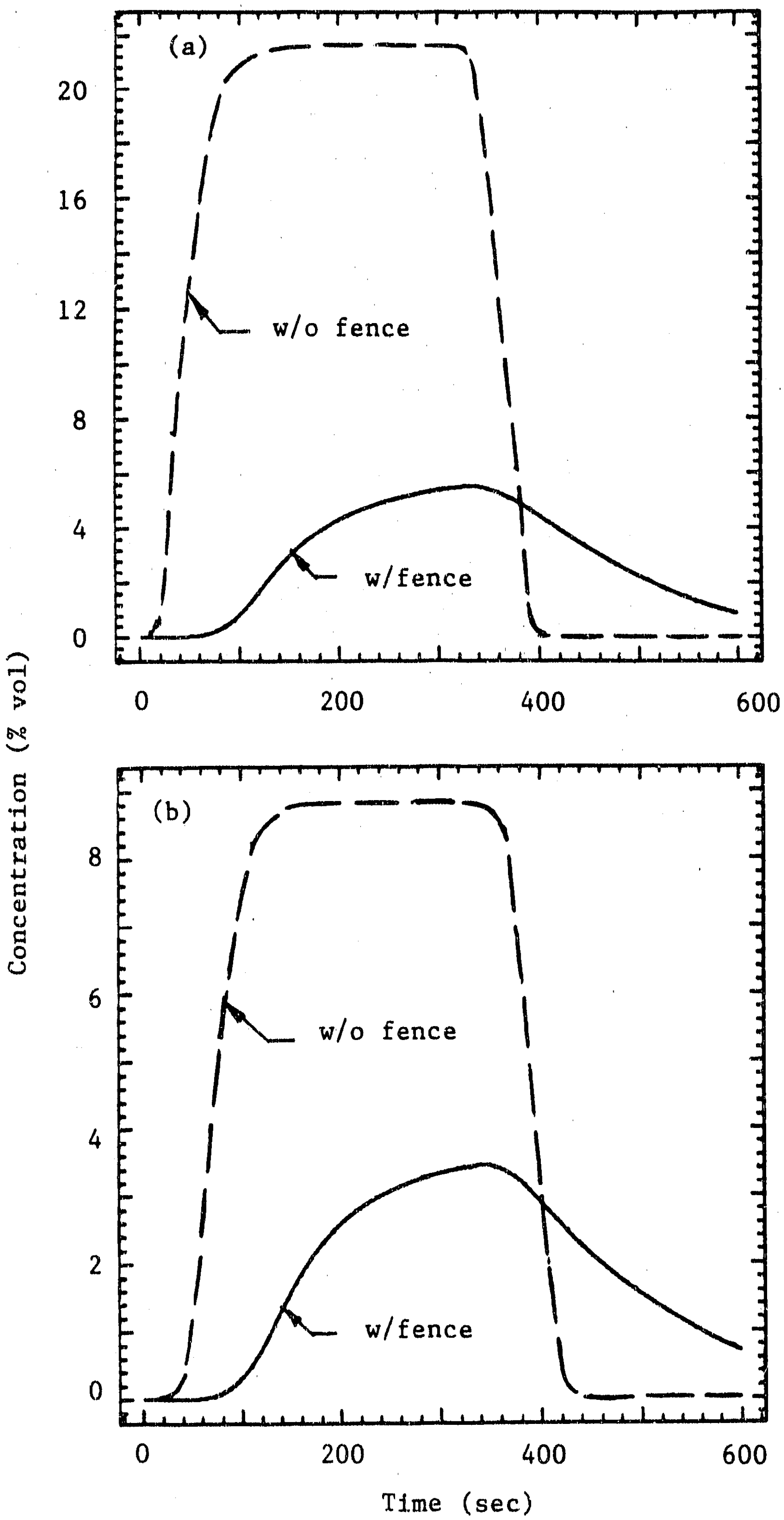

Fig. 2.37. Comparison of predicted time series of concentration for Falcon-4 at two locations: (a) 50 m downwind and 1 m high, (b) 150 m downwind and 1 m high. Both downwind distances are measured from the rear fence.

3. MODEL-DATA COMPARISON

In this section, the numerical results are compared with field data for the four Falcon tests described in Section 2. The field data were taken at the rate of one sample/sec but were averaged over five seconds for comparison with the numerical results. Such an averaging time is believed to be long enough for the turbulent time scales and yet is short enough for retaining the dynamical characteristics of the transient gas cloud. Both fields of concentration and temperature are considered and the comparison is conducted for locations both inside and outside of the vapor fence. Specifically, comparisons are made for time series of the field variables, the peak values of concentration along the cloud centerline, and contour plots of concentration on selected crosswind planes. The model performance is also assessed quantitatively using the ratio method recommended by Ermak and Merry (1988), regarding cloud arrival and persistence times for concentration levels of practical importance, the maximum change in temperature, the peak values of concentration, and the maximum downwind distance to 2.5% and 5% concentrations.

The specific locations selected for comparison of time series of temperature and concentration are listed in Tables 3.1 and 3.2. All the selected locations except one are on the cloud centerline where maximum concentration and minimum temperature usually occur. As discussed in Section 2, in order to reduce computing costs, all the model simulations were performed for one-half of the vapor cloud, thus it is necessary to compare model results with field data nearest to the cloud centerline, instead of those on the array centerline. Representative wind trajectories (which were constructed from the wind field data and should approximate the centerlines of the vapor clouds) and sensor locations for the four tests are depicted in Fig. 3.1. These results indicate that the cloud centerline is aligned fairly well with that of the sensor array for all the tests except Falcon-1, in which case the angle between the wind trajectory and the array centerline is nearly 20°. Thus the assumption of symmetry in the model simulations is expected to yield a greater error for Falcon-1 than for the other tests.

Table 3.1. Locations for model-data comparison of temperature.

Test / (x,y,z) in meters	Falcon-1	Falcon-2	Falcon-3	Falcon-4
(-32, 0, 1)	X	X		X
(-2, 0, 1)	X	X	X	X
(50, 0, 1)	X	X	X	X
(50, 0, 5)	X	X	X	X
(150, 0. 1)	X	X	X	
(150, 0. 5)		X	X	

Table 3.2. Locations for model-data comparison of concentration.

Test / (x,y,z) in meters	Falcon-1	Falcon-2	Falcon-3	Falcon-4
(-62, 0, 1)		X	X	
(-62, 20, 1)	X	X		
(-32, 0, 1)		X	X	X
(-2, 0, 1)			X	X
(50, 0, 1)	X		X	X
(50, 0, 5)	X		X	X
(150, 0, 1)	X		X	X
(150, 0. 5)	X		X	X
(250, 0, 1)	X	X	X	X
(250, 0, 5)	X	X	X	X

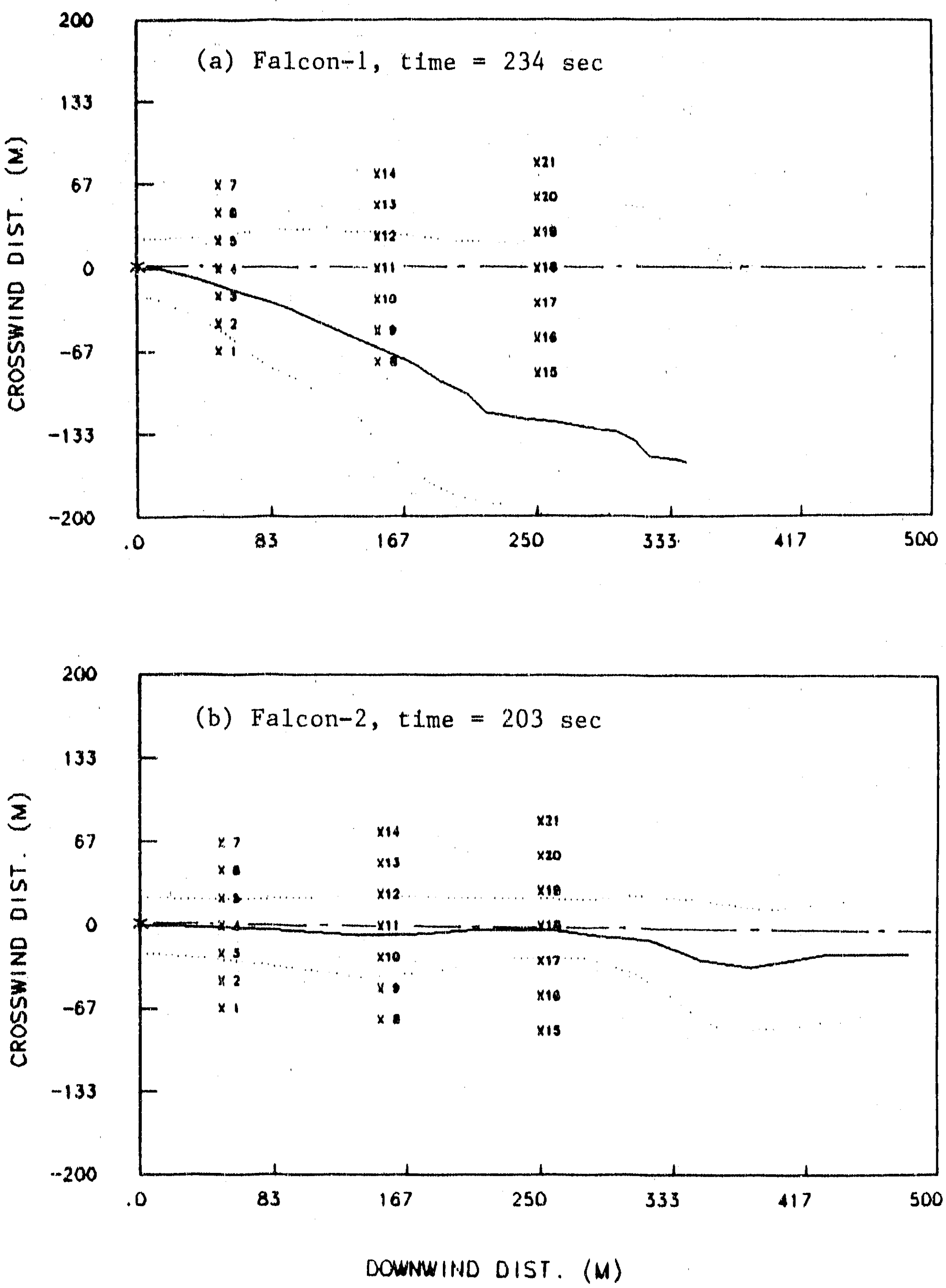

Fig. 3.1. Wind trajectory and sensor locations (marked by x) for Falcon-1 through Falcon-4.

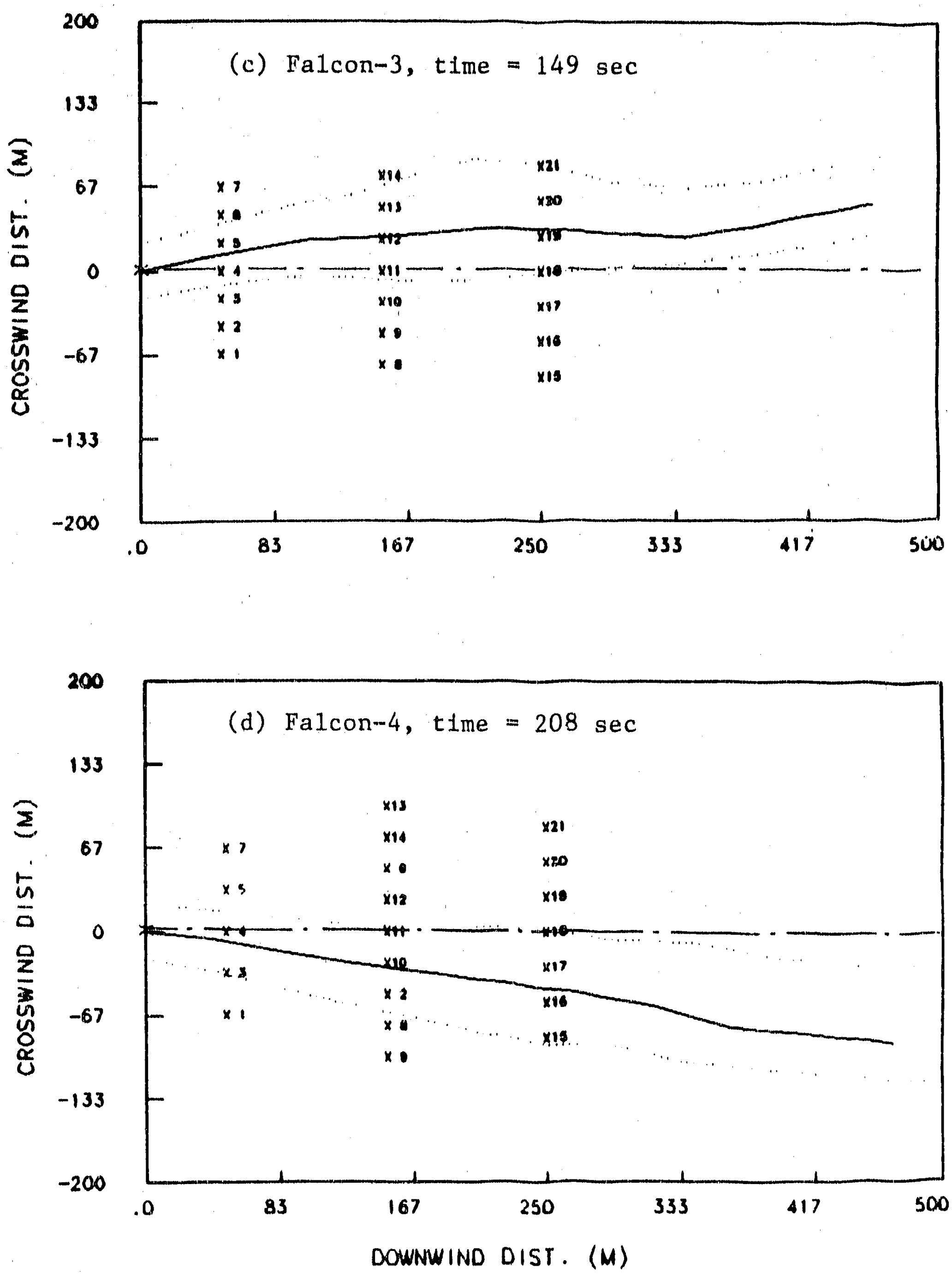

Fig. 3.1. Continued

3.1 Falcon-1

In Figs. 3.2 through 3.4, a comparison of predicted vs. measured concentration and temperature for three locations inside the fence enclosure is made. In Fig. 3.2, the predicted temperature and the measured data at the center of spill are compared. Despite the fact that the model overpredicts the decrease in temperature by ~35% and the predicted curve for late times recovers too rapidly to the ambient temperature, the shapes of the two curves, nevertheless, agree reasonably well. A similar agreement is observed in Fig. 3.3 for a location near the rear fence. In Fig. 3.4, the predicted concentration for a location near the fence side is compared with measurements taken by a JPL (Jet Propulsion Laboratory) sensor, which unfortunately is the only gas sensor operational inside the vapor fence for this test. The predicted higher concentration is consistent with the prediction of lower temperature. The field data at these locations seem to suggest a more diluted and slightly more persistent cloud than predicted.

In Figs. 3.5 through 3.9, the predicted temperature and concentration for downwind locations at 50 m, 150 m, and 250 m behind the rear fence are compared with data measured near (but generally not coincident with) the cloud centerline. Considering the complexities of the vapor dispersion phenomena, the overall agreement between model predictions and field data is very reasonable. In particular, the predicted results for locations at 1 m high appear to agree quite well with field measurements, with respect to the shapes of the curves, the peak values of the individual variables, the arrival and departure times, etc. For locations at 5 m high, the actual vapor cloud appears to be less coherent than predicted by the numerical model. The large discrepancies at the 5 m height are believed due to the presence of the less stable cloud/air interface in that vicinity (see Fig. 3.12 for the actual cloud height), coupled with a rather coarse (~ 2 m) grid spacing nearby. Also, the discrepancies might have been aggravated by the model's assumption of symmetry and the considerable distance between the gas sensors considered and the actual cloud centerline (e.g., in Fig. 3.9, gas sensor G15 at 250 m is perhaps 40 m away from the cloud centerline).

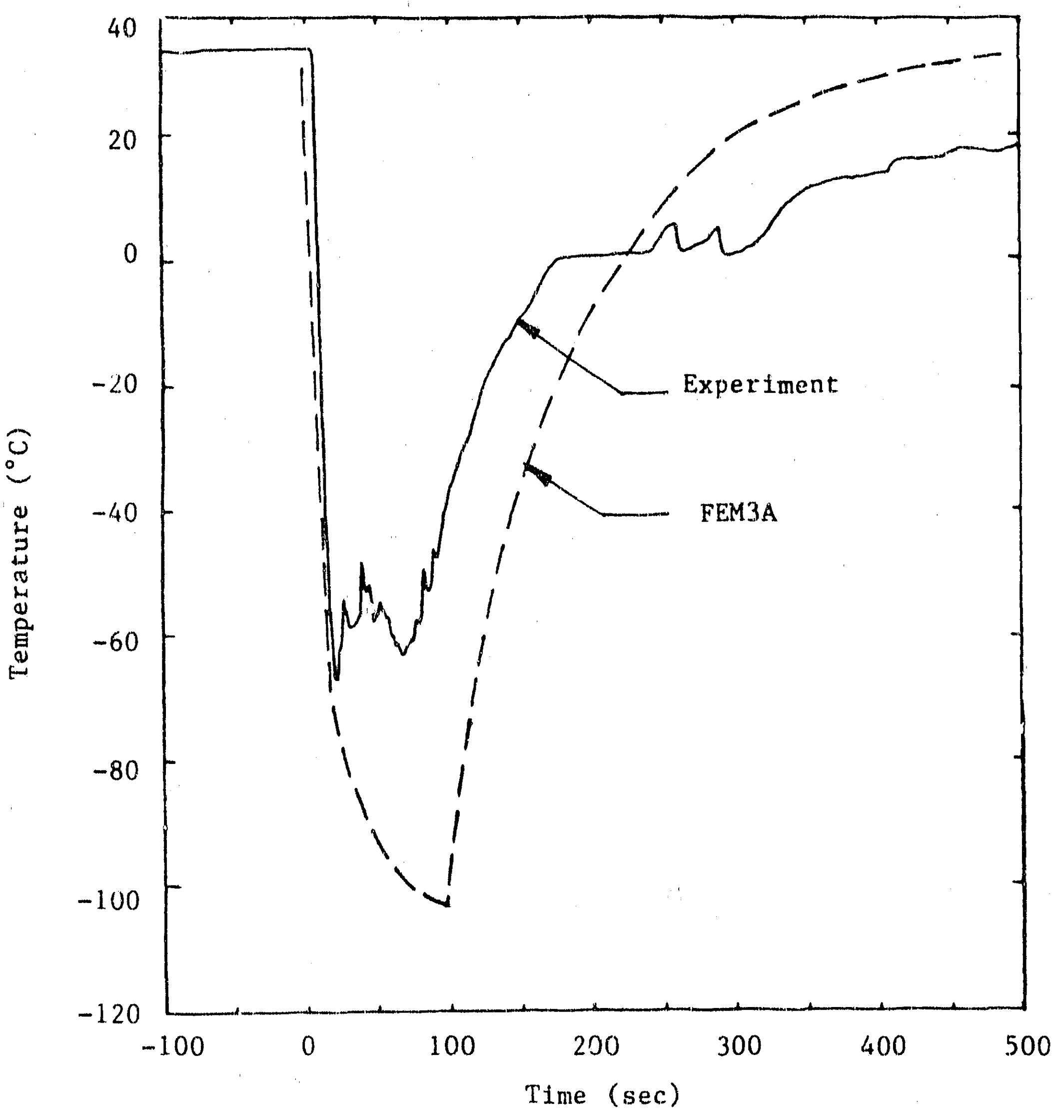

Fig. 3.2. Falcon-1 predicted versus meausred temperature near the center of spill at (x,y,z) = (-32m,0,1m).

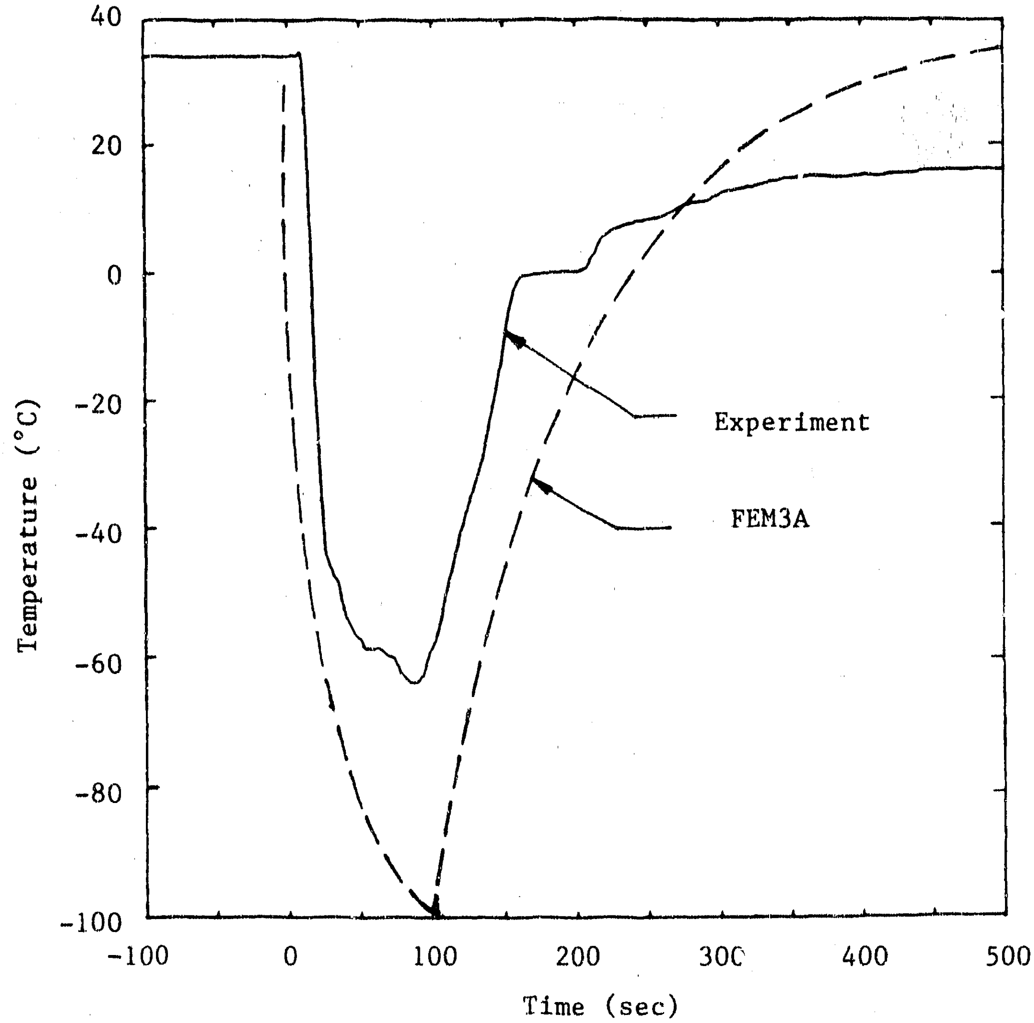

Fig. 3.3. Falcon-1 predicted versus measured temperature in front of the rear fence at (x,y,z) = (-2m,0,1m).

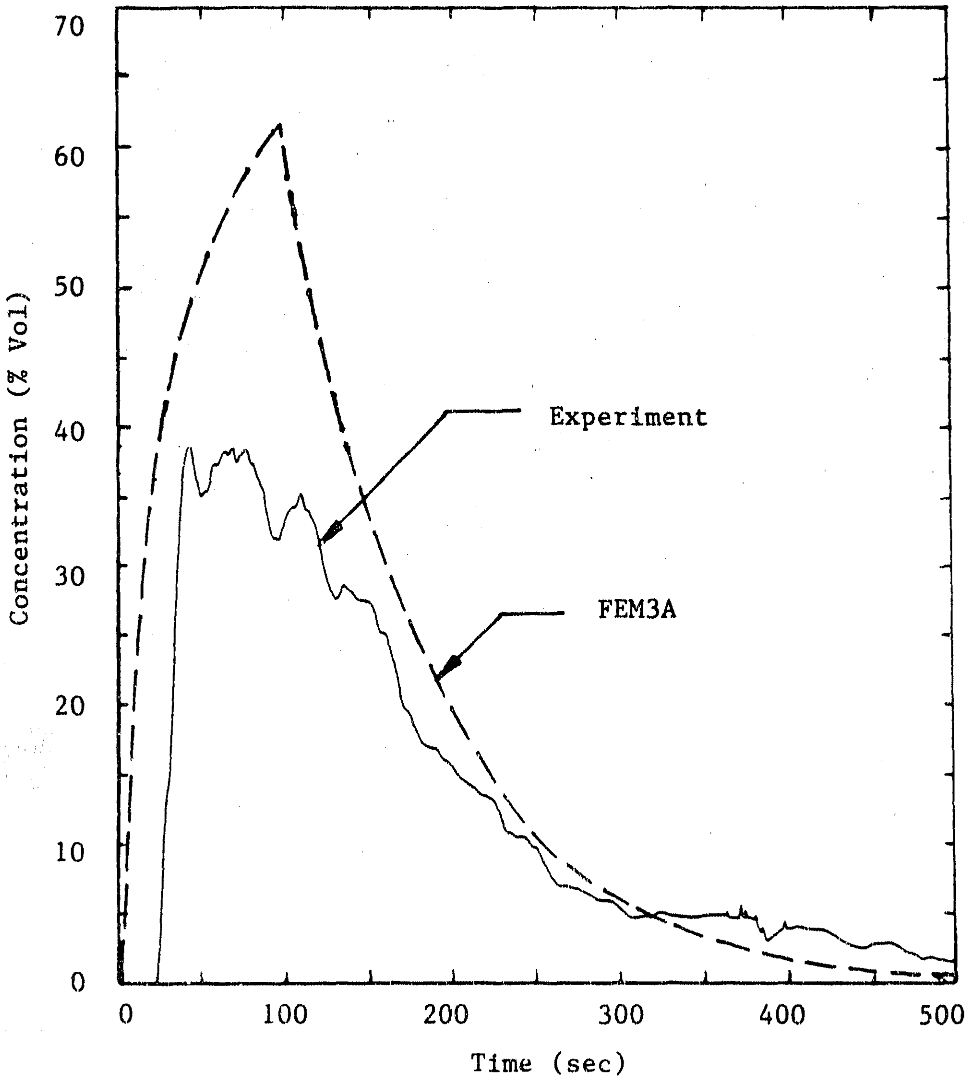

Fig. **3.4.** Falcon-1 predicted versus measured concentration within the fence side enclosure and near the fence side. The predicted values are for location at (x, y, z) = (-60m, 20m, 1m) and the measurements are for location at (x, y, z) = (-62m, 20m, 1m).

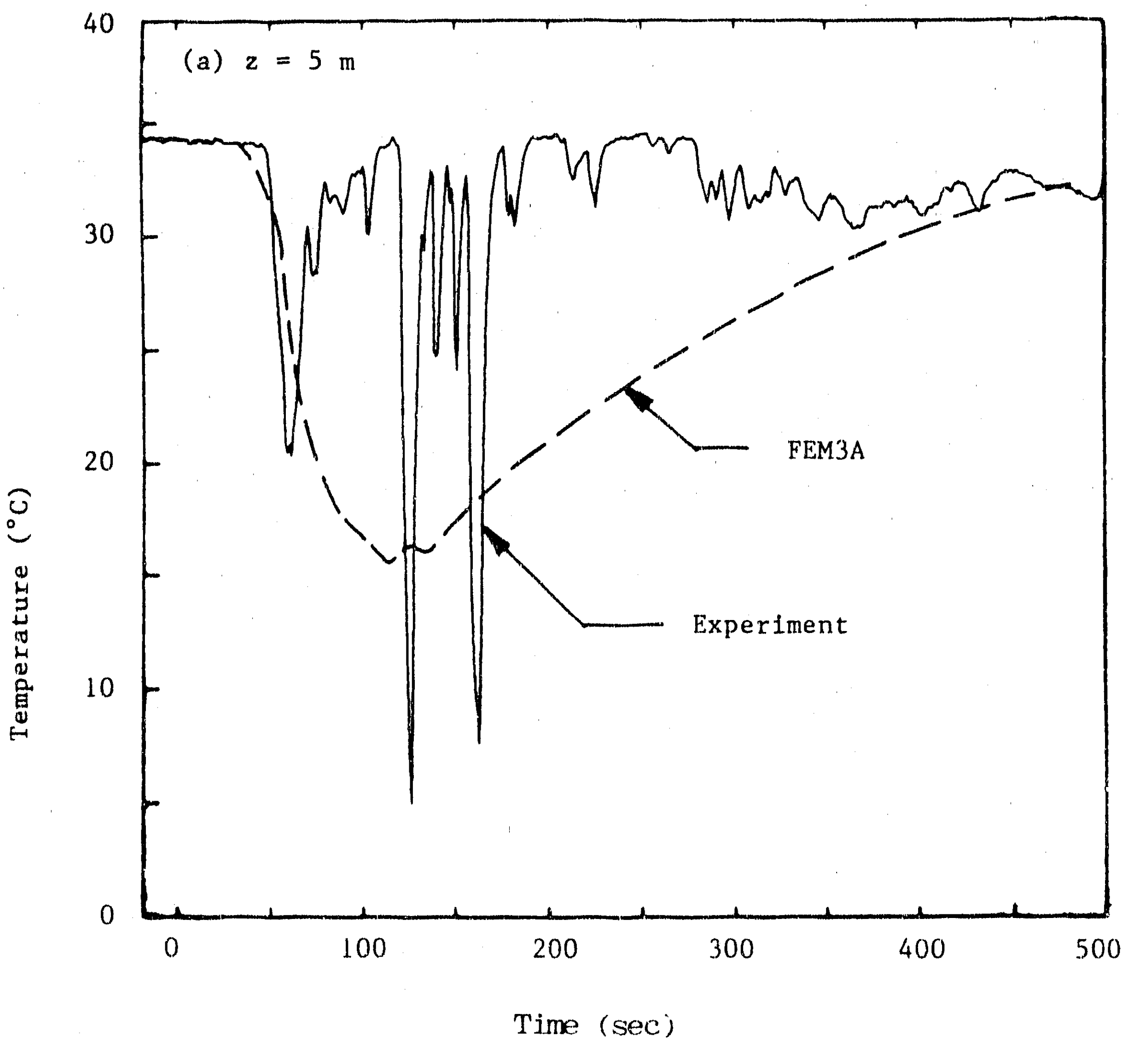

Fig. 3.5. Falcon-1 predicted versus measured temperature for two different heights at 50 m behind the rear fence The predicted values are from the vertical plane of symmetry and the measurements are from gas sensor G04 (which is near the cloud centerline).

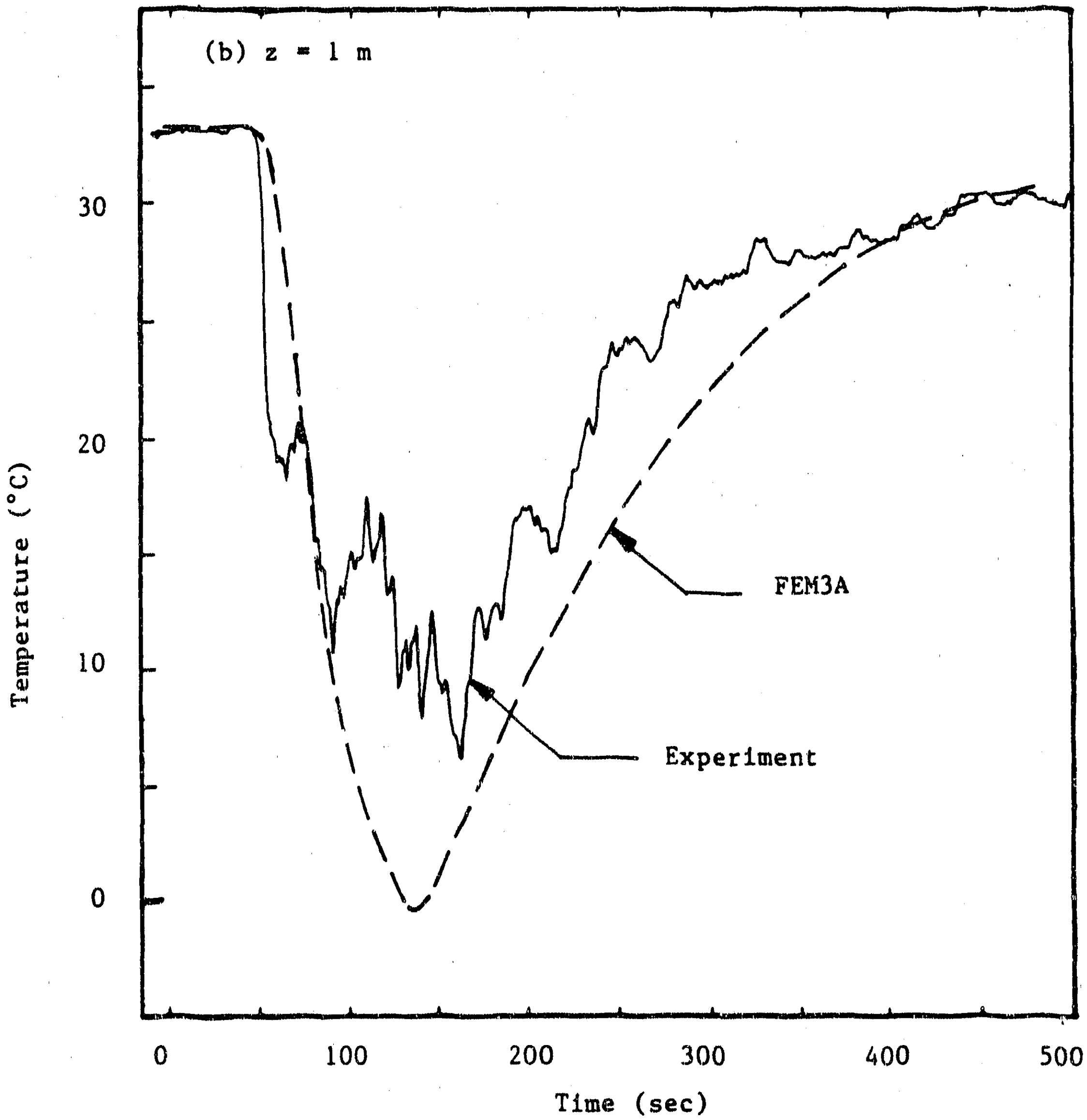

Fig. 3.5. Continued.

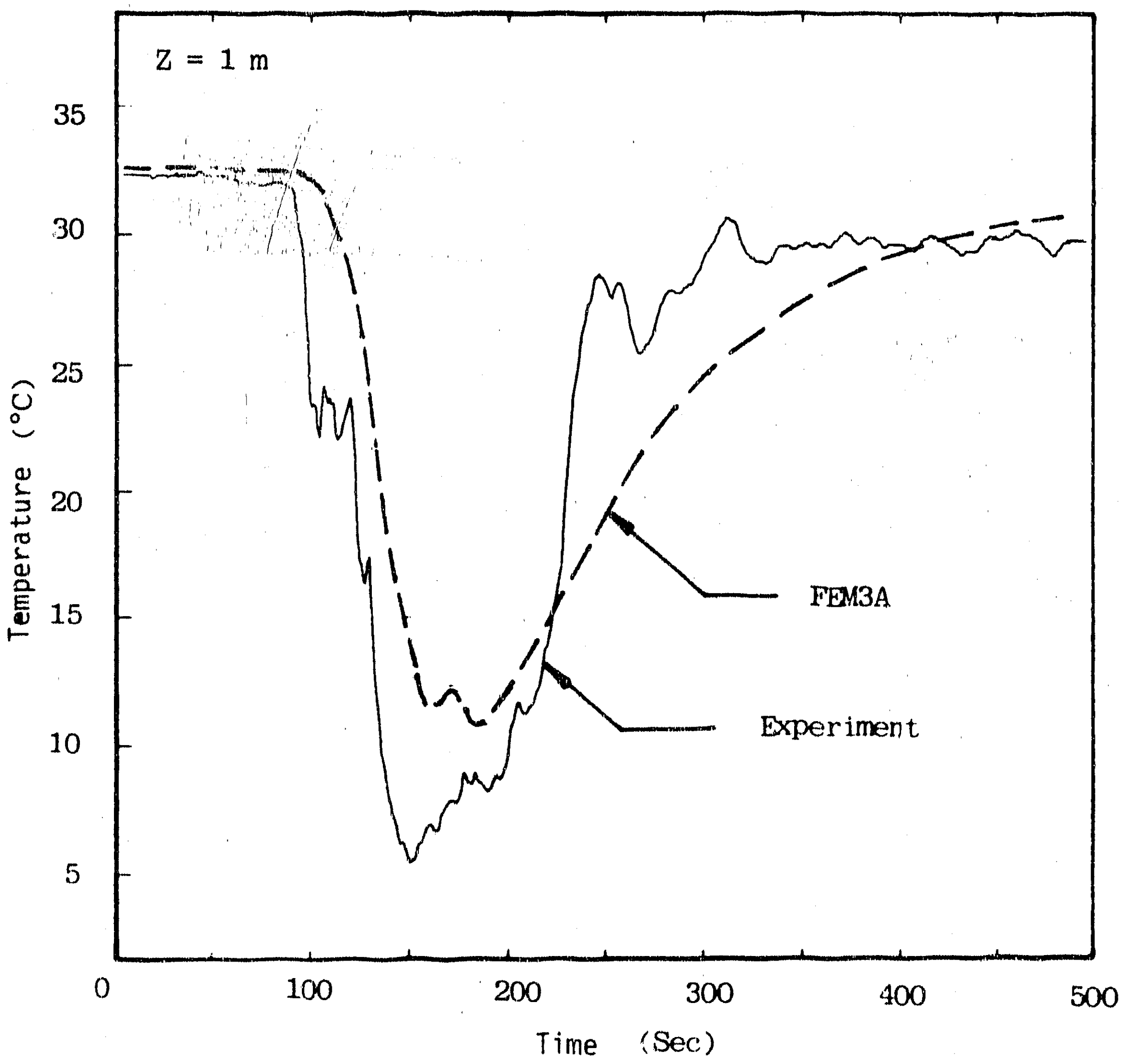

Fig.3.6. Falcon-1 predicted versus measured temperature for a location 1 m above ground surface and 150 m behind the rear fence. The predicted values are from the vertical plane of symmetry, and the measurements are from gas sensor G09 (which is near the cloud centerline).

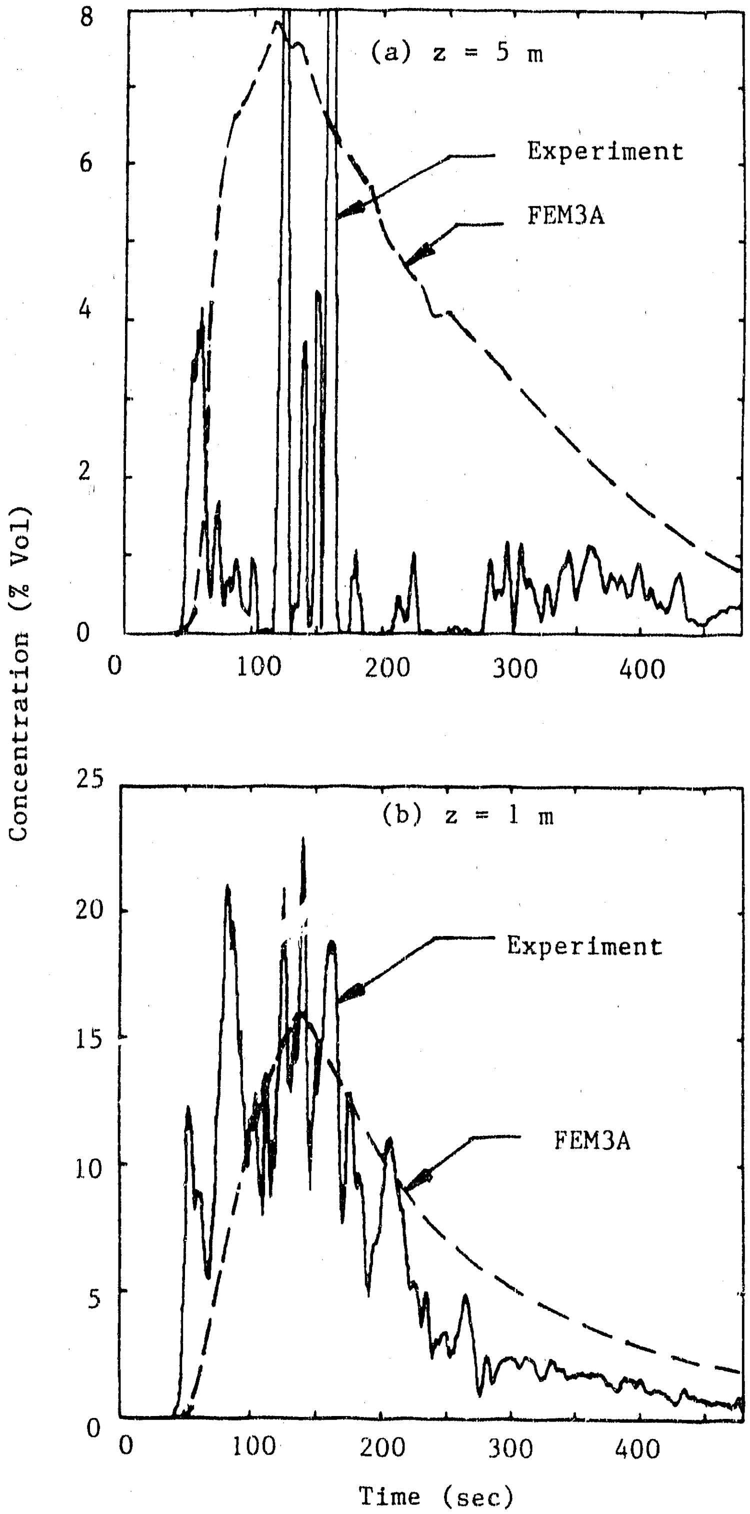

Fig.3.7. Falcon-1 predicted versus measured concentration for two different heights at 50 m behind the rear fence. The predicted values are from the vertical plane of symmetry and the measurements are from gas sensor G04 (which is near the cloud centerline).

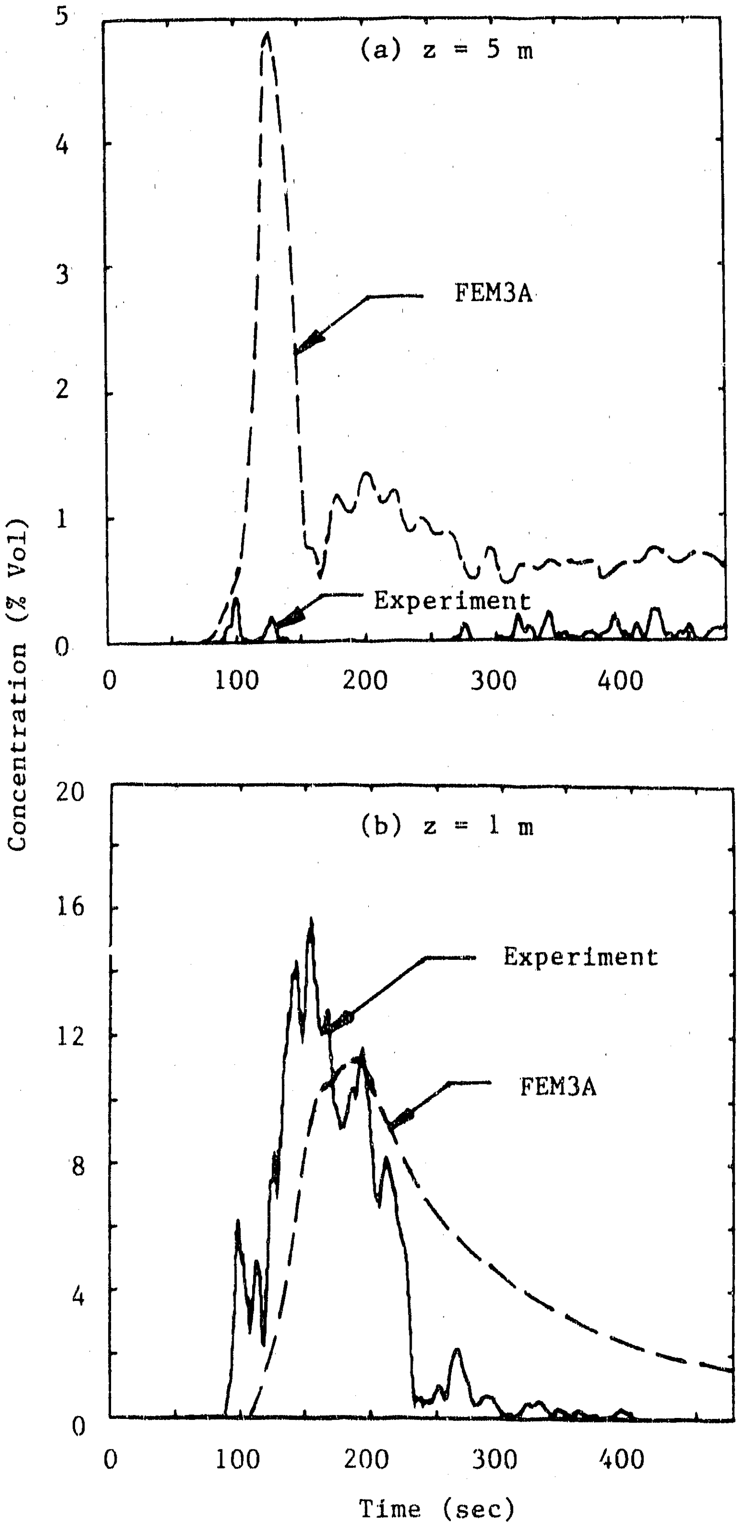

Fig.3.8. Falcon-1 predicted versus measured concentration for two different heights at 150 m behind the rear fence. The predicted values are from the vertical plane of symmetry and the measurements are from gas sensor G09 (which is near the cloud centerline).

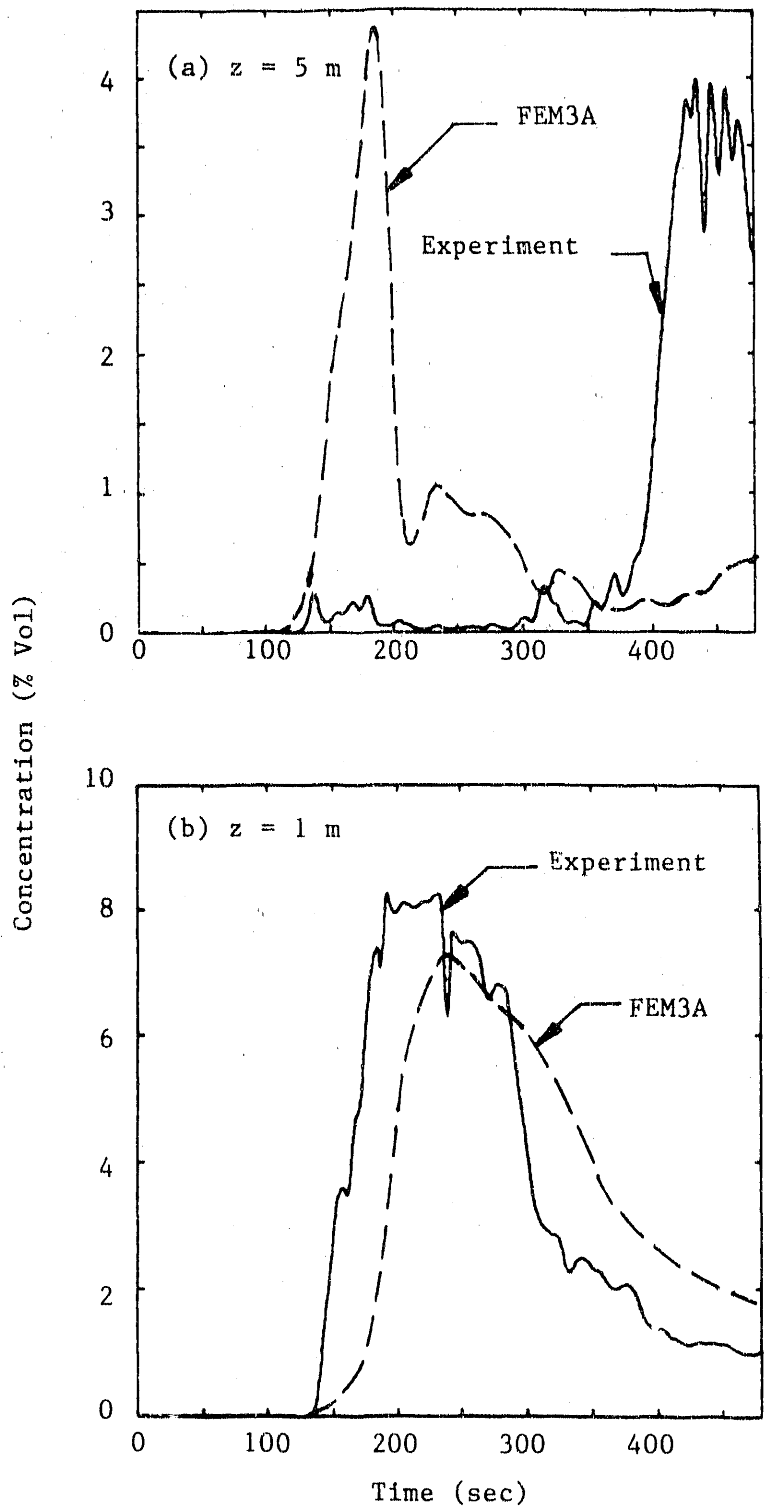

Fig.3.9. Falcon-1 predicted versus measured concentration for two different heights at 250 m behind the rear fence. The predicted values are from the vertical plane of symmetry and the measurements are from gas sensor G15 (which is near the cloud centerline).

In Fig. 3.10, the predicted concentrations for the three downwind locations, all at 1 m above the ground surface, are superimposed. This figure indicates a slow dissipation of the gas cloud, together with a 50 to 60 s difference in cloud arrival times among adjacent locations, which are consistent with the observed data.

The predicted concentration contours for the crosswind plane at 150 m downwind are shown in Fig. 3.11 for time = 180 and 300 s, respectively; the corresponding experimental results are shown in Fig. 3.12. As seen in these figures, the numerical model predicts an "average" cloud height between 5 and 6 m, which is comparable to the experimental value of approximately 5 m. Unfortunately, it is not possible to compare the cloud width, because the cloud at these times already went beyond the edges of the sensor array and the computational domain. The values of maximum concentration agree reasonably well for time = 180 s. However, for time = 300 s, the present model has yielded somewhat higher concentration, suggesting that the actual cloud was diluted faster than simulated.

Finally, the maximum values of concentration along the "cloud centerline" are compared in Fig. 3.13 (due to significant cloud bifurcation of Falcon-1, it is more appropriate to compare the predicted centerline values against the measured values at similar locations, rather than the measured peak values over the entire crosswind plane). Overall, the model is underpredicting the concentration by as much as 35%. Considering the symmetry assumption and the simple approach used to model the source conditions, including superheating and turbulence inside the fence, such discrepancies are within reasonable expectations.

3.2 Falcon-2

Due to internal software problems, no concentration data was taken by the LLL-IR gas sensors during this test. Consequently, the model-data comparison in this case is somewhat less extensive as the other cases. The predicted temperature and concentration at several locations within the vapor fence are compared with data in Figs. 3.14 through 3.18. Despite

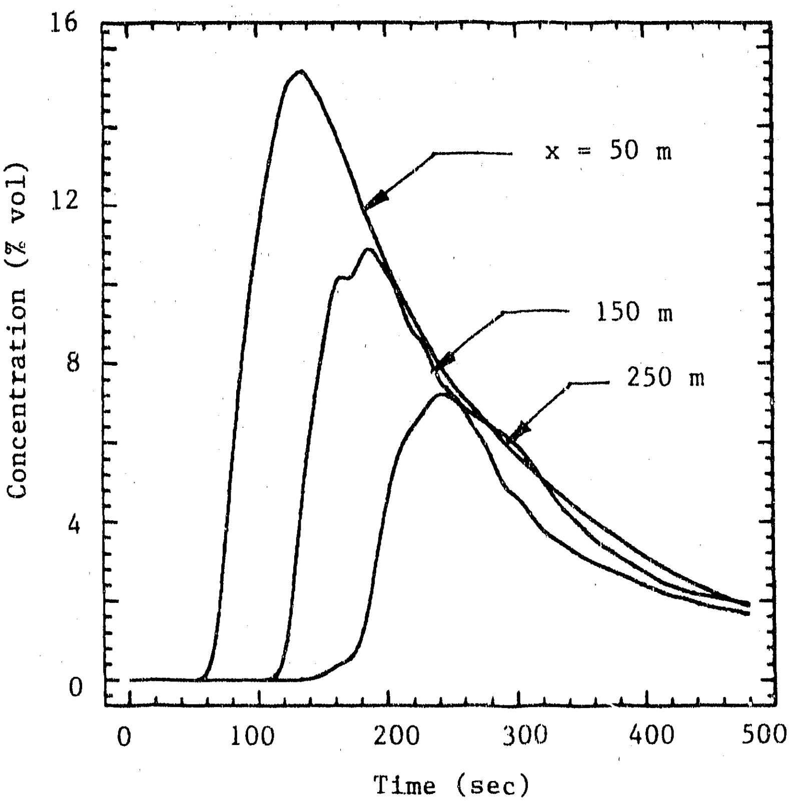

Fig. 3.10. Falcon-1 predicted time series of concentration for three locations behind the rear fence, which are all on the plane of symmetry and 1 m above the ground surface.

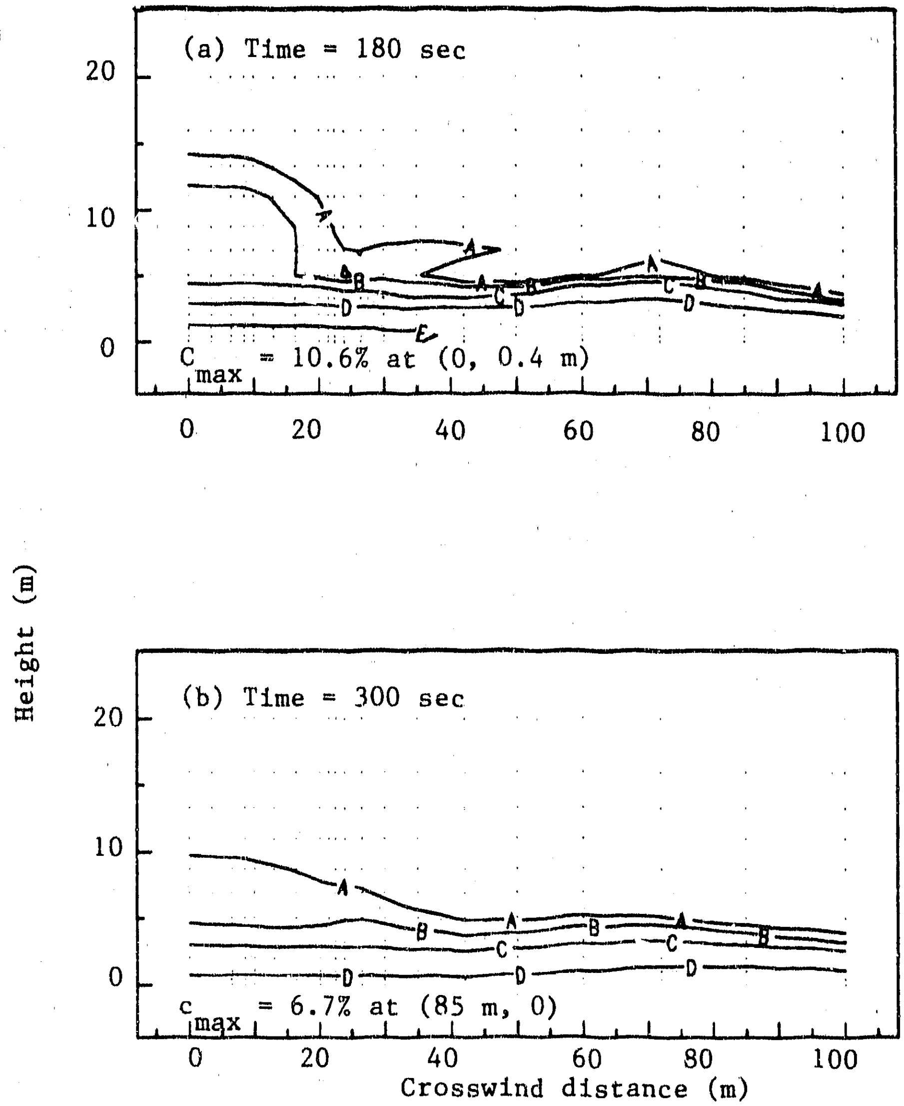

Fig. 3.11. Falcon-1 predicted concentration contours on the crosswind plane at 150 m behind the rear fence. The contour levels are (in % vol): A = 0.5, B = 1, C = 2, D = 5, and E = 10.

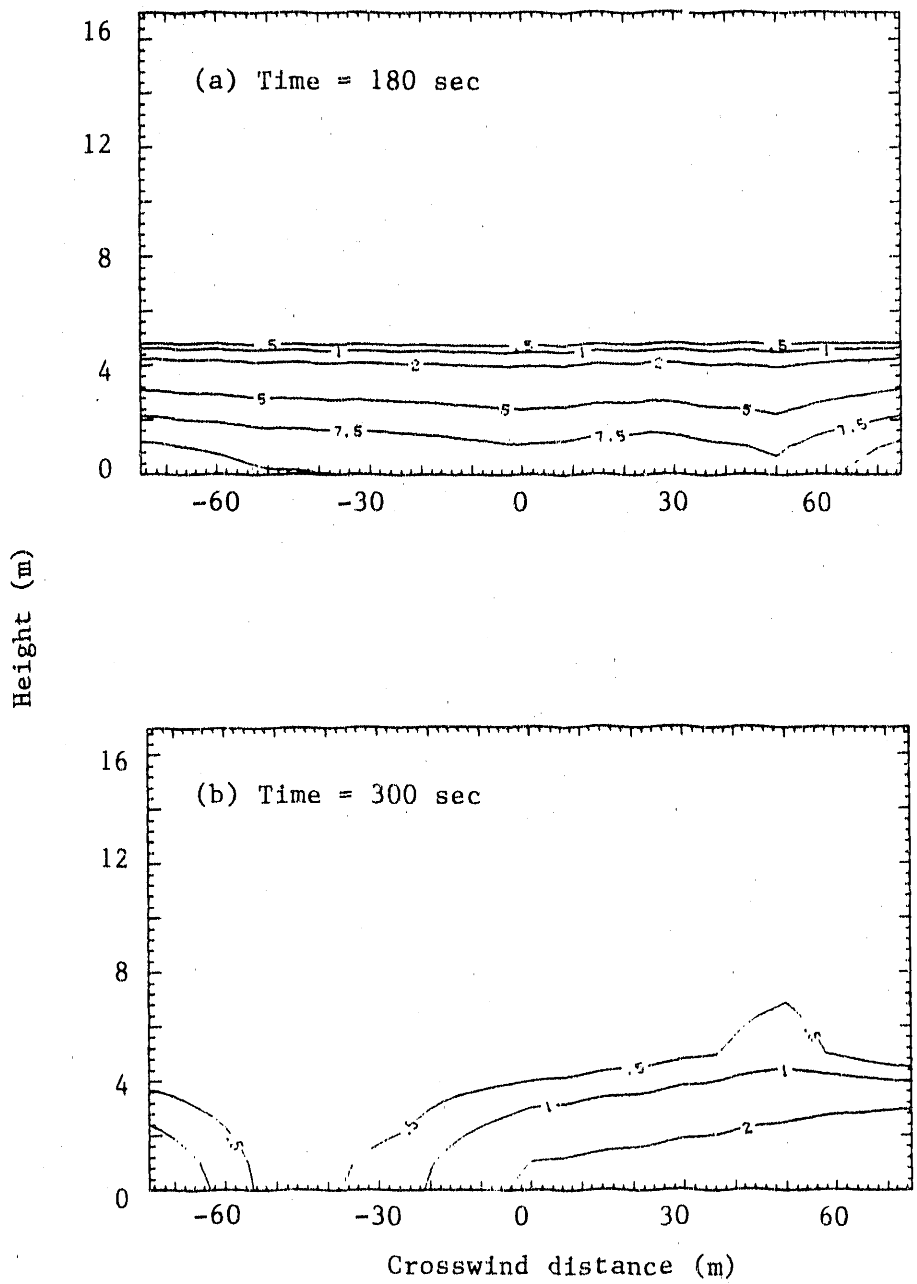

Fig. 3.12. Falcon-1 experiment concentration contours on the crosswind plane 150 m behind the rear fence.

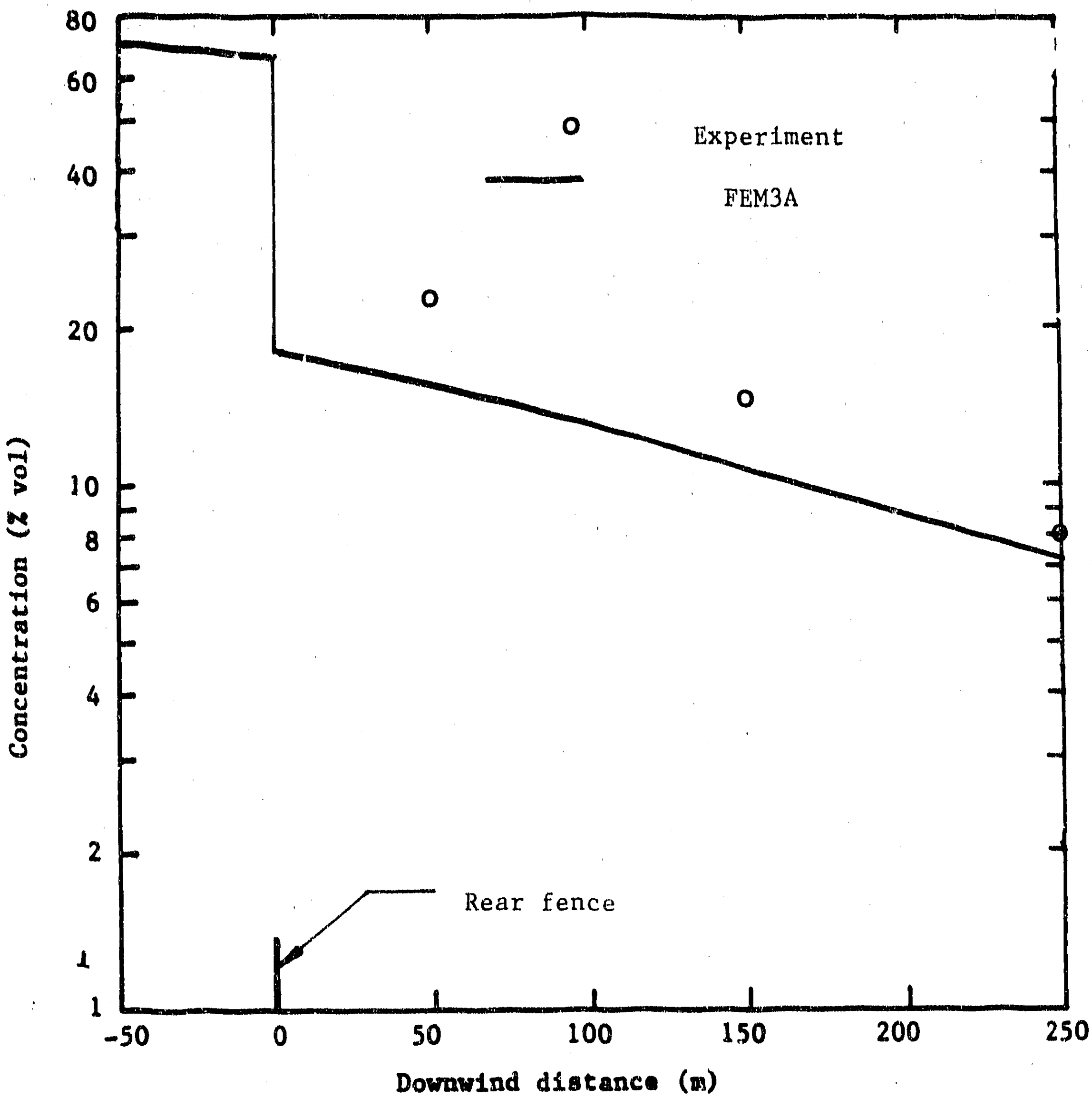

Fig. 3.13. Comparison of predicted versus measured maximum concentrations along "cloud centerline" and at 1 m high for Falcon-1.

a difference of about 25 s in cloud arrival times and somewhat shorter persistence time of the predicted cloud. the general agreement between model results and field data, regarding the peak values and the shapes of the curves, is quite reasonable. Most of the discrepancies are believed due to the simplicity of the present source and turbulence submodels. For instance, the constant diffusivity of 0.8 m^2/s used within the fence may be somewhat too high, especially for the locations of Figs. 3.17 and 3.18.

In Figs. 3.19 through 3.21, the time-series of temperature and concentration are compared with observed data for several locations near the cloud centerline at 50 m, 150 m, and 250 m downwind, respectively. Since no concentration data at the heights of 1 m and 5 m were available for the two inner rows, only temperature curves are presented at these locations. Except for an overprediction of the temperature change by a factor of 2 in Fig. 3.19(b). the model has predicted accurately the cloud arrival time and the predicted field variables appear to agree well with experimental measurements, within approximately a factor of 1.5. In Fig. 3.22, the predicted time-series of concentration for three downwind locations are superimposed. This figure indicates a 25 to 30 s difference in cloud arrival time among adjacent locations, which is consistent with the measured temperature at these locations. Also revealed in this figure is the relatively slow mixing process within the vapor cloud, a common feature in heavy-gas dispersion.

The predicted concentration contours on the crosswind plane at 250 m behind the fence are shown in Fig. 3.23 for time = 180 and 240 s. The predicted cloud height is 8 to 9 m and its half-width is approximately 70 m. Experimental results for the corresponding times are shown in Fig. 3.24, which indicates a similarly low but somewhat wider and unsymmetric cloud (in contrary to a more symmetric cloud suggested by the wind trajectory in Fig. 3.1(b)), together with slightly lower concentration near the ground surface. In Fig. 3.25, a model-data comparison is made for the two clouds, when each of them reaches its widest horizontal extent (notice a time lag of 20 s). Compared to field data, the model yields a cloud (0.5% contour) which is somewhat lower (9 m versus 13 m) and narrower

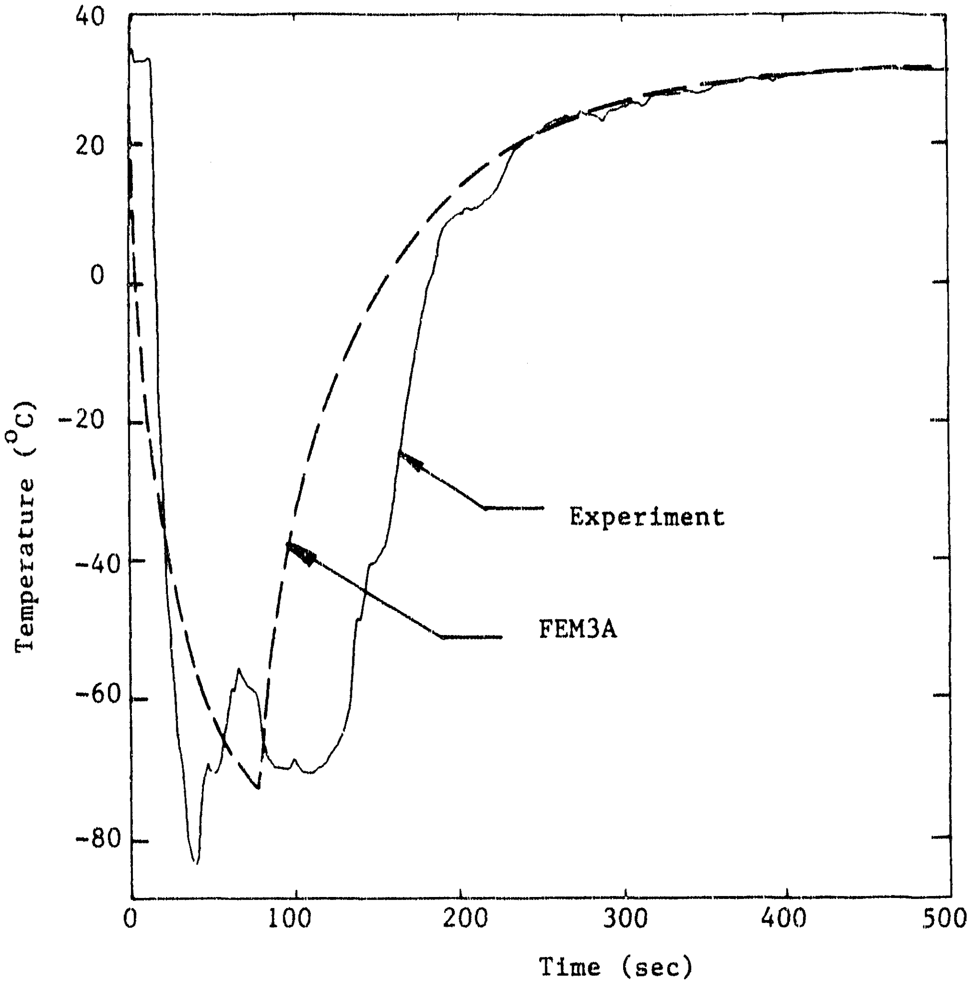

Fig. 3.14. Falcon-2 predicted versus measured temperature near the center of spill at (x,y,z) = (-32 m, 0, 1 m).

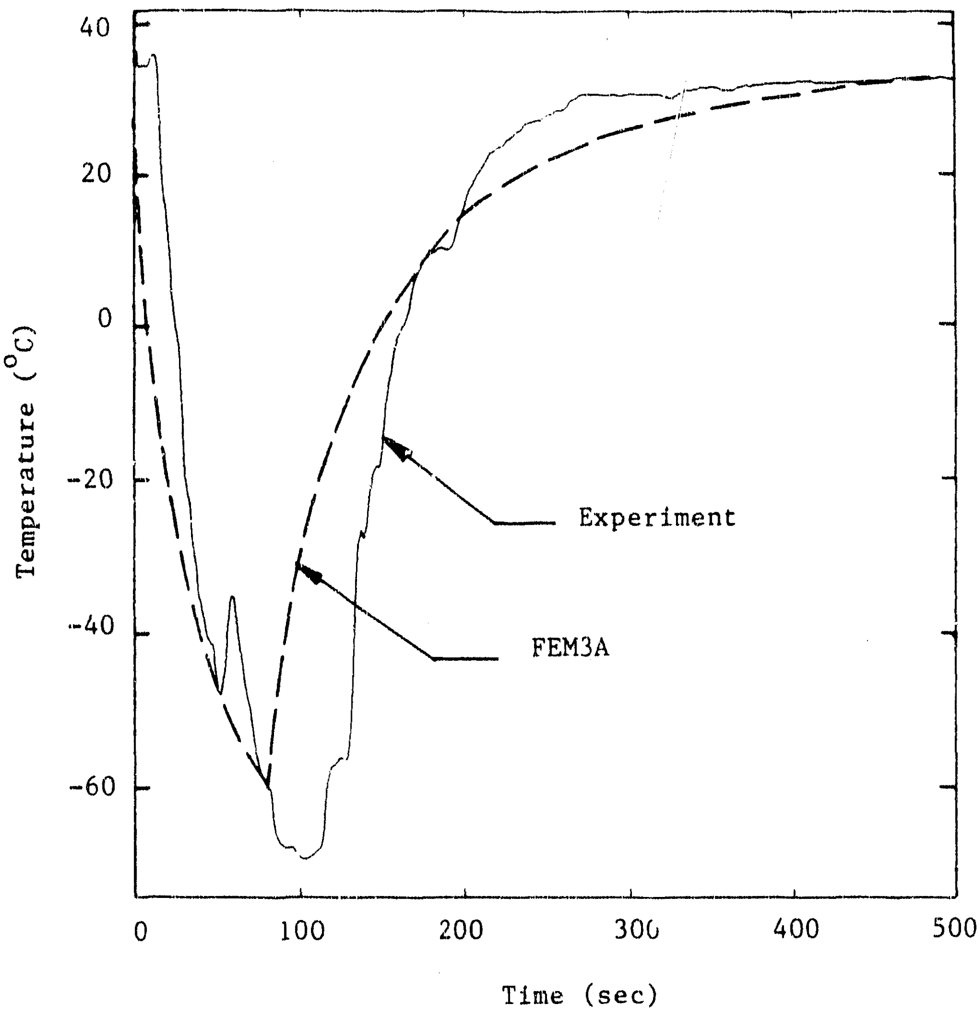

Fig. 3.15. Falcon-2 predicted versus measured temperature in front of the rear fence at (x,y,z) = (-2m, 0, 1 m).

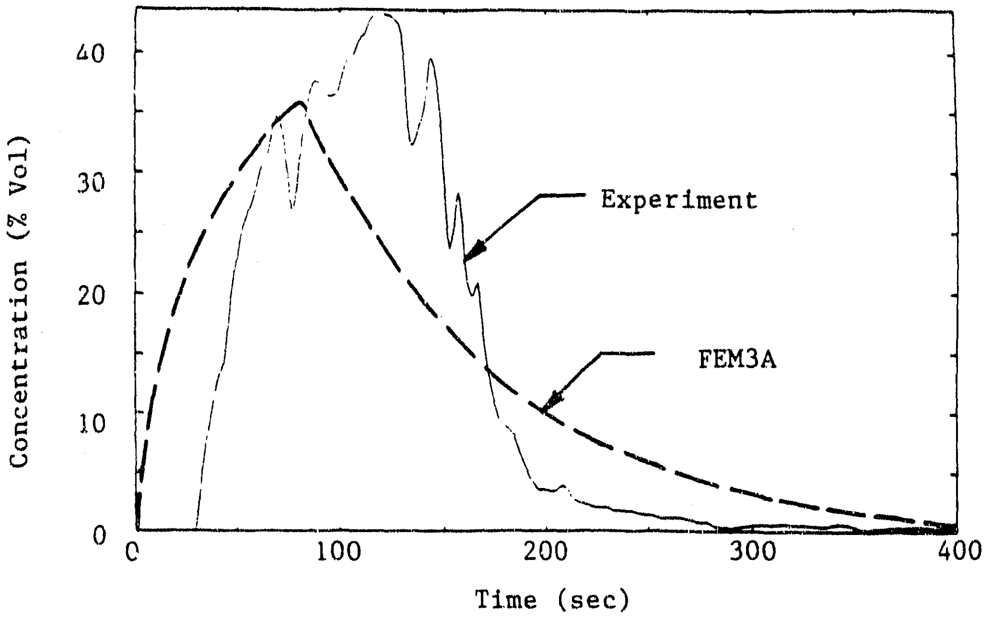

Fig. 3.16. Falcon-2 predicted versus measured concentration behind the billboard at (x,y,z) = (-62 m, 0, 1 m).

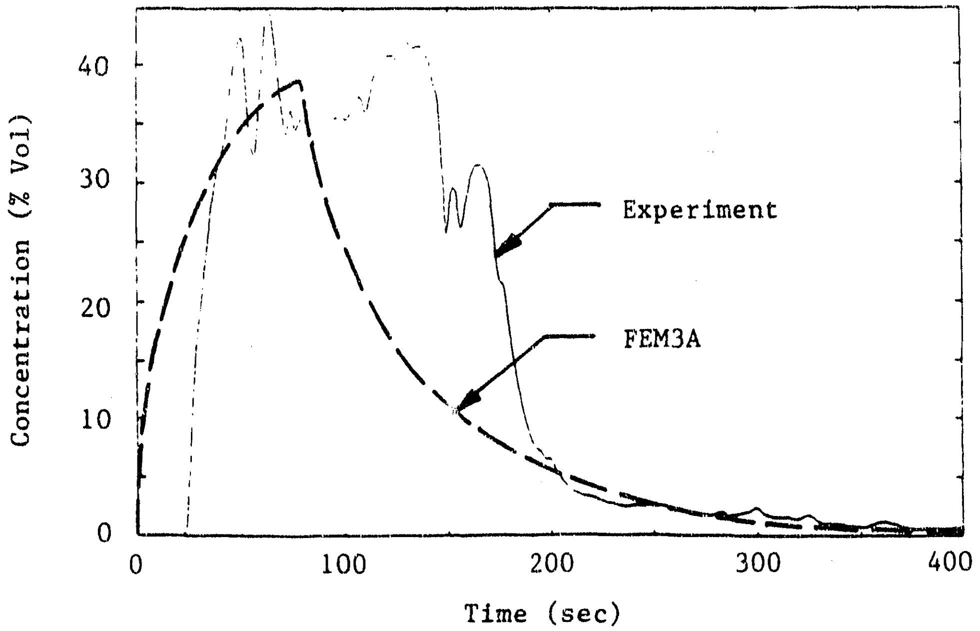

Fig. 3.17. Falcon-2 predicted versus measured concentration near the center of spill at (x,y,z) = (-32 m, 0, 1 m).

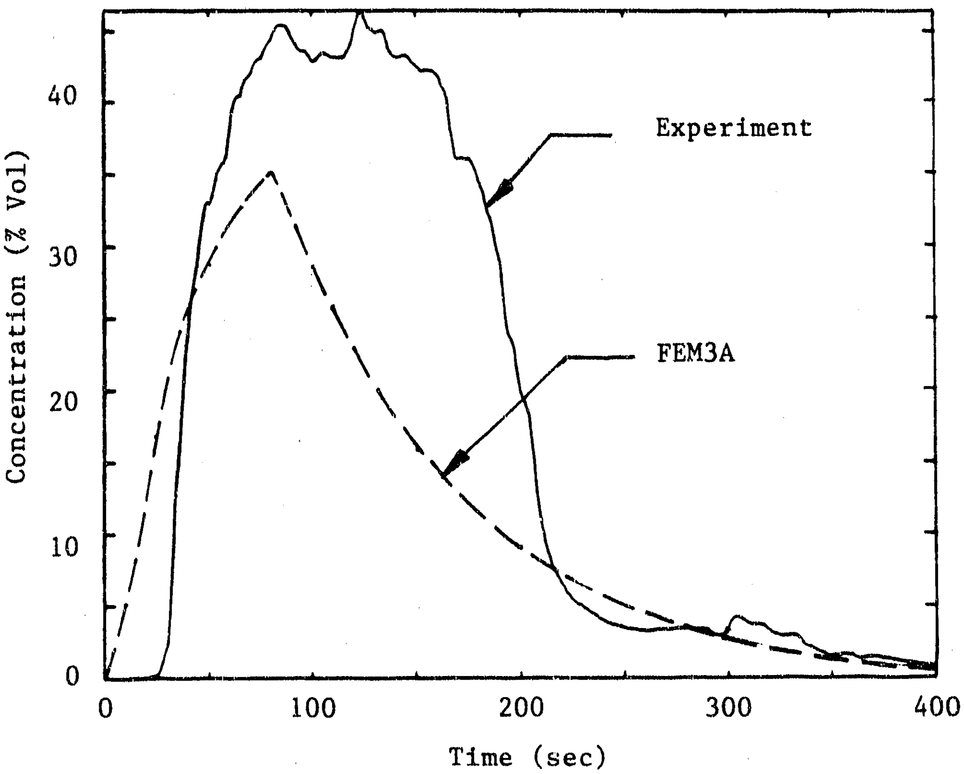

Fig. **3.18.** Falcon-2 predicted versus measured concentration within the fence enclosure and near the fence side at (x, y, z) = (-62 m, 20 m, 1 m).

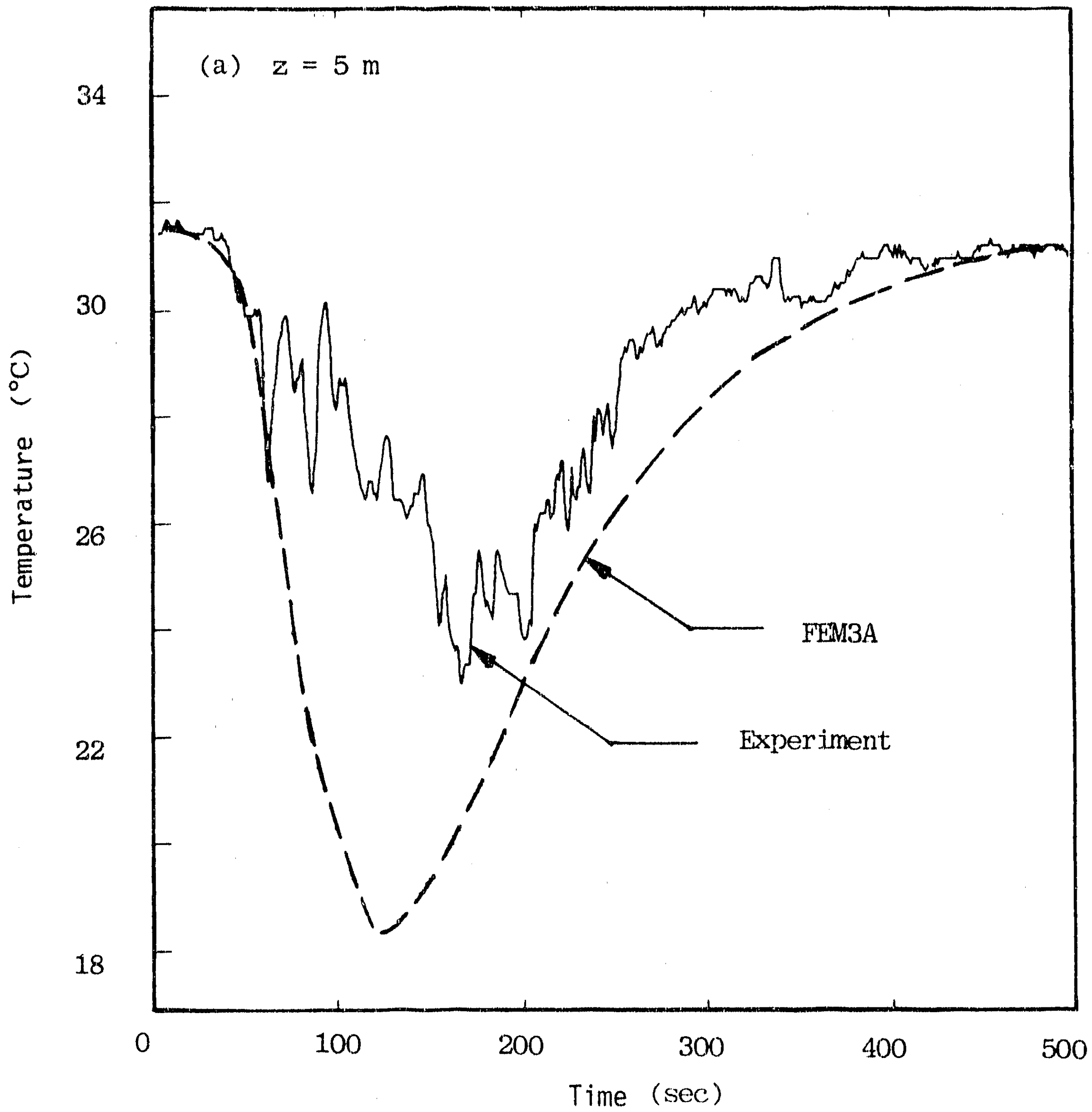

Fig. 3.19. Falcon-2 predicted versus measured temperature for two different heights at 50 m behind the rear fence. The predicted values are from the vertical plane of symmetry, and the measurements are from gas sensor G04 (which is near the cloud centerline).

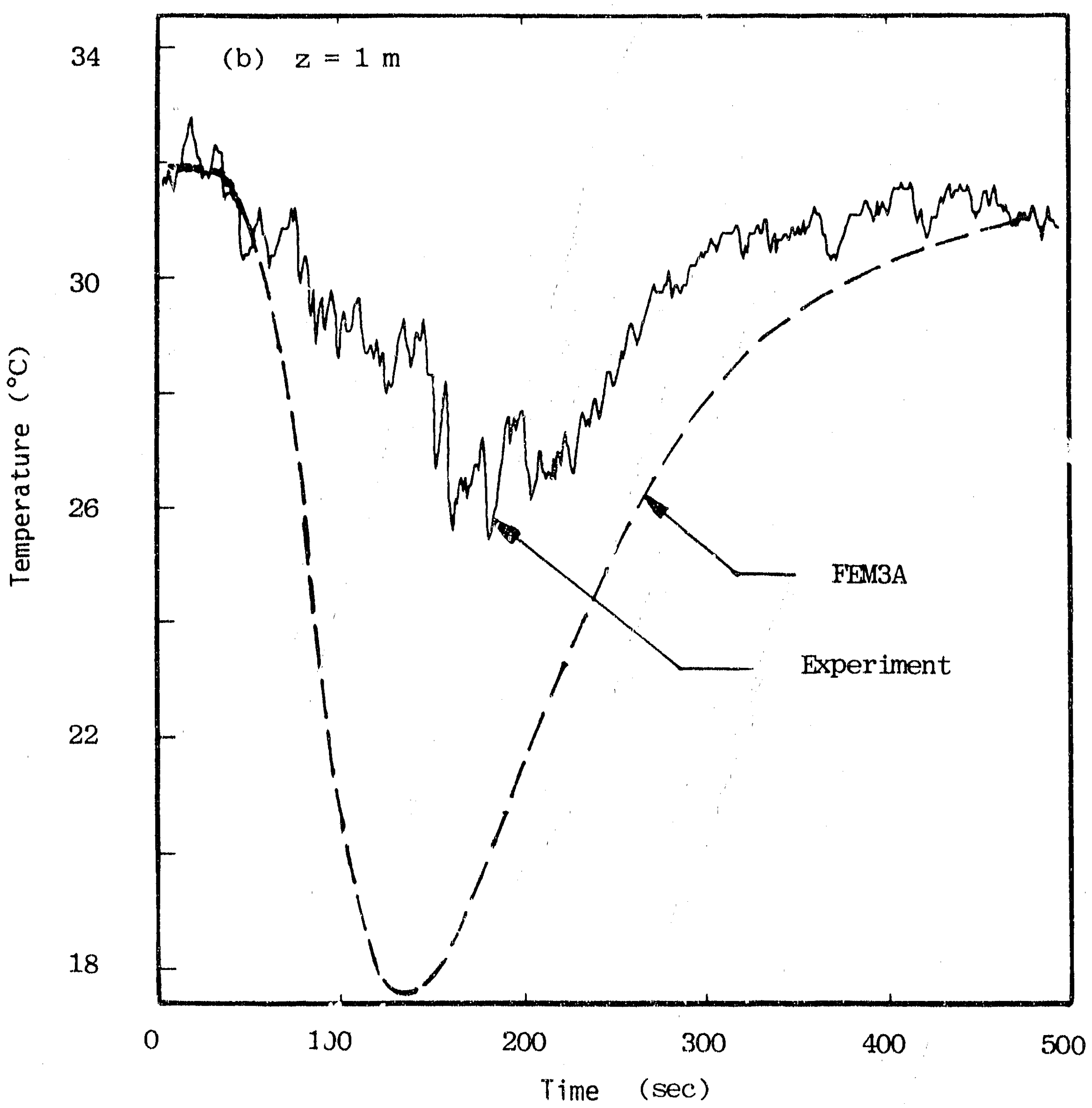

Fig. 3.19. Continued.

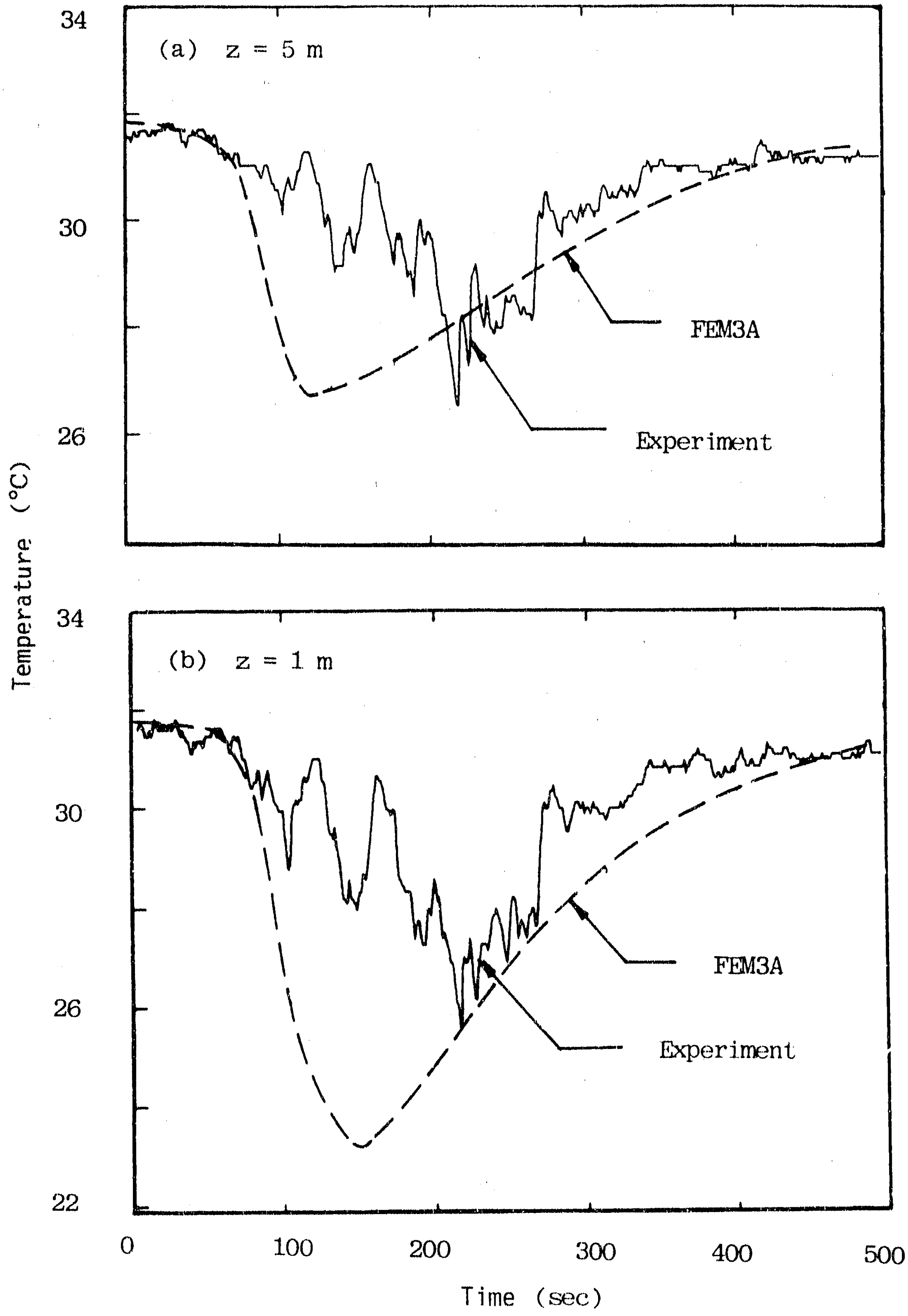

Fig. 3.20. Falcon-2 predicted versus measured temperature for two different heights at 150 m behind the rear fence. The predicted values are from the vertical plane of symmetry, and the measurements are from gas sensor G12 (which is near the cloud centerline).

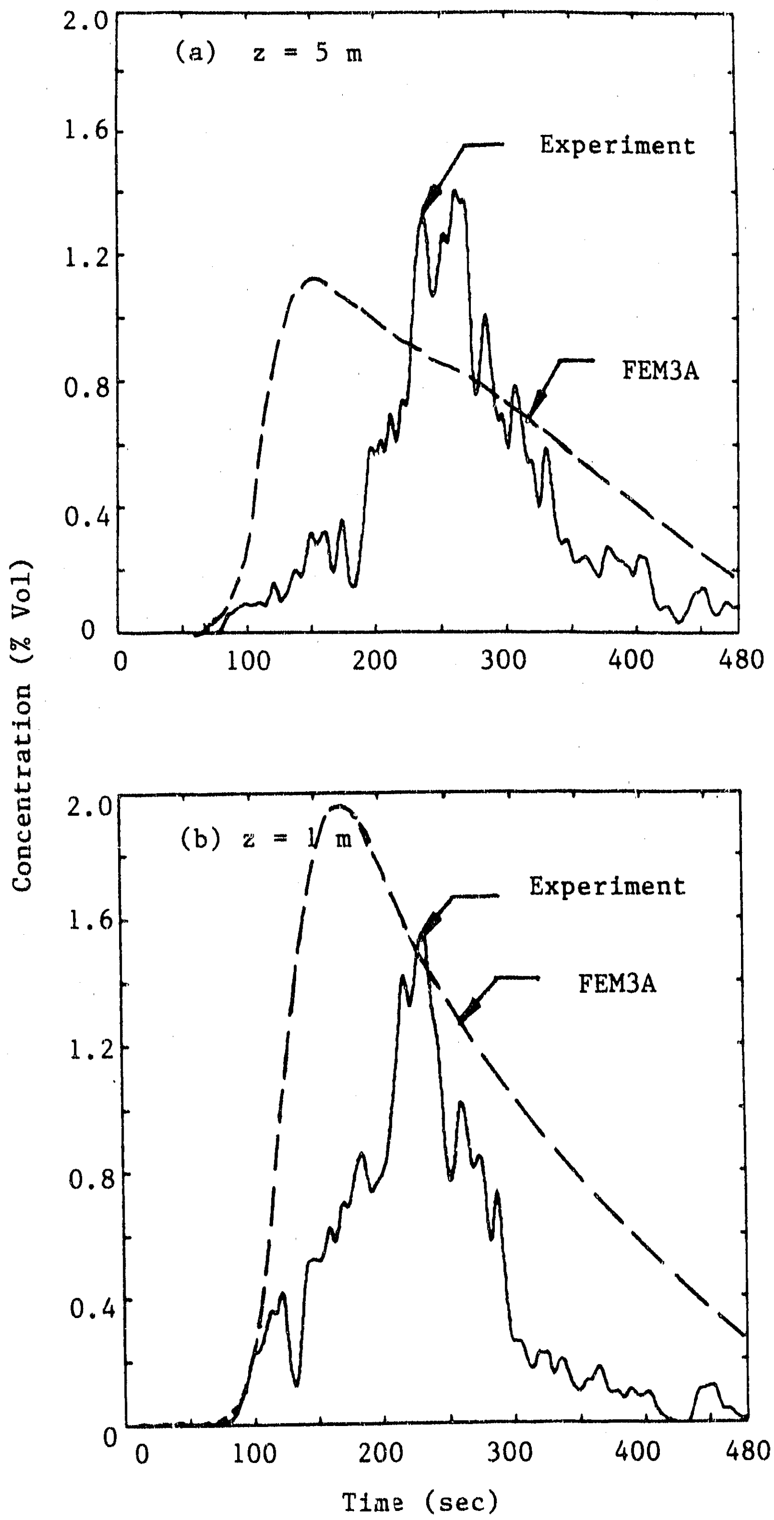

Fig. 3.21. Falcon-2 predicted versus measured concentration for two different heights at 250 m behind the rear fence. The predicted values are from two points on the plane of symmetry; the measurements are from gas sensors of G18 (z = 1 m) and G19 (z = 5 m), respectively.

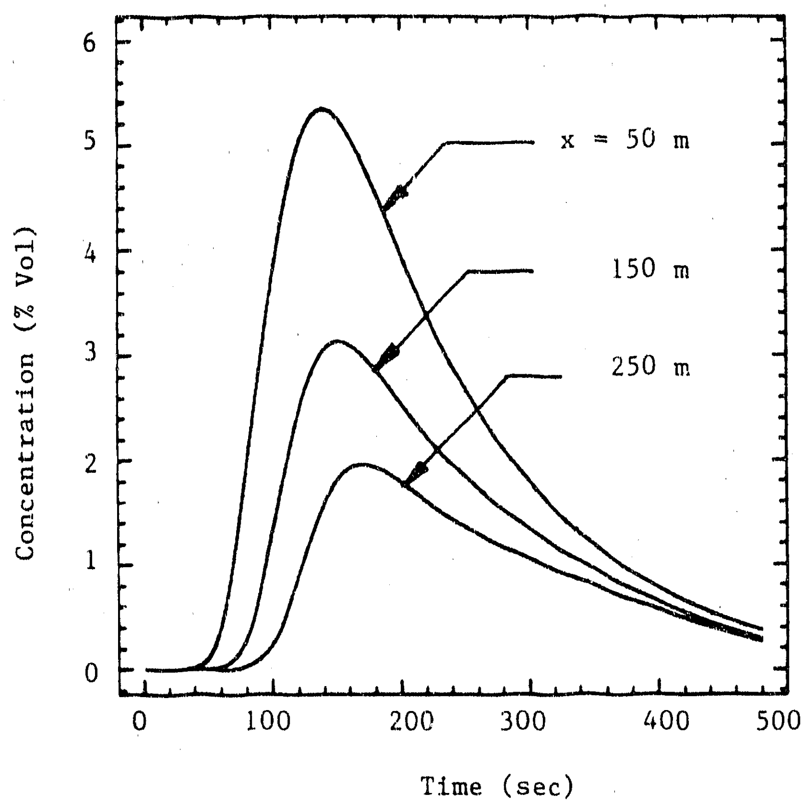

Fig. 3.22. Falcon-2 predicted time series of concentration for three locations behind the rear fence, which are all on the plane of symmetry and 1 m above the ground surface.

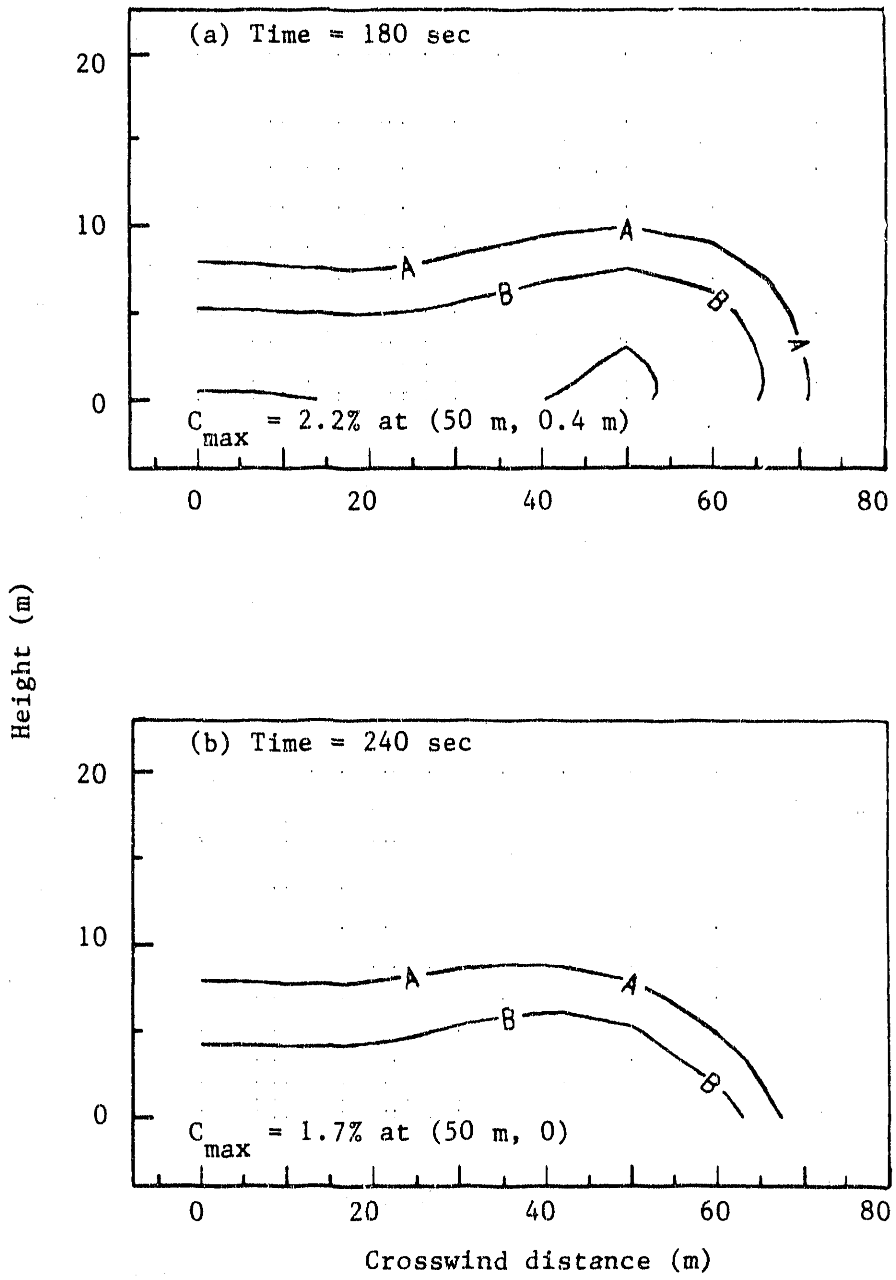

Fig. 3.23. Falcon-2 predicted concentration contours on the corsswind plane at 250 m behind the rear fence. The contour levels are (in % Vol): A=0.5, B=1, and C=2.

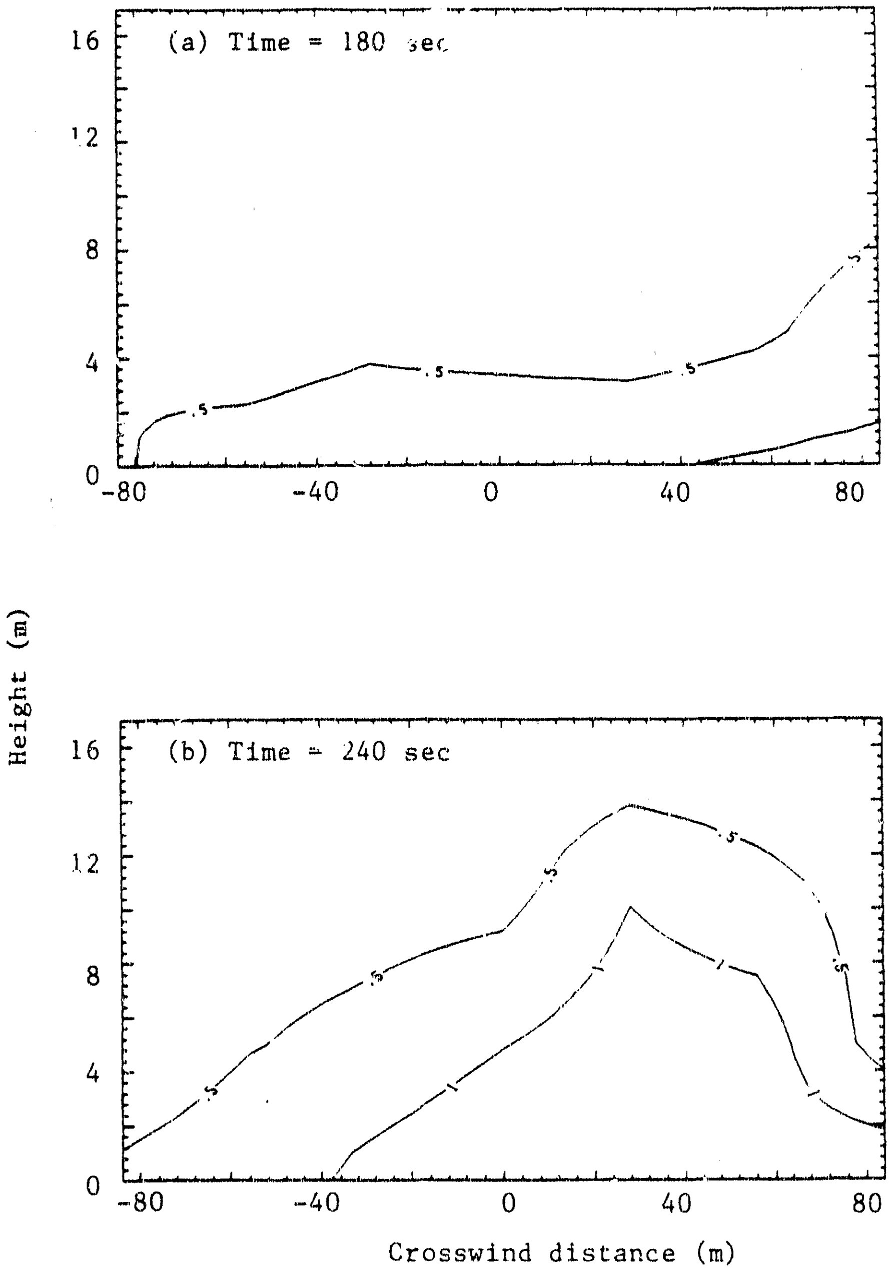

Fig. 3.24. Falcon-2 experiment concentration (in % Vol) contours on the crosswind plane at 250 m behind the rear fence.

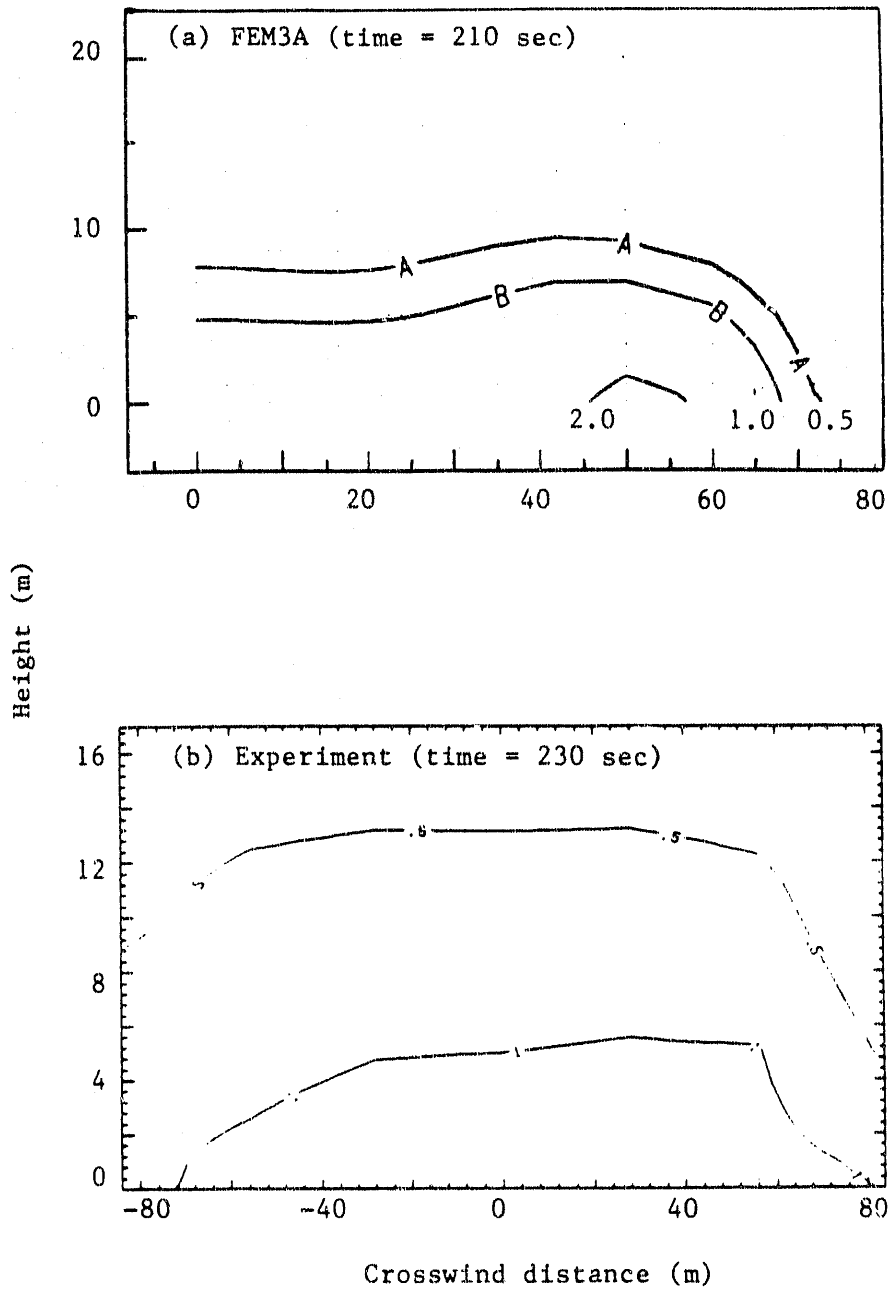

Fig. 3.25. Comparison of predicted versus measured concentrations (in % Vol) on the crosswind plane at 250 m behind the rear fence.

(145 m versus >160 m), with slightly higher concentration. The agreement between model and data for the 1% contour (which is perhaps more important for a combustible gas such as LNG) is, however, much closer with regard to its height and the horizontal extent.

Finally, the predicted and measured peak values of concentration along the cloud centerline are compared in Fig. 3.26. Based on the two values of experimental data available, the model predictions are within ±25% of those observed in the field test. Also superimposed in the figure are the rsults from a simultion without the vapor fence and the billboard. Effectiveness of the vapor ence in this case is very significant. For instance, the distance reduction for the 2.5% concentration is approximately a factor of 2.5, from 500 m (estimated) to 200 m. The distance reduction for the 5% concentration is nearly a factor of 4.

3.3 Falcon-3

The Falcon-3 test is basically a repeat of Falcon-2 with a slightly higher spill rate and approximately twice as long in spill duration. Unfortunately, the occurrence of many RPTs during the early stage of spill caused some of the instruments inside the vapor fence to malfunction, thus greatly reducing the amount of field measurements available for comparison. Nevertheless, data for a few of the locations are still largely valid and are thus used for comparison in Figs. 3.27 through 3.30. The plateau of the measured concentration after 175 s in Fig. 3.27 is due to instrumentation failure (The thermocouple deployed at the same location failed at approximately 60 s after spill started). Overall a good agreement is seen between model predictions and measured data except perhaps in Fig. 3.30, which indicates the actual cloud lingered considerably longer than predicted. This discrepancy is not clearly understood, since the recorded temperature in Fig. 3.28 for the same location does not seem to substantiate the long cloud persistence time observed in Fig. 3.30. Besides the above anomaly, both Figs. 3.28 and 3.29 display some abrupt

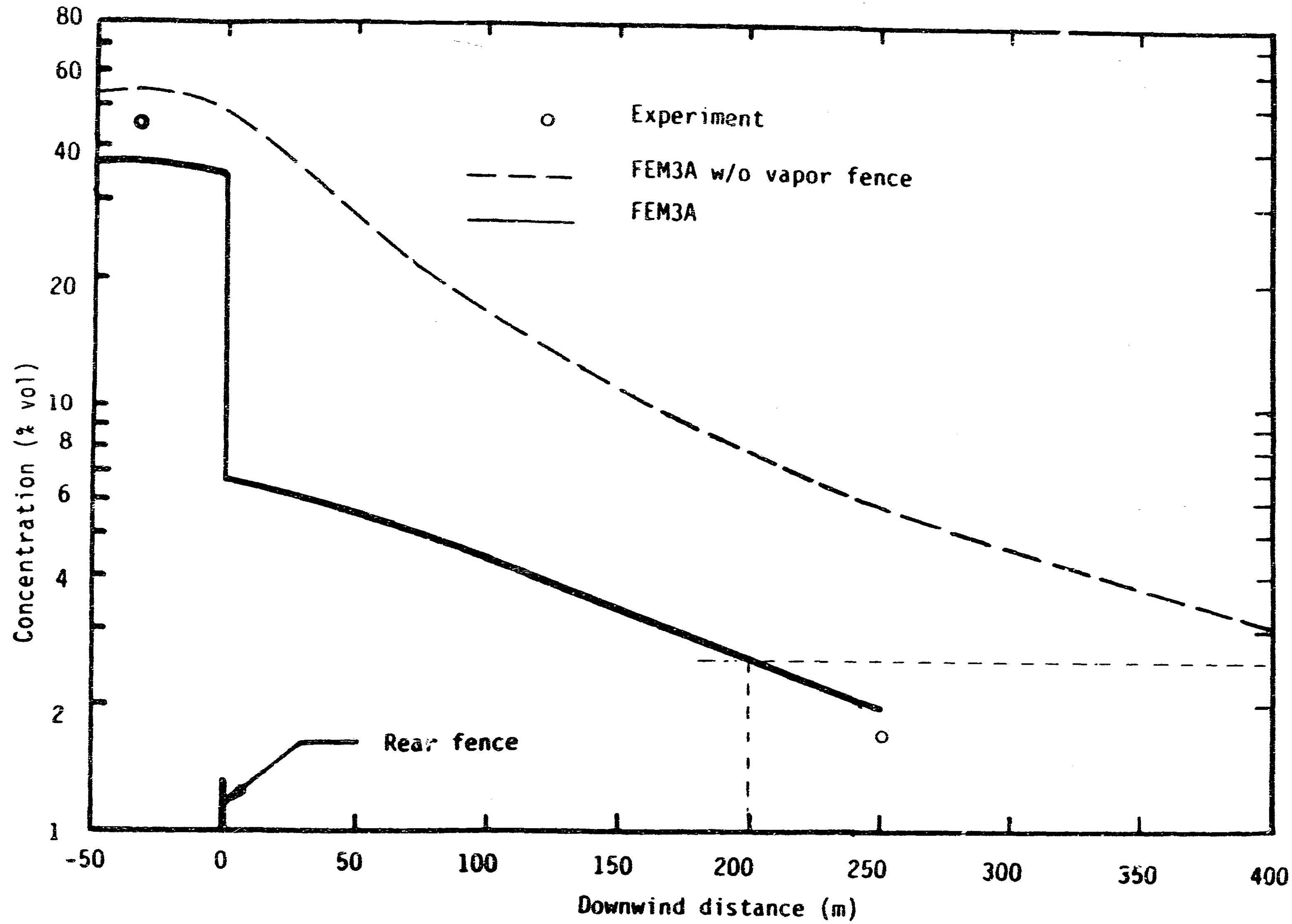

Fig. 3.26. **Comparison of predicted versus measured peak concentrations in the downwind direction and at 1 m high for Falcon-2.**

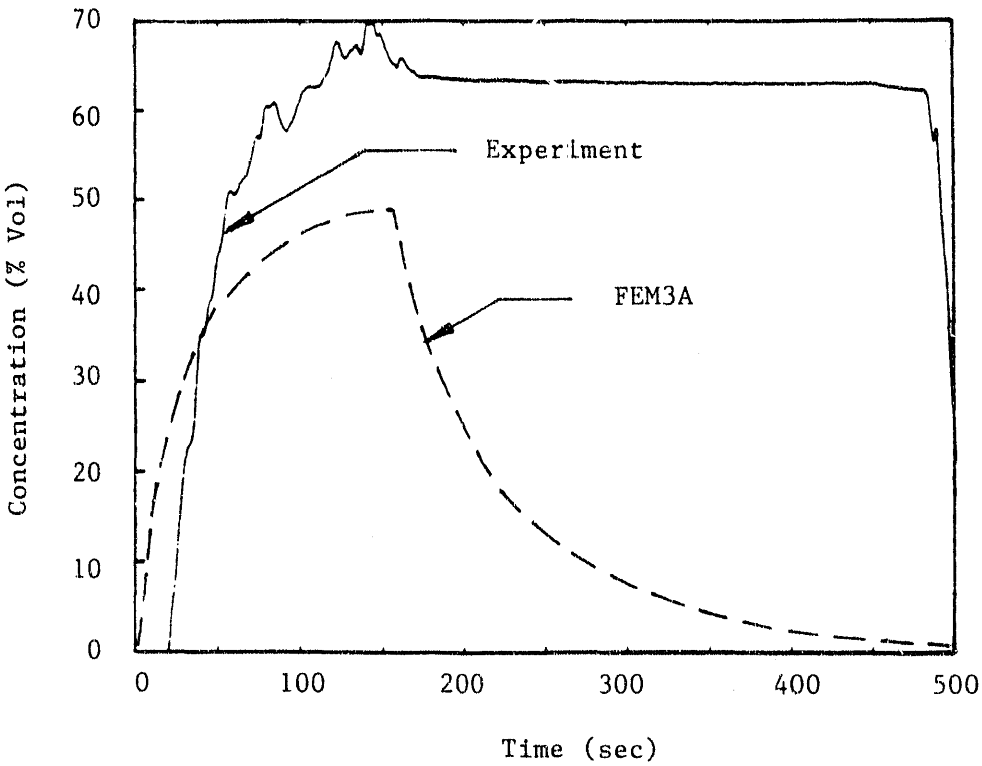

Fig. 3.27. Falcon-3 predicted versus measured concentration near the center of spill at (x,y,z) = (-32m, 0, 1m).

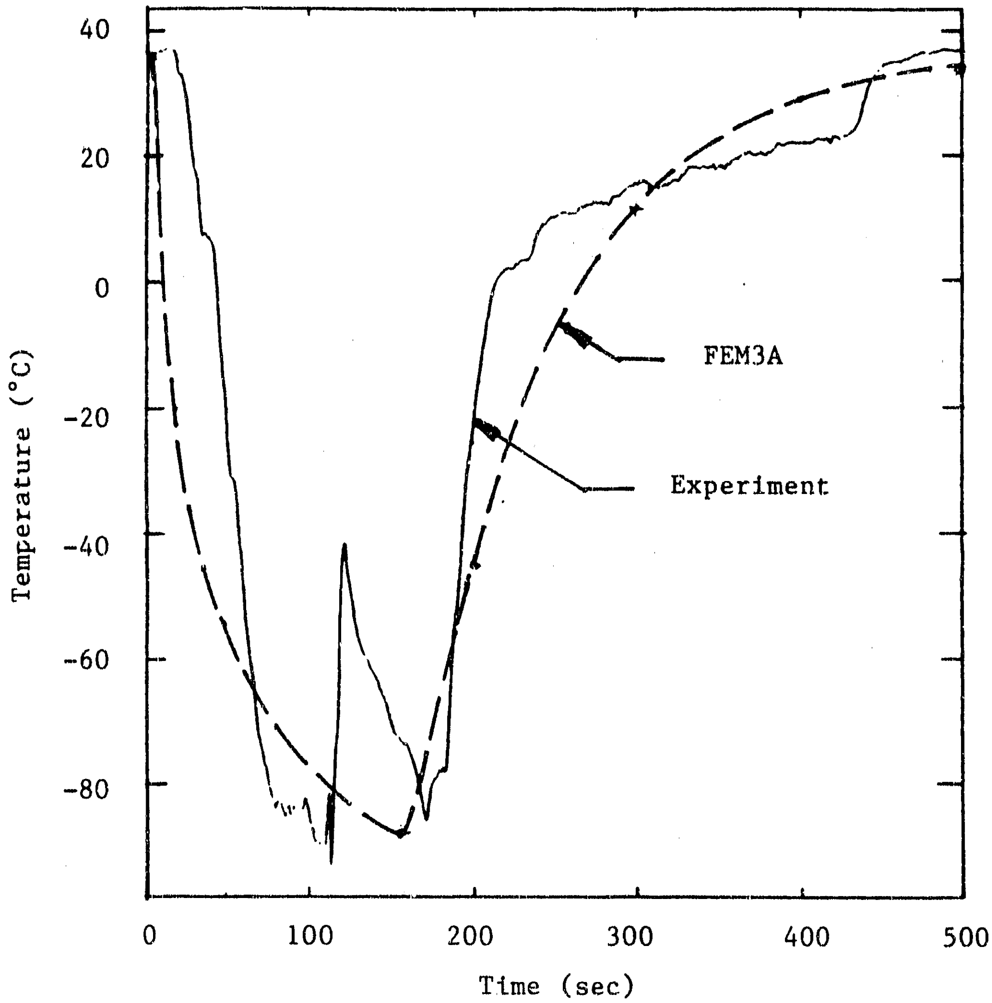

Fig. 3.28. Falcon-3 predicted versus measured temperture in front of the rear fence at (x,y,z) = (-2 m,0, 1 m).

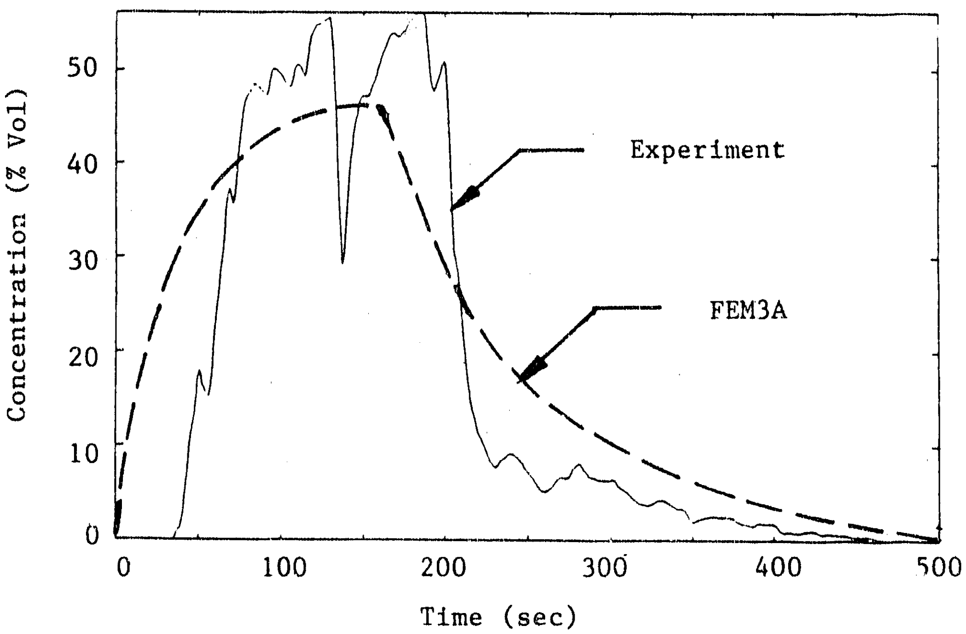

Fig. 3.29. Falcon-3 predicted versus measured concentration behind the billboard at (x,y,z) = (-62 m, 0, 2 m).

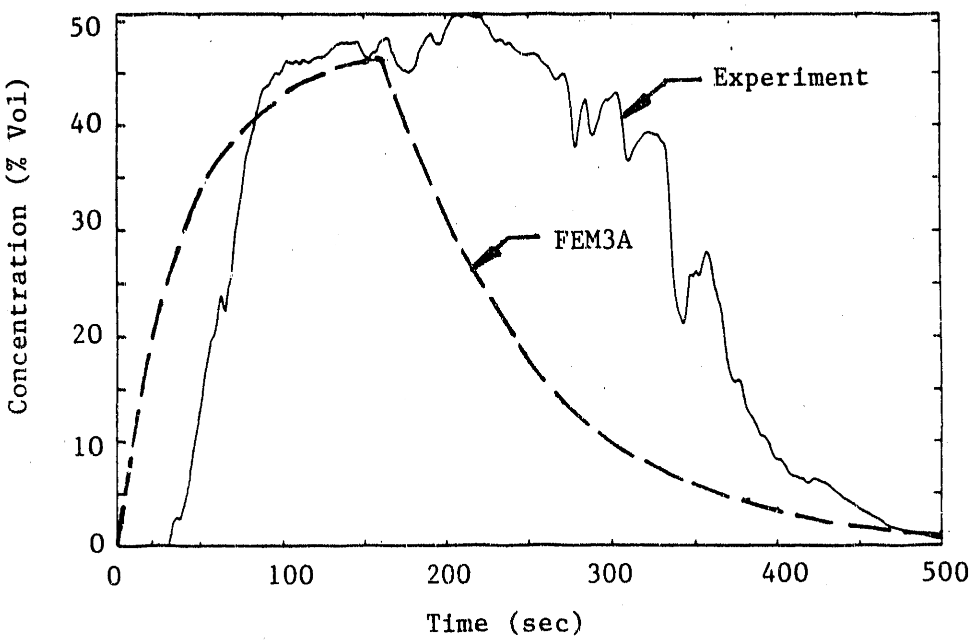

Fig. 3.30. Falcon-3 predicted versus measured concentration in front of the rear fence at $(x,y,z) = (-2\text{ m}, 0, 1\text{ m})$.

changes in the measured field variables for a brief period of time, which are most likely caused by the RPTs (significant RPTs started at approximately 90 s after the spill began).

In Figs. 3.31 through 3.35, the predicted time-series of temperature and concentration are compared with field data for downwind locations at 50 m, 150 m, and 250 m, respectively. As seen in these figures, the numerical results are very consistent and generally correlate quite well with field data. regarding cloud arrival/departure times, the magnitude of the variables, and the shapes of the curves (indeed, the high-frequency components due to small eddies not adequately modeled must be neglected). The predicted concentration at 1 m high for three downwind locations are shown in Fig. 3.36. Suggested in this figure is a 25-30 s difference in cloud arrival time among adjacent locations, which is consistent with the field data. Again, a relatively slow mixing precess within the vapor cloud as observed in Falcon-2 is also indicated by this plot.

The predicted concentration contours for the crosswind plane 150 m behind the rear fence are shown in Fig. 3.37 for time = 120 and 240 s, respectively. As is seen, although the cloud height does not change significantly (from 11 m to slightly below 10 m), its half-width has increased drastically from 55 to 95 m approximately in two minutes. The corresponding experimental results are shown in Fig. 3.38, which indicates a similarly low but perhaps somewhat wider cloud. If the cloud centerline is considered to be at sensor G12, as suggested by the wind trajectory displayed in Fig. 3.1(c), the cloud half-width would be ~60 m at 120 s and would be greater than 95 m at 240 s. Despite the model prediction of a somewhat narrower cloud and slightly higher concentration near the ground surface, the overall agreement between model predictions and field measurements is very good.

In Fig. 3.39, the predicted peak concentrations along the cloud centerline are compared with field measurements. Again, the agreement is very good with regard to the concentration values and their variations in the downwind direction. The high value of concentration measured near the center of spill at x = -32 m (see also Fig. 3.27) is probably due to a less

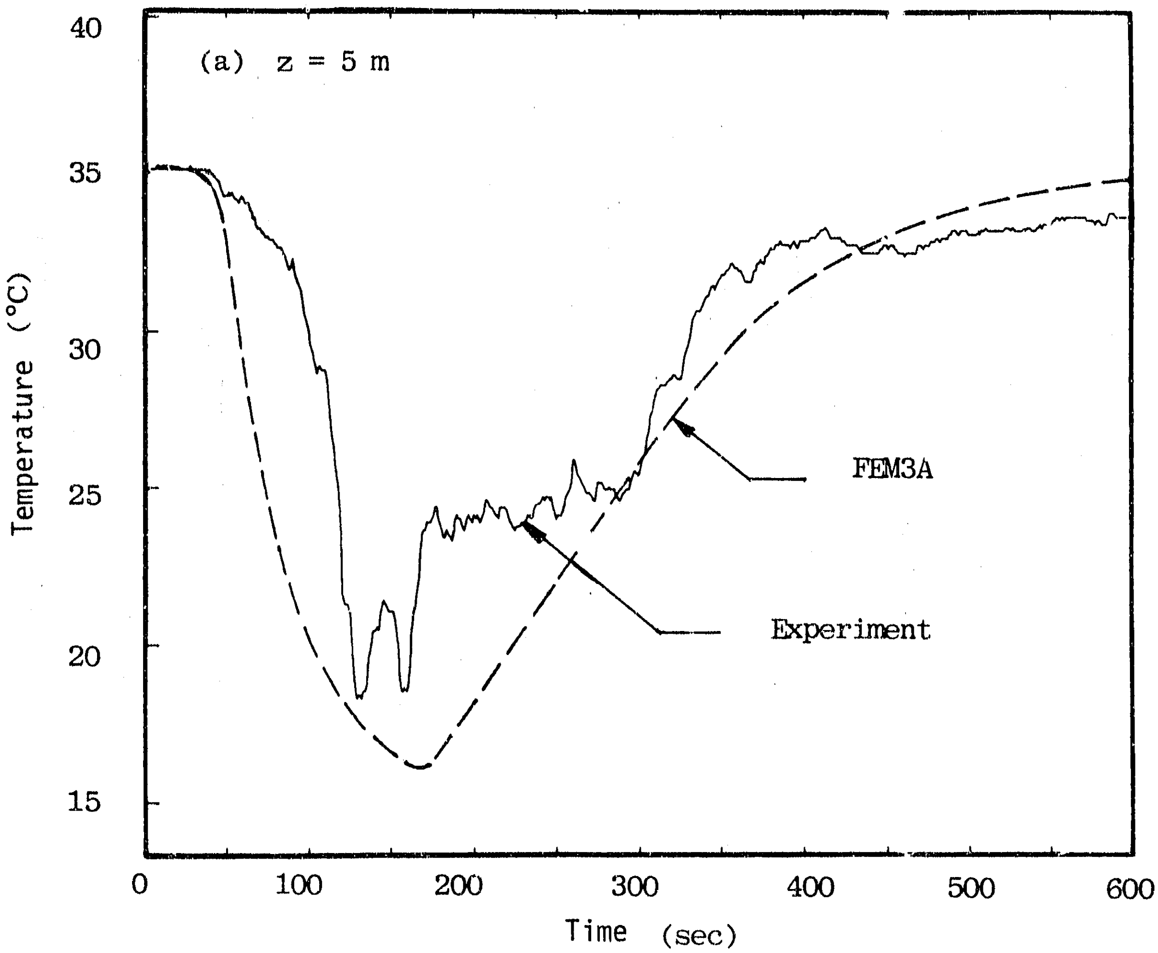

Fig. 3.31. Falcon-3 predicted versus measured temperature for two different heights at 50 m behind the rear fence. The predicted values are from the vertical plane of symmetry, and the measurements are from gas sensor G05 (which is near the cloud centerline).

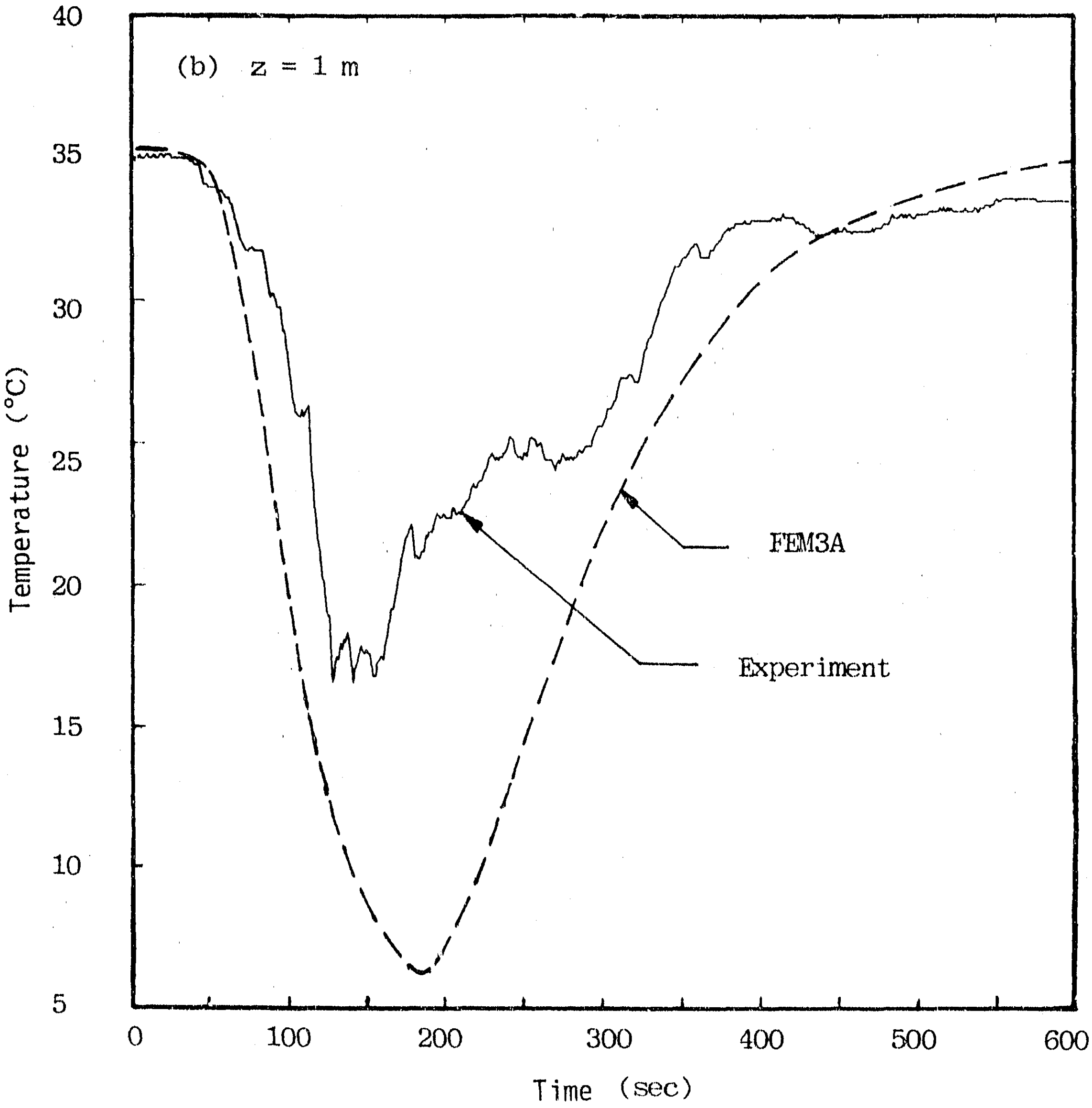

Fig. 3.31. Continued.

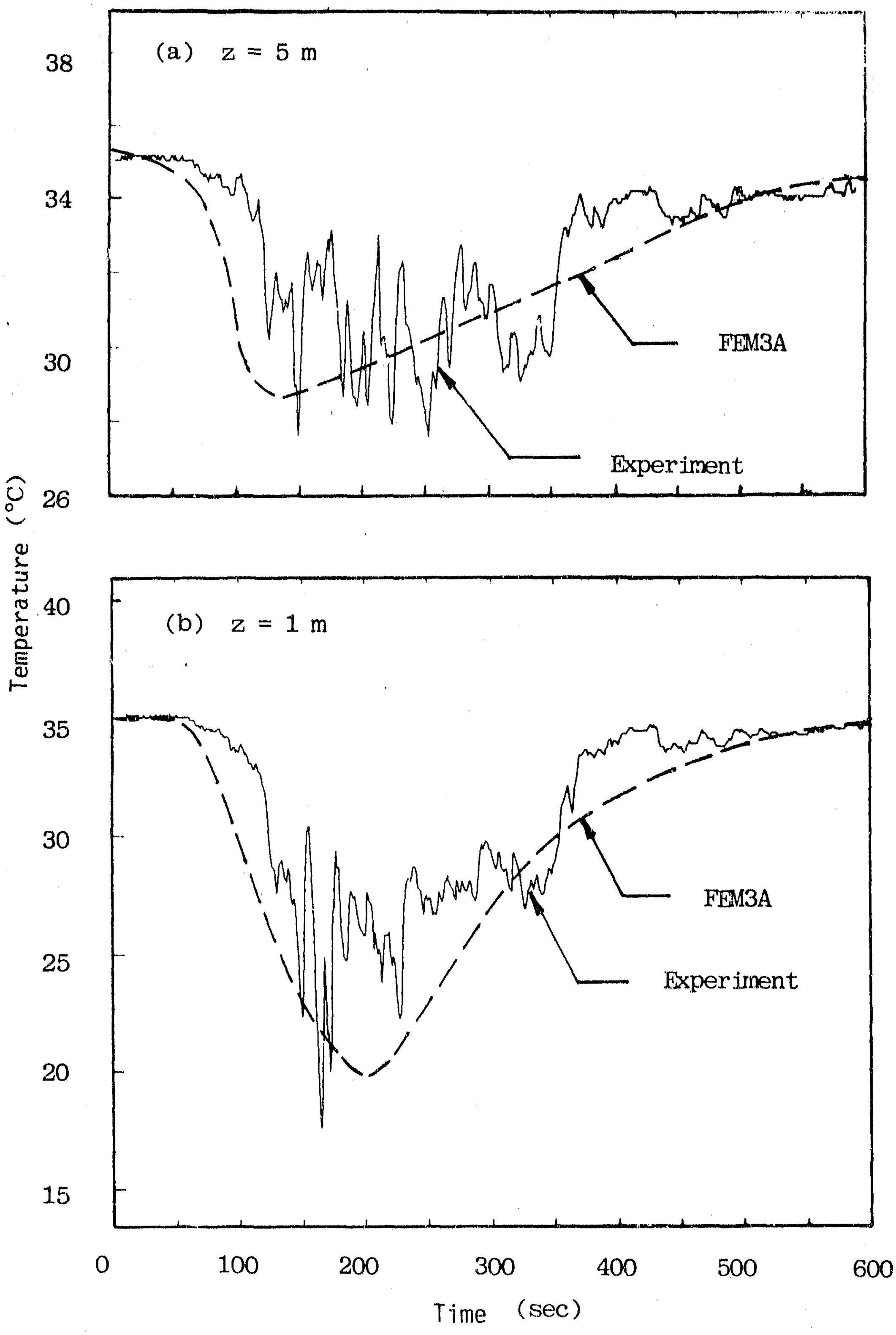

Fig. 3.32. Falcon-3 predicted versus measured temperature for two different heights at 150 m behind the rear fence. The predicted values are from the vertical plane of symmetry, and the measurements are from gas sensor G12 (which is near the cloud centerline).

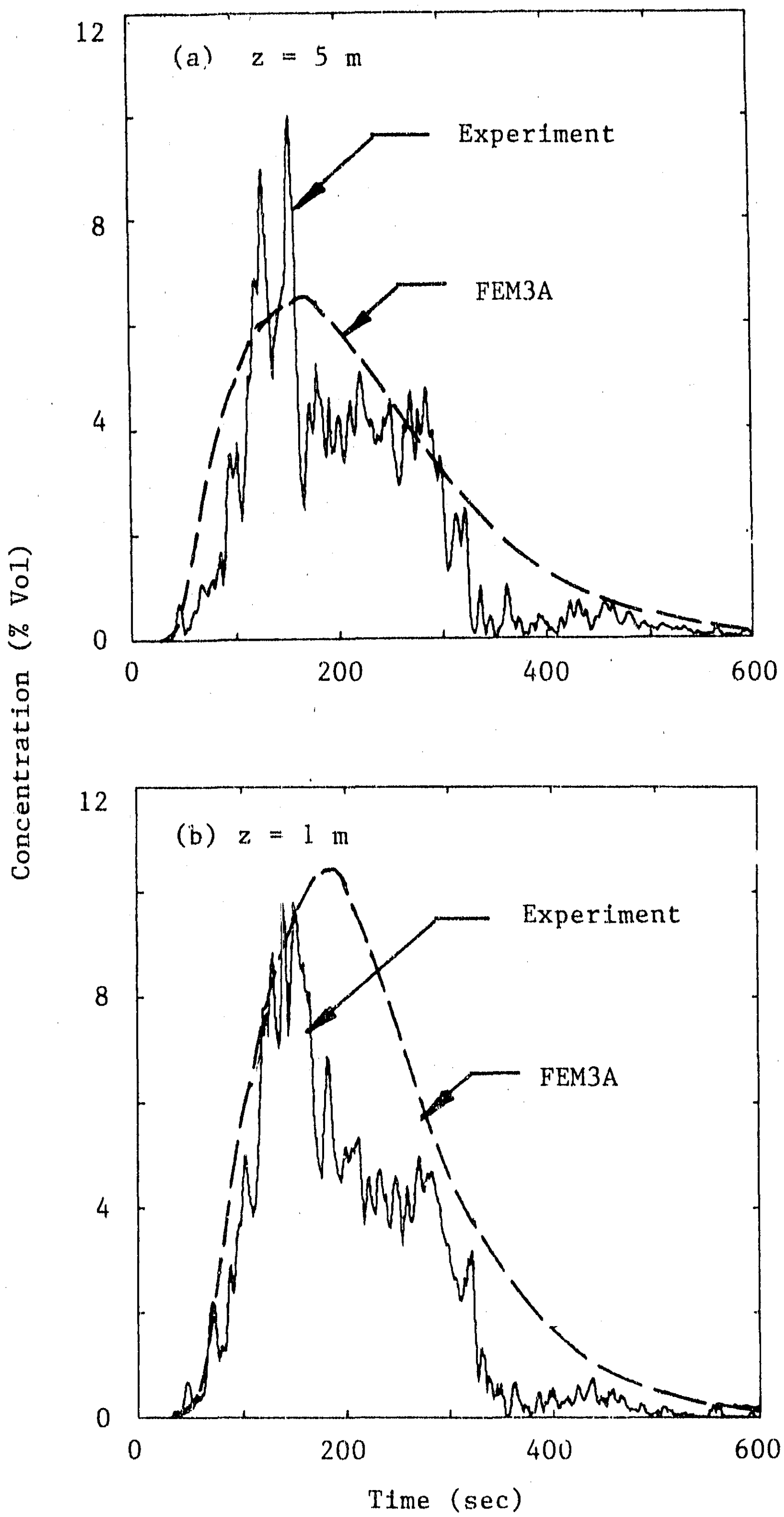

Fig. 3.33. Falcon-3 predicted versus measured concentration for two different heights at 50 m behind the rear fence. The predicted values are from the vertical plane of symmetry and the measurements are from gas sensor G05 (which is near the cloud centerline).

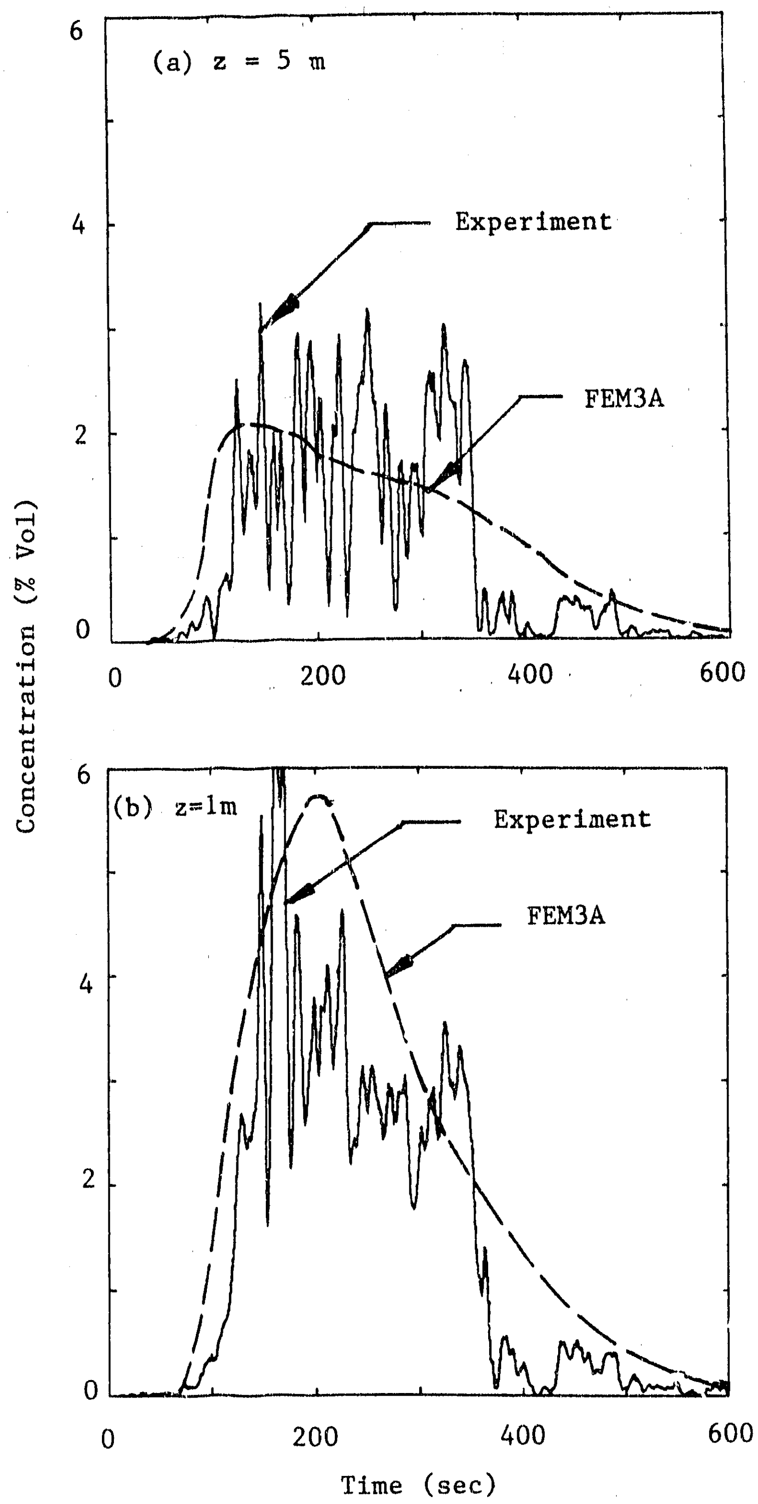

Fig. 3.34. Falcon-3 predicted versus measured concentration for two different heights at 150 m behind the rear fence. The predicted values are from the vertical plane of symmetry and the measurements are from gas sensor G12 (which is near the cloud centerline). In (b), experiment has a spike of 7.6% at time ≅ 160 sec.

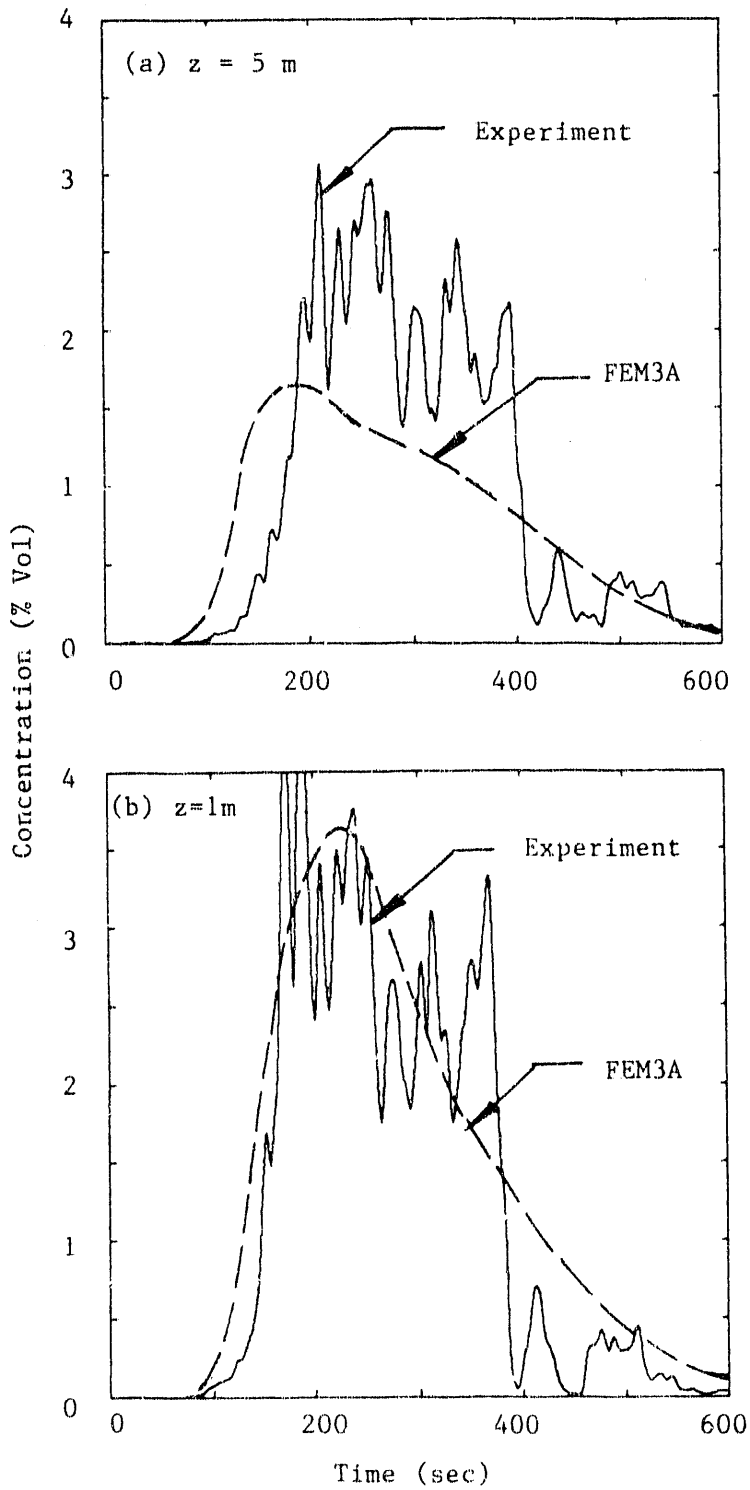

Fig. 3.35. Falcon-3 predicted versus measured concentration for two different heights at 250 m behind the rear fence. The predicted values are from the vertical plane of symmetry and the measurements are from gas sensor G19 (which is near the cloud certerline). In (b), experiment has a spike of 4.5% at time ≅ 170 sec.

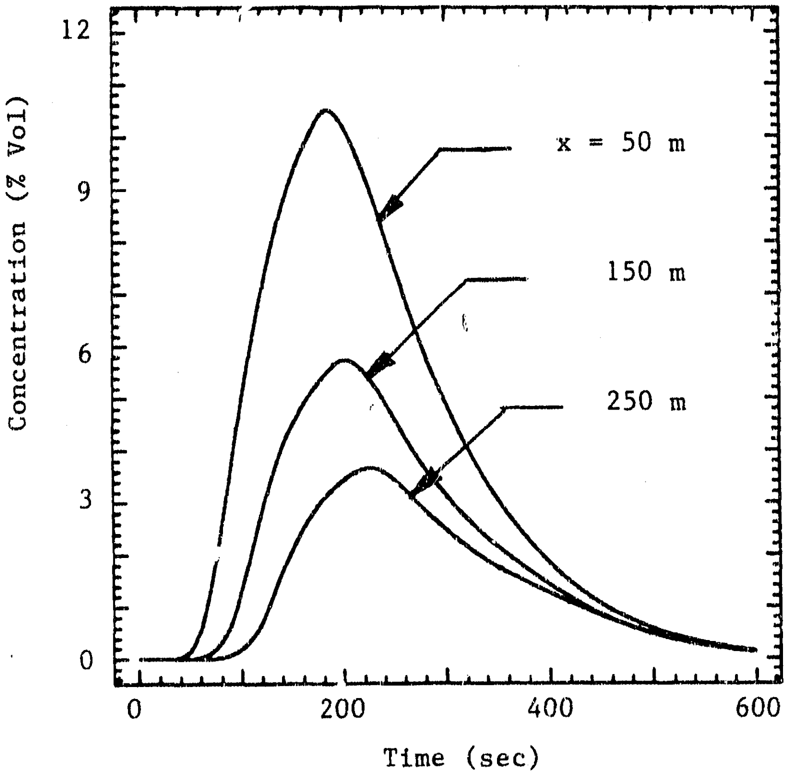

Fig. 3.36. Falcon-3 predicted time series of concentration for three locations behind the rear fence, which are all on the plane of symmetry and 1 m above the ground surface.

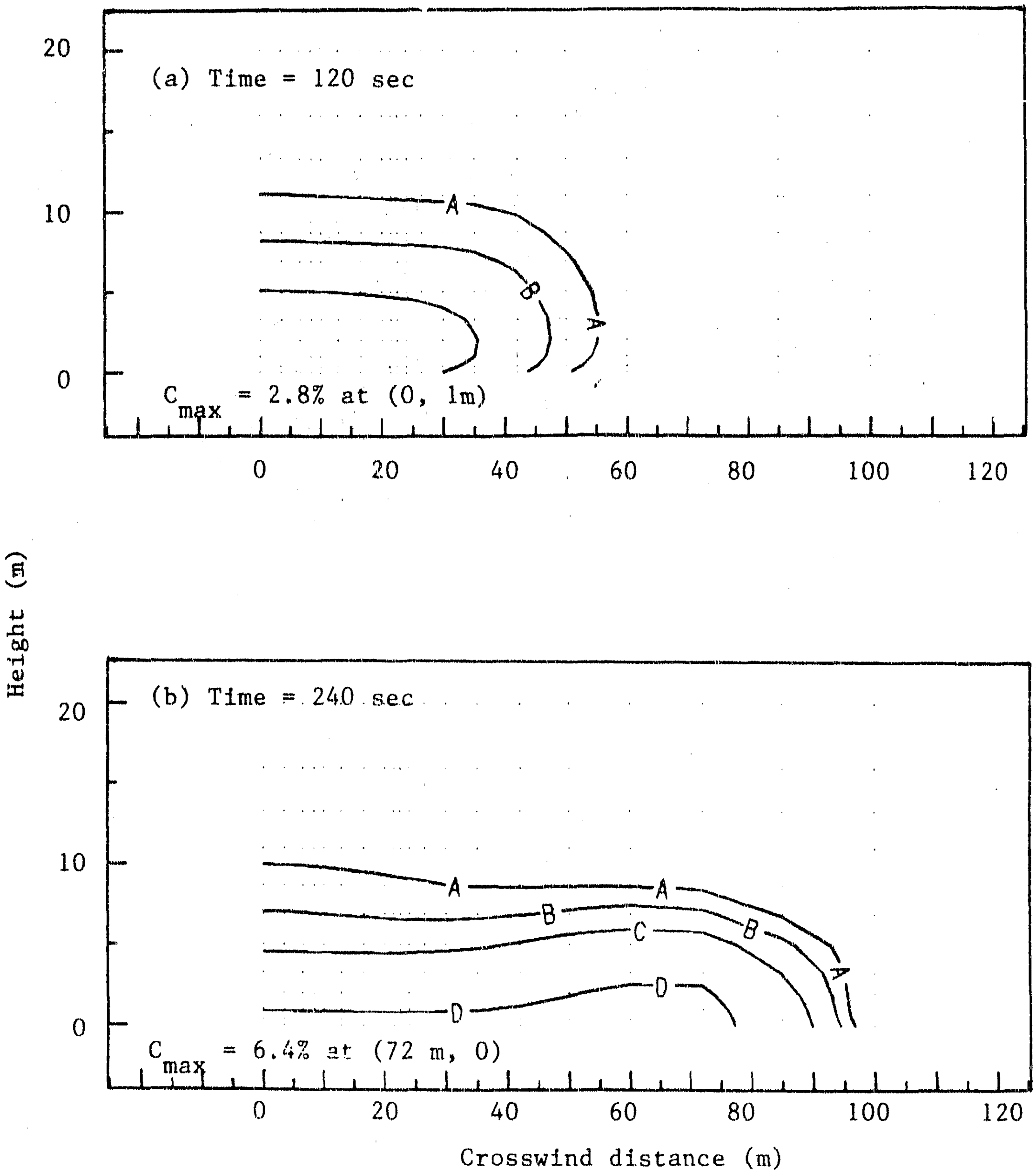

Fig. 3.37. Falcon-3 predicted concentration contours on the crosswind plane at 150 m behind the rear fence. The contour levels are (in % Vol): A=0.5, B=1, C=2, and D=5.

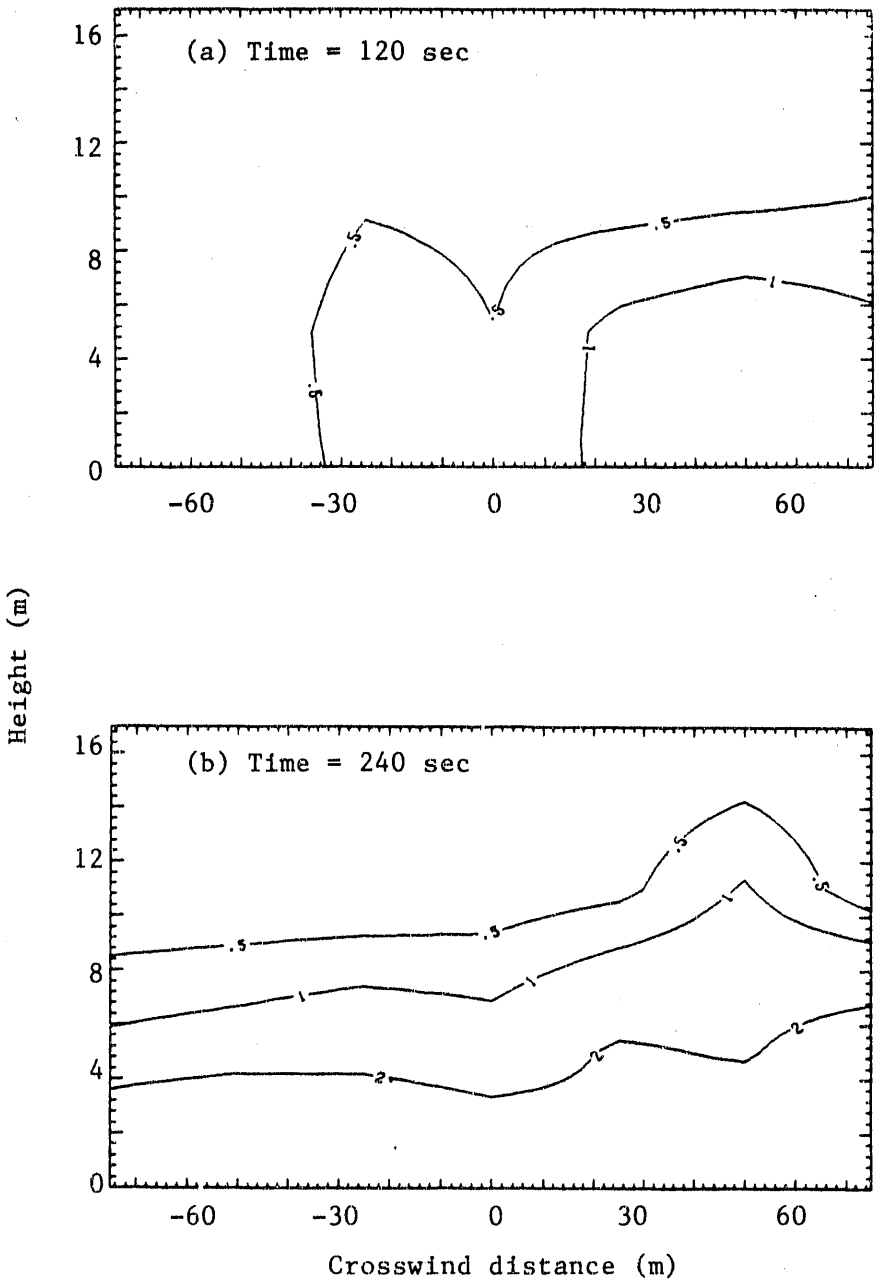

Fig. 3.38. Falcon-3 experiment concentration contours on the crosswind plane 150 m behind the rear fence.

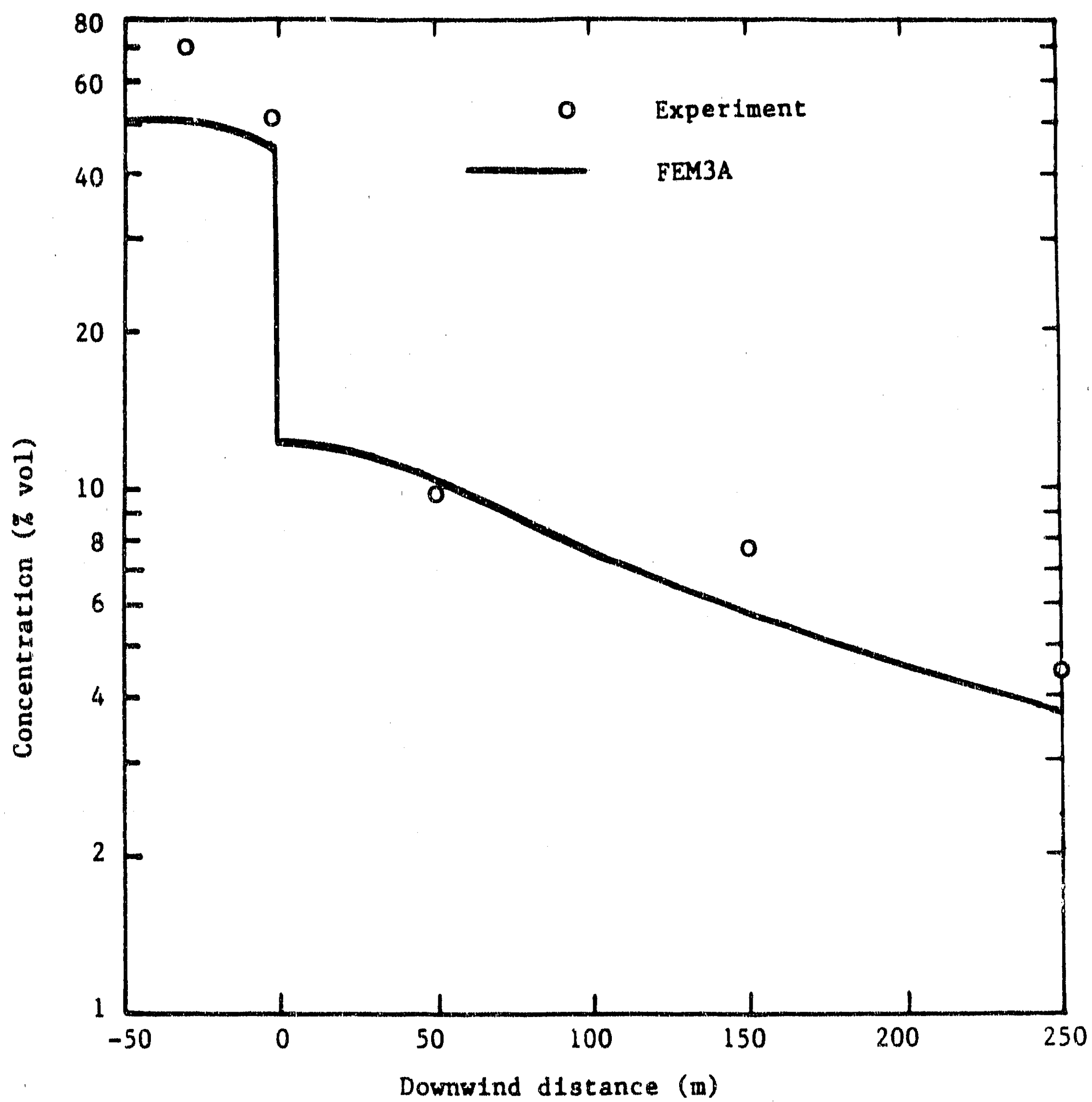

Fig. 3.39 Comparison of predicted versus measured peak concentrations in the downwind direction and at 1 m high for Falcon-3.

homogeneous cloud created by RPTs during the test and/or due to sensor problems prior to its complete failure after time = 175 s.

3.4 Falcon-4

Like the other tests, the predicted temperature and concentration inside the fence are first compared with available measurements in Figs. 3.40 and 3.41. As seen in these figures, the numerical results are very consistent and correlate quite well with the measured data, regarding the magnitude and cloud persistence time. Because this test has the smallest spill rate and was conducted under the highest wind speed, the field measurements are seen to have more high-frequency components (or higher intermittency) due to small eddies in the ambient atmosphere. These high-frequency components, understandably, can't be adequately resolved by the present finite grid model and thus are less relevant for the present model-data compraison.

In Fig. 3.42 through 3.45, the predicted time-series of temperature and concentration are compared with field data for downwind locations at 50 m, 150 m, and 250 m, respectively. Again, the numerical results are very consistent and generally correlate well with field data, regarding cloud arrival/departure times and the shapes of the curves. The predicted concentrations at 1 m high for three downwind locations are also shown in Fig. 3.46. Suggested in this figure is a ~20 s difference in cloud arrival time among adjacent locations, which is consistent with the measured concentration at these locations as shown in Figs. 3.43 through 3.45.

In Fig. 3.47, the predicted concentration contours on a crosswind plane 150 m behind the rear fence are shown for time = 180 and 300 s, respectively. In two minutes, the cloud height is seen to decrease only slightly from 10 m to 9 m but its half-width has increased rapidly from 40 m to 55 m approximately. The corresponding experimental results are shown in Fig. 3.48 (the hump in 3.48(b) is probably due to a puff of cloud passing through),

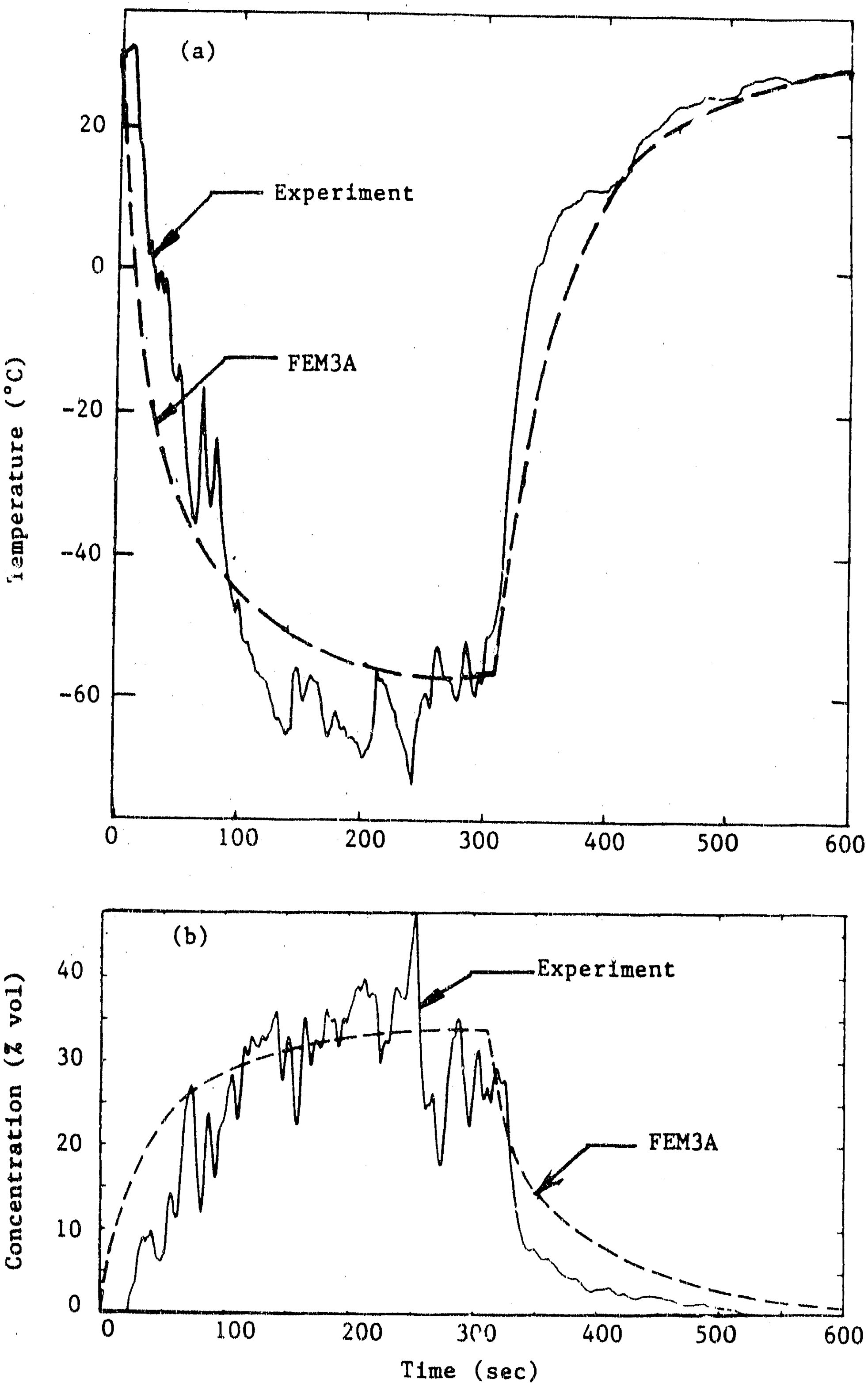

Fig. 3.40. Falcon-4 predicted versus measured temperature and concentration near the center of spill at (x, y, z) = (-32 m, 0, 1 m).

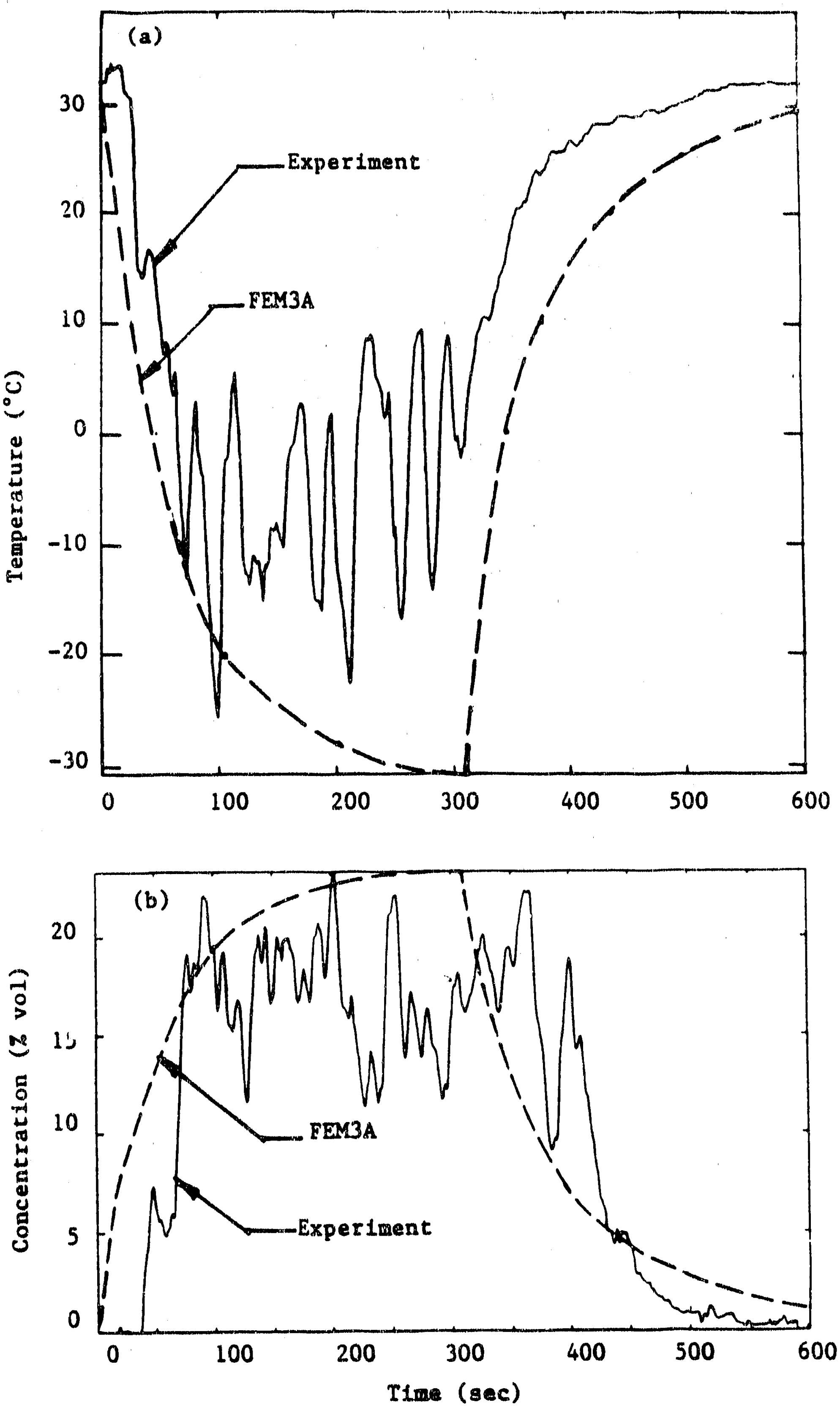

Fig. 3.41. Falcon-4 peredicted versus measured temperature and concentration in front of the rear fence at (x, y, z) = (-2 m, 0, 1 m)

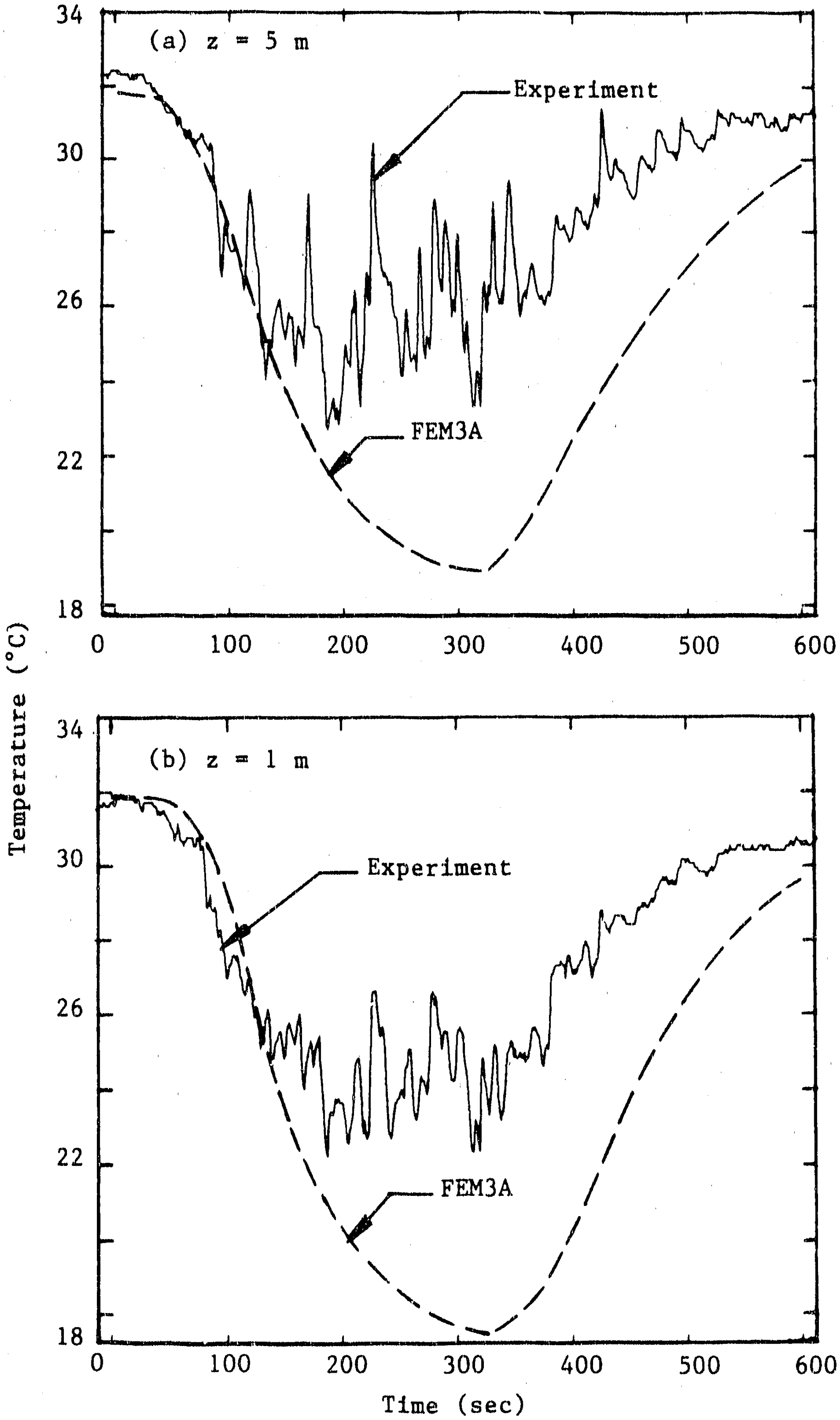

Fig. 3.42 Falcon-4 predicted versus measured temperature for two different heights at 50 m behind the rear fence. The predicted values are from the vertical plane of symmetry and the measurements are from gas sensor G04 (which is near the cloud centerline).

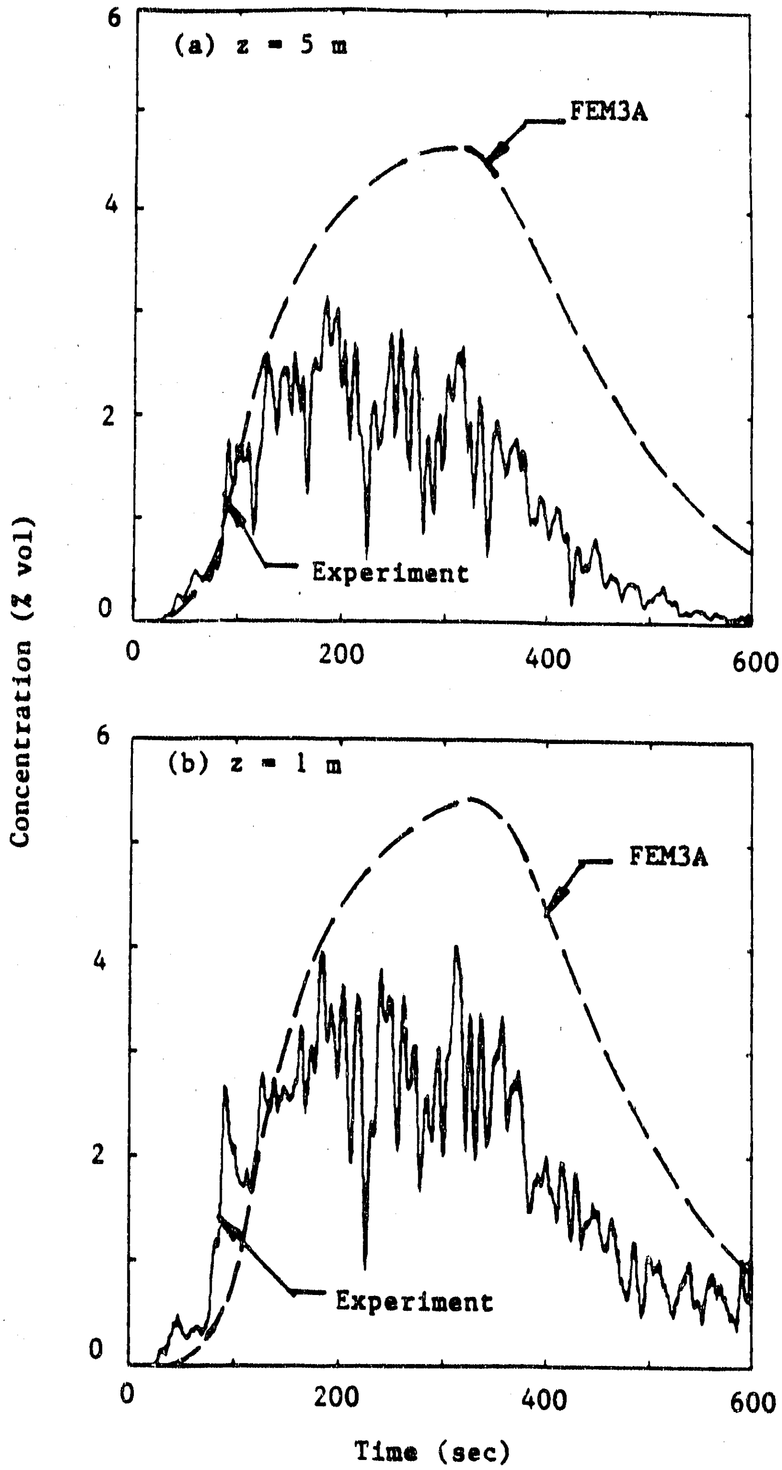

Fig. 3.43. Falcon-4 predicted versus measured concentration for two different heights at 50 m behind the rear fence. The predicted vaues are from the vertical plane of symmetry and the measurements are from gas sensor G04 (which is near the cloud centerline).

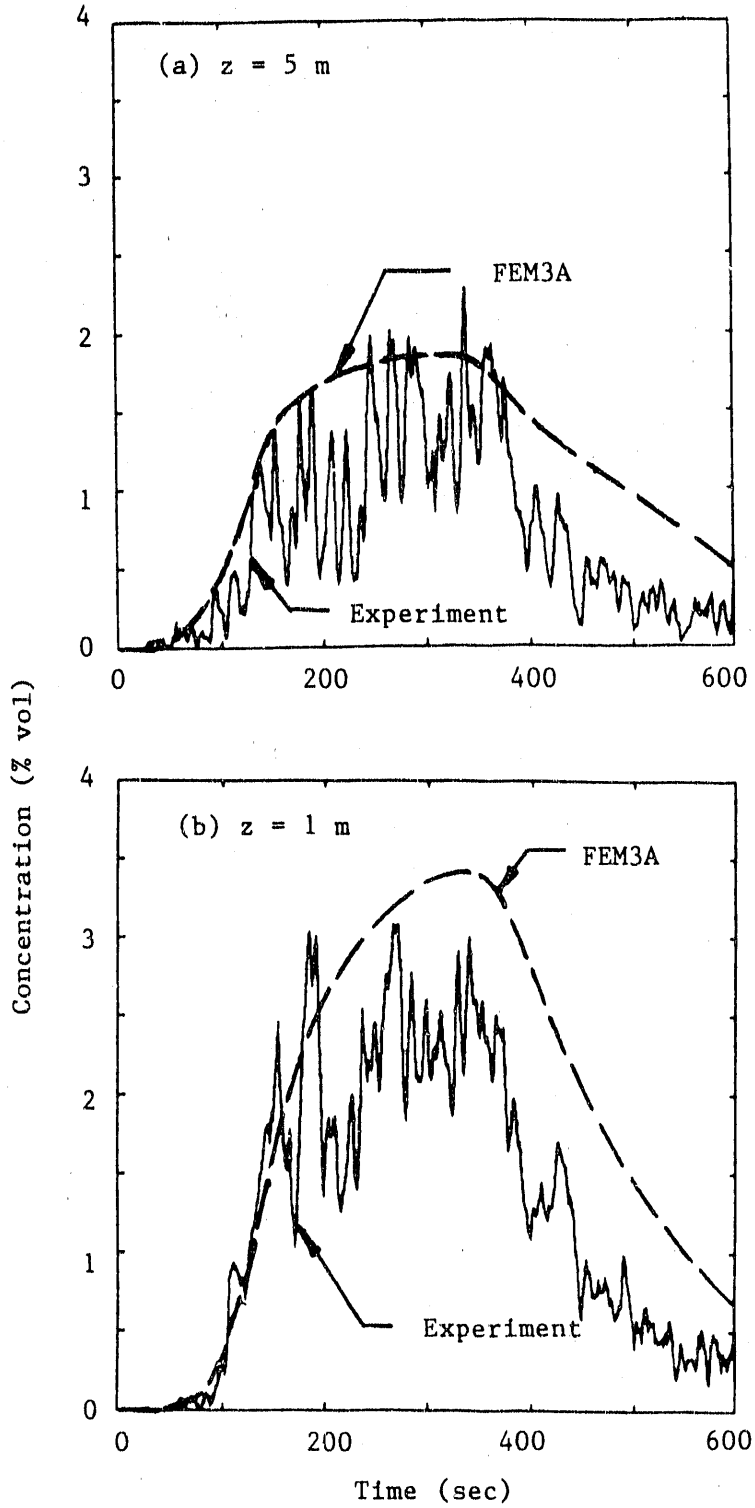

Fig. 3.44. Falcon-4 predicted versus measured concentration for two different heights at 150 m behind the rear fence. The predicted values are from the vertical plane of symmetry and the measurements are from gas sensor G02 (which is near the cloud centerline).

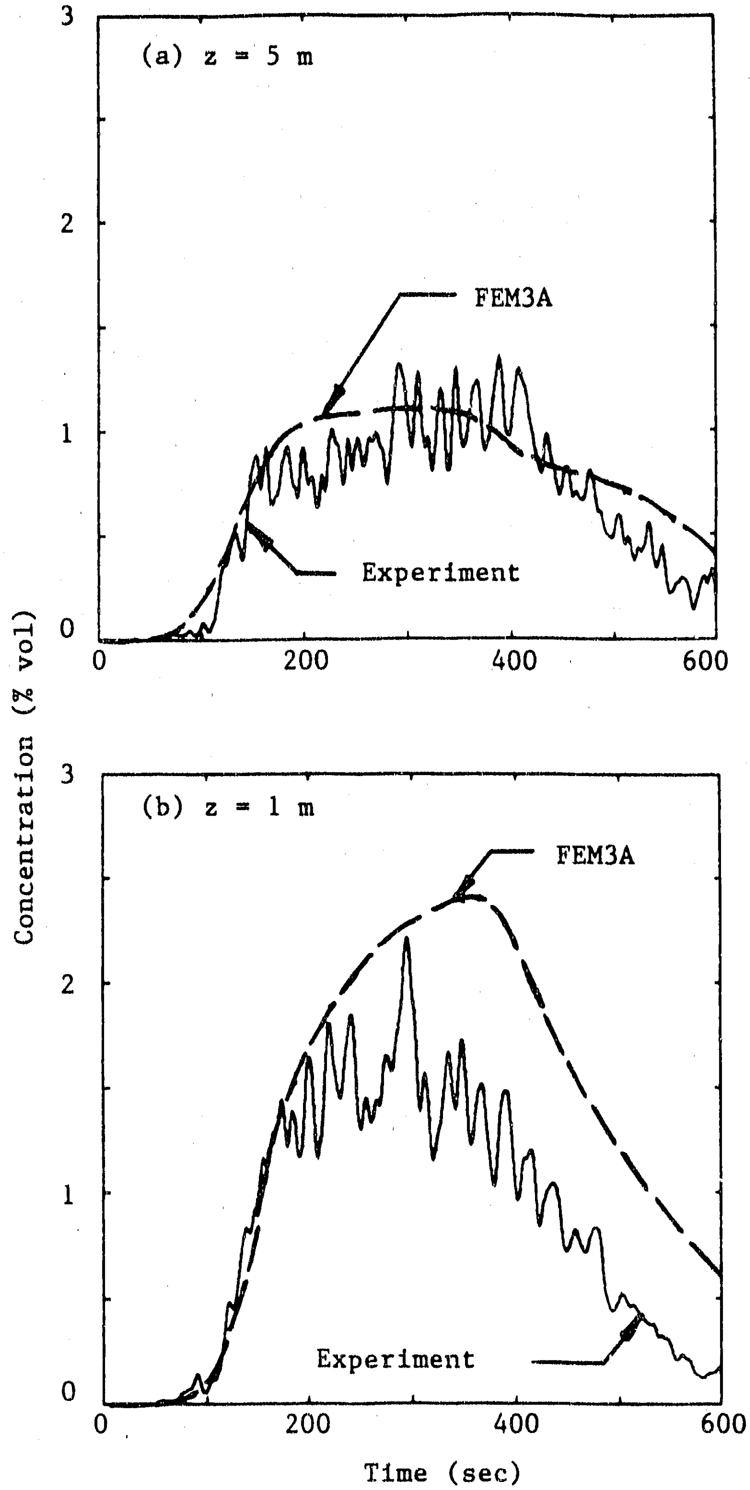

Fig. 3.45. Falcon-4 predicted versus measured concentration for two different heights at 250 m behind the rear fence. The predicted values are from the vertical plane of symmetry and the measurements are from gas sensor G16 (which is near the cloud centerline).

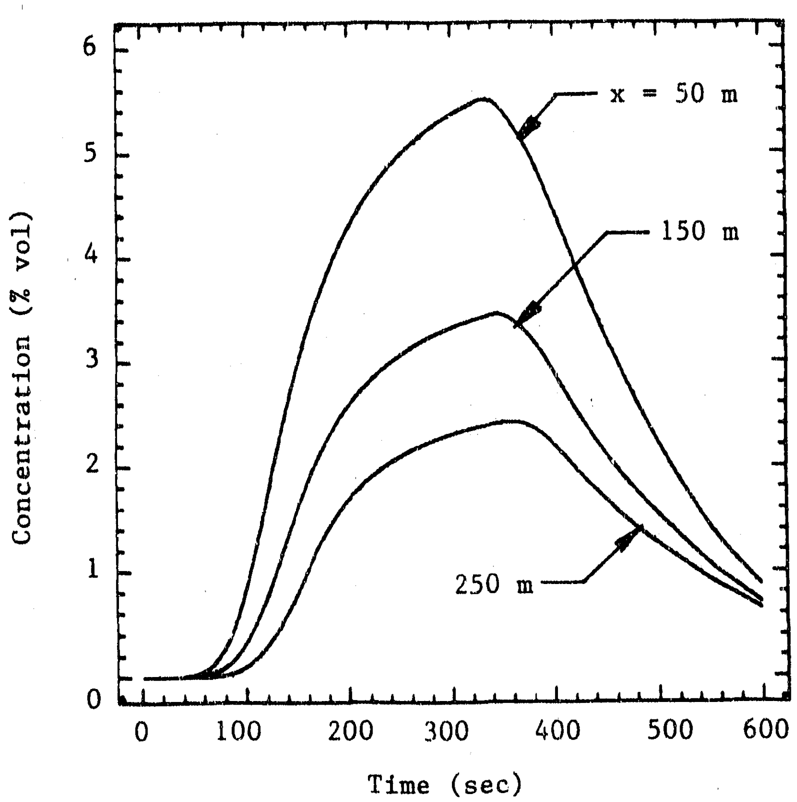

Fig. 3.46. Falcon-4 predicted time series of concentration for three locations behind the rear fence, which are on the plane of symmetry and 1 m above the ground surface.

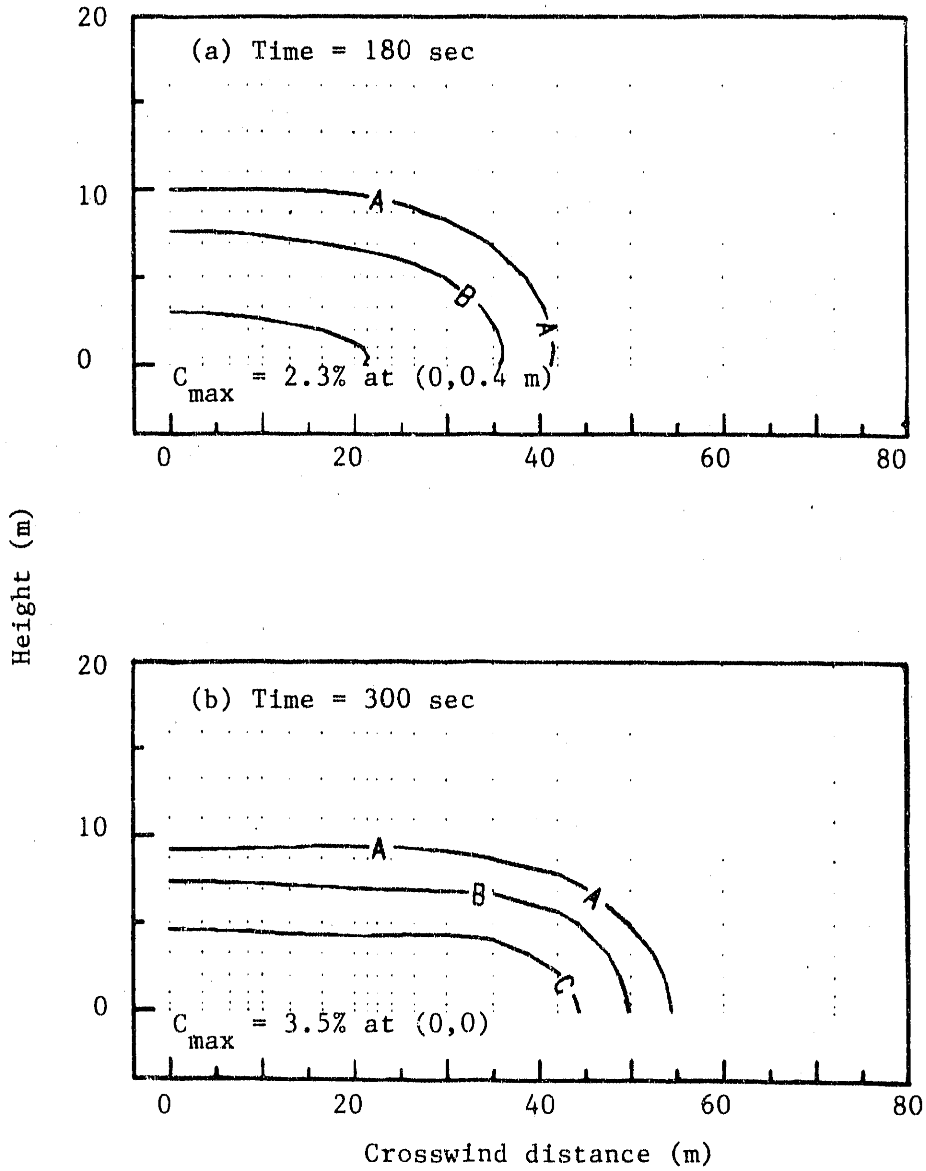

Fig. 3.47. Falcon-4 predicted concentration contours on the crosswind plane at 150 m behind the rear fence. The contour levels are (in % Vol): A=0.5, B=1.0, and C=2.0.

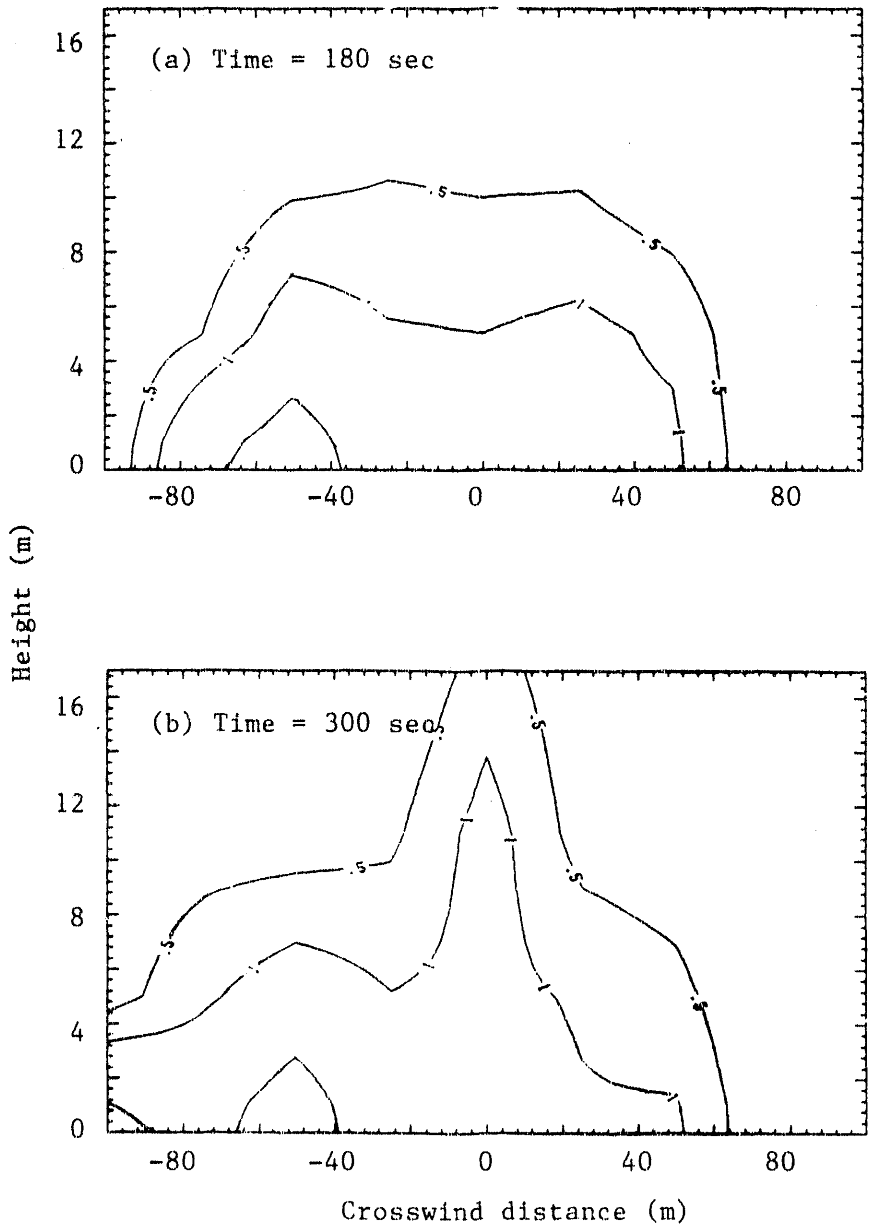

Fig. 3.48. Falcon-4 experiment concentration contours on the crosswind plane 150 m behind the rear fence.

which indicates a cloud of roughly the same height as predicted. However, the actual cloud width is considerably wider and its concentration near the ground is slightly lower.

In Fig. 3.49, the predicted peak concentrations along the cloud centerline are compared with field measurements. The agreement is excellent with regard to the concentration values and their variations in the downwind direction. Also superimposed in the figure are the results of a simulation without the vapor fence and the billboard. Without the fence, the concentration would have been nearly twice as high at 250 m and four times higher at 50 m. Also, the downwind distance to the 2.5% concentrtion would have been 365 m, instead of 230 m.

3.5 Comparison via the Ratio Method

In this subsection, the overall performance of the numerical model is assessed via applying the ratio method to the predicted and measured field variables as recommended by Ermak and Merry (1988). Included in such direct comparison are, for all four Falcon experiments, the maximum drop in temperature, cloud arrival and persistence times for certain concentration levels of practical importance, the peak values of concentration, and the maximum downwind distances to concentrations of 2.5% and 5% (the lower flammability limit of LNG). The relevant values are obtained from the figures presented earlier (either measured directly or, in a few cases, using linear interpolation/extrapolation of the plotted results) and summarized in Tables 3.3 through 3.8. These results are then plotted in Figs. 3.50 through 3.55.

In Fig. 3.50, the cloud persistence time inside the vapor fence based on the 5% and 15% concentration levels is displayed. The agreement between model predictions and measured data is very good, with fifteen of the sixteen data points falling within the range of 2/3 and 1 1/2 and the remaining one within a factor of 2. In Figs. 3.51 and 3.52, the cloud arrival and persistence times for concentrations of 1% and 2.5% at sample locations behind the vapor fence are depicted (see Tables 3.4 and 3.5 for their respective values). With only a

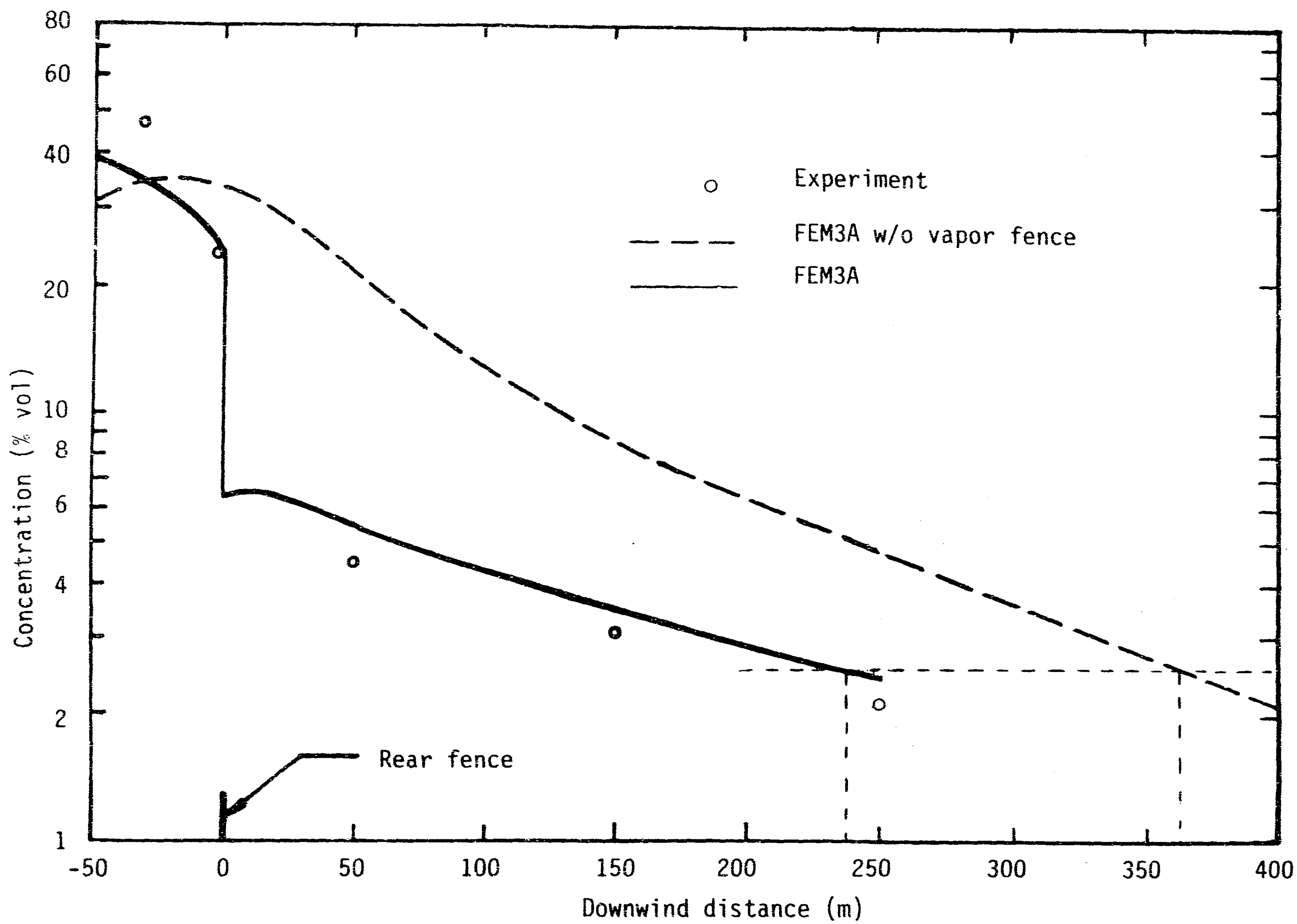

Fig. 3.49. Comparison of predicted versus measured peak concentrations in the downwind direction and at 1 m high for Falcon-4.

Table 3.3. Predicted versus observed cloud persistence times t_m/t_o (in sec) for concentration higher than 5% and 15% at sample locations within the vapor fence.

C	(x,y,z) in meters \ Test	Falcon-1	Falcon-2	Falcon-3	Falcon-4
5%	(-62, 0, 1)		262/161	363/269(1)	
	(-62, 20, 1)	315/347	241/199		
	(-32, 0, 1)		207/183	322/?(2)	446/346
	(-2, 0, 1)			360/396	420/391
15%	(-62, 0, 1)		153/128	243/166(1)	
	(-62, 20, 1)	216/174	136/173		
	(-32, 0, 1)		123/153	223/?(2)	325/272
	(-2, 0, 1)			250/327	276/332

Remarks:
(1) Field data measured at height of 2 m.
(2) Sensor failed at t>175 s approximately.

Table 3.4. Predicted versus observed cloud arrival times t_m/t_o (in sec) for concentration of 1% or 2.5% at sample locations behind the vapor fence.

(x,y,z) in meters \ Test	Falcon-1	Falcon-2	Falcon-3	Falcon-4
(50, 0, 1)	64/49	104/(2)	75/88	135/95
(50, 0, 5)	64/49	97/(2)	66/91	124/125
(150, 0, 1)	125/95	139/(2)	113/124	192/180
(150, 0, 5)	108/∞(1)	110/(2)(1)	91/121(1)	135/135(1)
(250, 0, 1)	191/150	123/207(1)	161/162	155/155(1)
(250, 0, 5)	143/398(1)	129/227(1)	130/175(1)	185/228(1)

Remarks:
(1) For concentration of 1%.
(2) No field data available.

Table 3.5. Predicted versus observed cloud persistence times t_m/t_o (in sec) for concentration of 1% or 2.5% at sample locations behind the vapor fence.

Test / (x,y,z) in meters	Falcon-1	Falcon-2	Falcon-3	Falcon-4
(50, 0, 1)	344/226	175/(2)	289/245	345/290
(50, 0, 5)	273/116	151/(2)	267/234	318/198
(150, 0, 1)	254/139	83/(2)	206/227	222/187
(150, 0, 5)	178/0(1)	200/(2)(1)	294/236(1)	357/275(1)
(250, 0, 1)	217/182	184/56(1)	138/205	377/292(1)
(250, 0, 5)	100/208(1)	66/60(1)	234/233(1)	200/194(1)

Remarks:

(1) For concentration of 1%.
(2) No field data available.

Table 3.6. Predicted versus measured maximum downwind distances (in meters, measured from the rear fence) for concentration of 2.5% and 5% at sample locations behind the vapor fence.

Concentration & Source / Test	2.5%			5%		
	Model	Data	Ratio	Model	Data	Ratio
Falcon-1	498	440	1.13	340	330	1.03
Falcon-2	200	N/A	—	70	N/A	—
Falcon 3	330	353	0.93	183	230	0.80
Falcon 4	230	203	1.13	65	28	2.32
Falcon-4 (no fence)	365	N/A	—	230	N/A	—

Table 3.7. Predicted versus observed decrease in temperature $\Delta T_p/\Delta T_o$ (in °C) at sample locations inside and outside of the vapor fence.

Test / (x,y,z) in meters	Falcon-1	Falcon-2	Falcon-3	Falcon-4
(-32, 0, 1)	134/100	105/116		90/105
(-2, 0, 1)	129/98	95/105	124/126	62/58
(50, 0, 1)	33/27	14.5/7	29/18.5	14.5/9.5
(50, 0, 5)	19/29	13/8.5	19/17	13/9.5
(150, 0, 1)	24/28	8.5/6.5	15.5/17.5	
(150, 0, 5)		5.5/5.5	7/7.5	

Table 3.8. Predicted versus observed peak values of concentration C_m/C_o (in % Vol) at sample locations inside and outside of the vapor fence.

Test / (x,y,z) in meters	Falcon-1	Falcon-2	Falcon-3	Falcon-4
(-62, 0, 1)		36/43.5	46/56	
(-62, 20, 1)	62.5/38.5	35/46.5		
(-32, 0, 1)		38.5/44	47.5/70	34/47.5
(-2, 0, 1)			46/51	23.5/23.5
(50, 0, 1)	15.5/23	5.4/(2)	10.5/9.7	5.4/4.0
(50, 0, 5)	7.8/4.4	4.7/(2)	6.5/10	4.6/3.2
(150, 0, 1)	11.2/15.6	3.1/(2)	5.7/7.6	3.4/3.0
(150, 0, 5)	4.8/0.4	1.7/(2)	2.1/3.2	1.8/2.2
(250, 0, 1)	7.2/8.2	1.9/1.5	3.6/4.5	2.4/2.2
(250, 0, 5)	4.4/4.0	1.1/1.4	1.7/3.1	1.1/1.3

Remarks:

(1) Field data measured at location (-62, 0, 2).

(2) No field data available.

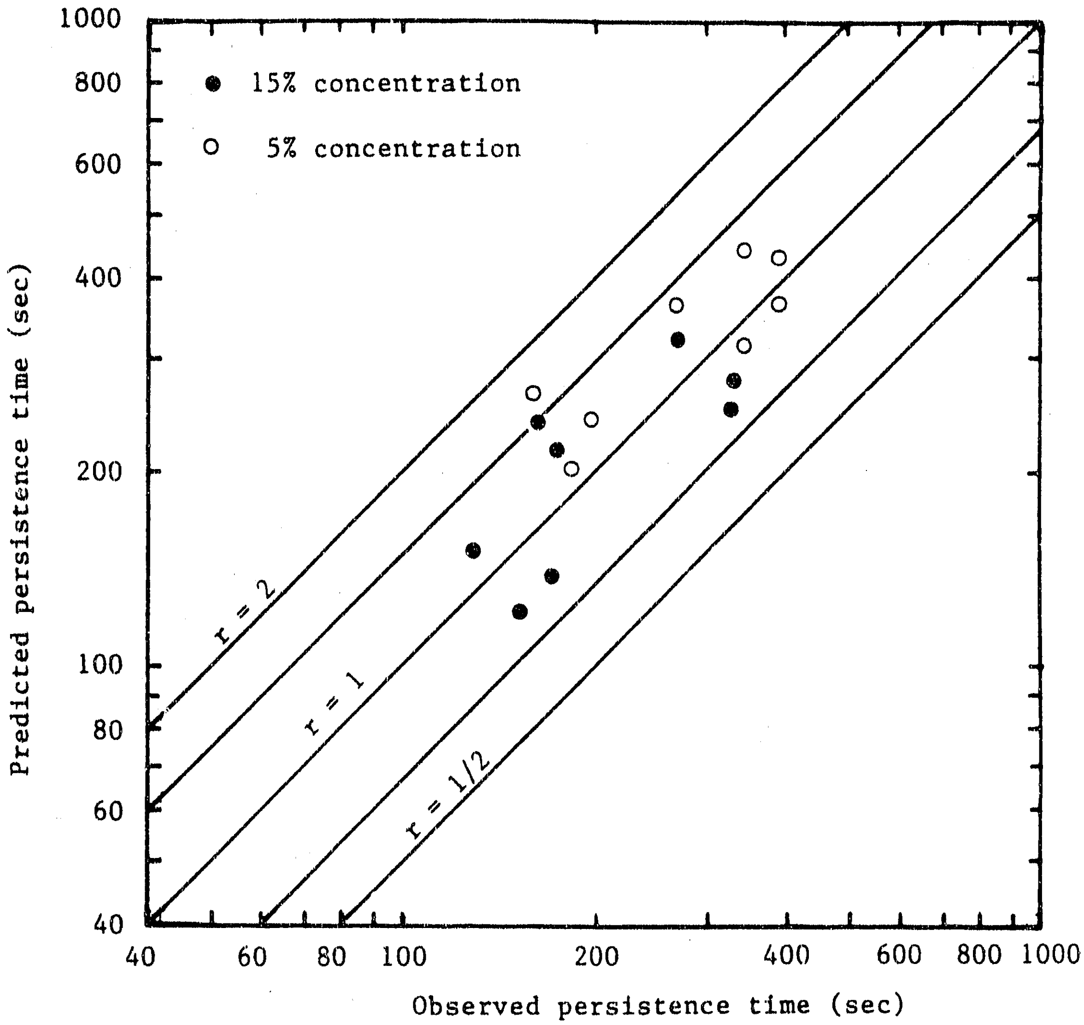

Fig. 3.50. Predicted versus observed cloud persistence times for concentration higher than 5% and 15% at sample locations within the vapor fence.

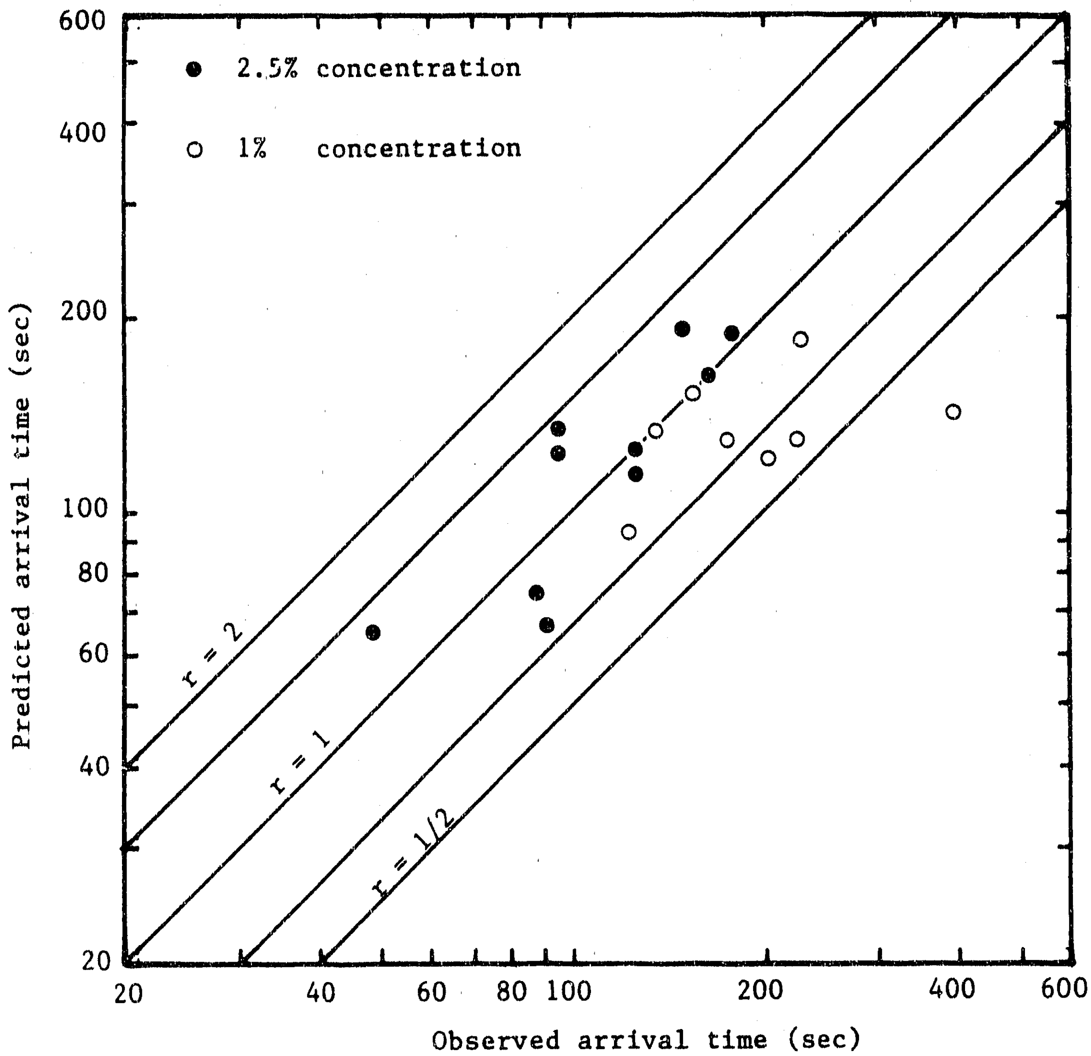

Fig. 3.51. Predicted versus observed cloud arrival times for concentrations of 1% or 2.5% at sample locations behind the vapor fence.

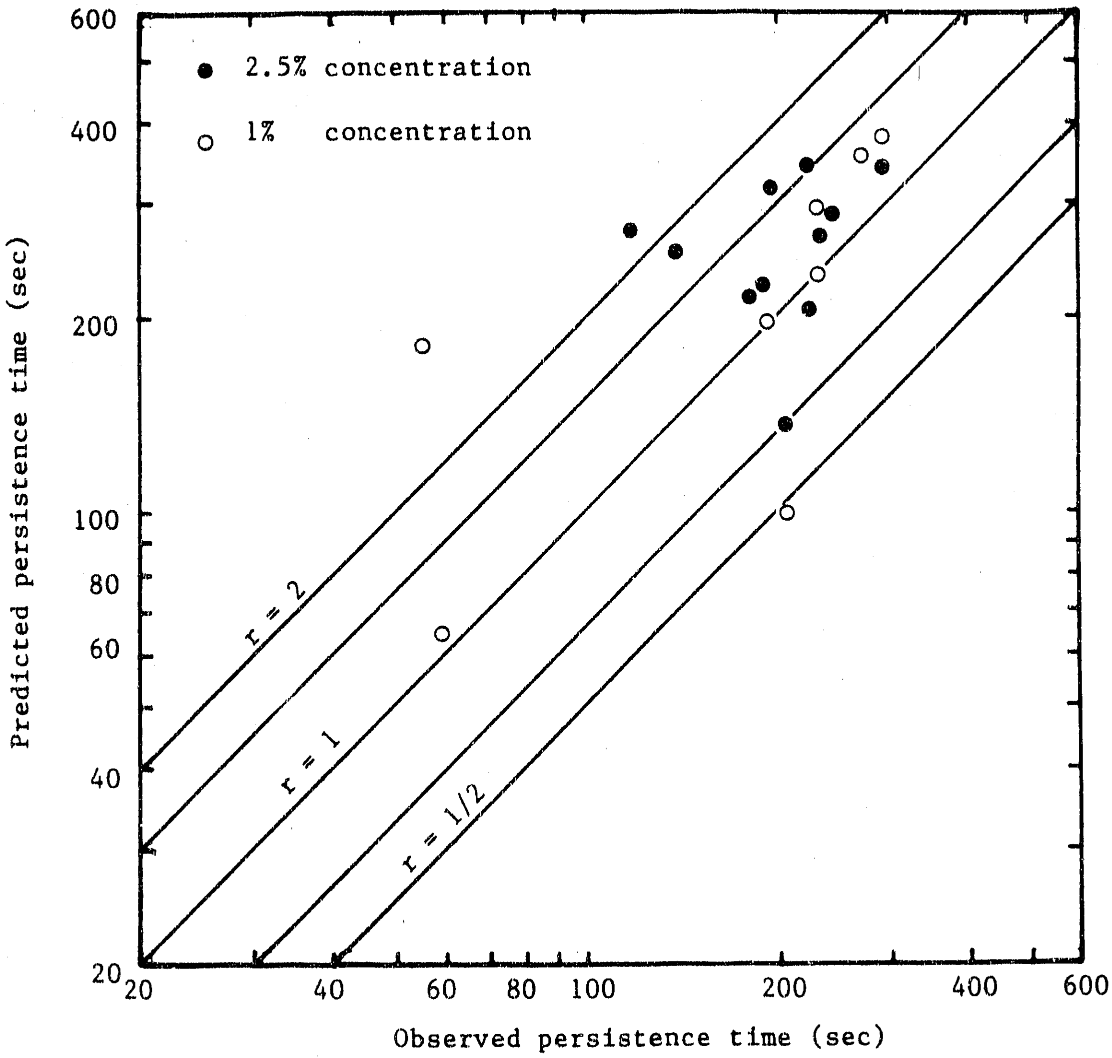

Fig. 3.52. Predicted versus observed cloud persistence times for concentration higher than 1% or 2.5% at sample locations behind the vapor fence.

few exceptions, the predictive values are within the range of 1/2 and 2 (mostly between 2/3 and 1 1/2). The exceptions include those locations at 5 m high in the Falcon-1 test, where a cloud/air interface with large gradients exists and is thus more difficult to predict well, and the location of (250 m, 0, 1 m) in Falcon-2, wherein significant cloud meandering appears to have occurred (see, e.g., Fig. 3.24), as opposed to a symmetric cloud assumed in the numerical model.

The predicted versus measured maximum downwind distances for concentration of 2.5% and 5% are tabulated in Table 3.6 and plotted in Fig. 3.53. Except for Falcon-2, which did not have concentration data at 1-m high for the 50-m and 150-m rows, all the remaining three tests were analyzed. Of the six values of ratio, five of them are within the range of 2/3 and 1 1/2, and the remaining one is slightly larger than 2 for the distance of the 5% concentration of Falcon-4.

Finally, the predicted versus observed maximum decrease in temperature and the peak values of concentration at all sampled locations, both inside and outside of the vapor fence, are presented in Tables 3.7 & 3.8 and plotted in Figs. 3.54 & 3.55. As is seen in Fig. 3.54, all the data points are bounded by a ratio between 1/2 and 2, with the majority falling within the range of 2/3 and 1 1/2. With one exception (out of the figure) of the data point for location (150 m, 0, 5 m) of Falcon-1 for reasons alluded to earlier, similar model performance is observed in Fig. 3.55 for the peak values of concentration.

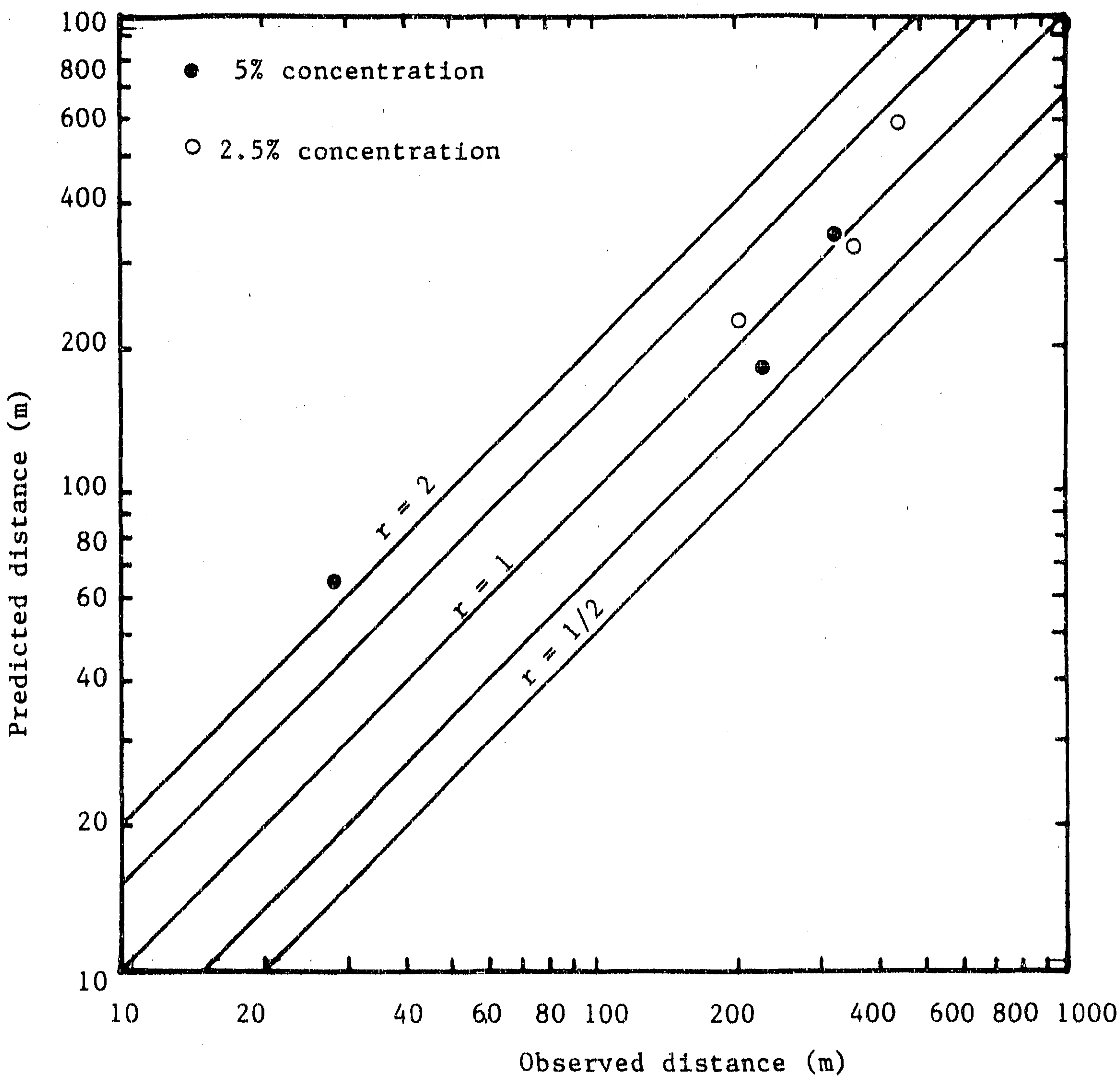

Fig. 3.53. Predicted versus meausred maximum downwind distances for concentration of 2.5% and 5%.

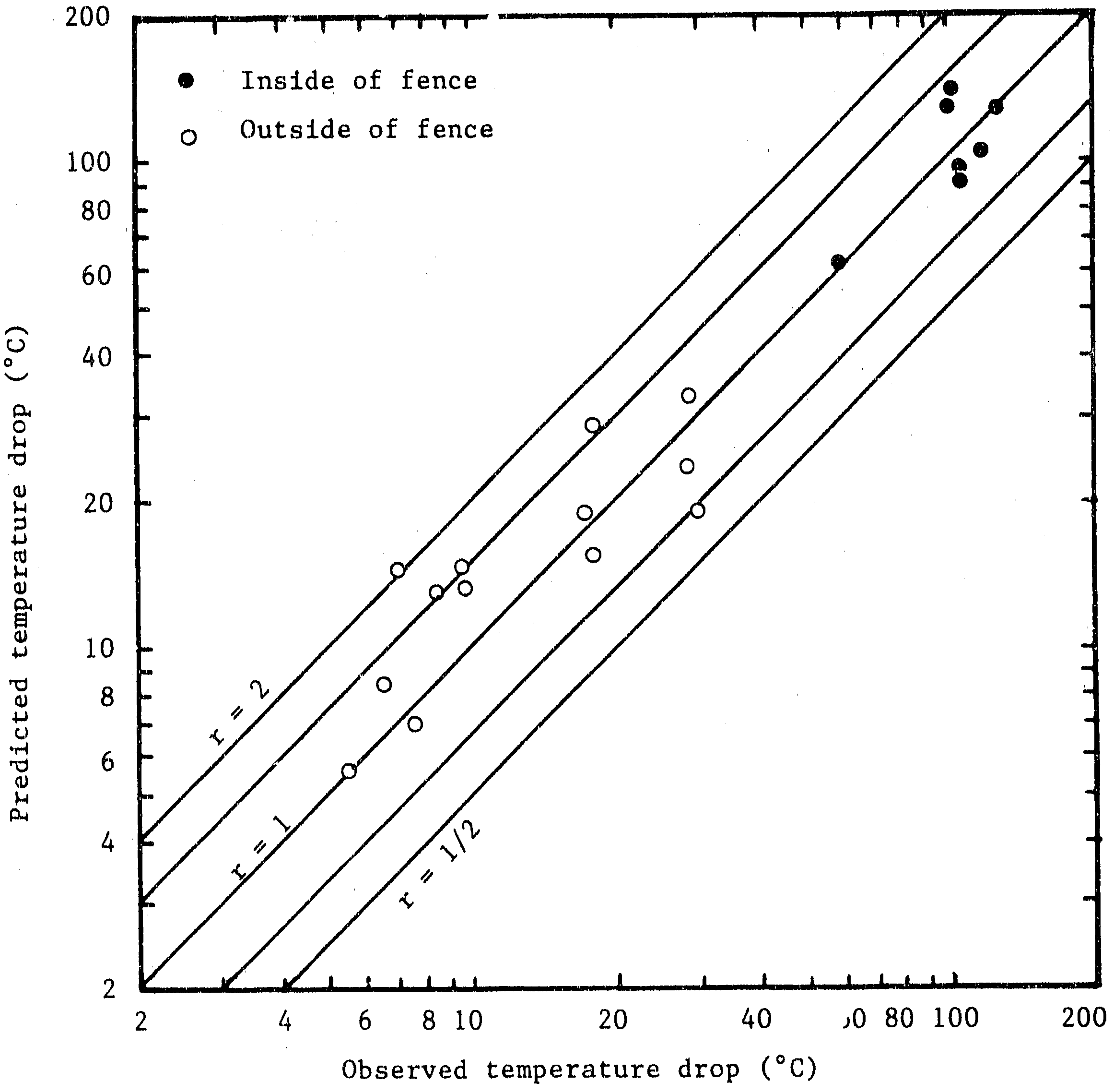

Fig. 3.54. Predicted versus observed decrease in temperature at sample locations inside and outside of the vapor fence.

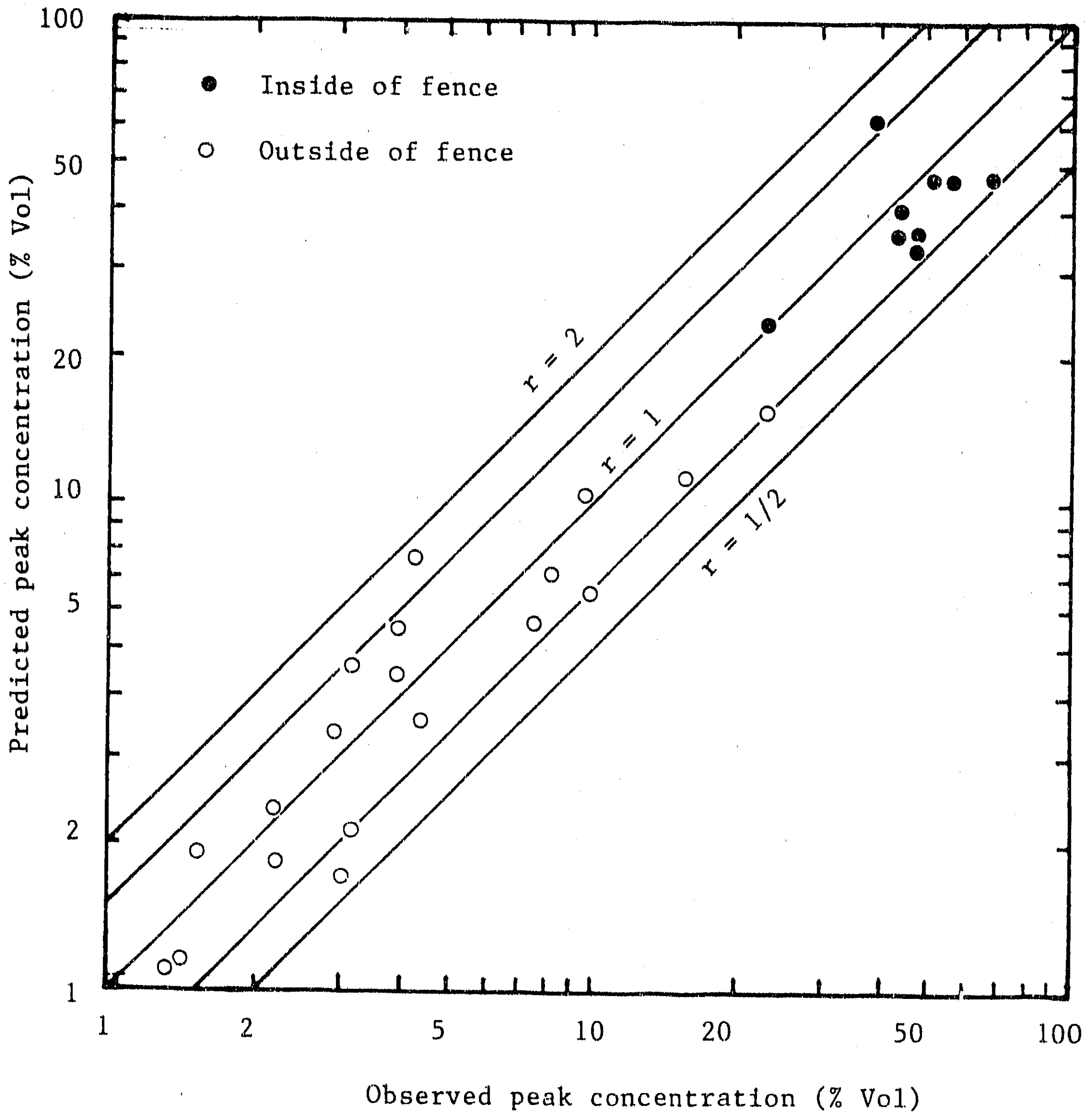

Fig. 3.55. Predicted versus observed peak values of concentration at sample locations inside and outside of the vapor fence.

4. CONCLUSIONS AND RECOMMENDATIONS

In this exploratory study, the FEM3A model has been applied to simulate four large-scale LNG vapor barrier field experiments and a detailed model-data comparison was made to evaluate its performance. The following are conclusions and recommendations based on the numerical results and a comparison with available field data.

1. The FEM3A model, with minor modifications, was able to reproduce the results of the vapor barrier field tests with reasonable accuracy. Specifically, a comparison between the predicted and measured variables, including the maximum change in temperature, the peak values of concentration, representative cloud arrival and persistence times, and the downwind distances to concentration of 2.5% and 5%, was made and the majority of the results agree well within a factor of two.
2. The predicted results of Falcon-1 are consistent with field observations, i. e., a vapor cloud overfilling the fenced enclosure, as opposed to a vapor cloud essentially contained within the fence at all times as observed in a pre-spill wind tunnel simulation. The surprising results of the Falcon-1 test are believed partly due to the greatly enhanced turbulence mixing (mainly induced by the extremely high LNG exiting velocity) and partly due to superheating of the LNG source by the water underneath. Although certain field data appear to substantiate the above claims, insufficient measurements of concentration and temperature in the source area have prevented us from reaching a more definite conclusion. If technically possible, laboratory experiments are highly recommended for testing the superheating hypothesis.
3. Based on the numerical results from simulations with and without the fenced enclosure for Falcon-2 and Falcon-4, an LNG vapor fence was observed to have the following advantages: significantly reduced concentration in the near field, delayed cloud arrival times at downwind locations, and a much shortened downwind distance of hazardous area. However, a vapor fence could also prolong the persistence time of the vapor cloud

in the source area, thus increasing the potential for ignition and combustion within the vapor fence and the area nearby.

4. Since the actual centerline of the Falcon-1 vapor cloud was about 20° off the center plane of the instrumentation array, the present assumption of the vapor cloud being symmetric about the center plane of the sensor array was not strictly valid. A full domain simulation with the correct mean wind direction is necessary for a more appropriate model-data comparison. Such a simulation would require substantial computer resources but is, nevertheless, computationally feasible and recommended to be performed in future studies.
5. Due to the complexity of the source conditions, which generally involve LNG pool spread, heat transfer and evaporation, and perturbations to turbulent mixing, etc., such processes have been parameterized with relatively simple submodels. Although such an approach appears to have performed reasonably well, the predicted cloud widths were generally narrower than observed. More sophisticated modeling of the source conditions and turbulent mixing may be necessary in order to simulate the cloud dispersion accurately at all locations. This is particularly true for the case of Falcon-1 wherein the dispersion process appears to be largely dominated by the spill conditions.
6. All the simulations presented herein were performed without the presence of water vapor. Although humidity did not appear to be a crucial factor in the unconfined LNG spills such as the Burros and Coyotes (Chan and Ermak, 1984), its effects were relatively significant in the marine environment (Colenbrander and Puttock, 1984) and may prove to be important for the present spills involving vapor barriers, especially under the conditions of the Falcon-1 experiment. A humidity submodel should probably be implemented in FEM3A for future investigation of such effects.

ACKNOWLEDGEMENTS

This work was performed under the auspices of the U.S. Department of Energy by the Lawrence Livermore National Laboratory under Contract W-7405-Eng-48. The funding for this study was provided by the Gas Research Institute (GRI) under contract 5088-252-1704. Ted Williams was the GRI project manager. The author would like to thank Ron Koopman for many stimulating discussions and Louise Morris for her assistance in generating the relevant experimental results. Ted Williams of GRI and Philip Gresho of LLNL offered many helpful comments on the draft. Marilyn Borton and Lonnette Robinson patiently and skillfully typed the manuscript.

REFERENCES

Britter, R. E. Atmospheric Dispersion of Dense Gases, Annual Review of Fluid Mechanics, 21, pp. 317-344, 1989.

Chan, S. T. and D. L. Ermak. Recent Results in Simulating LNG Vapor Dispersion Over Variable Terrain, Proceedings of the IUTAM Symposium on Atmospheric Dispersion of Heavy Gases and Small Particles, Springer-Verlag, pp.105-114, 1984.

Chan, S. T., D. L. Ermak, and L. K. Morris. FEM3 Model Simulations of Selected Thorney Island Phase I Trials, Journal of Hazardous Materials, 16, pp. 267-292, 1987.

Chan, S. T. FEM3A-A Finite Element Model for the Simulation of Gas Transport and Dispersion: User's Manual, Lawrence Livermore National Laboratory, UCRL-21043, April 1988.

Colenbrander, G. W. and J. S. Puttock. Maplin Sands Experiments 1980: Interpretation and Modeling of Liquefied Gas Spills onto the Sea, Proceedings of the IUTAM Symposium on Atmospheric Dispersion of Heavy Gases and Small Particles, Springer-Verlag, pp. 277-295, 1984.

Ermak, D. L. and M. H. Merry. A Methodology for Evaluating Heavy-Gas Dispersion Models, UCRL-21025, Lawrence Livermore National Laboratory, Livermore, CA. September 1988.

Gas Research Institute. Falcon Series Data Report: 1987 LNG vapor Barrier Verification Field Trials, GRI Report No. 89/0138, June 1990.

Ruff, M., F. Zumsteg, and T. K. Fannelop. Water Content and Energy Balance for Gas Cloud Emanating from a Cryogenic Spill, Journal of Hazardous Materials, 19, pp. 51-68, 1988.

U.S. DOT, Large LNG Spills Verification Field Trials, 1985.

Waite, P. J., R. J. Whitehouse, E. B. Winn, and W. A. Wakeham. The Spread and Vaporization of Cryogenic Liquids on Water, Journal of Hazardous Materials, 8, pp. 165-184, 1983.

Wiersma, S. J. and T. A. Williams. Vapor Fences for LNG Dispersion Control, Presented at the 1990 A.G.A. Distribution/Transmission Conference, Los Angeles, May 1990.

APPENDIX. THE FEM3A MODEL

In this appendix, we describe in some detail the theoretical basis of the FEM3A model (For more details, see Chan, 1988). Included are the governing equations, boundary conditions, initial conditions, and the submodels for representing the source and turbulence parameterization. The material phase-change submodel is not described because the dispersion simulations described in this report did not involve phase change. The spatial discretization and time integration procedures are also given.

Governing Equations

The following three-dimensional, time-dependent conservation equations, written for the mean (time-averaged) quantities in a turbulent flow field, are being solved in FEM3A:

$$\frac{\partial(\rho \mathbf{u})}{\partial t} + \rho \mathbf{u} \cdot \nabla \mathbf{u} = -\nabla p + \nabla \cdot (\rho \mathbf{K}^m \cdot \nabla \mathbf{u}) - (\rho - \rho_h)\mathbf{g} \; , \qquad \text{(A.1)}$$

$$\nabla \cdot (\rho \mathbf{u}) = 0 \; , \qquad \text{(A.2)}$$

$$\begin{aligned} \frac{\partial \theta}{\partial t} + \mathbf{u} \cdot \nabla \theta = & \frac{1}{\rho C_p} \nabla \cdot (\rho C_p \mathbf{K}^\theta \cdot \nabla \theta) \\ & + \frac{C_{pv} - C_{pa}}{C_p} (\mathbf{K}^c \cdot \nabla q_v) \cdot \nabla \theta \\ & + \frac{C_{pl} - C_{pa}}{C_p} (\mathbf{K}^c \cdot \nabla q_l) \cdot \nabla \theta - \frac{L}{C_p} (\frac{\partial q_v}{\partial t})_{pc} \; , \end{aligned} \qquad \text{(A.3)}$$

$$\frac{\partial q_v}{\partial t} + \mathbf{u} \cdot \nabla q_v = \frac{1}{\rho} \nabla \cdot (\rho \mathbf{K}^C \cdot \nabla q_v) + (\frac{\partial q_v}{\partial t})_{pc} \; , \qquad \text{(A.4)}$$

$$\frac{\partial q_l}{\partial t} + \mathbf{u} \cdot \nabla q_l = \frac{1}{\rho} \nabla \cdot (\rho \mathbf{K}^C \cdot \nabla q_l) - (\frac{\partial q_v}{\partial t})_{pc} \; , \qquad \text{(A.5)}$$

and

$$\rho = \frac{PM}{RT} = \frac{PM_a}{RT\left[1 + (\frac{M_a}{M_v} - 1)q_v - q_l\right]} \; . \qquad \text{(A.6)}$$

In the above equations,

$\mathbf{u}$	=	velocity field = (u, v, w),
ρ	=	mixture density,
p	=	pressure deviation from a hydrostatic pressure field (p_h)

corresponding to an isothermal state.

ρ_h = density field corresponding to the same isothermal state,

$\mathbf{g}$ = acceleration due to gravity,

θ = potential temperature deviation from the reference (isothermal) temperature field,

q_v = mass fraction of material in vapor phase,

q_l = mass fraction of material in liquid phase,

$\mathbf{K}^m$, $\mathbf{K}^\theta$, $\mathbf{K}^c$ = eddy diffusion tenors for momentum, energy, and species, respectively,

C_{pa} = specific heat of the ambient atmosphere,

C_{pv} = specific heat of the dispersed material in vapor phase,

C_{pl} = specific heat of the liquid material,

C_p = specific heat of the mixture = $C_{pv}q_v + C_{pl}q_l + (1 - q_v - q_l)C_{pa}$,

L = Latent heat of phase change for the dispersed material,

∇ = gradient operator,

t = time,

$(\frac{\partial q_v}{\partial t})_{pc}$ = time rate of change of material vapor due to phase change,

M = molecular weight of the mixture,

M_a = molecular weight of air,

M_v = molecular weight of the material in vapor form,

P = total pressure = $p_h + p$,

R = universal gas constant,

T = absolute temperature $= (\theta + \theta_o)[(P/P_o)R/MC_p] \simeq \theta + \theta_o$. P/P_o is approximately equal to unity for problems of current interest, which is fortunate since the last equation is strictly valid only when R/MC_p is constant.

The above set of equations, together with appropriate initial and boundary conditions, are solved to obtain the fields of velocity, pressure, temperature, mass fraction of the dispersed material (in vapor and liquid phases), and density of the mixture as functions of time and space. If the dispersed material is in vapor form only, Eq. (A.5) is removed from the above system and the terms involving q_l and $(\frac{\partial q_v}{\partial t})_{pc}$ in Eqs. (A.3), (A.4), and (A.6) are omitted. This was the case for the simulations presented in this report.

The equations for energy and species, as seen above, contain no source terms other than that due to material phase-change. The source material and the associated temperature are, in the present code, defined by either appropriate boundary conditions (to simulate an evaporating area source for continuous or finite-duration spills) or initial conditions (for instantaneous sources). Such source characterization will be discussed in the subsequent subsections.

Submodels

Source characterization. For continuous or finite-duration spills, the released source materials are modelled by vertically injecting the materials, in both vapor and liquid phases, from a predetermined area. Over such area, a constant mass flux $\dot{m}(\dot{m} = \rho v$, v being the vertical velocity component) is imposed for the duration of the release (the product of $\dot{m}$ with the size of the source area is equal to the total material spill rate).

The total mass flux per unit area can be separated into

$$\dot{m}_v = \dot{m}F \quad \text{for material vapor ,} \tag{A.7a}$$

and

$$\dot{m}_l = \dot{m}(1 - F) \quad \text{for liquid material .} \tag{A.7b}$$

In the above equation, F is the material fraction in vapor phase as determined by

$$F = C_{pl}(T_l - T_b)/L \ , \tag{A.8}$$

where

C_{pl} = specific heat of liquid at constant pressure,

T_l = liquid temperature,

T_b = boiling point of liquid at atmospheric pressure, and

L = latent heat of vaporization.

Equation (A.7) is implemented in the computer code as boundary conditions for the species equations in the following form,

$$K_v^c \frac{\partial q_v}{\partial n} = \dot{m}(F - q_v)/\rho \tag{A.9a}$$

and

$$K_v^c \frac{\partial q_l}{\partial n} = \dot{m}(1 - F - q_l)/\rho \tag{A.9b}$$

in which K_v^c is the eddy diffusivity in the vertical direction for the material species.

For the temperature equation, consideration of enthalpy balance leads to

$$K_v^\theta \frac{\partial \theta}{\partial n} = \dot{m}\{[C_{pv}F + C_{pl}(1 - F)](T_l - T_o)/C_p - \theta\}/\rho \ , \tag{A.10}$$

in which the new symbols are defined as

K_v^θ = eddy diffusivity in the vertical direction of the energy equation, and

T_o = reference temperature (above which θ is computed).

During source injection, the following boundary condition is also specified over the source area for the vertical momentum equation,

$$\rho v = \dot{m} \tag{A.11}$$

After the spill is terminated, the above boundary conditions are changed to correspond to zero fluxes ($\dot{m} = 0$ in Eqs. (A.9) through (A.11)) for the relevant variables.

For instantaneous releases, a different source submodel is employed. For each instantaneous source, a group of mesh points are designated to represent the desired source configuration filled with the material to be released. In each source region with the total mass fraction given, appropriate initial concentrations for vapor and liquid, and the corresponding temperature are determined by the code based on local thermodynamic equilibrium. In order to minimize the spatial oscillations in the concentration and temperature solutions due to the presence of short wave lengths (relative to the grid spacings) in the initial conditions (typically the step-function type), the initial concentration and temperature fields are often extended (smoothed) by trivariate Gaussian functions in the region immediately surrounding the nodes representing the sources. Additionally, velocity is specified to be zero and hydrostatic pressure is assumed to prevail within each source region. After a steady-state flow field has been established in a prerelease calculation with the source region(s) treated as obstructions(s), the constraints of zero velocity and hydrostatic pressure within these regions are removed to simulate the instantaneous release of the sources at zero time.

Turbulence Parameterization. Currently, FEM3A treats turbulence by using a K-theory local equilibrium model. The turbulence diffusion tensors $\mathbf{K}^m$, $\mathbf{K}^\theta$, and $\mathbf{K}^c$ are assumed to be diagonal and it is further assumed that $\mathbf{K}^\theta = \mathbf{K}^c$. Specifically, the vertical diffusion coefficient is given by

$$K_v = \frac{k[(u_{a*})^2 + (w_*)^2]^{1/2} z}{\Phi} , \qquad \text{(A.12)}$$

where

k = von Karman's constant = 0.4,

u_{a*} = friction velocity of the ambient atmosphere,

z = height above ground surface,

w_* = in-cloud "convection velocity" $= 0.5\ \{(g/T)v_E(T_{gr} - T)z\}^{1/3}$

g = acceleration of gravity,

T = cloud temperature (°K),

T_{gr} = ambient ground temperature (°K),

v_E = effective heat-transfer velocity from the ground into the vapor cloud, and

Φ = Monin-Obukhov profile function.

The form of the Monin-Obukhov profile function, Φ, is taken form Dyer (1974). When the Richardson number (Ri, to be defined later) is greater or equal to zero, Φ is defined as

$$\Phi = 1 + 5 \cdot Ri \qquad Ri \geq 0 \tag{A.13a}$$

for all three (momentum, energy, and species) vertical diffusion coefficients. When the Richardson number is less than zero, Φ is defined as

$$\Phi = \begin{cases} (1 - 16 \cdot Ri)^{-1/4} & \text{for momentum,} \\ (1 - 16 \cdot Ri)^{-1/2} & \text{for energy and species,} \end{cases} \qquad Ri < 0 \tag{A.13b}$$

The above equation indicates that, as the Richardson number becomes increasingly negative, the effects of convection are felt more strongly on the turbulent transport of heat and species than on momentum.

The local Richardson number is, in turn, defined by an *ad hoc* approach of "combining" the turbulence in the ambient atmosphere and the density stratification effects of the dispersing species,

$$Ri = Ri_a \frac{u_{a*}^2}{(u_{a*}^2 + w_*^2)} + nk^2(z/h_c)^n \frac{(\rho - \rho_a)}{\rho} \frac{gz}{(u_{a*}^2 + w_*^2)} \tag{A.14}$$

where the new symbols are defined below:

Ri_a = Richardson number of the ambient atmosphere $= z/L$, L being the Monin-Obukhov length scale,

ρ_a = density of the ambient atmosphere,

n =2, an empirical constant based on the two-dimensional experimental results of McQuaid (1976),

h_c = characteristic cloud height.

The first term on the right hand side of Eq. (A.14) is designed to include the turbulence in the ambient atmosphere and the second term represents the effects of density stratification, which is generally a reduction of turbulence in the stably stratified, dense gas cloud. As can be seen, for isothermal, neutrally buoyant gas or in the absence of a dispersing cloud, the present submodel recovers the ambient diffusivities. A typical Richardson number profile has a zero value at ground level and a maximum value near the top of the vapor cloud, where large-density gradient and small-shear stress normally exist.

The horizontal diffusion coefficient, K_h, is expressed as

$$K_h = \beta k u_{a*} z / \Phi_a, \tag{A.15}$$

where $\Phi_a = \Phi(Ri_a)$ and β is an empirical parameter with a value of 6.5, which was inferred from the Pasquill-Gifford curves for the horizontal and vertical dispersion coefficients σ_y and σ_z.

Ground Heat Transfer. For heavy gas dispersion problems involving cryogenic materials, e.g., liquefied natural gas (LNG), the effects of heat transfer from the warmer ground surface into the colder vapor cloud could significantly affect the dispersion process of the vapor cloud. The main effects from such ground heating are the decrease in mixture density and the increase of turbulence intensity, both of which tend to enhance the mixing and dilution of the vapor cloud.

A bulk coeffient submodel is currently used for the energy equations to account for the heat flux from the ground surface, i.e.,

$$K_v^\theta \frac{\partial \theta}{\partial n} = v_E(\theta_{gr} - \theta) \quad . \tag{A.16}$$

In this formula, v_E is an effective energy transfer velocity obtained from field measurements, θ_{gr} is the ground temperature, and θ is the temperature associated with the lower boundary of the computational domain.

Boundary Conditions

Figure A.1 illustrates some typical boundary conditions used in the simulation of heavy gas dispersion. Note the orientation of the coordinate system and the corresponding velocity components being used, which were chosen merely for the convenience of handling both two- and three-dimensional problems in one code. The origin of the coordinate system is normally placed at the center of the source area (in the case of a continuous/finite-duration spill) and the mean wind is assumed to be parallel to the x-y plane.

A wind profile is generally specified at the upwind boundary. This profile is expressed as a function of height above ground level (usually a logarithmic profile). A parabolic profile based on measured data, together with specified shear stress on the ground, is recommended to permit better simulation of the ambient wind profile without requiring the fine resolution of the surface "logarithmic region." The remaining variables on this surface are normally specified to correspond to the ambient conditions.

Natural boundary conditions are normally specified at the downwind (outflow) boundary. These conditions include zero normal "traction" for momentum in the x-direction and zero normal gradients for the remaining variables. On the top and lateral boundaries, which presumably are "far enough" from the vapor cloud, the respective normal velocity component and normal gradients of the remaining variables are set to be zero. If a lateral bounday is near the vapor cloud, the use of "open boundary" conditions is usually more appropriate. They include zero "traction" for the mementum equation in the normal direction and zero normal gradients for the remaining variables.

On the ground surface (either flat or variable) excluding the source area, either no-slip (zero velocity) or generalized "partial slip" boundary conditions can be specified for the

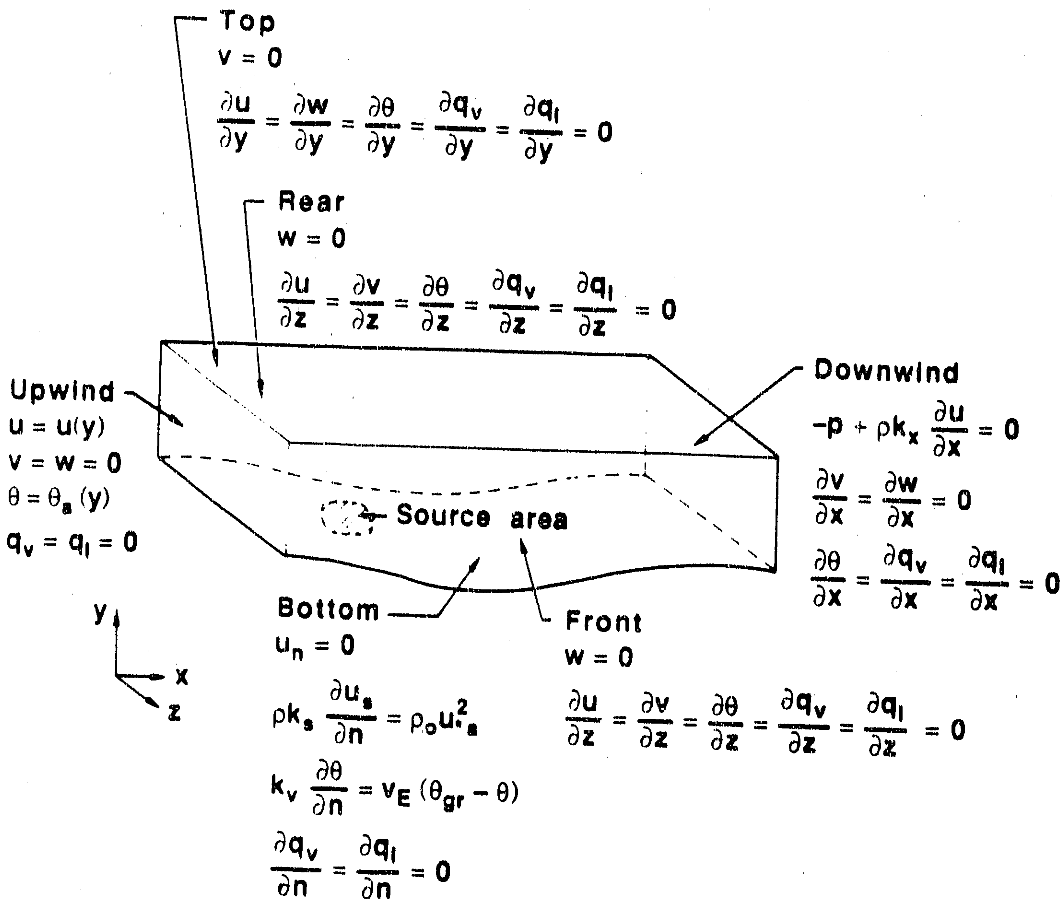

Figure A.1. Typical boundary conditions for the governing equations solved by the FEM3A model.

momentum equations. No-slip boundary condition are appropriate if sufficiently fine grid spacings are used to resolve the surface sublayer; otherwise, the "partial slip" boundary conditions are perhaps more appropriate. The latter usually implies that the normal velocity component is set to zero and shear stresses are specified in the tangential directions. For the case involving variable terrain, in order to apply "partial slip" boundary conditions, appropriate normal and tangential directions must be determined for the nodal points involved. In our current model, one of the tangential directions is chosen to be parallel to the x-y plane and, in this direction, a shear stress of $\rho_o u_{*a}^2$ is specified. Zero shear stress is specified along the other tangential direction because of the lack of field data in that direction and because the associated shear stress is much smaller. The appropriate boundary condition for mass fractions outside the source area is $\frac{\partial q_v}{\partial n} = \frac{\partial q_l}{\partial n} = 0$, i.e., there is no loss or gain of species at the ground surface.

For flat terrain, because the solution is symmetric about the vertical center plane, only one-half of the domain has to be considered. In this case, the center plane becomes the front surface, and symmetry boundary conditions are applied.

For finite duration spills, the flux boundary conditions of Eqs. (A.9) through (A.11) are imposed over the source area until the simulated source injection is terminated, after which the corresponding fluxes are set equal to zero for each appropriate variable.

For instantaneous spills, the mesh points and elements designated to represent the source containments are first specified to have zero velocity and pressure when a steady state flow field around the source(s) is being computed. These boundary conditions are then removed at zero time of the dispersion simulation to model the instantaneous release of the material within the source containments(s).

Initial Conditions

Before the start of a dispersion simulation, initial conditions corresponding to the ambient atmosphere must be established first. These initial conditions may, depending on the preexisting temperature field, correspond to either an isothermal or a stratified atmospheric flow. Generating the ambient flow field requires that the code be run without the species equations for a sufficient length of time (to reach a steady state wind field within the computational domain) prior to the actual vapor dispersion simulation. With an assumed wind field and appropriate boundary conditions, the code first performs a least-squares mass adjustment to obtain a mass-consistent wind field. Then it integrates in time the momentum equations with continuity constraints (and the temperature equation if required) until the solution reaches "steady" state. Such a mas-consistent, steady-state wind field and corresponding temperature field are then used as initial conditions in the vapor cloud dispersion simulation.

For instantaneous spills, the steady state wind field should also account for the presence of the source containments which are treated as obstructions via imposing the appropriate boundary conditions discussed above. In addition to such a steady-state wind field, in an all-vapor dispersion simulation, the initial mass fraction of vapor and the corresponding temperature must also be specified for each of the instantaneous source. For simulations involving vapor/liquid materials, the initial total mass fraction of the dispersed material is usually specified for each source, from which the model will determine the appropriate vapor/liquid distribution based on a local thermodynamic equilibrium submodel.

For continuous or finite-duration spills, since the injection-like source submodel (via boundary conditions. Eqs. (A.9) through (A.11)) is employed, the initial conditions for the species equations are always set to be zero. Also, for problems involving flat terrain, a wind field having a vertical profile identical to that at the inlet plane is often a good approximation to the initial velocities required in the dispersion simulation.

Spatial Discretization and Time Integration

In FEM3A, Eqs. (A.1) through (A.5) are discretized spatially without the terms involving $(\frac{\partial q_v}{\partial t})_{pc}$ by the Galerkin Finite Element Method (GFEM). The primary unknowns,

$U, V, W (U = \rho u, V = \rho v, W = \rho w)$, p, θ, q_v, and q_l are approximated as

$$U = \sum_{j=1}^{n} \Phi_j(\mathbf{x}) U_j(t) \quad ,$$

with similar expressions for V, W, θ, q_v, q_l, and

$$p = \sum_{j=1}^{M} \psi_j(\mathbf{x}) p_j(t) \quad ,$$

where, in the discretized domain, there are n nodes for velocity, temperature, and mass fractions and m nodes for pressure. The approximation functions, $\{\phi_i(\mathbf{x})\}$, are piecewise continuous polynomials that are one degree higher than those for the pressure approximation, $\{\psi_i(\mathbf{x})\}$. Currently, eight-node (four-node in two dimensions) isoparametric elements with trilinear (bilinear in two dimensions) approximations for velocity, temperature, mass fractions of the dispersed material, and piecewise constant approximation for pressure are used; thus, m is the total number of elements. When standard GFEM procedures are applied to Eqs. (A.1) through (A.5), the following coupled system of matrix equations is obtained:

$$M\dot{U} + [K + N(U)]u + CP = F \quad . \tag{A.17}$$

$$C^T U = 0 \quad , \tag{A.18}$$

$$M_s\dot{\theta} + [K_\theta + N_s(u)]\theta = F_\theta \quad . \tag{A.19}$$

$$M_s\dot{q}_v + [K_v + N_s(u)]q_v = F_v \quad . \tag{A.20}$$

and

$$M_s\dot{q}_l + [K_l + N_s(u)]q_l = F_l \quad , \tag{A.21}$$

where U and u are $3n$ global vectors containing all nodal values of $\rho\mathbf{u}$ and $\mathbf{u}$, respectively, P is an m global vector containing pressure values, M, K, and N (all $3n \times 3n$) are the mass matrix, the diffusion matrix, and the advection matrix, respectively, C is the $3n \times m$ pressure gradient matrix, its transpose, C^T, is the $m \times 3n$ divergence matrix, and F is a $3n$ global vector incorporating natural boundary conditions and the buoyancy force.

The matrices for temperature (θ) and the mass fractions of material vapor (q_v) and liquid material (q_l) are defined similarly, except their "size" is n instead of $3n$.

Equation (17) through (21) are integrated in time via a modified forward Euler method; that is, the physical diffusion tensors are augmented with a balancing diffusion tensor to compensate for the negative diffusion caused by the simple forward Euler method. Given U^n, which satisfies $C^T U^n = 0$, the time-marching algorithm is composed of the following steps:

1. Form the acceleration vector (without the pressure gradient),

$$A^n = M^{-1}[F^n - Ku^n - N(U^n)u^n] \quad . \tag{A.22}$$

2. Solve the linear algebraic system (discretized Poisson equation) for the compatible pressure via

$$(C^T M^{-1} C)P^n = C^T A^n \quad . \tag{A.23}$$

3. Update the mass flux, accounting for the pressure gradient.

$$U^{n+1} = U^n + \Delta t(A^n - M^{-1}CP^n) \quad . \tag{A.24}$$

4. Finally, in an "uncoupled step," update the temperature and mass fractions of the dispersed material.

$$\theta^{n+1} = \theta^n + \Delta t M_s^{-1}[F_\theta^n - K_\theta \theta^n - N_s(u^n)\theta^n] \tag{A.25}$$

$$q_v^{n+1} = q_v^n + \Delta t M_s^{-1}[F_v^n - K_v q_v^n - N_s(u^n)q_v^n] \tag{A.26}$$

and

$$q_l = q_l^n + \Delta t M_s^{-1}[F_l^n - K_l q_l^n - N_s(u^n)q_l^n] \quad . \tag{A.27}$$

Several cost-effective techniques, including mass lumping, reduced quadrature, subcycling, balancing diffusion, and others that significantly reduce computing costs without seriously compromising solution accuracy, have been implemented in the present model. These techniques were described in greater length by Gresho et al. (1984).

After solving Eqs. (A.22) through (A.27), the mixture density is computed from equation (A.6), i.e.,

$$\rho^{n+1} = \frac{P^n M_a}{RT^{n+1}[1 + (\frac{M_a}{M_v} - 1)q_v^{n+1} - q_l^{n+1}]} \tag{A.28}$$

APPENDIX REFERENCES

Chan, S.T. (1988) "FEM3A—A Finite Element Model for the Simulation of Gas Transport and Dispersion: User's Manual," UCRL-21043, Lawrence Livermore National Laboratory, Livermore, CA.

Dyer, A.J. (1974). "A Review of Flux-Profile Relationships," *Boundary- Layer Meteor.*, 7, 363–372.

Gresho, P.M., S.T. Chan, C.D. Upson, and R.L. Lee (1984). "A Modified Finite Element Method for Solving the Time-Dependent, Incompressible Navier-Stokes Equations: Part 1—Theory; Part 2—Applications," *Int. J. Num. Meth. Fluids, 4,* 557–598 and 619–640.

McQuaid, Jr. (1976). "Some Experiments on the Structure of Stably Stratified Shear Flows," Technical Paper P21, *Safety in Mines Research Establishment,* Sheffield, U.K.

END

DATE FILMED

02 / 08 / 91